

UC Berkeley

UC Berkeley Electronic Theses and Dissertations

Title

Experimental and Theoretical Studies of the Effects of Ti(IV) Tetrahedral Distortion on Adsorption and Catalysis by Ti/SiO₂

Permalink

<https://escholarship.org/uc/item/2xb5m3dx>

Author

Leonhardt, Branden Erich

Publication Date

2023

Peer reviewed|Thesis/dissertation

Experimental and Theoretical Studies of the Effects of Ti(IV) Tetrahedral Distortion on
Adsorption and Catalysis by Ti/SiO₂

By

Branden Leonhardt

A dissertation submitted in partial satisfaction of the

requirements for the degree of

Doctor of Philosophy

in

Chemical Engineering

in the

Graduate Division

of the

University of California, Berkeley

Committee in charge:

Professor Alexis T. Bell, Chair

Professor Martin Head-Gordon

Professor Alexander Katz

Fall 2023

*Experimental and Theoretical Studies of the Effects of Ti(IV) Tetrahedral Distortion on
Adsorption and Catalysis by Ti/SiO₂*

© Copyright 2023
Branden Leonhardt

Abstract

Experimental and Theoretical Studies of the Effects of Ti(IV) Tetrahedral Distortion on Adsorption and Catalysis by Ti/SiO₂

by

Branden Leonhardt

Doctor of Philosophy in Chemical Engineering

University of California, Berkeley

Professor Alexis T. Bell, Chair

This thesis investigates the existence and role of tetrahedral distortion of amorphous silica-supported titanol ($\equiv\text{Ti-OH}$) groups on their adsorptive and catalytic properties. Chapter 1 defines what distortion means and where it comes from and reviews the literature on distorted metal centers of silica-supported metal cations (SSMCs). We identify the significance of $\equiv\text{Ti-OH}$ groups and include a review of what has been studied specifically for $\equiv\text{Ti-OH}$ groups. We also review the literature on how SSMCs are currently modeled using computational chemistry (DFT) and identify development opportunities.

Chapter 2 presents experimental and theoretical evidence of distorted $\equiv\text{Ti-OH}$ groups supported on SiO₂ and examines the effect of distortion on the strength of adsorption of polar molecules. For the theoretical portion, we developed a model to represent isolated $\equiv\text{Si-OH}$ or $\equiv\text{Ti-OH}$ groups on the surface of amorphous silica. The $\equiv\text{M-OH}$ group is represented by a small cluster surrounded by a much larger cluster representing the surrounding amorphous silica. The small cluster's properties are described by high-level density functional theory (DFT) (i.e., the quantum mechanical (QM) region), whereas the large surroundings are represented by molecular mechanics (MM). We validated the QM/MM model by demonstrating that the predicted enthalpy of adsorption for seven polar molecules on $\equiv\text{Si-OH}$ groups agrees satisfactorily with experimentally measured values determined by microcalorimetry. We also found that enthalpies of adsorption on isolated $\equiv\text{Si-OH}$ groups determined from isotherms obtained by IR agree very well with the microcalorimetric values. We used IR spectroscopy to measure isotherms for pyridine adsorption to Lewis acidic Ti isolated $\equiv\text{Ti-OH}$ groups grafted to amorphous silica. The isosteric enthalpy of adsorption decreased in magnitude with increasing pyridine coverages up to a coverage of 15% and then remained relatively constant for higher coverages. Our QM/MM calculations made with our model revealed that the enthalpy of adsorption is proportional to the area of the triangular O-Ti-O facets of the $\equiv\text{Ti-OH}$ group to which pyridine is bound. $\equiv\text{Ti-OH}$ sites exhibiting facet areas consistent with those deduced from X-Ray Absorption Spectroscopy (XAS/EXAFS) measurements bind pyridine with adsorption enthalpies consistent with the observed plateau for pyridine coverage above 15%. Larger tetrahedral facet areas are required to explain the coverage-dependent adsorption enthalpies below 15% coverage, showing evidence of distorted $\equiv\text{Ti-OH}$ structures. Distorted $\equiv\text{Ti-OH}$ sites are also qualitatively consistent with reduced-intensity pre-edge X-Ray Absorption Near Edge Structure (XANES) measurements reported in this study. We carried out energy decomposition analysis (EDA) calculations to understand the underlying physical

phenomenon governing the change in the enthalpies of adsorption pyridine as a function of tetrahedral facet area.

Chapter 3 presents the effects of $\equiv\text{Ti-OH}$ site distortion in Ti/SiO_2 on the kinetics and mechanism of gas-phase cyclohexene (C_6H_{10}) epoxidation to form cyclohexene oxide ($\text{C}_6\text{H}_{10}\text{O}$). We develop a steady-state microkinetic model (MKM) to investigate the effects of distortion on predicted kinetic observables (apparent activation energy (E_a) and reaction orders in the partial pressures of C_6H_{10} and H_2O_2) and to establish whether a literature-proposed mechanism is consistent with observed kinetics. We discover that the predicted kinetics are inconsistent with experiments if the facet area distribution, given in Chapter 2 of this thesis, is the same facet area distribution under reaction conditions. This is due to the prediction of strong $\text{C}_6\text{H}_{10}\text{O}$ adsorption and inhibition. We find that much smaller facets than in the as-prepared material are required for good agreement ($<3.54 \text{ \AA}^2$) since $\text{C}_6\text{H}_{10}\text{O}$ does not inhibit these facets. We find small facets are generated under reaction conditions when $\text{C}_6\text{H}_{10}\text{O}$ adsorbs to $\equiv\text{Ti-OH}$ sites. This is because the facets opposite the one on which $\text{C}_6\text{H}_{10}\text{O}$ adsorbs of the same $\equiv\text{Ti-OH}$ site become contracted. We find that these vacant, contracted facets are active for epoxidation. We also find that the predicted activity remains essentially constant with the level of $\equiv\text{Ti-OH}$ site distortion. This new mechanism shows quantitative agreement between experiments and our predictions for all rate parameters.

In Chapter 4, we conduct a preliminary study of isopropanol (IPA) dehydration to propene and water. The mechanism occurs through an E2 (concerted) mechanism with more C-H bond-breaking character than C-O. We find that only 6% of active Ti sites are present, which was determined by combining the results of kinetic site-blocking measurements and in-situ FTIR spectroscopy. Theoretical calculations support the formation of Ti isopropoxide groups and show that these groups do not lead to appreciable propene formation rates. Further calculations reveal that sites must have tetrahedral facets larger than 4.2 \AA^2 for calculations to agree with experimentally observed partial pressure dependencies. Such large facets only occur for about 8% of $\equiv\text{Ti-OH}$ sites, reminiscent of the active fraction for IPA dehydration determined experimentally. This chapter shows that bulk spectroscopic techniques cannot identify the active sites for IPA dehydration since they are a minority species. Further research is needed to determine the active sites for this reaction.

Chapter 5 presents a summary and conclusions of this work and offers suggestions for future investigations.

Dedication

This is dedicated to my grandparents, Walter and Rosemarie.

Table of Contents

Abstract.....	1
Dedication.....	i
Table of Contents.....	ii
List of Figures.....	iii
List of Tables.....	xiii
Acknowledgments.....	xiv
1. Introduction.....	1
2 Experimental and Theoretical Evidence for Distorted Tetrahedral $\equiv\text{Ti-OH}$ Sites Supported on Amorphous Silica and Their Effect on the Adsorption of Polar Molecules.....	5
2.1 Abstract.....	5
2.2 Introduction.....	5
2.3 Methods.....	6
2.4 Results and Discussion.....	12
2.5 Conclusions.....	30
2.6 Acknowledgments.....	31
2.7 Supporting Information.....	32
3 The Effects of $\equiv\text{Ti-OH}$ Site Distortion and Product Adsorption on the Mechanism and Kinetics of Cyclohexene Epoxidation over Ti/SiO_2	61
3.1 Abstract.....	61
3.2 Introduction.....	61
3.3 Methods.....	65
3.4 Results and Discussion.....	69
3.5 Conclusions.....	86
3.6 Acknowledgments.....	87
3.7 Supporting Information.....	88
4 Preliminary Experimental and Theoretical Study of Unimolecular Isopropanol Dehydration over Ti/SiO_2	102
4.1 Introduction.....	102
4.2 Methods.....	103
4.3 Results and Discussion.....	106
4.4 Conclusions.....	126
4.5 Acknowledgments.....	127
5 Conclusions and Future Work.....	128
6 References.....	131

List of Figures

Figure 1.1: The two general representations of silica utilized in the literature as exemplified by a silanol ($\equiv\text{Si-OH}$) group. A) a small silsesquioxane model and B) a large amorphous silica model.....	2
Figure 1.2: Illustration of what is meant by the “tetrahedral facet area” of a $\equiv\text{Ti-OH}$ site.	3
Figure 2.1: Representative images of $\equiv\text{Si-OH}$ models employed in this study. A) T8 silsesquioxane B) T4 sized model of the amorphous model generated by Tielens et al. C) T8 sized model of the amorphous model D) QM/MM model that uses the model in Figure 2.1C as the QM region and an MM region that terminates 11Å in radius from the central $\equiv\text{Si-OH}$ site. E) Same as Figure 2.1D but the MM region extends 20Å from the central $\equiv\text{Si-OH}$ site. F) Same as Figure 2.1D but the MM region extends 29Å from the central $\equiv\text{Si-OH}$ site	11
Figure 2.2: Illustrations of $\equiv\text{Ti-OH}$ sites (only the QM region is shown) generated by selecting seven isolated $\equiv\text{Si-OH}$ sites and replacing the Si atom with Ti followed by geometry optimization of the QM region. Large red spheres: oxygen, large dark grey spheres: silicon, large white spheres: titanium, small white spheres: hydrogen. An example of the “tetrahedral facet area” is highlighted on site 1.....	12
Figure 2.3: A) FTIR spectra of pyridine adsorbed on $\text{SiO}_2\text{-1023}$ (T = 460 K) and B) isotherms collected using the integrated area of the peak centered at 1594 cm^{-1} for temperatures in the range of T = 420 K-460 K.	14
Figure 2.4: A) FTIR spectra of d_3 -acetonitrile adsorbed on $\text{SiO}_2\text{-1023}$ (T = 460 K) and B) isotherms collected using the integrated area of the peak centered at 2271 cm^{-1} for temperatures in the range of T = 420 K-460 K.	16
Figure 2.5: A) FTIR spectra of acetone adsorbed on $\text{SiO}_2\text{-1023}$ (T = 460 K) and B) isotherms collected using the integrated area of the peak centered at 1712 cm^{-1} for temperatures in the range of T = 420 K-460 K.	17
Figure 2.6: Adsorption configurations of acetone adsorbed to silanol groups on silica, as proposed in literature. ⁵⁵ The optimal bond distance between bifurcated silanols is shown, as calculated by others. ⁷⁶	17
Figure 2.7: A) FTIR spectra of trimethyl acetonitrile adsorbed on $\text{SiO}_2\text{-1023}$ (T = 460 K) and B) isotherms collected using the integrated area of the peak centered at 2243 cm^{-1} for temperatures in the range of T = 440 K-460 K.	18
Figure 2.8: Comparison of experimentally measured (connected lines) and theoretically predicted (bars) values of ΔH_{ads} . All calculations were performed for T = 460 K; however, similar conclusions are reached at other calculated temperatures. FTIR EAI = Fourier-transform Infrared Spectroscopy Equilibrium Adsorption Isotherm. Error bars for the T8 amorphous QM/MM model show the spread of predicted values of ΔH_{ads} made from multiple local minimum geometries, while the bar represents the Boltzmann-weighted ΔH_{ads} . Error bars on all experiments are $\pm 10\%$ of the reported value of ΔH_{ads}	20

Figure 2.9: A) Diffuse-reflectance UV/Vis spectrum of Ti/SiO₂₋₁₀₂₃ at 553.15 K under flowing He and B) pre-edge XANES spectra of Ti/SiO₂₋₁₀₂₃ and Ti[OSiPh₃]₄ . The pre-edge XANES spectra for Ti/SiO₂₋₁₀₂₃ was taken under flowing He.....	24
Figure 2.10: A) Difference spectrum for pyridine adsorbed on Ti/SiO_{2,1023} (sample 2) (T = 503.15 K, P _{py} = 0.42kPa). B) pyridine coverage on Ti/SiO_{2,1023} (sample 2) (mol Py/mol Ti) as a function of partial pressure (bar). Langmuir-Freundlich isotherm fits are shown as lines. Covers T-range 503.15 K through 623.15 K except 593.15 K. C) Isothermic enthalpy of adsorption of pyridine to ≡Ti-OH sites as a function of pyridine coverage (mol Py/ mol Ti). Facet areas calculated from the correlation presented in Figure 2.10D are labeled. The solid black line shows the predicted ΔH _{adso} of pyridine to a ≡Ti-OH site with a facet area derived from EXAFS (3.76Å ²), while dashed black lines are one standard error of the ΔH _{adso} prediction from the correlation in Figure 2.10D. The blue-shaded regions are guides for the eye. D) QM/MM calculations of ΔH _{adso} (T = 598 K) as a function of the tetrahedral facet area of the ≡Ti-OH site to which pyridine is bound). The solid line is the linear fit, while the dashed lines are one standard error of the estimated value of ΔH _{adso}	25
Figure 2.11: The dependence of each component of the EDA on the tetrahedral facet area.....	30
Figure S2.1: Mass thermogram of SiO_{2,Hyd} . Horizontal red dashed lines mark the mass utilized to calculate Δm _{TGA} in equation (1) of the main text.....	32
Figure S2.2: Mass thermogram of SiO_{2,1023} . Horizontal red dashed lines mark the mass utilized to calculate Δm _{TGA} in equation (1) of the main text.....	32
Figure S2.3: A) Normalized X-Ray Absorption Spectrum of Ti[SiOPh₃]₄ at ambient conditions. B) Magnitude and C) imaginary components of the Fourier-transformed k ² -weighted EXAFS	33
Figure S2.4: N ₂ adsorption isotherms for SiO_{2,hyd} and SiO_{2,1023}	34
Figure S2.5: FTIR Spectra of SiO_{2,hyd} , SiO_{2,1023} , and Ti/SiO_{2,1023} (sample 2). All spectra were normalized by the integrated absorbance of the Si-O-Si overtone region from 1735cm ⁻¹ to 2000cm ⁻¹	34
Figure S2.6: FTIR spectra of the OH stretching region of dehydroxylated fumed silica during pyridine adsorption. These spectra were acquired at 460K. In all spectra, we observed a sharp artefact near ~3743cm ⁻¹ which is the same frequency of isolated silanol groups for the bare material. We attribute this artefact to low transmittance in this region, and high noise, caused by the presence and abundance of isolated silanol groups.....	35
Figure S2.7: Linearly proportional relationship (R ² = 0.9983) between the integrated absorbance of the perturbed SiO-H stretching vibration and the integrated absorbance of the pyridine ring-breathing vibrational mode (8a, 1594cm ⁻¹) during pyridine adsorption experiments.....	36
Figure S2.8: FTIR spectra of pyridine adsorbed to SiO_{2,Hyd} at T = 460 K.	37
Figure S2.9: Reported heats of adsorption for pyridine adsorption to SiO ₂ measured from microcalorimetry experiments. The value derived by this work using FTIR and Langmuir modeling is shown, as well as the enthalpy of liquefaction. The vertical line	

shows the estimated surface density of isolated and geminal silanols as estimated by the Zhuravlev model.....	38
Figure S2.10: Representative peak deconvolution procedure during CD ₃ CN adsorption on SiO _{2,1023} (T = 460K, P _{acetone} = 0.5 kPa). Red curve is the cumulative peak fit, while black curve is the measured data. Gray curves are individual contributions. The C≡N stretching peak (2271cm ⁻¹) was fit as a Gauss-Lorentz function with 80% Lorentz weight.	39
Figure S2.11: FTIR spectra of the OH stretching region of dehydroxylated fumed silica during CD ₃ CN adsorption. These spectra were acquired at 460K. In all spectra, we observed a sharp artefact near ~3743cm ⁻¹	40
Figure S2.12: Linearly proportional relationship (R ² = 0.9994) between the integrated absorbance of the perturbed SiO-H stretching vibration and the integrated absorbance of the C≡N stretching frequency during CD ₃ CN adsorption experiments.	41
Figure S2.13: FTIR spectra of the C=O stretching region of an empty in-situ FTIR cell while flowing acetone at various partial pressures. These spectra were acquired at 460K. ..	42
Figure S2.14: Representative peak deconvolution procedure during acetone adsorption on SiO _{2,1023} (T = 420K, P _{acetone} = 0.36 kPa). Red curve is the cumulative peak fit, while black curve is the measured data. Gray curves are individual contributions from gas-phase acetone (left), acetone adsorbed to isolated/geminal silanols (middle), and acetone adsorbed to bifurcated silanols (right). Gas-phase acetone peak is represented by a gaussian, while adsorbed acetone peaks are Lorentzian peaks.....	43
Figure S2.15: FTIR spectra of the OH stretching region of dehydroxylated fumed silica during acetone adsorption. These spectra were acquired at 460K. In all spectra, we observed a sharp artefact near ~3743cm ⁻¹ . We attribute this artefact to low transmittance in this region caused by the presence and abundance of isolated silanol groups (relative to the path length).	44
Figure S2.16: Linearly proportional relationship (R ² = 0.9994) between the integrated absorbance of the perturbed SiO-H stretching vibration and the integrated absorbance of the C=O stretching frequency during acetone adsorption experiments.	45
Figure S2.17: Representative peak deconvolution procedure during trimethylacetonitrile adsorption on SiO _{2,1023} (T = 460K, P _{acetone} = 0.25 kPa). Red curve is the cumulative peak fit, while black curve is the measured data. Gray curves are individual contributions. The C≡N stretching peak (2243cm ⁻¹) was fit as a Gauss-Lorentz function with 50% Lorentz weight.	46
Figure S2.18: FTIR spectra of the OH stretching region of dehydroxylated fumed silica during trimethylacetonitrile adsorption. These spectra were acquired at 460K at the partial pressures shown in Figure 2.5B of the main text.	47
Figure S2.19: Linearly proportional relationship (R ² = 0.9997) between the integrated absorbance of the perturbed SiO-H stretching vibration and the integrated absorbance of the C≡N stretching frequency during CD ₃ CN adsorption experiments.	48
Figure S2.20: Effect of cluster model size on predicted enthalpies of adsorption. Models are listed by “Panel” as shown in Figure 2.1 of the main text. Panels D-F are QM/MM	

calculations that utilize Panel C as the QM region. The radii of the silica surrounding the central $\equiv\text{Si-OH}$ for Panels D-F are labeled.....	49
Figure S2.21: Relationship between Proton Affinity ⁷⁵ and the Boltzmann averaged heat of adsorption prediction for all polar molecules in the database shown in Figure 2.8 of the main text. This includes trimethylacetonitrile, d ₃ -acetonitrile, acetone, pyridine, ammonia, triethylamine, and tetrahydrofuran.	49
Figure S2.22: Relationship between Proton Affinity and magnitude of the SiO-H str. redshift (in cm^{-1}) for all polar molecules in the database shown in Figure 2.8 of the main text. This includes trimethylacetonitrile, d ₃ -acetonitrile, acetone, pyridine, ammonia, triethylamine, and tetrahydrofuran. The magnitude of the SiO-H str. redshift was taken as the maximum, centered value of the broad peak typically located between 3000-3600 cm^{-1} . For ammonia, triethylamine, and tetrahydrofuran, the redshifted values were taken as reported in the literature. ^{43,46}	50
Figure S2.23: Diffuse-reflectance UV/Vis spectrum of Ti/SiO₂₋₁₀₂₃ (sample 2) at 553.15K under flowing He after thermal treatment at 673K for 1h.	50
Figure S2.24: Normalized intensity (absorbance at peak center) of the pre-edge XANES feature measured for Ti/SiO_{2,1023} as a function of temperature under flowing He (Black) and the normalized intensity of the same feature for Ti[SiOPh ₃] ₄ at room temperature (red diamond).	51
Figure S2.25: Representative FTIR spectra of two consecutive pyridine adsorption experiments (i.e., two pellets of the same material) with SiO_{2,1023} ($T = 503\text{K}$, $P_{\text{Pyridine}} = 0.49\text{kPa}$) to demonstrate subtraction procedure. This demonstrates that our experimental method is reproducible and that features associated with pyridine interacting with silanols can be effectively subtracted in this way.	52
Figure S2.26: Integrated absorbance of the pyridine ring-breathing vibration (8a) as a function of partial pressure of pyridine and temperature. The circles show the integrated absorbance for one run, while the “+” show the subtracted peak areas from two consecutive runs for a representative temperature (503K). Since the “+” symbols fall on $y = 0$, this demonstrates experimental reproducibility.	53
Figure S2.27: A representative example of subtraction of the overlapping features associated with pyridine adsorption to silanols ($T = 503\text{K}$, $P_{\text{py}} = 0.42\text{kPa}$). The top line shows the FTIR spectrum of pyridine interacting with Ti/SiO_{2,1023} (sample 2 in this case). The middle line shows the FTIR spectrum of pyridine interacting with SiO_{2,1023} at identical conditions. The bottom line shows the subtraction result, which is the same spectra shown in Figure 2.10A. The spectra are offset for clarity.	53
Figure S2.28: Langmuir isotherm fit attempt to the pyridine adsorption data to Ti/SiO_{2,1023} (sample 2)	54
Figure S2.29: $\Delta H_{\text{isoo}}(\theta)$ as a function of pyridine fractional coverage when extrapolation of the Langmuir-Freundlich isotherms beyond 20% of the minimum/maximum coverage for a given isostere are allowed.....	55

Figure S2.30: $\Delta H_{iso}(\theta)$ as a function of pyridine fractional coverage when extrapolation of the Langmuir-Freundlich isotherms beyond 30% of the minimum/maximum coverage for a given isostere are allowed.....	55
Figure S2.31: Pyridine coverage on Ti/SiO _{2,1023} (sample 1) (mol Py/mol Ti) as a function of partial pressure (kPa). Langmuir-Freundlich isotherm fits are shown as lines. Covers T-range 503.15 K through 623.15K. Langmuir-Freundlich fits for each temperature are shown as continuous lines.	56
Figure S2.32: Comparison between the EDA calculation of pyridine bound to the $\equiv\text{Ti-OH}$ site of a T8 Silsesquioxane and the expected EDA based on the linear fits presented in Figure 2.11 of the main text.....	60
Figure 3.1: Illustration of what is meant by the “tetrahedral facet area” of a $\equiv\text{Ti-OH}$ site shown for the optimized structure of site 1 of our $\equiv\text{Ti-OH}$ site database. The equation on the left shows how the facet area is calculated, which is simply Heron’s formula for the area of a triangle. Large red spheres: oxygen, large dark grey spheres: silicon, large white spheres: titanium, small white spheres: hydrogen.	62
Figure 3.2: An expanded version of the literature proposed mechanism, hereafter called “Mechanism 1”. The rate constants for each elementary step are labeled, which will be discussed in detail in Methods.....	64
Figure 3.3: Effect of the tetrahedral facet area on ΔH_{adso} (T = 403.15 K) for multiple polar molecules present within the reactor during C ₆ H ₁₀ epoxidation. Reference states are one vacant $\equiv\text{Ti-OH}$ site and one gas-phase molecule. Lines shown linear models with the equation representing that line shown in the inset. The dashed lines show one standard error of the y-estimate.....	70
Figure 3.4: Optimized geometry of H ₂ O ₂ molecularly bound to site 1 of our $\equiv\text{Ti-OH}$ site database. Large red spheres: oxygen, large dark grey spheres: silicon, large white spheres: titanium, small white spheres: hydrogen.....	71
Figure 3.5: Optimized geometries of C ₆ H ₁₀ O to site 2, facet 2. A) the vector normal to the C-O-C triangle of the epoxide is nearly perpendicular to the $\equiv\text{Ti-OH}$ bond B) the vector normal to the C-O-C triangle of the epoxide is nearly parallel to the $\equiv\text{Ti-OH}$ bond. Large red spheres: oxygen, large dark grey spheres: silicon, large white spheres: titanium, small white spheres: hydrogen, large black spheres: carbon.	72
Figure 3.6: Representative optimized geometry of the $\equiv\text{Ti-OOH}$ structure for Site 2 (left) and schematic representing the formation of $\equiv\text{Ti}(\eta^2\text{-OOH})$ sites and the calculated average enthalpy and entropy change (right). Calculations are relative to a vacant site and gas-phase H ₂ O ₂ . Large red spheres: oxygen, large dark grey spheres: silicon, large white spheres: titanium, small white spheres: hydrogen.....	72
Figure 3.7: Two angles of view (A and B are the same structure) of the optimized geometry for the H ₂ O ₂ dissociation transition state (state C [‡]) for Site 1 – Facet 1 of our database. The average enthalpy and entropy, with the standard deviations, are displayed in the center of the figure (relative to a vacant site and gas-phase H ₂ O ₂). Large red spheres: oxygen, large dark grey spheres: silicon, large white spheres: titanium, small white spheres: hydrogen.....	73

Figure 3.8: Representative images of “In-Plane” and “Straddled” transition state geometries for epoxidation by site 1 of our database (left). The “In-Plane” transition structure shows two shaded triangles describing the meaning of “In-Plane.” Both triangles are in-plane with one another. Large red spheres: oxygen, large dark grey spheres: silicon, large white spheres: titanium, small white spheres: hydrogen, large black spheres: carbon. The effect of facet area on the enthalpies (relative to a vacant site and gas-phase H_2O_2 and C_6H_{10}) of transition states (right). The piecewise function in the inset shows the equations for both linear correlations. Dashed lines show one standard error in the estimated enthalpies from each correlation.74

Figure 3.9: MKM results for Mechanism 1 as a function of the tetrahedral facet area. Panels plot A) the apparent activation energy (E_a), B) reaction order in $\text{P}_{\text{H}_2\text{O}_2}$, C) reaction order in $\text{P}_{\text{C}_6\text{H}_{10}}$, and D) the fractional coverage of significant intermediates at $T = 403.15 \text{ K}$, $\text{P}_{\text{H}_2\text{O}_2} = 3 \text{ kPa}$, $\text{P}_{\text{C}_6\text{H}_{10}} = 3 \text{ kPa}$, $\text{P}_{\text{C}_6\text{H}_{10}\text{O}} = 30 \text{ Pa}$, and $\text{P}_{\text{H}_2\text{O}} = 30 \text{ Pa}$. The data points utilize DFT-calculated (thermally corrected to 403.15 K) enthalpies from structures specific to each site in our database - in situations where the energy of a state was not calculated for a specific facet, it was estimated from the linear correlations and averages presented in the previous section. The solid lines are the predicted values of the parameter in question for a given facet area calculated only using enthalpies from the linear correlations and averages presented in the previous section. The dashed lines show \pm two times the standard deviation of the parameter in question when the standard errors in the linear correlations presented in Figure 3.3 and the standard deviations in the averages used for transition state enthalpies are propagated. The results from Notestein and coworkers³² are displayed as the shaded region and take into account one standard error in the parameter measured. A vertical blue line shows the facet area of a tetrahedral $\equiv\text{Ti-OH}$ site constructed from EXAFS measurements (3.76 \AA^2) which represent the majority of $\equiv\text{Ti-OH}$ sites in the as-synthesized material.75

Figure 3.10: Effects of $\text{C}_6\text{H}_{10}\text{O}$ adsorption on the tetrahedral facet area of the vacant facets opposite the facet to which $\text{C}_6\text{H}_{10}\text{O}$ adsorbs. Sites 1-4 are the only sites in our database with more than one accessible facet. The horizontal dashed lines show the range of facet areas for Facet 2 and 3 after $\text{C}_6\text{H}_{10}\text{O}$ adsorption to Facet 1. Large red spheres: oxygen, large dark grey spheres: silicon, large white spheres: titanium, small white spheres: hydrogen, large black spheres: carbon.77

Figure 3.11: Mechanism 2, which includes the possibility of Facet 2 epoxidation catalysis with (Pathway B) and without (Mechanism 1-Facet 2) a $\text{C}_6\text{H}_{10}\text{O}$ co-adsorbed to Facet 1. .78

Figure 3.12: A) Enthalpy landscapes for all pathways in Mechanism 2 computed over Site 1. The reference state for Pathway B is adjusted to allow for easier visual comparison. B) Pathway B enthalpy landscape computed using DFT methods (solid line) and estimated Pathway B enthalpies using linear correlations and averages for a tetrahedral facet area equal to 3.49 \AA^2 . This facet area is the size of Facet 2 after the adsorption of $\text{C}_6\text{H}_{10}\text{O}$ to Facet 1.....79

Figure 3.13: Comparison of kinetic predictions for Mechanisms 1 and 2 as a function of facet area for the A) apparent activation energy, B) reaction order in H_2O_2 (top right), C) reaction order in C_6H_{10} (bottom left), and D) the degree of rate control for Mechanism

2 (bottom right). Conditions are $T = 403 \text{ K}$, $P_{\text{H}_2\text{O}_2} = 3 \text{ kPa}$, $P_{\text{C}_6\text{H}_{10}} = 3 \text{ kPa}$, $P_{\text{C}_6\text{H}_{10}\text{O}} = 30 \text{ Pa}$, $P_{\text{H}_2\text{O}} = 30 \text{ Pa}$. For Mechanism 2, the modified facet area is the largest of the two facets (Facet 1), with the Facet 2 area equal to 3.75 \AA^2 . The experimental results are displayed as the shaded region and take into account one standard error in the parameter measured. Black data points are the MKM results using the Gibbs free energies calculated for specific sites undergoing Mechanism 1. The yellow data point shows the MKM results for Mechanism 2 over Site 1. Black lines show the MKM results when the linear correlations in Figure 1 are used to estimate the enthalpies of states for Mechanism 1. Yellow lines show the MKM results for Mechanism 2 as a function of the Facet 1 area, the assumptions of which are outlined in the text. The dashed lines show \pm two times the standard deviation of the parameter in question when the standard errors in the linear correlations presented in Figure 3.3 and the standard deviations in the averages used for transition state enthalpies are propagated.

.....	84
Figure 3.14: A) The apparent activation energy, B) Reaction order in $P_{\text{H}_2\text{O}_2}$, C) Reaction order in $P_{\text{C}_6\text{H}_{10}}$, and D) the degree of rate control for each transition state in Mechanism 2 as a function of the partial pressure of $\text{C}_6\text{H}_{10}\text{O}$ and H_2O . Conditions are $T = 403 \text{ K}$, $P_{\text{H}_2\text{O}_2} = 3 \text{ kPa}$, and $P_{\text{C}_6\text{H}_{10}} = 3 \text{ kPa}$. The Facet 1 area is varied parametrically from 3.76 \AA^2 to 3.82 \AA^2 . The Facet 2 area is equal to 3.75 \AA^2 . Error bars for model calculations were omitted for clarity.	86
Figure S3.1	88
Figure S3.2: Representative optimized geometry of H_2O molecularly bound to Site 1 of our $\equiv\text{Ti-OH}$ database. Large red spheres: oxygen, large dark grey spheres: silicon, large white spheres: titanium, small white spheres: hydrogen.	89
Figure S3.3: Comparison of ΔH_{ads} of cyclohexene oxide to $\equiv\text{Ti-OH}$ sites with the vector normal to the COC bond parallel or perpendicular to the $\equiv\text{Ti-OH}$ bond.	90
Figure S3.4: Effect of tetrahedral facet area on $\Delta G_{\text{app}} \ddagger$ for Mechanism 1. $\Delta G_{\text{app}} \ddagger = \ln(\text{TOFs} - 1) - \ln k_B T h * -R(403.15 \text{ K})$. Conditions are $T = 403.15 \text{ K}$, $P_{\text{H}_2\text{O}_2} = 3 \text{ kPa}$, $P_{\text{C}_6\text{H}_{10}} = 3 \text{ kPa}$, $P_{\text{C}_6\text{H}_{10}\text{O}} = 30 \text{ Pa}$, and $P_{\text{H}_2\text{O}} = 30 \text{ Pa}$. The experimental value is shown as a horizontal green line. ³² The orange data points utilize DFT-calculated (thermally corrected to 403.15 K) enthalpies from structures specific to each site in our database - in situations where the energy of a state was not calculated for a specific facet, it was estimated from the linear correlations and averages presented in the previous section. The solid lines are the predicted values of the parameter in question for a given facet area calculated only using enthalpies from the linear correlations and averages presented in the previous section. The dashed lines show \pm two times the standard deviation of the parameter in question when the standard errors in the linear correlations presented in Figure 3.3 and the standard deviations in the averages used for transition state enthalpies are propagated.	95
Figure S3.5: Effect of tetrahedral facet area on the degree of rate control for Mechanism 1. Conditions are $T = 403.15 \text{ K}$, $P_{\text{H}_2\text{O}_2} = 3 \text{ kPa}$, $P_{\text{C}_6\text{H}_{10}} = 3 \text{ kPa}$, $P_{\text{C}_6\text{H}_{10}\text{O}} = 30 \text{ Pa}$, and $P_{\text{H}_2\text{O}} = 30 \text{ Pa}$	96

- Figure S3.6: Optimized geometry of State C^{‡3}, H₂O₂ dissociation over Facet 2 with C₆H₁₀O co-adsorbed to Facet 1 over Site 1. Large red spheres: oxygen, large dark grey spheres: silicon, large white spheres: titanium, small97
- Figure S3.7: Optimized geometry of State C^{‡4}, O-atom transfer to cyclohexene over Facet 2 with C₆H₁₀O co-adsorbed to Facet 1 over Site 1. The C-backbone of cyclohexene is pointed away from the surface and the C=C bond is straddling the Ti-O-Si bond. Large red spheres: oxygen, large dark grey spheres: silicon, large white spheres: titanium, small white spheres: hydrogen, large black spheres: carbon97
- Figure S3.8: Effect of the tetrahedral facet area on the fractional coverage of relevant intermediates for Mechanism 1 and 2. For Mechanism 2, the Facet 1 area is varied with Facet 2 = 3.75 Å². Conditions are T = 403 K, P_{H₂O₂} = 3 kPa, P_{C₆H₁₀} = 3 kPa, P_{C₆H₁₀O} = 30 Pa, P_{H₂O} = 30 Pa. The dashed lines show ± two times the standard deviation of the parameter in question when the standard errors in the linear correlations presented in Figure 3.3 of the main text and the standard deviations in the averages used for transition state enthalpies are propagated.99
- Figure S3.9: Effect of the tetrahedral facet area on Δ*G*_{app} ‡ for Mechanism 1 and 2. For Mechanism 2, the Facet 1 area is varied with Facet 2 = 3.75 Å². Conditions are T = 403 K, P_{H₂O₂} = 3 kPa, P_{C₆H₁₀} = 3 kPa, P_{C₆H₁₀O} = 30 Pa, P_{H₂O} = 30 Pa. The dashed lines show ± two times the standard deviation of the parameter in question when the standard errors in the linear correlations presented in Figure 3.3 of the main text and the standard deviations in the averages used for transition state enthalpies are propagated. The experimental value is shown as a horizontal green line.³²100
- Figure S3.10: Effect of product partial pressure and facet area on the fractional coverage of kinetically relevant intermediates calculated from the MKM based on Mechanism 2. Conditions are T = 403 K, P_{H₂O₂} = 3 kPa, and P_{C₆H₁₀} = 3 kPa. The Facet 1 area is varied parametrically from 3.76 Å² to 3.82 Å². The Facet 2 area is equal to 3.75 Å².101
- Figure 4.1: Overall stoichiometry for unimolecular dehydration of isopropanol to form propene and water.102
- Figure 4.2: A) Diffuse-Reflectance UV/Vis spectra of **Ti/SiO₂₋₁₀₂₃** under ambient (300 K, 100 mL/min He), dehydrated (T = 553.15 K, He, sample was pre-treated at 673 K for 1 h under flowing He) and reaction conditions (T = 553.15 K, 3 kPa IPA/He). B) Direct band-edge energies determined from Tauc plots for **Ti/SiO₂₋₁₀₂₃** (open circles) under dehydrated conditions (t = 0 min), and under 3 kPa IPA/He as a function of time. Also shown is the band-edge energy determined for **Ti/SiO₂₋₁₀₂₃** at ambient conditions (blue line), and the edge energies of various Ti isopropoxide silsesquioxane structures taken from ref.¹¹³ The dashed line is a guide for the eye.106
- Figure 4.3: Pre-edge XANES spectra of **Ti/SiO₂₋₁₀₂₃** at ambient (T = 300 K, He), dehydrated (spectra recorded at T = 553.15 K, He. The sample was pre-treated at 673 K for 1 h under flowing He before cooling to 553.15 K), and under 1.5 kPa of IPA/He. The pre-edge spectra for Ti[OSiPh₃]₄, a Ti tetrahedral standard, was previously measured in ref. X is reproduced above (green line).107

- Figure 4.4: In-situ FTIR spectra of **Ti/SiO₂₋₁₀₂₃** and **SiO₂₋₁₀₂₃** under 3 kPa IPA/He taken after 1 h. T = 553.15 K. Both spectra were baseline-subtracted.108
- Figure 4.5: A) IPA dehydration activity over **Ti/SiO₂₋₁₀₂₃** as a function of time on stream (mass = 25 mg, P_{IPA} = 3 kPa, total flow = 51 mL/min). The inset shows the deactivation equation and fit parameters that give the best fit (in a least-squares sense) B) Deactivation subtracted IPA dehydration activity as a function of time on stream. ..109
- Figure 4.6: A) Arrhenius plot of the average TOF value for each temperature derived from the data in Figure 4B. B) Effect of IPA and water partial pressures on the TOF over **Ti/SiO₂₋₁₀₂₃**. We note the TOF was not corrected for deactivation.110
- Figure 4.7: A) IPA dehydration activity over **Ti/SiO₂₋₁₀₂₃** as a function of time on stream (mass = 25 mg, P_{d-IPA} = 3 kPa, total flow = 51 mL/min) using perdeuterated IPA initially, followed by switching to perhydrogenated IPA (P_{IPA} = 3 kPa). The inset shows the deactivation equation and fit parameters that give the best fit (in a least-squares sense) to the perdeuterated TOF data before switching to perhydrogenated IPA B) Ratio of the TOF measured using perhydrogenated IPA to the deactivation model extrapolated TOF fit to the TOF data collected with perdeuterated IPA at early times on stream. 111
- Figure 4.8: Illustration of the continuum of possible dehydration mechanisms and their expected KIEs for T = 553.15 K.^{116,118}112
- Figure 4.9: A) The effect of pyridine cofeeding at multiple partial pressures as a function of time on stream (T = 553.15 K). The TOF values were not deactivation subtracted. The deactivation function is shown as a solid line. B) Normalized TOF as a function of the partial pressure of pyridine. The TOF values were normalized to the initial TOF just before pyridine injection. For pyridine partial pressures in which multiple TOF values were collected, the average was used. The line shows the fit function in the inset. ..112
- Figure 4.10: A) in-situ FTIR spectra of pyridine adsorbed to **Ti/SiO₂₋₁₀₂₃** at multiple pyridine partial pressures and in the presence of 3 kPa IPA (T = 553 K). B) Normalized TOF as a function of pyridine partial pressure (reproduced from Figure 4.9B), and the intensity of the peak centered near 1604 cm⁻¹ as a function of pyridine partial pressure. The second y-axis describing the intensity was scaled such that 0.000 abs.u. equaled a normalized TOF of 1, and 2.52x10⁻³ abs.u. equaled a normalized TOF of 0.39 (see text). The line shows the fit function in the inset.115
- Figure 4.11: Optimized geometries for the adsorption of IPA (State C2) and the formation of a ≡Ti-OiPr (State C3), optimized at the ωB97X-D/def2-SVP level of theory. The MM region extends 29 Å in radius from the central Ti atom, but it is not shown for clarity.117
- Figure 4.12: A) QM/MM calculations of Δ*H_{adso}* (T = 553.15 K) as a function of the tetrahedral facet area of the ≡Ti-OH site to which IPA is bound). The solid line is the linear fit, while the dashed lines are one standard error of the estimated value of Δ*H_{adso}* adopted from Chapter 2 for the same correlation derived from enthalpies of pyridine adsorption to ≡Ti-OH sites. B) The fractional coverage of states C1, C2, C3, and C4 as a function of the tetrahedral facet area. P_{IPA} = 3 kPa, P_W = 13 Pa, T = 553.15 K..118
- Figure 4.13: Optimized geometries of a ≡Ti-OiPr (State C3) and the intra-molecular H shift to form propene (State C^{‡1}). All structures were optimized at the ωB97X-D/def2-SVP

- level of theory. The MM region extends 29Å in radius from the central Ti atom, but it is not shown for clarity.119
- Figure 4.14: Optimized geometries of a $\equiv\text{Ti-OiPr}$ (State C3) and the H shift to a Ti-O-Si bond to form propene (State C \ddagger ²). All structures were optimized at the $\omega\text{B97X-D/def2-SVP}$ level of theory. We note that State C4 was not computed since it was not needed to assess the forward rate of propene formation from C3 through transition state C \ddagger ². The MM region extends 29Å in radius from the central Ti atom, but it is not shown for clarity.120
- Figure 4.15: Optimized geometry of State C1 (vacant site) using Site 7 of our database. The MM region extends 29Å in radius from the central Ti atom, but it is not shown for clarity. The tetrahedral facet with an area of 4.07 Å² is highlighted using a yellow triangle.122
- Figure 4.16: Optimized geometries of a molecularly adsorbed IPA molecule to Site 7 (State C2) and E2 (concerted) transition states for propene formation where the β -H is abstracted by the Ti-O-Si bond (State C \ddagger ³) or by the titanium hydroxyl (State C \ddagger ⁴). All structures were optimized at the $\omega\text{B97X-D/def2-SVP}$ level of theory. The MM region extends 29Å in radius from the central Ti atom, but it is not shown for clarity.122
- Figure 4.17: Modified Ti sites structures all based on Site 7. A) Optimized geometry of a Ti dimer which was generated by replacing the Si that formed two Si-O-Ti bonds with the central Ti in Site 7. B) Optimized geometry of the $\equiv\text{Ti-OH}$ site from Site 7 that now forms a H-bond with a neighboring silanol group. The H-bond distance is shown.124
- Figure 4.18: A) Optimized geometries of a molecularly adsorbed IPA molecule to the dimer form of Site 7 (State C2, Ti-O-Ti) and E2 (concerted) transition states for propene formation where the β -H is abstracted by the Ti-O-Ti bond (State C \ddagger ^{3, Ti-O-Ti}). B) Optimized geometries of a molecularly adsorbed IPA molecule to the H-bonded form of Site 7 (State C2, SiOH) and E2 (concerted) transition states for propene formation where the β -H is abstracted by the titanium hydroxyl (State C \ddagger ^{4, SiOH}). All structures were optimized at the $\omega\text{B97X-D/def2-SVP}$ level of theory. The MM region extends 29Å in radius from the central Ti atom, but it is not shown for clarity.124
- Figure 4.19: The apparent order in the partial pressure of water (P_w) as a function of the tetrahedral facet area assuming State C2 is the true resting state for IPA dehydration. $T = 553.15\text{ K}$, $P_{\text{IPA}} = 3\text{ kPA}$126

List of Tables

Table 1.1: Summary of the reactions catalyzed by SSMCs and their proposed dehydrated and oxidized structures	1
Table 2.1: Bond lengths and tetrahedral facet areas of $\equiv\text{Ti-OH}$ sites*	12
Table 2.2: Assigned adsorption modes, peak centers, and Langmuir fitting parameters determined via FTIR coverage experiments for polar molecules adsorbed to $\text{SiO}_2\text{-1023}$	18
Table 2.3: Gas phase entropies and entropies of adsorption, $P^\circ = 1$ bar – comparison between predictions and experiments	22
Table 2.4: ICP characterization, UV Vis edge energies	24
Table 2.5: Linear fit parameters for lines in Figure 2.11	30
Table S2.1: EXAFS fitting parameters for $\text{Ti}[\text{OSiPh}_3]_4$ fit from 1-2.2 Å	33
Table S2.2: Assigned adsorption modes, peak centers, and Langmuir fitting parameters determined via FTIR coverage experiments for pyridine adsorbed to $\text{SiO}_2\text{-Hyd}$	37
Table 3.1: Predicted rate parameters for cyclohexene epoxidation via Mechanism 2 over Site 1 compared with those determined experimentally	81
Table S3.1: Gas phase entropies ($T = 298.15$ K, $P^\circ = 1$ bar) – comparison between qRRHO predictions and literature	88
Table S3.2: Enthalpies and entropies of formation of $\equiv\text{Ti-OOH}$ sites + $\text{H}_2\text{O}(\text{g})$ (state C4 in Mechanism 1) from H_2O_2 and $\equiv\text{Ti-OH}$ sites	90
Table S3.3: Enthalpies and entropies of activation ($T = 403.15$ K) of $\equiv\text{Ti-OOH}$ sites + $\text{H}_2\text{O}(\text{g})$ (state $\text{C}^\ddagger 1$ in Mechanism 1&2) from H_2O_2 and $\equiv\text{Ti-OH}$ sites	91
Table S3.4: Enthalpies and entropies of activation ($T = 403.15$ K) of O-atom transfer to cyclohexene (state $\text{C}^\ddagger 2$ in Mechanism 1&2) for in-plane geometries	92
Table S3.5: Enthalpies and entropies of activation ($T = 403.15$ K) of O-atom transfer to cyclohexene (state $\text{C}^\ddagger 2$ in Mechanism 1&2) for straddled geometries	93
Table 4.1: Enthalpy, entropy and Gibbs free energy estimates for States C3 and $\text{C}^\ddagger 1$	120
Table 4.2: Enthalpy, entropy, and Gibbs free energy estimates for States C3 and $\text{C}^\ddagger 2$	121
Table 4.3: Enthalpy, entropy, and Gibbs free energy estimates for States C2, $\text{C}^\ddagger 3$, and $\text{C}^\ddagger 4$	123
Table 4.4: Enthalpy, entropy, and Gibbs free energy estimates for E2 dehydration over Ti-O-Ti and H-bonded $\equiv\text{Ti-OH}$ sites	125

Acknowledgments

I could make these acknowledgments 100+ pages long, but it still wouldn't capture my appreciation for all those who have supported me. Getting a Ph.D. has been challenging, and I have many to thank.

Right away, I'd like to thank Prof. Bell. I have learned much from him over the last five and a half years. He has taught me how to step back and look at the bigger picture when conducting research. This skill is valuable because it allows one to maintain a clear, overarching vision, which is very hard to do when you're buried deep in the details. I would also like to thank him for his patience during obstacles. Prof. Bell loves research, and it shows. He was always excited to learn new things from my work, which motivated me.

Next, I want to thank Prof. Head-Gordon. Martin's encouragement and excitement about our research always motivated me to work better. His true love of science always inspired me to push forward when there were obstacles. The fact that he met regularly with me nearly every week was a delight because he was not required to do so. For this, I am very grateful.

Next, I would like to thank the Bell Choir and the Head-Gordon lab. Hengyuan Shen, Leonardo dos Anjos Cunha, Hassan Aljama, Christiana Linninger, Jeroen Van der Mynsbrugge, Liang Qi, Yan Fei Zhang, Neelay Phadke, Chris Ho, Julie Rorrer, Danna Nozik, and Paul Kim were all very helpful in getting my PhD project started. They taught me a lot about designing experiments and running DFT calculations and were always ready for thought-provoking discussions. They were my role models and represented great researchers I hoped to become someday. I would also like to thank Natalie Lefton and Afnan Alghannam, who are still in the lab today, for their fantastic companionship and discussions.

Next up is Dr. Marjorie Went. I TA'd the senior-level capstone design course with Dr. Went in Spring 2021. That experience was transformative. I learned much from her about teaching students; I appreciate this.

Thank you to Prof. Katz, Carraro, and McCloskey for a great 1st semester of grad classes at Berkeley – I learned so much and was adequately prepared for prelims.

I'd also like to thank Carlet Altamirano and Jeff King, who, without their support, would never have written this dissertation because I'd still be dealing with university bureaucracy.

I would also like to thank the many people who got me to Berkeley in the first place. When I was 18, I had no idea what I wanted to pursue in college. There was a strong chance I would go for theatre and try my luck at being an actor. Dr. Steve Acquah, at Florida State University, took me under his wing as an undergraduate intern in the Harry Kroto lab. If not for that experience, I may have never become a chemical engineer. Steve inspired me to love science and recommended that I pursue a bachelor's degree in chemical engineering rather than chemistry. For this, I cannot thank him enough.

I also would like to thank other significant mentors. Prof. Michael Tiemann at Universität Paderborn and my graduate student mentor, Markus Schmitz. Dr. Richard Liang, Dr. Ayou Hao, Dr. Jin Gyu Park, Dr. Songlin Zhang, and Dr. Liyu Dong at the High-Performance Materials Institute. Dr. Telotte and Dr. Dan Hallinan at the FAMU-FSU College of Engineering.

Finally, I want to thank my entire family, who have always supported me through my education and life. A specific shout-out goes to my brother, Tyler, who was always open to helping me debug a script here and there.

Thank you all!

1. Introduction

Silica-supported metal cations (SSMCs or M/SiO₂) are active for a wide variety of reactions. When synthesized at low metal loadings, these structures are found to be isolated, monomeric, tetrahedral species grafted directly to the silica surface through covalent M-O-Si bonds (e.g., ≡M-OH, =M(O)₂), as shown in Table 1.1 and references therein. Compared to bulk metal oxides, SSMCs have several advantages. First, in an SSMC, the active metal is isolated and localized to the surface of the support, making all metal sites accessible to reactants in the fluid phase. By contrast, a significant portion of the active metal in metal oxides is situated within the bulk material, leaving them inaccessible to reactants and unable to catalyze reactions. Second, the study of SSMCs enables the use of element-specific spectroscopy, such as UV/Visible spectroscopy (UV/Vis), to exclusively interrogate the local environment of reactant-accessible metal sites under ambient, dehydrated, and reaction conditions.¹ Bulk oxides do not provide this advantage as most metal ions are embedded within the bulk structure of the oxide, making it challenging to observe signals specific to surface sites where catalysis occurs. Therefore, SSMCs are advantageous for developing relationships between active site structures and chemical transformations, which is crucial for the rational design of new heterogeneous catalysts.

Table 1.1: Summary of the reactions catalyzed by SSMCs and their proposed dehydrated and oxidized structures

Metal	Ti	Zr	Sn	V	Nb	Ta	Cr	Mo	W
Reaction*	Epox./ Cond.	Cond./ Keton.	Transfer Hyd.	Ox.	Epox.	Epox.	Alkene Poly.	Ox./ Met.	Met.
Proposed Structure									
Ref.	2-7	8	9	10-14	10	15,16	17	18-20	21

*Epox. = Epoxidation, Cond. = Aldol condensation, Hyd. = Hydrogenation, Poly. = Polymerization, Ox. = Oxidation, Met = Metathesis

An aspect of SSMCs that has become a subject of discussion in the recent literature is that though each metal atom in an SSMC may be *accessible* to reactants, not all sites are necessarily active. For example, Howell et al. have shown that only ~5% of W(6+) in W/SiO₂ metathesis catalysts reduce to form W(4+), the proposed active form of W.²¹ A more prototypical example is the Phillips catalyst (Cr/SiO₂), whose active Cr has been reported to be typically less than 20%, even at low Cr loadings where Cr atoms are sufficiently dispersed.¹⁷ Furthermore, density functional theory (DFT) investigations have shown that, due to the distribution of O-Si-O bond angles, the amorphous silica support can distort the tetrahedral structure of the supported metal species, causing significant changes to their adsorptive and catalytic properties.^{18,22,23} Thus, it has been proposed that a heterogeneous distribution of activities exists in actual SSMC materials, leading to a small fraction of active sites dominating the observed activity.²⁴ The distribution of O-Si-O bond angles in amorphous silica has been experimentally verified, while the presence of distorted metal sites has yet to be established unequivocally.²⁵

There is also still some controversy about how to represent the structures of SSMCs in theoretical studies (usually, density functional theory (DFT) studies) which are used to calculate enthalpies and entropies of adsorption and activation. The structures used so far can be coarsely partitioned into two categories. The first category involves relatively symmetrical metal sites. These models usually assume the structure of a corner-substituted silsesquioxane, as depicted in Figure 1.1A.^{2,8,11-13,26} These models are small and computationally efficient but neglect distortion

and possible electrostatic and/or dispersion interactions between adsorbates and the surrounding silica support. Large, amorphous representations are used with mixed basis sets in the second category (Figure 1.1B).²² A large basis set for DFT calculations is utilized in the region nearest to the adsorption site, with a smaller (less accurate) basis set outside of this region. These models are more realistic and include the effects of distortion, but they are computationally expensive. Second derivatives of the potential energy surface are rarely calculated due to the large number of basis functions. Surprisingly, it has not yet been established whether either model of amorphous silica is accurate when used to compute adsorption enthalpies (ΔH_{ads}^o) of polar molecules.

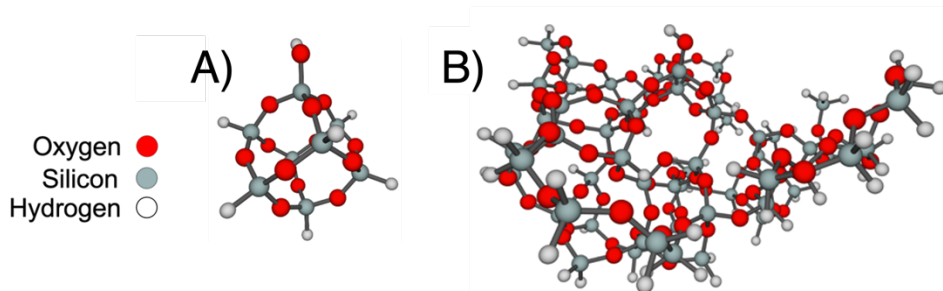


Figure 1.1: The two general representations of silica utilized in the literature as exemplified by a silanol ($\equiv\text{Si-OH}$) group. A) a small silsesquioxane model and B) a large amorphous silica model.

Of all SSMCs, the most interesting is Ti/SiO_2 . Isolated titanol groups supported on silica ($(\text{SiO})_3\equiv\text{Ti-OH}$ (hereafter referred to as $\equiv\text{Ti-OH}$) are known to catalyze a variety of reactions, e.g., epoxidation of alkenes, amination of alcohols, ammoxidation of ketones, and dehydration of alcohols.²⁷ Due to its industrial relevance, there is a considerable focus on the epoxidation of alkenes with this material.^{10,27-35} This catalyst differs from other SSMCs because the fraction of active $\equiv\text{Ti-OH}$ sites has been claimed to reach 100% at low $\equiv\text{Ti-OH}$ loadings for cyclooctene epoxidation. It has also been suggested that all Ti sites exhibit identical activity based on the observation that site titration shows a linear decrease in activity with the surface concentration of titrant.³⁰ These findings contrast with other studies of SSMCs that show only small fractions of sites are active. Thus, the question arises as to whether distorted $\equiv\text{Ti-OH}$ sites exist on the surface of Ti/SiO_2 , and if they do, can this fact be confirmed by experimental observations?

Evidence for and effects of tetrahedral distortion on the adsorptive and catalytic properties of Ti/SiO_2 are investigated in this thesis. Chapter 2 presents evidence for site distortion obtained from *in-situ* FTIR spectroscopy measurements of the isosteric enthalpy of adsorption (ΔH_{ads}^o) for pyridine adsorbed to the metal centers of $\equiv\text{Ti-OH}$ sites. This method was used because it can distinguish pyridine adsorbed to $\equiv\text{Ti-OH}$ vs. $\equiv\text{Si-OH}$ sites. These measurements are conducted for samples of Ti/SiO_2 that contain low loadings of Ti, which exhibit spectroscopic signatures consistent with isolated $\equiv\text{Ti-OH}$ sites. It is found that the isosteric ΔH_{ads}^o is constant above 15% coverage but then decreases progressively (becomes more favorable) at lower coverages. To relate the magnitude of a given value of ΔH_{ads}^o to the structure of a $\equiv\text{Ti-OH}$ site, requires an accurate method for predicting ΔH_{ads}^o as a function of $\equiv\text{Ti-OH}$ site distortion. Chapter 2 presents a method for doing so by considering a more frequently studied phenomenon: ΔH_{ads}^o for the adsorption of polar molecules to silanol ($\equiv\text{Si-OH}$) groups. Our method successfully predicts ΔH_{ads}^o for the adsorption of polar molecules to silanol ($\equiv\text{Si-OH}$) groups within 10% of the experimentally measured value. We then use our validated computational method to investigate the effects of tetrahedral distortion of titanol ($\equiv\text{Ti-OH}$) groups on ΔH_{ads}^o for pyridine. “Tetrahedral distortion” is defined by a geometric descriptor, the tetrahedral facet area, as shown in Figure 1.2. Calculations

made with our model revealed that ΔH_{ads}^o is proportional to the facet area of the $\equiv\text{Ti-OH}$ group to which pyridine is bound. $\equiv\text{Ti-OH}$ sites exhibiting facet areas consistent with those deduced from experimental X-Ray Absorption Spectroscopy (XAS/EXAFS) measurements (3.76 \AA^2) bind pyridine with ΔH_{ads}^o corresponding to the observed plateau for pyridine coverage above 15%. Larger tetrahedral facet areas are required to explain the coverage-dependent enthalpies of adsorption below 15% coverage, evidencing distorted $\equiv\text{Ti-OH}$ structures.

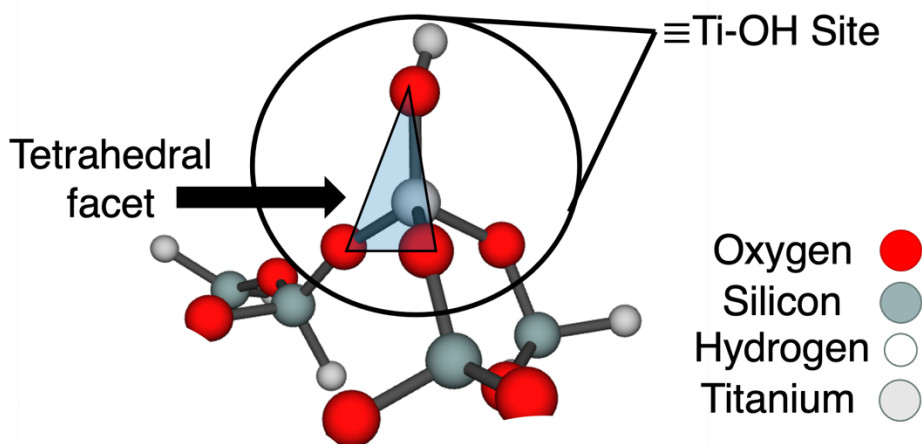


Figure 1.2: Illustration of what is meant by the “tetrahedral facet area” of a $\equiv\text{Ti-OH}$ site.

Chapter 3 explores the impact of tetrahedral distortion on the gas-phase kinetics of cyclohexene epoxidation to form cyclohexene oxide and water. This reaction was selected because its gas phase kinetics have recently been reported and, hence, could be used for comparison with our calculations.³² This study also proposed a reaction mechanism that was consistent with the reported kinetics. We, therefore, investigated the impact of site distortion on the predicted kinetics with the aim of determining whether the proposed mechanism is consistent with the observed kinetics. We found that the mechanism is inconsistent with the observed kinetics because of severe product inhibition for tetrahedral facet areas $> 3.54 \text{ \AA}^2$, which includes all experimentally observed facets. This insight led us to identify a new mechanism in which strong adsorption of product $\text{C}_6\text{H}_{10}\text{O}$ to $\equiv\text{Ti-OH}$ sites significantly reduces the facet areas of the other facets of the same $\equiv\text{Ti-OH}$ site, enabling them to avoid product inhibition and become active for cyclohexene epoxidation. Our model predicts that the *in-situ* generated, reduced-area facets lead to kinetic parameters that agree quantitatively with those determined experimentally. This chapter also connects the observed kinetic equivalence of Ti SSMCs for epoxidation and the heterogeneous distribution of activities expected for SSMCs, as noted earlier.

Chapter 4 investigates whether the findings from Chapter 3 are general or if they depend on the reaction in question. We addressed this through a combined experimental and theoretical study of the kinetics for gas-phase unimolecular isopropanol (IPA) dehydration to form propene and water. The most significant finding from this work is that the fraction of $\equiv\text{Ti-OH}$ sites performing IPA dehydration is very low ($< 6\%$), indicating that the active site for IPA dehydration is a minority species. This finding starkly contrasts what had been found for epoxidation, implying that the fraction of active sites is likely dependent on the reaction of interest. A preliminary computational investigation of the IPA dehydration mechanism was also conducted which found that the formation of titanium isopropoxide ($\equiv\text{Ti-OiPr}$) groups was favorable and dominated the surface coverages of most $\equiv\text{Ti-OH}$ sites. The formation of propene from $\equiv\text{Ti-OiPr}$ was energetically unfavorable, which supported the experimental finding that a majority of $\equiv\text{Ti-OH}$ sites were not

active for this reaction. This chapter demonstrates that bulk spectroscopic techniques cannot interrogate the active site for IPA dehydration since it is present as a minority species, and that further work is necessary to identify the active site.

Chapter 5 presents a summary and conclusions of this work and offers suggestions for future investigations.

2 Experimental and Theoretical Evidence for Distorted Tetrahedral $\equiv\text{Ti-OH}$ Sites Supported on Amorphous Silica and Their Effect on the Adsorption of Polar Molecules¹

2.1 Abstract

This study presents experimental and theoretical evidence for distorted $\equiv\text{Ti-OH}$ groups supported on amorphous SiO_2 and examines the influence of distortion on the strength of adsorption of polar molecules. For the theoretical part of this effort, we developed a model for isolated $\equiv\text{Si-OH}$ or $\equiv\text{Ti-OH}$ groups on the surface amorphous silica. The $\equiv\text{M-OH}$ group is represented by a T8-11 cluster surrounded by a T747 cluster representing the surrounding amorphous silica. The properties of the small cluster are described by high-level density functional theory (DFT) (i.e. the quantum mechanical (QM) region), whereas the large surroundings is represented by molecular mechanics (MM). The QM/MM model was validated by demonstrating that the predicted enthalpy of adsorption for seven polar molecules on $\equiv\text{Si-OH}$ groups agrees satisfactorily with experimentally measured values determined by microcalorimetry. We also found that enthalpies of adsorption on isolated $\equiv\text{Si-OH}$ groups determined from isotherms obtained by IR agree very well with the microcalorimetric values. IR spectroscopy was then used to measure isotherms for pyridine adsorption to Lewis acidic Ti isolated $\equiv\text{Ti-OH}$ groups grafted to amorphous silica. The isosteric enthalpy of adsorption decreased in magnitude with increasing pyridine coverages up to a coverage of 15% and to then remained relatively constant for higher coverages. QM/MM calculations made with our model revealed that the enthalpy of adsorption is proportional to the area of the triangular O-Ti-O facets of the $\equiv\text{Ti-OH}$ group to which pyridine is bound. $\equiv\text{Ti-OH}$ sites exhibiting facet areas consistent with those deduced from X-Ray Absorption Spectroscopy (XAS/EXAFS) measurements bind pyridine with enthalpies of adsorption consistent with the observed plateau for pyridine coverage above 15%. Larger tetrahedral facet areas are required to explain the coverage-dependent enthalpies of adsorption below 15% coverage, evidencing distorted $\equiv\text{Ti-OH}$ structures. Distorted $\equiv\text{Ti-OH}$ sites are also qualitatively consistent with reduced-intensity pre-edge X-Ray Absorption Near Edge Structure (XANES) measurements reported in this study. Energy decomposition analysis (EDA) calculations were carried out to understand the underlying physical phenomenon governing the change in the enthalpies of adsorption pyridine as a function of tetrahedral facet area

2.2 Introduction

Silica-supported metal cations (SSMCs), such as Ti, Cr, W, Mo, Zr, V, and Nb are widely used as catalysts to promote industrially relevant chemical reactions, such as alkene epoxidation, alkene polymerization, and alkene metathesis.^{2,8,10,14,18,27,36-38} At low metal loadings, metal cations are present as isolated species (e.g., $\equiv\text{M-OH}$, $\equiv\text{M(O)}_2$) grafted to the surface of silica through covalent M-O-Si bonds (where M = Ti, Cr, W, etc.). Recent experimental and computational studies suggest that the distribution of O-Si-O bond angles amorphous silica can distort the structure of the supported $\equiv\text{M-OH}$ and $\equiv\text{M(O)}_2$ species, thereby affecting their adsorptive and catalytic properties.^{22,23} Although the catalytic relevance of distortion of these species has been reported for over a decade, many recent computational studies have assumed relatively

¹ This chapter was recently accepted in Journal of Physical Chemistry C and has been adapted for inclusion in this dissertation with permission from the coauthors H. Shen, M. Head-Gordon, and A. T. Bell. H. Shen contributed the Energy Decomposition Analysis calculations.

symmetrical metal sites to compute the enthalpy landscape on which reactions occur.^{2,8,11–13,26} Furthermore, these models typically assume the structure of a corner-substituted silsesquioxane. While this model is computationally efficient, it neglects non-local interactions between the adsorbate and the surrounding silica support. Therefore, it is not known whether silsesquioxane-based models of silica are accurate when used to compute adsorption enthalpies. This is an important question given the extensive theoretical work on microporous-silica and zeolites, which have concluded that small cluster models are generally insufficient because they neglect long-range electrostatic and short-range van der Waals (VDW) interactions between the surrounding silica of the micropore and the adsorbate.^{39,40} Thus, the successful application of theory to the investigation of supported $\equiv\text{M-OH}$ and $=\text{M}(\text{O})_2$ species requires the identification of a physically meaningful representation for SSMCs that can then be used to determine what effects geometrical distortions of their structure have on their adsorptive and catalytic properties.

In this study, we explore alternative representations of amorphous silica in theoretical studies of the adsorption of polar molecules on silanol ($\equiv\text{Si-OH}$) groups and isolated titanol ($\equiv\text{Ti-OH}$) groups on the surface of amorphous silica. Silanol groups are considered because of the large body of experimental work concerning the enthalpy of adsorption of polar molecules on such groups.^{41–47} The reason for choosing $\equiv\text{Ti-OH}$ groups is that they have been the subject of many experimental and theoretical studies.^{2,7,33,48,49} We also examine whether distortion of the geometry of $\equiv\text{Ti-OH}$ groups affects the enthalpy of adsorption of polar molecules on these groups. To address these questions, we have explored the influence of cluster size on the predicted enthalpies of adsorption for polar molecules interacting with isolated $\equiv\text{Si-OH}$ groups and their agreement with microcalorimetric measurements. To investigate the adsorption of polar molecules on silica-supported $\equiv\text{Ti-OH}$ groups, we prepared a sample of Ti/SiO_2 and confirmed experimentally that all Ti was dispersed as isolated $\equiv\text{Ti-OH}$ groups. We then used IR spectroscopy of adsorbed pyridine to obtain adsorption isotherms from which the isosteric enthalpies of adsorption could be determined. This experimental approach was validated by demonstrating that the enthalpy of adsorption for polar molecules adsorbed on $\equiv\text{Si-OH}$ groups is consistent with the value determined by microcalorimetry. Ultimately, we used our IR approach to identify that the enthalpy of pyridine adsorption on isolated $\equiv\text{Ti-OH}$ groups is coverage dependent and to demonstrate that our theoretical approach shows that the variation of the isosteric enthalpy of adsorption of pyridine, ΔH_{ads}^0 , is a consequence of the geometric distortion of a portion ($\sim 15\%$) of the supported $\equiv\text{Ti-OH}$ groups. Physical insights into how distortion impacts ΔH_{ads} of pyridine were obtained by carrying out an energy decomposition analysis (EDA).⁵⁰

2.3 Methods

2.3.1 Silica Preparation

Fumed silica, an amorphous, non-porous material was obtained from Sigma Aldrich (surface area = $395 \text{ m}^2/\text{g} \pm 25 \text{ m}^2/\text{g}$). All samples underwent consistent pre-treatment to ensure reproducibility. First, the raw material was dispersed in boiling water (1:1 by volume) for 24 h (with constant stirring), cooled, and filtered. The silica cake was dried in an oven at 353 K under nitrogen overnight to form silica chips. The chips were ground in a mortar and pestle and sieved to a consistent particle size ($250 \text{ }\mu\text{m} < \phi_d < 500 \text{ }\mu\text{m}$). This sample is referred to as $\text{SiO}_{2,\text{Hyd}}$. To dehydroxylate $\text{SiO}_{2,\text{Hyd}}$, it was heated in 100 mL/min of Praxair Extra Dry air at 1023 K (3 K/min

ramp rate) for 8 h and cooled to room temperature. The resulting material is referred to as **SiO₂₋₁₀₂₃**.

2.3.2 Thermogravimetric Analysis (TGA) of silanol density

TGA was conducted using a TGA Q5000 instrument equipped with a high-temperature platinum or ceramic crucible. All sample mass thermograms were corrected for buoyancy effects by subtracting the mass thermogram of an empty pan with an identical thermal program. To determine the silanol density, ~10-20 mg of silica was heated in a flow of 100ml/min air (Praxair UHP air) to 383 K at 5 K/min and held at this temperature for 1h, followed by heating to 1273 K at 5 K/min. To calculate the silanol density, equation (1) was used.

$$\text{Silanol density} \left(\frac{\text{OH}}{\text{nm}^2} \right) = \frac{2(\Delta m_{TGA})N_{Avogadro}}{M_{H_2O}A_{BET}} \quad (1)$$

where Δm_{TGA} is the cumulative mass loss between the stable mass at 383 K and the final mass at 1273 K in grams, M_{H_2O} is the molar mass of water in g/mol, $N_{Avogadro}$ is Avogadro's number, A_{BET} is the BET surface area in nm², and the factor of 2 accounts for the fact that every molecule of water evolved comes from the condensation of two silanol groups. **SiO_{2,Hyd}** was found to contain 4.8±0.1 OH/nm² from this method (Figure S2.1), which is in excellent agreement with Zhuravlev et al. for fully hydroxylated silica materials.⁵¹ Using the same method, **SiO₂₋₁₀₂₃** was found to contain 1.4 OH/nm², which is within the expected range after the thermal treatment employed (Figure S2.2).⁵¹

2.3.3 Wet impregnation of SiO₂₋₁₀₂₃ with Cp₂TiCl₂ and calcination to form Ti/SiO₂₋₁₀₂₃

Ti was grafted onto the surface of **SiO₂₋₁₀₂₃** using Cp₂TiCl₂ (Strem Chemicals) as the Ti precursor. This step was conducted under air-free conditions utilizing an N₂ Schlenk line.⁵ N₂ was supplied at 10 psig from a cylinder (Praxair) and passed over a Vici Valco N₂ purifier prior to use in the Schlenk line. First, **SiO₂₋₁₀₂₃** was charged to a three-neck flask connected to a Schlenk filter, a septum, and a glass stopper. The flask was evacuated and backfilled with N₂ three times. Then, the sample was dehydrated for 2 h under dynamic vacuum (10⁻¹ mbar) at 503 ± 20 K at 10-20 K/min using a sand bath. Meanwhile, the desired amount of Cp₂TiCl₂ was charged to a separate three-neck flask connected to the Schlenk line, a Schlenk funnel, and a septum. The flask was also evacuated and backfilled with N₂ three times. Then, it was left under dynamic vacuum (10⁻¹ mbar) for 2 h. Next, 60 mL of anhydrous chloroform was added to the titanium precursor (now under N₂) and was allowed to stir for 1 h. After cooling the silica to room temperature, the vessel was filled with dried N₂ and the titanium precursor/chloroform solution was transferred to the silica via a cannula. The suspension was stirred and allowed to react for 2 h, after which the entire glassware setup was rotated 180° and the liquid suspension was passed through a Schlenk filter. Finally, residual chloroform was removed by evacuation for 1 h into a liquid N₂ trap placed upstream of the vacuum pump to leave a milky orange powder (**SiO_{2-CP}**). At this point, the sample was exposed

to ambient conditions and immediately calcined in air (Praxair Extra Dry) at 823 K (3 K/min ramp rate) for 8 h producing a bright white powder (**Ti/SiO₂₋₁₀₂₃**).

2.3.4 Synthesis of **Ti[SiOPh₃]₄**

The synthesis of **Ti[SiOPh₃]₄** was carried out following the procedure of Johnson et al.⁵² Briefly, 2 g of Ph₃SiOH (Sigma-Aldrich) was charged to a Schlenk flask inside a N₂-purged glovebox. The flask was sealed and transferred to a Schlenk line where it was evacuated and purged with filtered N₂ three times. Then, 50 mL of toluene (Fischer Scientific) was cannula transferred to the Schlenk flask containing Ph₃SiOH and the solution was stirred for 10 minutes. Finally, 0.47 mL of Ti(OBuⁿ)₄ was added to the now-stirring solution (700 rpm). The product, **Ti[SiOPh₃]₄**, precipitated out immediately. The solution was detached from the Schlenk line and vacuum-filtered overnight to leave a bright white powder. The structure of **Ti[SiOPh₃]₄** was confirmed by X-ray absorption spectroscopy (Figure S2.3).

2.3.5 N₂ Physisorption Measurements

BET surface areas were calculated from N₂ physisorption isotherms measured at 77 K using a Micromeritics Gemini VII surface area and pore volume analyzer. The BET surface area for **SiO_{2,Hyd}** and **SiO₂₋₁₀₂₃** was 335 and 334 m²/g respectively. Both samples display IUPAC Type 2 N₂ adsorption isotherms consistent with a non-porous material (Figure S2.4). The measured BET surface area for **Ti/SiO₂₋₁₀₂₃** was 298 m²/g. Prior to isotherm measurement, samples were treated at 403 K under vacuum.

2.3.6 Diffuse Reflectance UV/Visible Spectroscopy (UV/Vis)

UV/Vis spectra were acquired on a Thermo Scientific Evolution 3000 UV/Vis spectrophotometer equipped with a Harrick Praying Mantis Diffuse Reflectance accessory. Reference spectra were acquired with BaSO₄ and transformations from percent reflectance to absorbance were calculated with the Kubelka-Munk function. Samples were heated under 100 ml/min of flowing He (Praxair UHP grade) to 673 K (6.25 K/min ramp rate), held at 673 K for 1h, then cooled to the conditions of interest. The UV/Vis spectrum of **SiO₂₋₁₀₂₃** was subtracted from that of **Ti/SiO₂₋₁₀₂₃**. To make a quantitative comparison with the literature, Tauc plots were constructed assuming direct transitions, and the direct edge energy was calculated using a sigmoidal fitting procedure as in previous work.⁵³

2.3.7 Fourier-Transform Infrared Spectroscopy (FTIR)

Catalyst samples (~30 mg) were pressed into self-supporting pellets and loaded into a stainless-steel sample holder that was then placed in a home-built in-situ transmission IR cell. The cell was connected to heated stainless-steel gas transfer lines. A septum adapter was placed upstream of the cell, allowing for continuous liquid injection (Legato 100 syringe pump) into the heated gas stream. The *in-situ* cell was equipped with a cylindrical heater, and the temperature was measured using a K-type thermocouple (Omega) in direct physical contact with the stainless-steel sample holder. The temperature was controlled using an Omega CS8DPT controller. Spectra were acquired using a Thermo Scientific Nicolet 6700 FTIR spectrometer with a liquid-nitrogen-cooled MCT detector.

All FTIR measurements followed the same sample pretreatment conditions. Samples were heated under 100 ml/min of flowing He (Praxair UHP grade) to 673 K (6.25 K/min ramp rate), held at 673 K for 1h, then cooled to the conditions of interest. For isotherm measurements, pyridine (Sigma-Aldrich), acetone (Sigma-Aldrich), and d₃-acetonitrile (Sigma-Aldrich) were injected into the heated He gas stream at a flowrate needed to obtain the desired partial pressures. The liquid injection rate was modified while the He flowrate was kept constant to accomplish this. Equilibration was determined when the area of the IR band corresponding to adsorbed pyridine, acetone, or d₃-acetonitrile no longer changed, which typically occurred within 3 min. All spectra were collected as an average of 64 scans with 1 cm⁻¹ resolution.

Peak deconvolution and fits were performed with Origin software. For pyridine adsorption experiments, ring-breathing vibrational absorbance features were integrated numerically after baseline subtraction. For d₃-acetonitrile, acetone, and trimethylacetonitrile, peaks were fit to the spectra. For d₃-acetonitrile and trimethylacetonitrile, we fit Gauss-Lorentz functions with 80% and 50% Lorentzian weights, respectively, as these provided the best fits to our data. Others have found these line shapes to fit spectra of CD₃CN adsorbed to Sn and Zn sites within zeolites.⁵⁴ These weights were kept fixed for all conditions. Peak centers and full-width half-maxima (FWHM) were allowed to vary freely but did not change by more than 2 cm⁻¹ for both parameters. For acetone, two Lorentz line shapes were fit to the spectra to represent two distinct adsorbed species.⁵⁵ Peak centers were kept fixed at 1712 cm⁻¹ and 1699.5 cm⁻¹ with FWHM fixed at 16 cm⁻¹ and 20.1 cm⁻¹, respectively, for all conditions. The magnitudes and trends of the FWHM reported here for both components are consistent with those reported by others.⁵⁵

2.3.8 X-ray absorption spectroscopy (XAS)

XAS spectra at the Ti K-edge were acquired on beamline 10-BM at the Advanced Photon Source at Argonne National Laboratory. The energy was referenced to Ti foil (4966 eV) taken in transmission mode. Before measurement, **Ti[SiOPh₃]₄** was diluted with boron nitride. The XAS of **Ti/SiO₂₋₁₀₂₃** was acquired in fluorescence mode using a Vortex detector and an in-situ cube cell. Multiple spectra were merged to improve the signal-to-noise ratio as much as reasonably possible. Data was collected from 4780 eV to 5767 eV with a step size of 0.1 eV in the pre-edge region. Due to the low loadings of Ti in **Ti/SiO₂₋₁₀₂₃** samples, the EXAFS region of the XAS yielded low signal, so only pre-edge data was acquired. All data workup and analysis were conducted using Athena and Artemis software.⁵⁶ After background subtraction, all spectra were normalized to the absorbance in the region 150-400 eV above the edge. Pre-edge features were baseline corrected using an arctan function, as reported previously.⁴⁹ An EXAFS fit for **Ti[SiOPh₃]₄** was performed in the range 1.2-2.2 Å in R-space. Initial guesses for Ti-O scattering paths were calculated from the crystal structures of **Ti[SiOPh₃]₄** using the FEFF6 plug-in within Artemis.^{52,56}

2.3.9 QM/MM and QM calculations

All geometry optimizations and frequency calculations (to confirm minima on the potential energy surface) for all structures were performed with ωB97X-D/def2-SVP.⁵⁷ Single-point energy calculations, used for calculating ΔH_{ads}^0 , were performed with ωB97M-V/def2-TZVP.⁵⁸ The larger basis set and more advanced functional yield statistically higher quality interaction energies.⁵⁹ All electronic structure calculations employed the pruned SG-3 (99, 590) quadrature grid.⁶⁰ Enthalpy

and entropy corrections at a given temperature used a quasi-rigid rotor harmonic oscillator model (qRRHO).^{61,62} In cases where multiple local minima were found for the same adsorption phenomenon, (i.e., pyridine adsorption to an isolated silanol), ΔH_{ads}^o was calculated by a Boltzmann weighted average. Boltzmann factors were calculated using estimated ΔG_{ads}^o for each optimized geometry.

Calculations for the T8 silsesquioxane model, as well as models B and C in Figure 2.1 (below) were DFT calculations (i.e., full QM). All of the atoms in the T8 silsesquioxane structure were allowed to relax, whereas, for models B and C the terminal hydrogens were fixed in place. For larger models, such as D, E, and F, Quantum-mechanics/Molecular Mechanics (QM/MM) calculations were performed as implemented utilizing the P2 set of MM parameters.^{61,63} This methodology defines a QM region on the silica surface that includes the central $\equiv\text{Ti-OH}$ or $\equiv\text{Si-OH}$ site along with a number of surrounding silica atoms. We extended the QM region out to the next-next nearest neighbor Si atom from the central $\equiv\text{Ti-OH}$ or $\equiv\text{Si-OH}$ site; therefore, the QM region typically involved 8-11 tetrahedral atoms (T-atoms). The QM region also included all adsorbate atoms. The QM region was terminated with hydrogen atoms that are fixed in place and aligned with the boundary Si-O bonds at a distance of $0.92 R(\text{Si-O})$, where $R(\text{Si-O})$ is the bond distance of the Si-O bond from the Si in the QM region, and the O in the MM region.⁶³ The Si atoms in the QM region that connect to the terminal hydrogen atoms are also fixed in place. An example of the QM region for the $\equiv\text{Si-OH}$ site is shown in panel C of Figure 2.1; whereas panels D, E, and F, show progressively larger MM regions. This methodology assumes that the MM region is included in the DFT Kohn-Sham equation as fixed point charges, the values of which are part of the P2 set of parameters.⁶¹ Since MM parameters were not developed for silanol groups in the MM region, all silanol (Si-OH) groups were replaced by terminal H atoms which are modeled as boundary O atoms in the QM/MM formalism.⁶¹ For all calculations, the MM region remains fixed in place. The MM region was not preoptimized prior to MM parameter fitting in its original implementation.⁶¹ We adopted the same approach here; however, we note that further research could investigate the sensitivity of MM parameter fits, used in QM/MM calculations, on MM region preoptimization since this could impact reaction energies for metal sites on amorphous supports.⁶⁴ Additionally, adsorbate atoms and MM region atoms interact via a pairwise VDW potential modeled by a standard Lennard-Jones function. The Lennard-Jones function uses the P2 parameters for the MM region developed previously for all siliceous-zeolites⁶¹, while adsorbate atoms take on their parameters as listed in the CHARMM database. All computations were performed using the Zeolite package within Q-Chem version 5.⁶⁵

2.3.10 Models for SiO_2 and Ti/SiO_2

Two categories of models for SiO_2 were examined. The first was a small cluster model (T8 silsesquioxane) that has been used frequently to model silica and silica-supported metals for catalytic reactions.^{2,8,11-13,26,66} We next considered progressively larger models of amorphous silica taken from the structure of this material generated by Tielens et al.^{67,68} Representative images of each type of model we considered are shown in Figure 2.1.

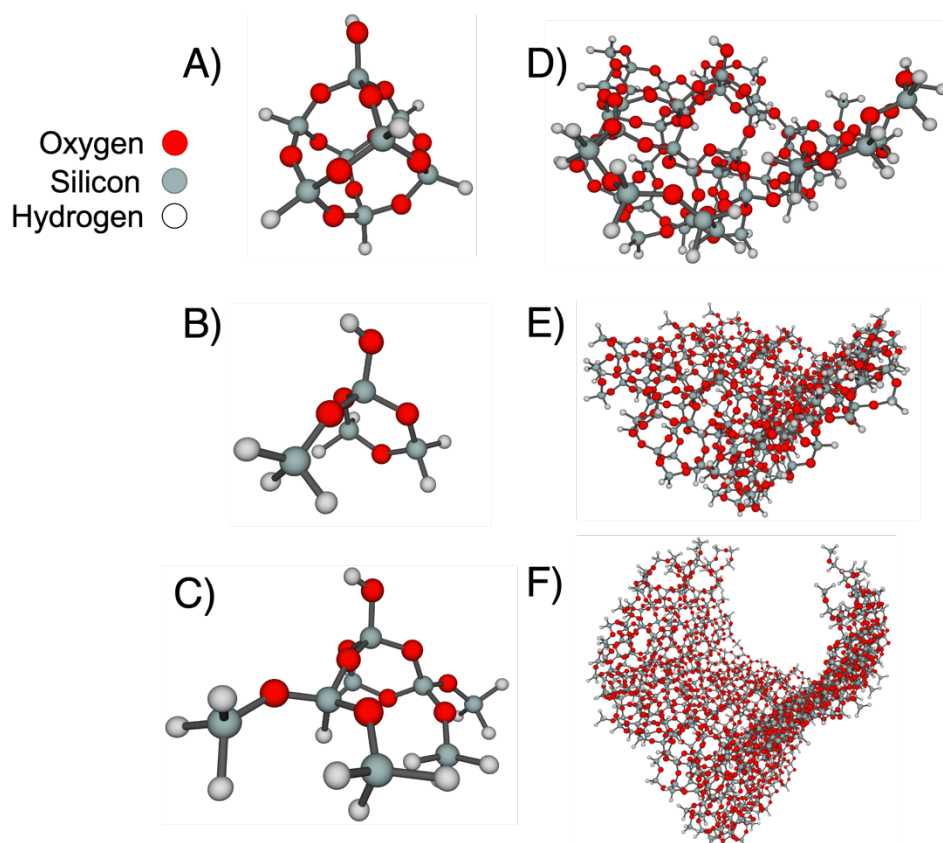


Figure 2.1: Representative images of $\equiv\text{Si-OH}$ models employed in this study. A) T8 silsesquioxane B) T4 sized model of the amorphous model generated by Tielens et al. C) T8 sized model of the amorphous model D) QM/MM model that uses the model in Figure 2.1C as the QM region and an MM region that terminates 11Å in radius from the central $\equiv\text{Si-OH}$ site. E) Same as Figure 2.1D but the MM region extends 20Å from the central $\equiv\text{Si-OH}$ site. F) Same as Figure 2.1D but the MM region extends 29Å from the central $\equiv\text{Si-OH}$ site

As mentioned in the previous section, models A-C are full QM calculations while D-F are QM/MM calculations that utilize model C as the QM region. Model D includes an MM region that extends 11 Å in radius from the central $\equiv\text{Si-OH}$ site, while Model E and F extend the region 20 Å and 29 Å in radius.

We also utilized seven amorphous silica geometries (adopted from Tielens et al.) in our study of $\equiv\text{Ti-OH}$ sites to examine the effect of distortion on enthalpies of adsorption.⁶⁷ $\equiv\text{Ti-OH}$ sites were generated by selecting seven isolated $\equiv\text{Si-OH}$ sites and replacing the Si atom with a Ti atom followed by geometry optimization of the QM region (Figure 2.2). The local geometries of each $\equiv\text{Ti-OH}$ site (with an MM region extending 29Å in radius) examined in this study, along with the $\equiv\text{Ti-OH}$ T8 Silsesquioxane, are displayed in Table 2.1. Notably, the T8 Silsesquioxane shows a narrow distribution of Ti-O bond lengths compared to the amorphous models. Experimental characterization suggests that the average Ti-O bond lengths in Ti/SiO₂ materials lie between 1.80 Å and 1.81 Å and that the coordination of Ti atoms with O atoms is 4.^{5,49} Thus, the average bond lengths of our models are all within 2% of the experimental value.

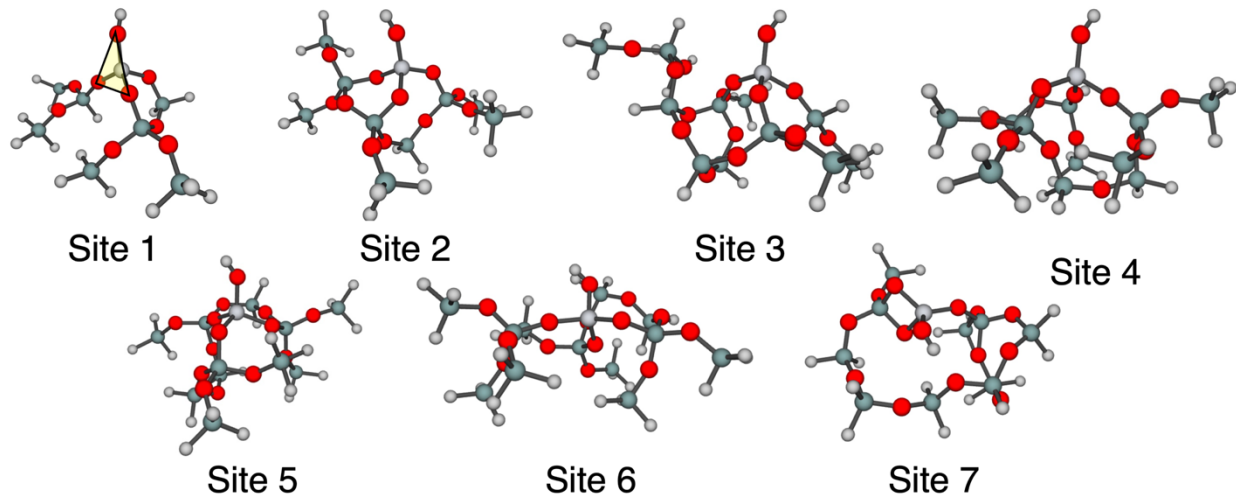


Figure 2.2: Illustrations of $\equiv\text{Ti-OH}$ sites (only the QM region is shown) generated by selecting seven isolated $\equiv\text{Si-OH}$ sites and replacing the Si atom with Ti followed by geometry optimization of the QM region. Large red spheres: oxygen, large dark grey spheres: silicon, large white spheres: titanium, small white spheres: hydrogen. An example of the “tetrahedral facet area” is highlighted on site 1.

Table 2.1: Bond lengths and tetrahedral facet areas of $\equiv\text{Ti-OH}$ sites*

Bond lengths (Å)								
Bond	Site 1	Site 2	Site 3	Site 4	Site 5	Site 6	Site 7	T8 silsesquioxane
Ti-OH	1.743	1.751	1.745	1.753	1.743	1.774	1.767	1.773
Ti-O1	1.779	1.786	1.795	1.773	1.792	1.801	1.816	1.780
Ti-O2	1.814	1.808	1.807	1.787	1.803	1.830	1.799	1.781
Ti-O3	1.832	1.816	1.814	1.797	1.891	1.816	1.835	1.781
Average	1.792	1.790	1.790	1.778	1.807	1.805	1.804	1.779
Tetrahedral facet areas (Å ²)								
Facet	Site 1	Site 2	Site 3	Site 4	Site 5	Site 6	Site 7	T8 silsesquioxane
Facet 1	3.941	3.829	3.769	3.790	3.941	3.789	4.071	3.702
Facet 2	3.614	3.674	3.763	3.631	3.769	3.666	3.789	3.699
Facet 3	3.597	3.667	3.623	3.620	3.509	3.464	3.331	3.687
Facet 4	3.505	3.529	3.590	3.461	3.745	3.883	3.301	3.463

*Optimized at the $\omega\text{B97X-D/def2-SVP}$ level of theory

2.4 Results and Discussion

2.4.1 Determination of ΔH_{ads}^0 for polar adsorbates on $\equiv\text{Si-OH}$ groups

The value of ΔH_{ads}^0 for the interaction of polar adsorbates with the silanol groups on the surface of $\text{SiO}_2\text{-1023}$ was obtained by measuring the integrated absorbance for a characteristic IR band of the adsorbate as a function of adsorbate partial pressure and system temperature. The adsorption isotherms obtained this way were well described by a Langmuir isotherm and analyzed accordingly. This procedure is illustrated below for the case of pyridine adsorption.

The Langmuir isotherm for pyridine adsorption is given as follows:

$$q_{ads} = q_{sat} \frac{K_{ads}P_{Py}}{(1 + K_{ads}P_{Py})} \quad (2)$$

Here q_{ads} , q_{sat} , K_{ads} , and P_{Py} refer to the quantity of adsorbed molecules of pyridine [mol Py], the amount of pyridine adsorbed at saturation [mol Py], the adsorption equilibrium constant, and the partial pressure of pyridine in the gas stream normalized by the standard pressure, 1 bar, respectively. A relationship between the amount of pyridine adsorbed and the integrated absorbance is derived from Beer's law. Thus,

$$q_{ads} = \frac{A_{py}S}{\epsilon} \quad (3)$$

where A_{py} , S , and ϵ are the integrated absorbance [cm^{-1}], the cross-sectional area of the pellet in the IR beam [cm^2], and the integrated molar extinction coefficient [$\text{cm}/\text{mol Py}$], respectively. Substituting equation (3) into equation (2) gives:

$$\frac{A_{py}S}{\epsilon} = \frac{A_{max}S}{\epsilon} \frac{K_{ads}P_{Py}}{(1 + K_{ads}P_{Py})} \quad (4)$$

Both S and ϵ appear on the left and right-hand sides of equation (4) and hence cancel out, resulting in equation (5).

$$A_{py} = A_{max} \frac{K_{ads}P_{Py}}{(1 + K_{ads}P_{Py})} \quad (5)$$

The equilibrium constant can be described in terms of ΔH_{ads}^o and ΔS_{ads}^o , the entropy of adsorption, both of which refer to the standard-state pressure of 1 bar and a standard coverage of 0.5 monolayers:

$$K_{ads} = \exp\left(-\frac{\Delta H_{ads}^o}{RT} + \frac{\Delta S_{ads}^o}{R}\right) \quad (6)$$

Selecting a standard state coverage of 0.5 monolayers ensures that configurational entropy is identically zero, and thus ΔS_{ads}^o represents only molecular entropic changes. Thus, for a set of IR spectra measured at multiple temperatures and partial pressures of adsorbate, it is possible to fit A_{max} , ΔH_{ads}^o , and ΔS_{ads}^o to the data. One can then normalize A_{max} by the integrated absorbance of the Si-O-Si overtone bands to allow for comparison between different silica samples.

2.4.2 Pyridine Adsorption on SiO₂₋₁₀₂₃

Figure 2.3A shows that the FTIR spectrum of pyridine adsorbed on SiO₂₋₁₀₂₃ exhibits two characteristic peaks at 1444 cm^{-1} and 1594 cm^{-1} . Both peaks correspond to ring-breathing vibrational modes (19b and 8a, respectively) for pyridine interaction with the hydrogen atom of $\equiv\text{Si-OH}$ groups.^{69,70} Varying the partial pressure and temperature changes the absorbance intensity of both peaks. A plot of the integrated absorbance vs. the partial pressure of pyridine is well-described by a Langmuir isotherm and is shown in Figure 2.3B. Values of A_{max} , ΔH_{ads}^o , and ΔS_{ads}^o

for both peaks obtained by fitting equations 4 and 5 to the data are presented in Table 2.2. We note that the values of these parameters are very similar for both features. This is to be expected because the peaks 19b and 8a have similar extinction coefficients.⁷¹ The value obtained for ΔH_{ads}^o is -70 ± 1.8 kJ/mol and that for ΔS_{ads}^o is -120 ± 3.2 J/mol·K.

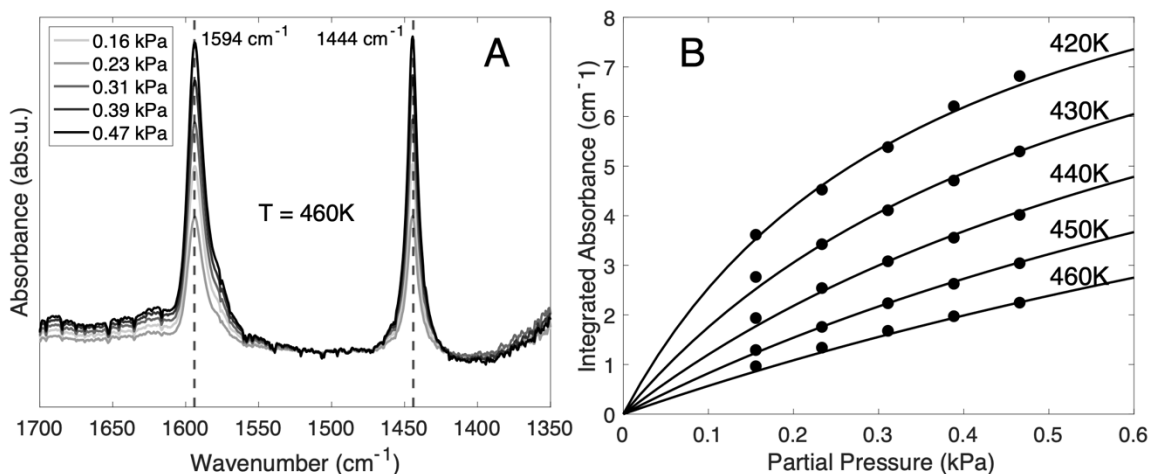


Figure 2.3: A) FTIR spectra of pyridine adsorbed on **SiO₂-1023** (T = 460 K) and B) isotherms collected using the integrated area of the peak centered at 1594 cm⁻¹ for temperatures in the range of T = 420 K-460 K.

The next question to address is whether the value of ΔH_{ads}^o determined corresponds to the interaction of pyridine solely with silanol groups rather than a combination of physisorbed (i.e., non-specific/liquid-like) pyridine and specifically adsorbed pyridine. An important indicator of the latter process is obtained by examining the effect of pyridine adsorption on the frequency of the $\equiv\text{SiO-H}$ stretching vibration. As shown in Figure S2.5, in the absence of pyridine the SiO-H stretching vibration occurs at 3743 cm⁻¹ at 460 K. Upon adsorption of pyridine, the absorbance of this band decreases and a new, broad band centered at 3050 cm⁻¹ appears (Figure S2.6). The 700 cm⁻¹ red-shift in the frequency of the $\equiv\text{SiO-H}$ stretching vibration is a consequence of pyridine interacting with the $\equiv\text{Si-OH}$ group. Figure S2.7 shows a near-perfect correlation between the integrated area of the perturbed $\equiv\text{SiO-H}$ peak and the ring-breathing vibrational modes corresponding to pyridine itself, strongly suggesting that the value of ΔH_{ads}^o determined from the isotherm presented in Figure 2.3B corresponds to adsorption of pyridine on silanol groups.

It is necessary, as well, to demonstrate that the measured value of ΔH_{ads}^o corresponds to interactions specifically with isolated/geminal silanols, as opposed to vicinal silanols. We note in this connection that previous research has shown that polar molecules such as triethylamine and pyridine bind overwhelmingly to isolated/geminal silanols, and that vicinal silanols remain inert to these adsorbates.^{45,72} To establish that this is the case in our work, we conducted a control experiment with our starting material **SiO₂-Hyd**. **SiO₂-Hyd** contains, approximately the same concentration of isolated silanols per gram as **SiO₂-1023**⁵¹, but a higher concentration of H-bonded vicinal silanols (Figure S2.5). The isotherms for pyridine adsorption obtained by IR spectroscopy yielded a slightly higher value of $\Delta H_{ads}^o \sim -80$ kJ/mol, and an identical saturation absorbance parameter (Figure S2.8 and Table S2.2). The identical saturation absorbance parameter confirms previously proposed arguments that pyridine binds exclusively to isolated/geminal silanols, whose

densities do not change greatly under the thermal treatments used here. The effect of dehydroxylation on ΔH_{ads}^o is small and similar to that determined by microcalorimetry for triethylamine adsorption on progressively dehydroxylated silica.⁴¹ In that study, a decrease in the measured value of ΔH_{ads}^o of ~ 10 kJ/mol was also observed for silica treated at higher temperatures. However, triethylamine coverages tracked with isolated/geminal silanol densities for all materials, indicating that the change in the enthalpies of adsorption resulted from subtle modifications of isolated/geminal silanol sites through a currently unknown mechanism. These subtle modifications are evidenced by a small red-shift (~ 3 cm⁻¹) in the isolated silanol SiO-H stretching frequency for the **SiO₂-Hyd** vs. **SiO₂-1023** bare materials (Figure S2.5).

Thus, the value of ΔH_{ads}^o for pyridine measured here (~ -70 kJ/mol) corresponds to the change in enthalpy of gas-phase pyridine to pyridine adsorbed to isolated/geminal silanols on the silica support at $T = 420$ - 460 K.

The enthalpies of adsorption of pyridine to SiO₂, as measured by calorimetry reported in the literature can vary. While our value agrees well with the dominant value measured from microcalorimetry by Kuznetsov et al. (~ -72 kJ/mol)⁴³, this value differs from measurements reported by Dumesic and coworkers (-95 kJ/mol). The latter measurements were made at much lower coverages (< 0.1 Pyridine molecules/nm²). Kuznetsov et al. report similar initial enthalpies of adsorption (i.e., one data point at -93 kJ/mol), but the coverage over which this value persisted (< 0.1 Pyridine molecules/nm²) was significantly lower than the estimated isolated/geminal silanol density of their materials (see Figure S2.9).⁴³ Conversely, they observed a relatively stable value (-72 kJ/mol) over a coverage range equal to the sum of the calculated isolated/geminal silanol density (~ 1.8 OH/nm²). Therefore, we propose that the site responsible for a ΔH_{ads}^o of -95 kJ/mol observed at low coverages is distinct from an isolated/geminal silanol site and that the majority of isolated/geminal silanols adsorb pyridine with ΔH_{ads}^o of -72 kJ/mol. However, we note that further investigations will be needed to unequivocally determine the physical origin of the high-energy site noted by other researchers.

2.4.3 D₃-Acetonitrile Adsorption on SiO₂-1023

Figure 2.4A shows the IR spectra of d₃-acetonitrile adsorbed to **SiO₂-1023**. A well-defined peak is observed at 2272 cm⁻¹ corresponding to the C \equiv N stretching frequency of d₃-acetonitrile interacting with \equiv Si-OH groups.^{43,73,74} We note that at the conditions shown in Figure 2.4, there is no evidence for a band at 2263 cm⁻¹ characteristic of non-specifically adsorbed (physisorbed) d₃-acetonitrile.^{73,74} An example of our peak fitting procedure is presented in Figure S2.10.

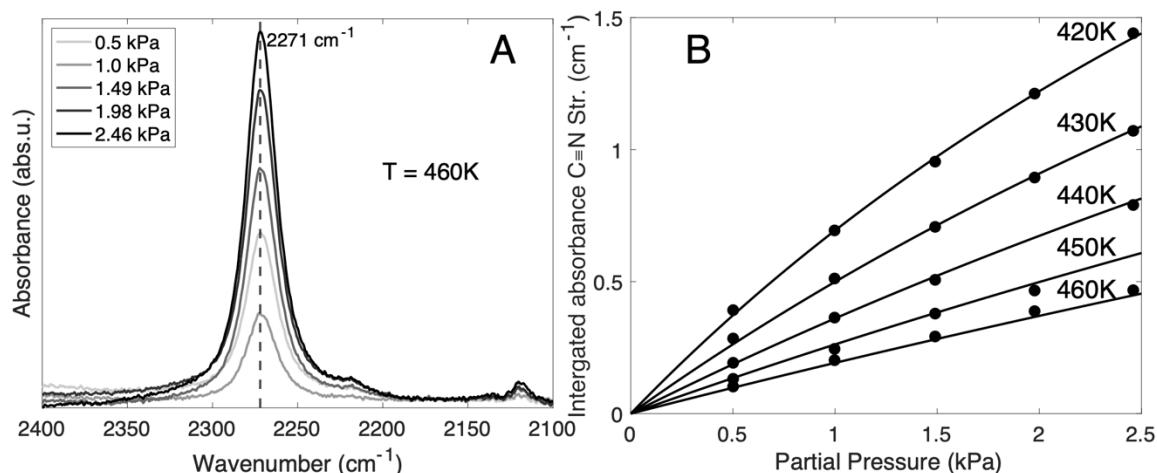


Figure 2.4: A) FTIR spectra of d_3 -acetonitrile adsorbed on $\text{SiO}_2\text{-1023}$ ($T = 460\text{ K}$) and B) isotherms collected using the integrated area of the peak centered at 2271 cm^{-1} for temperatures in the range of $T = 420\text{ K}$ - 460 K .

The value of ΔH_{ads}^o derived from the isotherms shown in Figure 2.4B is -55 kJ/mol and is essentially identical similar to that reported previously for d_3 -acetonitrile adsorbed onto silanol nests of zeolite beta (-55 kJ/mol)⁷³ and to the value for CH_3CN adsorption measured by microcalorimetry for silica (-55.4 kJ/mol).⁴³ The value of ΔS_{ads}^o for d_3 -acetonitrile adsorbed on silanol nests of zeolite beta is nearly 30% more negative than that measured in this work, suggesting that acetonitrile is more mobile on non-porous silica than confined within a micropore of zeolite beta. As with pyridine, the integrated absorbance of the $\text{C}\equiv\text{N}$ stretching vibration is linearly proportional to the perturbed SiO-H stretch integrated absorbance (Figures S11 and S12), indicating the dominant phenomenon measured corresponds to acetonitrile interactions with silanols.

2.4.4 Acetone Adsorption on $\text{SiO}_2\text{-1023}$

Adsorption of acetone onto $\text{SiO}_2\text{-1023}$ produces three detectable C=O stretching frequency bands at 1737 cm^{-1} , 1712 cm^{-1} , and 1699 cm^{-1} , as seen in Figure 2.5A. We note that a small shoulder was always observed at 1737 cm^{-1} in the absence of silica in our in-situ FTIR cell. This feature could be due to gas-phase acetone⁷⁵ or to a form of acetone interacting with the CaF_2 windows of the IR cell. This contribution was observed at all conditions and subtracted from the spectrum of acetone adsorbed on silica (Figure S2.13).

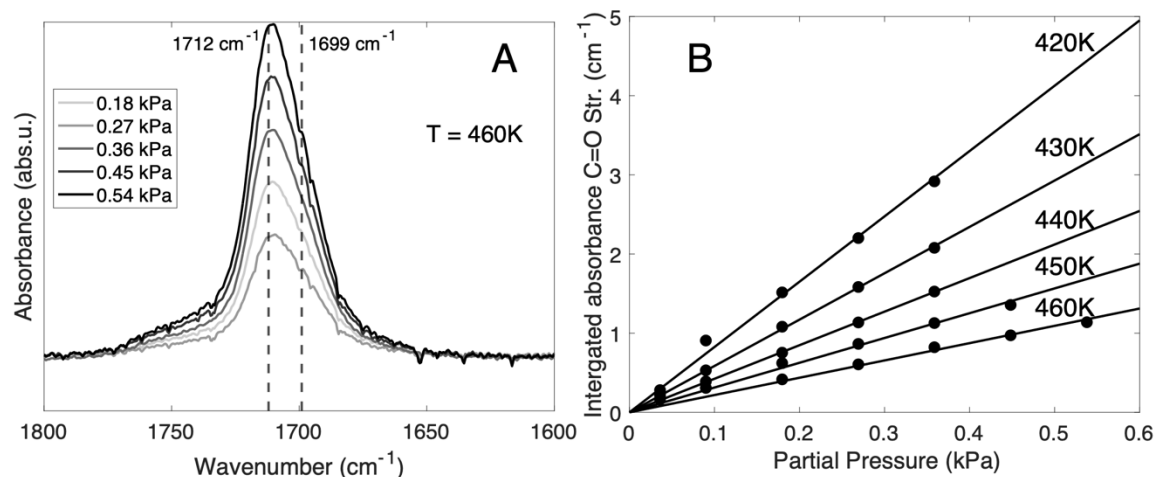


Figure 2.5: A) FTIR spectra of acetone adsorbed on SiO₂-1023 (T = 460 K) and B) isotherms collected using the integrated area of the peak centered at 1712 cm⁻¹ for temperatures in the range of T = 420 K-460 K.

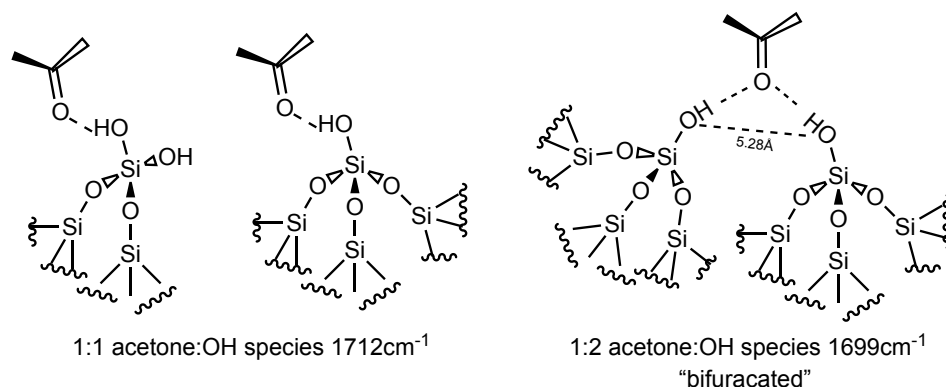


Figure 2.6: Adsorption configurations of acetone adsorbed to silanol groups on silica, as proposed in literature.⁵⁵ The optimal bond distance between bifurcated silanols is shown, as calculated by others.⁷⁶

2.4.5 Trimethyl acetonitrile Adsorption on SiO₂-1023

We also considered the adsorption of trimethyl acetonitrile ((CH₃)₃CCN) on SiO₂-1023. The IR spectrum for this adsorbate is presented in Figure 2.7A. The band appearing at 2243 cm⁻¹ is due to C≡N stretching vibrations and is like that seen for adsorbed CD₃CN. An example of our peak fitting procedure is displayed in Figure S2.17. The isotherms for trimethyl acetonitrile are shown in Figure 2.7B. The value of ΔH_{ads}^0 determined from these isotherms is -64 kJ/mol, which is ~18% more exothermic than that determined for CD₃CN on the same material (Table 2.2). This difference is consistent with the greater proton affinity of (CH₃)₃CCN compared to CD₃CN,⁷⁵ and results from inductive effects of exchanging hydrogen (deuterium in the case of CD₃CN) for electron-donating methyl groups. As with CD₃CN, the peak area for the C≡N stretching band is also linearly proportional to the perturbed SiO-H stretching frequency (Figures S18 and S19), indicating a silanol-adsorbate interaction.

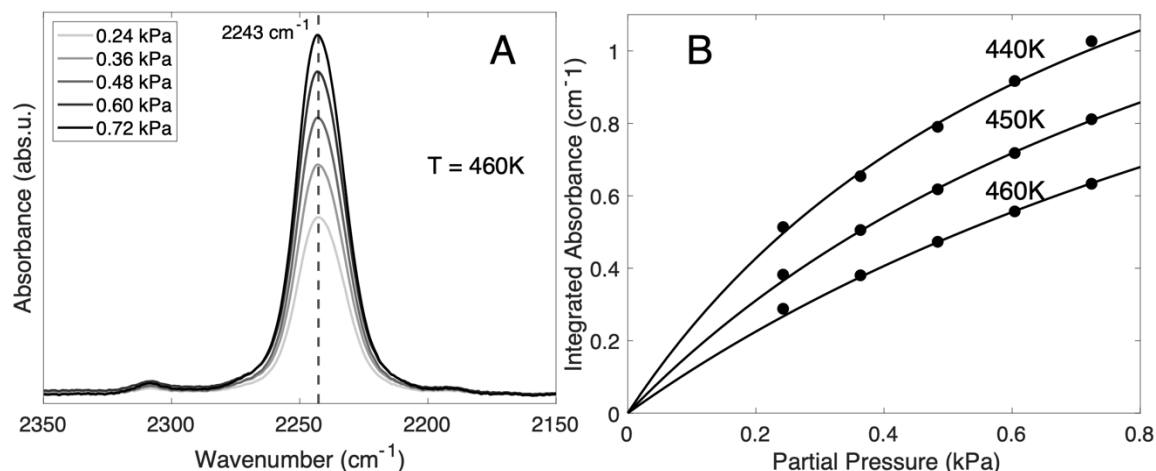


Figure 2.7: A) FTIR spectra of trimethyl acetonitrile adsorbed on SiO₂-1023 (T = 460 K) and B) isotherms collected using the integrated area of the peak centered at 2243 cm⁻¹ for temperatures in the range of T = 440 K-460 K.

Table 2.2 compiles all peak centers used for coverage measurements, as well as fit parameters for ΔH_{ads}^o , ΔS_{ads}^o ($P^o = 1$ bar), and the normalized saturation parameter (Q_{sat}).

Table 2.2: Assigned adsorption modes, peak centers, and Langmuir fitting parameters determined via FTIR coverage experiments for polar molecules adsorbed to SiO₂-1023

Interaction	Adsorption Mode	Peak Center (cm ⁻¹)	ΔH_{ads}^o (kJ/mol)	ΔS_{ads}^o (J/mol K)	Normalized* $Q_{sat} \times 10^2$
C ₅ H ₅ N-HO-Si≡	19b, ring-breathing	1444	-70 ± 1.8	-120 ± 3.2	5.68 ± 0.399
C ₅ H ₅ N-HO-Si≡	8a, ring-breathing	1594	-68 ± 1.5	-115 ± 2.8	8.08 ± 0.465
(CH ₃) ₂ C=O-HO-Si≡	C=O Str.	1712	-52 ± 1	N/M	N/M
(CH ₃) ₂ C=O-(HO-Si≡) ₂	C=O Str.	1699	-82 ± 1.9	-145 ± 3.3	2.36
CD ₃ CN-HO-Si≡	C≡N Str.	2272	-56 ± 1	-110 ± 1.5	3.83 ± 0.364
(CH ₃) ₃ CCN-HO-Si≡	C≡N Str.	2243	-64 ± 2	-104 ± 3.6	1.65 ± 0.108

*Unitless, normalized by the integrated absorbance of the Si-O-Si overtone region in the range 1735 cm⁻¹ – 2000 cm⁻¹

2.4.6 Theoretical calculations for polar molecules adsorbed on isolated silanol groups

Having validated the determination of thermodynamic parameters from adsorption isotherms obtained from IR spectra, we wanted to assess the ability of our theoretical approach to estimate the enthalpies of adsorption of polar molecules onto silanol groups present on the surface of amorphous silica. To this end, we examined two models for representing the surface of silica. The first was a silsesquioxane structure comprising eight corner-sharing Si groups (Figure 2.1A). The second model is the structure shown in Figure 2.1F, which agrees well with experimental determinations of silanol densities, ring-size distributions, and Si-O-Si bond angles.⁶⁷ Importantly, this model exhibits a silanol density of 1.7 OH/nm², which compares favorably with our measured value of 1.4 OH/nm² determined from TGA for SiO₂-1023.

We found that an MM region terminating approximately 11 Å from the central silicon atom of an isolated silanol group was sufficiently large enough to capture nearly all contributions of the MM region to the predicted ΔH_{ads}^o for pyridine (Figure S2.20). Interestingly, this also implies that the curvature of the model utilized for amorphous silica (see Figure 2.1F) has little impact on the ΔH_{ads}^o . The difference in ΔH_{ads}^o for adsorbed pyridine predicted using the site depicted in Figure 2.1B and Figure 2.1F is -32 kJ/mol, or, 41% of the ΔH_{ads}^o predicted with the largest model. Recent full QM DFT calculations (with counter-poise basis set superposition error corrections) modeling the adsorption of H₂O₂ and ethylene to silica-supported Nb metal sites found small differences (<10 kJ/mol) in predicted binding energies between large (12Å) and small (similar to Figure 2.1B) representations of the surrounding silica.⁷⁷ However, it is expected that H₂O₂ and ethylene would be less affected by cluster size compared to pyridine because they are smaller molecules and subject to weaker pairwise-additive VDW interactions.

Based on these considerations, to avoid the possible influence of edge effects from the MM portion of the cluster, we utilized a cluster that extended 29 Å from the Si atom of the silanol group, since the computational cost of using a larger MM region was negligible.

We compared our predicted values of ΔH_{ads}^o for triethylamine, ammonia, and tetrahydrofuran with those that we measured by IR spectroscopy and those reported in the literature determined by microcalorimetry.^{43,46} For ammonia, a detailed IR and calorimetric study revealed two dominant forms of ammonia adsorbed to SiO₂. We utilized the value reported for ammonia adsorption onto isolated silanol groups (-58.4 kJ/mol).⁴⁶

Figure 2.8 compares estimated values of ΔH_{ads}^o to experimental values reported here and in the literature. It is immediately apparent that the T8 silsesquioxane model of amorphous silica under binds all polar molecules in our dataset relative to experimental results. This finding is significant, considering that this model has been used extensively to calculate enthalpies of adsorption for various molecules interacting with silanol groups or ≡M-OH (M = Ti, Zr, etc.) groups supported on silica.^{2,8,11-13,26,66} We note, however, that computational studies of microporous silicates have reported that small cluster models cannot capture the non-local interactions between the adsorbate and the surrounding support material, leading to enthalpy of adsorption predictions that are typically too small relative to experimental benchmarks.⁶¹ It should be clear that these discrepancies are not the result of intrinsic DFT errors, which are expected to be relatively small (~ 4 kJ/mol) for the non-covalent interactions studied here.⁵⁹

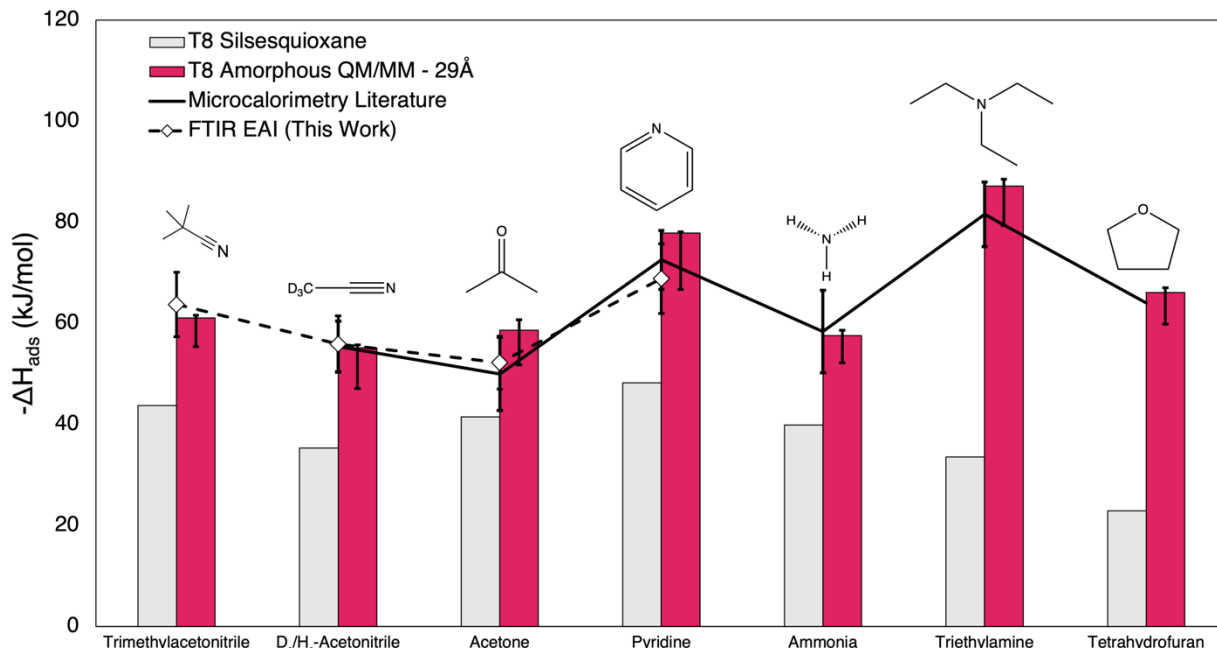


Figure 2.8: Comparison of experimentally measured (connected lines) and theoretically predicted (bars) values of ΔH_{ads}° . All calculations were performed for $T = 460$ K; however, similar conclusions are reached at other calculated temperatures. FTIR EAI = Fourier-transform Infrared Spectroscopy Equilibrium Adsorption Isotherm. Error bars for the T8 amorphous QM/MM model show the spread of predicted values of ΔH_{ads}° made from multiple local minimum geometries, while the bar represents the Boltzmann-weighted ΔH_{ads}° . Error bars on all experiments are $\pm 10\%$ of the reported value of ΔH_{ads}° .

A more detailed inspection of the isolated silanol in the amorphous model reveals that multiple adsorption geometries are plausible. In contrast to the T8 silsesquioxane, where the $\equiv\text{Si-OH}$ tetrahedron is symmetrical, the silanol tetrahedron on the amorphous model can be distorted. Moreover, the model of amorphous silica used shows that the silica surface is irregular; therefore, one should not expect identical values of ΔH_{ads}° for locally optimized adsorption geometries sampled around the silanol. To address this complication, we optimized multiple geometries starting from initial guesses at each face (or side) of the $\text{HO-Si}\equiv$ tetrahedron. We discovered multiple minima (for each adsorbate) and found that each geometry exhibited a different value of ΔH_{ads}° . For instance, we located 5 optimized geometries for pyridine bound in an H-bonding configuration with the silanol that exhibited specific ΔH_{ads}° of -80.5, -78.1, -71.5, -66.5, and -66.8 kJ/mol. Using our estimates of ΔS_{ads}° for each geometry enabled us to assess the corresponding values of ΔG_{ads}° . Using these values of ΔG_{ads}° , we calculated the Boltzmann weight for each geometry, yielding 0.554, 0.255, 0.156, 0.03, and 0.002, respectively, for $T = 460$ K. This demonstrates that multiple pyridine geometries bound to the same silanol can contribute to the measured value of ΔH_{ads}° . This observation is consistent with NMR studies indicating that pyridine undergoes significant rotational motion on silica silanols, even at $T = 174$ K.⁷⁸ Taking a Boltzmann average of the values of ΔH_{ads}° for different silanol geometries leads to $\Delta H_{ads}^{\circ} = -77.9$ kJ/mol, which agrees satisfactorily with experimental measurements.

The Boltzmann averaged ΔH_{ads}° for all adsorbates agree quantitatively with values determined experimentally from IR-based isotherms and measured microcalorimetrically. This agreement supports the model of amorphous silica and the computational protocol (QM/MM

method) utilized. Considering that the parameters for the MM region were derived initially for microporous silicates (zeolites), the agreement between predicted and experimentally measured enthalpies of adsorption indicates the transferability of the parameters.⁶¹

The observed values of ΔH_{ads}^o cannot be predicted reliably from a descriptor of the adsorbate basicity i.e., proton affinity, as seen in Figure S2.21, the correlation is weak and $R^2=0.79$. This implies that a significant portion of the total ΔH_{ads}^o arises from non-local interactions between the adsorbate and the surrounding silica, as mentioned previously. However, the degree of frequency redshift for the IR SiO-H stretch upon base complexation is more significantly correlated with proton affinity (Figure S2.22, $R^2=0.88$). This suggests that this spectroscopic phenomenon represents local interactions between the adsorbing base and the silanol group, and that it should not be used as a sole indicator of the relative stability of adsorbed polar bases.

We also note that a more rigorous calculation of ΔH_{ads}^o would require sampling all possible geometrical configurations for *all* silanol groups; however, this problem is currently intractable for a single silanol at the DFT level, let alone for all silanol groups present on the surface of amorphous silica. Thus, we will presume that the site used here is sufficiently representative of the surface of amorphous silica, as was noted by the authors of the model that we have used.⁶⁷ The agreement between experiments and our calculations, seen in Figure 2.8, supports this assumption.

2.4.7 Entropies of adsorption (ΔS_{ads}^o) for SiO₂

It is well-known that adsorbate entropies modeled using the rigid rotor - harmonic oscillator approximation (RRHO) can be inaccurate due to low-lying vibrational modes that should be modeled as hindered rotations or translations.⁷⁹ Our study employs a similar (and rougher) approach by representing low-frequency vibrational modes as free rotors.^{61,62} Our methods are reliable in predicting gas-phase entropies; however, the quasi-RRHO (qRRHO) approximation yields inaccurate predictions for ΔS_{ads}^o (Table 2.3). What is remarkable, though, is that Campbell and Sellers' empirical model for entropy loss upon adsorption (hereafter denoted as the "Campbell model") performs well, despite not being developed for adsorption on SiO₂.⁷⁹

Briefly, the Campbell model is a simple linear correlation relating the gas phase and adsorbed phase entropy (equation (7)).

$$S_{ads}^o(T) = S_{gas}^o(T) * 0.7 + 3.3R \quad (7)$$

where R is the ideal gas constant. This expression accurately predicts adsorbate entropies for n-alkanes and small polar molecules adsorbing to metal oxides, metals, and carbon surfaces. Thus, adsorbates retain nearly two-thirds of their entropy in the gas phase, which is thought to be due to hindered translations and rotations of adsorbates across the surfaces of these materials.⁷⁹ Notably, other studies have reported its accuracy in predicting the entropies of ethanol and water adsorbed to monomeric framework Sn sites in microporous silicates ("Sn-BEA zeolites").⁸⁰ The predictions by equation 7 agreed with ab initio molecular dynamics (AIMD) simulations which showed that ethanol and water retain significant localized translations around the Sn site. While the agreement of ΔS_{ads}^o predicted using equation 7 with experimental data should not be interpreted as a deep

understanding of the adsorption phenomena in question, it does suggest that significant adsorbate motion is retained relative to the assumptions of the RRHO model.

The discrepancy in the values of ΔS_{ads}^o observed experimentally and estimated from the Campbell model for trimethyl acetonitrile might be expected since the data used to develop the Campbell model did not include molecules with tert-butyl groups. The more positive value of ΔS_{ads}^o measured experimentally than that predicted may be due to total retention of internal entropy of rotation of the trimethyl group around the CN group of trimethyl acetonitrile. Developing methods for accurate predictions of ΔS_{ads}^o is an active area of research and lies outside the scope of this work, which is focused on ΔH_{ads}^o ; however, we note that simplified methods are needed for accurate prediction of both parameters using DFT potential energy surfaces, and a small number of DFT calculations. For now, we recommend a combination of QM/MM modeling for ΔH_{ads}^o combined with empirical estimates for ΔS_{ads}^o when accurate ΔG_{ads}^o estimates are desired.

Table 2.3: Gas phase entropies and entropies of adsorption, $P^o = 1$ bar – comparison between predictions and experiments

Molecule	$S_{gas,expt}$ (T=298 K)	$S_{gas,qRRHO}$ (T=298 K)	$S_{gas,qRRHO}$ (T=460 K)	$\Delta S_{ads,qRRHO}$ ^o (T=460 K)*	$\Delta S_{ads,Campbell}$ (T=460 K)** ₇₉	$\Delta S_{ads,expt}$
Pyridine	282.8 ⁸¹	281.1	322.2	-186.7	-124.1 ± 18	-120 ± 3.2
d3-acetonitrile	N/A	250.6	279.1	-149.6	-111.2 ± 18	-110 ± 1.5
h3-acetonitrile	245.5 ⁸²	242.7	267.9	N/A	-107.8 ± 18	N/A
Acetone	295.5 ⁵⁵	298.0	335.6	-185.0	-128.1 ± 18	-122 ⁵⁵
Trimethyl acetonitrile	333.2 ⁸³	329.4	389.5	-180.6	-144.3 ± 18	-104 ± 3.6

*Boltzmann average of multiple equilibrium geometries; **uses $S_{gas,qRRHO}$ to compute adsorbed phase entropy, then takes the difference to calculate $\Delta S_{ads,Campbell}$. Error bars represent one standard error reported in ref⁷⁹

2.4.8 Characterization of Ti/SiO_{2,1023}

DRUV/Vis spectra were acquired to determine the coordination of Ti in **Ti/SiO_{2,1023}**. The UV/Vis spectrum for **Ti/SiO_{2,1023}**, shown in Figure 2.9A, displays a sharp peak centered at 224 nm, consistent with ligand-to-metal charge transfer (LMCT) transitions of isolated, tetrahedral ≡Ti-OH centers.^{49,84} This spectrum was used to construct a direct-transition Tauc plot, from which the band-edge energy was calculated. As noted in Table 2.4, the band-edge energy for **Ti/SiO₂** is 4.75eV, which agrees very well with the values previously reported for Ti/SiO₂ prepared with very low loadings of Ti.^{31,36,37} A second sample of **Ti/SiO_{2,1023}** was prepared to confirm reproducibility. The sample exhibited a nearly identical UV/Vis spectrum and direct band-edge energy (Figure S2.24).

The Ti K-edge XAS spectrum displays a pre-edge feature centered between 4969.8 eV and 4970.1 eV. This feature arises from 1s→3d electronic transitions that become dipole-allowed due to 3d/4p mixing when the Ti and its ligands are in a tetrahedral geometry.⁸⁵ At ambient temperature (300 K), pre-exposure of **Ti/SiO_{2,1023}** to water vapor results in the coordination of water to Ti, breaking the Ti tetrahedral symmetry and producing a pre-edge feature that is weak in intensity

relative to the tetrahedral standard, **Ti[OSiPh₃]₄**, and centered at 4970.1eV (Figure 2.9B). Increasing the temperature under flowing helium drives off the water, reestablishing the tetrahedral geometry, and blue-shifting the peak by 0.3 eV to 4969.8eV and increasing its intensity 2-fold. The pre-edge intensity rises rapidly with the initial increase in temperature but changes less as the temperature reaches 673 K, indicating complete desorption of coordinated water, consistent with other studies for this material.⁴⁹ The pre-edge feature does not change significantly after lowering the temperature to 553 K following water desorption, indicating a weak thermal effect on peak intensity (Figure S2.24).

Previous studies on Ti/SiO₂ synthesized using similar techniques have reported lower pre-edge intensities than those found here.²⁹ However, it is important to note that these materials were vacuum treated only to 423 K, which is not sufficiently high to remove all coordinated water.⁴⁹ The normalized pre-edge peak intensity for **Ti/SiO_{2,1023}** is 17% lower than **Ti[OSiPh₃]₄**, even after desorption of coordinated water. It has been suggested that a lower intensity pre-edge peak for Ti/SiO₂ could be due to a linear combination of hexacoordinated and tetrahedral Ti metal centers⁸⁶; however, our UV/Vis results are inconsistent with this interpretation since there is no detectable presence of hexacoordinated species, which would be characterized by peaks >300nm.⁸⁴ An alternative explanation is suggested by recent DFT calculations. Tetrahedral distortion was found to significantly decrease the intensity of the pre-edge XANES feature predicted by Time-Dependent DFT for isolated V(V)/SiO₂ species.¹¹ A similar effect would be expected for Ti(IV) cations, as both V(5+) and Ti(IV) cations have identical electronic configurations. Moreover, the same electronic transition is being probed (1s→3d/4p transition) for both cations. Thus, at the extremes, two hypotheses about the structure of monomeric ≡Ti-OH in **Ti/SiO_{2,1023}** can be postulated from these findings. 1) The sample consists of many tetrahedral ≡Ti-OH sites that exhibit specific pre-edge intensities consistent with **Ti[OSiPh₃]₄** and a small fraction of tetrahedrally distorted ≡Ti-OH structures exhibiting weak pre-edge features. This hypothesis is similar to that proposed for Cr/SiO₂.⁸⁷ 2) All ≡Ti-OH sites are similarly distorted and produce a weaker pre-edge feature relative to **Ti[OSiPh₃]₄**. Ti K-edge XAS cannot discriminate between these two possibilities, since it is a bulk technique; however, the degree to which **Ti/SiO_{2,1023}** distortion can be interrogated will be discussed below by measuring the ΔH_{ads}^o of pyridine adsorption as a function of pyridine loading.

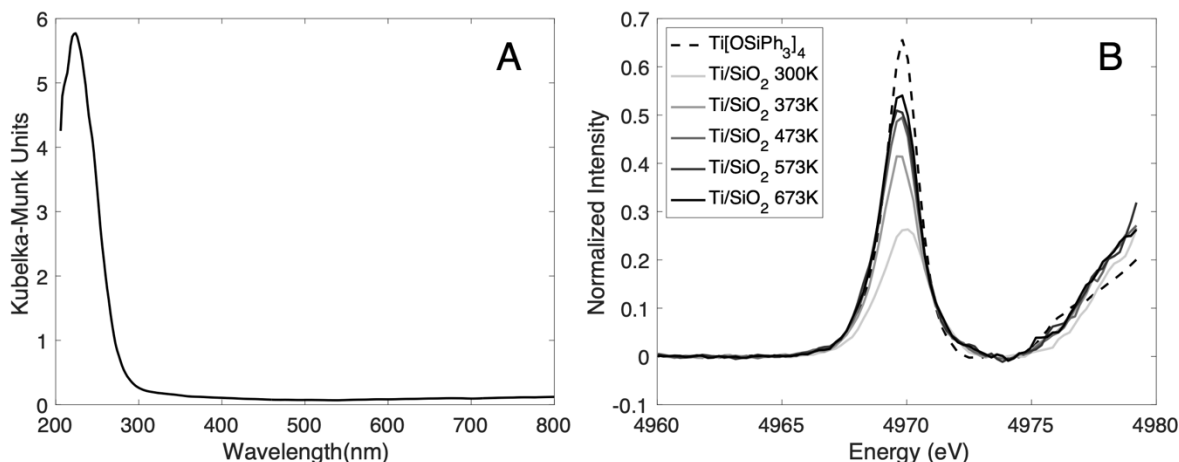


Figure 2.9: A) Diffuse-reflectance UV/Vis spectrum of $\text{Ti/SiO}_2\text{-1023}$ at 553.15 K under flowing He and B) pre-edge XANES spectra of $\text{Ti/SiO}_2\text{-1023}$ and $\text{Ti[OSiPh}_3\text{]}_4$. The pre-edge XANES spectra for $\text{Ti/SiO}_2\text{-1023}$ was taken under flowing He.

Table 2.4: ICP characterization, UV Vis edge energies

Material	LMCT Edge(eV)/ Peak(nm)	Ti/nm ²	Method	Ref
Ti/MCM-41	4.7	0.07	IWI*	88
Ti/SiO ₂	4.66/210	0.24	IWI*	89
Ti/SBA15	N.M./225	0.61	Ti(OiPr)[Osi(OiBu) ₃] ₃ – graft	7
Ti/SiO ₂	4.53/225	0.24	Calix[4]arene-Ti ^{IV} graft	49
Ti/SiO_{2,1023}	4.75/224	0.084	Cp – graft	This Work
Ti/SiO_{2,1023} (sample 2)	4.84/224	0.089	Cp – graft	This Work

*Incipient wetness impregnation

2.4.9 Pyridine adsorption on $\text{Ti/SiO}_2\text{-1023}$ – experiments and theory

An adsorbate that does not react and consume $\equiv\text{Ti-OH}$ sites is required to measure equilibrium adsorption isotherms. Unfortunately, we observed decomposition and consumption of $\equiv\text{Ti-OH}$ sites over time for all the adsorbates we tested for SiO_2 except pyridine. Thus, we restrict our analysis for $\text{Ti/SiO}_2\text{-1023}$ to pyridine.

The IR spectra of pyridine adsorbed to $\text{Ti/SiO}_2\text{-1023}$ were collected at temperatures of 503.15 K to 623.15 K and partial pressures between 0.035 and 0.49 kPa. Figure 2.10A shows the spectrum of adsorbed pyridine acquired at 503.15 K in the presence of 0.42 kPa pyridine. Peaks are observed at 1605 cm^{-1} , 1489 cm^{-1} , and 1447 cm^{-1} . These features correspond to ring-breathing vibrational modes of pyridine interacting directly with a Lewis acid center.²² No absorbance is observed between 1540-1550 cm^{-1} , indicating the absence of pyridinium ions which would be formed by pyridine adsorption at Brønsted acid sites.²² We also note that the band at 1605 cm^{-1} is red-shifted relative to that observed for pyridine adsorbed on P25 TiO_2 at 470 K (1609 cm^{-1})⁹⁰, suggesting the absence of TiO_2 , which is consistent with our UV/Vis observations (see Figure 2.9). The peak center is within a 2 cm^{-1} range for all conditions examined.

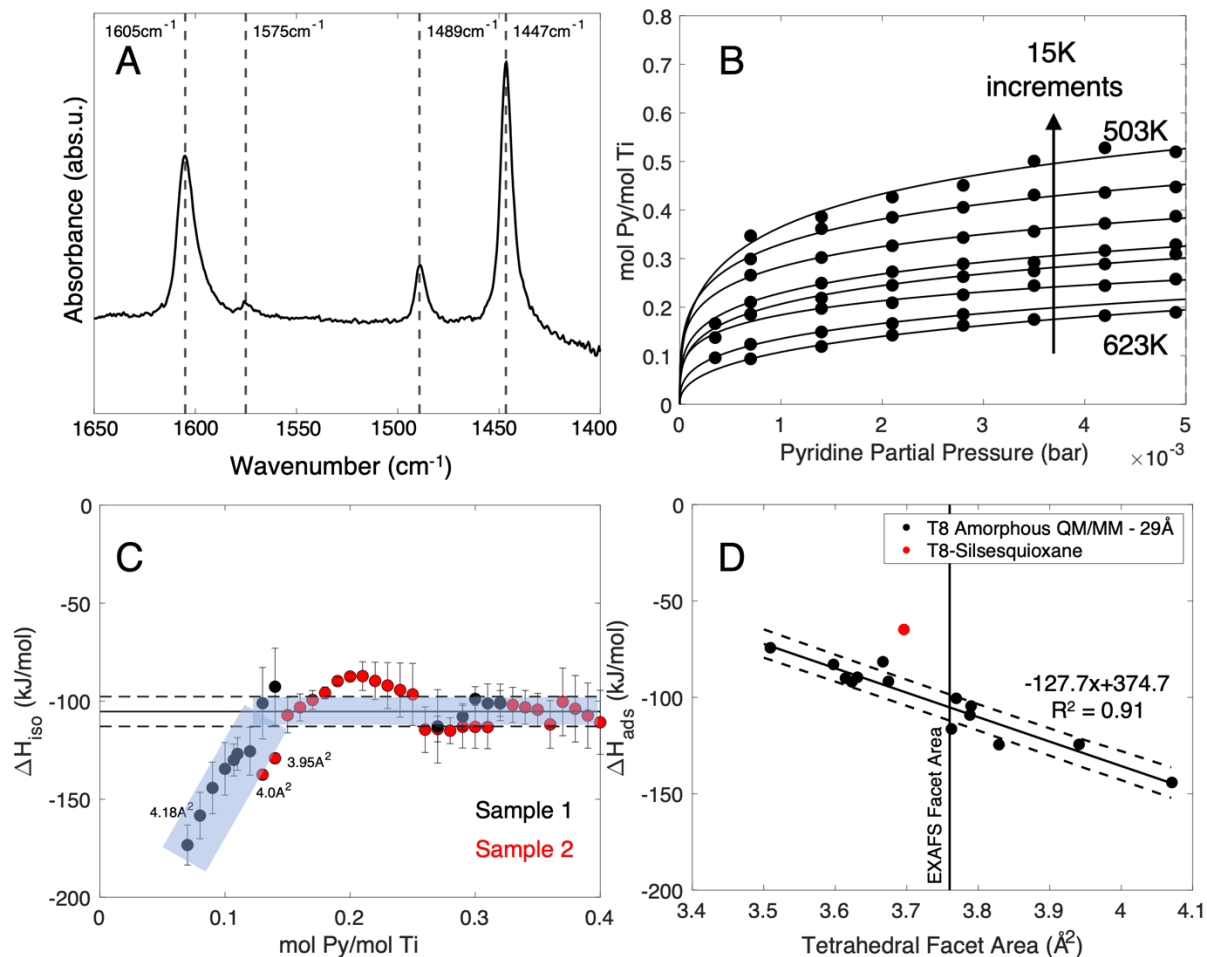


Figure 2.10: A) Difference spectrum for pyridine adsorbed on $\text{Ti/SiO}_{2,1023}$ (**sample 2**) ($T = 503.15 \text{ K}$, $P_{\text{py}} = 0.42 \text{ kPa}$). B) pyridine coverage on $\text{Ti/SiO}_{2,1023}$ (**sample 2**) (mol Py/mol Ti) as a function of partial pressure (bar). Langmuir-Freundlich isotherm fits are shown as lines. Covers T-range 503.15 K through 623.15 K except 593.15 K. C) Isosteric enthalpy of adsorption of pyridine to $\equiv\text{Ti-OH}$ sites as a function of pyridine coverage (mol Py/mol Ti). Facet areas calculated from the correlation presented in Figure 2.10D are labeled. The solid black line shows the predicted $\Delta H_{\text{ads}}^{\circ}$ of pyridine to a $\equiv\text{Ti-OH}$ site with a facet area derived from EXAFS (3.76 \AA^2), while dashed black lines are one standard error of the $\Delta H_{\text{ads}}^{\circ}$ prediction from the correlation in Figure 2.10D. The blue-shaded regions are guides for the eye. D) QM/MM calculations of $\Delta H_{\text{ads}}^{\circ}$ ($T = 598 \text{ K}$) as a function of the tetrahedral facet area of the $\equiv\text{Ti-OH}$ site to which pyridine is bound). The solid line is the linear fit, while the dashed lines are one standard error of the estimated value of $\Delta H_{\text{ads}}^{\circ}$.

To analyze pyridine features associated exclusively with adsorption to $\equiv\text{Ti-OH}$ sites, we subtracted the spectrum of pyridine bound to $\text{SiO}_{2,1023}$ at each condition using the same mass of powder ($\pm 1 \text{ mg}$) to form the pellet. To ensure the accurate removal of features during the subtraction process, we conducted a control experiment to subtract the spectra from two consecutive $\text{SiO}_{2,1023}$ (Figures S25, S26, and S27) runs. The subtracted peak areas equal zero, indicating that this procedure properly removes contributions associated with pyridine bound to silanol groups and confirms that our pellet preparation method is reproducible.

Having validated our subtraction procedure, we used it to remove the overlapping features of pyridine interacting with $\text{SiO}_{2,1023}$ from the spectrum of $\text{Ti/SiO}_{2,1023}$ acquired for all experimental conditions. After subtraction, we observed a new feature at 1575 cm^{-1} , attributed to

ring-breathing mode 19a, which can be observed when pyridine interacts molecularly with a Lewis acid center.²² The appearance of this mode after subtraction of the spectrum for pyridine adsorption on SiO₂ further lends credence to our subtraction protocol. Moreover, no significant distortion or over-subtraction artefacts were observed in all **SiO_{2,1023}** subtracted spectra (Figure 2.10A). Thus, the experimental protocol we have developed monitors the surface coverage of pyridine bound exclusively to ≡Ti-OH sites.

To calculate the fractional coverage (mol pyridine/mol Ti), we applied the appropriate extinction coefficient for the peak centered at 1605 cm⁻¹.^{71,91} We did not analyze the feature at 1447 cm⁻¹ because IR absorption from the CaF₂ optical windows of our in-situ cell began to interfere with this peak above 593 K. The temperature range of this experiment was broad compared with our experiment with **SiO_{2,1023}** alone; therefore, we also accounted for the temperature dependence of the extinction coefficient using the following expression:⁹²

$$\epsilon(T) = \epsilon_{1605cm^{-1}}(T = 423K) - 0.001 * (T - 423K) \quad (8)$$

where $\epsilon_{1605cm^{-1}}(T = 423 K)$ is equal to 0.9733 cm/μmol pyridine⁹¹ and T is the temperature of the experiment in Kelvin. We note that extinction coefficients for pyridine adsorbed to Lewis acid metal supported silicates fall in the range of 0.7-1.5 cm/μmol.⁷¹ We also note that our experimental setup, i.e., the brand of spectrometer, detector type, pellet size and mass were similar to those used for the experiment reported in the ref.⁹¹ This further supports the applicability of the extinction coefficients reported by the authors of this work to our experiments.

The adsorption isotherms for **Ti/SiO_{2,1023}** are shown in Figure 2.10B. In contrast to what was observed for pyridine adsorption to the silanol groups present on **SiO_{2,1023}**, the data for pyridine adsorption on **Ti/SiO_{2,1023}** cannot be described by a Langmuir isotherm, for which ΔH_{ads}° is assumed to be constant. (Figure S2.28). Therefore, we calculated the isosteric enthalpies of adsorption ($\Delta H_{iso}^{\circ}(\theta)$) as a function of pyridine coverage. To do so, we fitted the experimental data points shown in Figure 2.10B to a Langmuir-Freundlich isotherm (equation 9) and used this expression to estimate coverages between experimental data points.

$$Q = Q_o \frac{(AP)^n}{1 + (AP)^n} \quad (9)$$

Values of Q_o, A, and n were fitted to each isotherm (Figure 2.10B). We then estimated the partial pressure necessary to achieve a given mol Py/mol Ti to determine the isosteres, which were then used together with the Clausius-Clapeyron equation (equation (10)) to calculate the isosteric enthalpy of adsorption.

$$\Delta H_{iso}(\theta) \left[\frac{kJ}{mol} \right] = \left(\frac{d \ln(P_{pyridine}[bar])}{d \left(\frac{1}{RT} \right)} \right)_{\theta} \quad (10)$$

In carrying out this procedure, at least three data points were taken per isostere, and we only extrapolated an isotherm within 10% of the minimum/maximum coverage. This point is necessary since values of $\Delta H_{iso}^o(\theta)$ can be sensitive to extrapolation percentages (Figures S29 and S30) even though general trends are preserved. Thus, extrapolation by more than 10% should be avoided so that values of $\Delta H_{iso}^o(\theta)$ do not include these artefacts.

Figure 2.10C shows that for coverages less than 15%, the magnitude of $\Delta H_{iso}^o(\theta)$ decreases with increasing coverage and then becomes relatively constant for coverages above 15%. We found similar behavior for two different samples of **Ti/SiO₂₋₁₀₂₃** (see Figure S2.31 for fitting of the Langmuir-Freundlich isotherm for **Ti/SiO₂₋₁₀₂₃ (sample 1)** used to calculate $\Delta H_{iso}^o(\theta)$ for sample 1 in Figure 2.10C). To assess the possibility that distortion of tetrahedral $\equiv\text{Ti-OH}$ sites could explain the variation in adsorption enthalpy observed at low pyridine coverages, we calculated ΔH_{ads}^o for a series of representative $\equiv\text{Ti-OH}$ sites. Each of these sites was defined by replacing an $\equiv\text{Si-OH}$ group on the surface of our model of amorphous silica with a $\equiv\text{Ti-OH}$ group and then optimizing the resulting structure. Figure 2.2 illustrates the geometry of each $\equiv\text{Ti-OH}$ group obtained in this manner and the areas of the three triangular facets for each group. We note that the triangular facets of each $\equiv\text{Ti-OH}$ group exhibit different areas and that the set of areas is different for the seven $\equiv\text{Ti-OH}$ groups chosen as representatives. To pursue our objective, we calculated the enthalpies of pyridine adsorption on each facet for each of the seven $\equiv\text{Ti-OH}$ groups. The results, presented in Figure 2.10D, show that the value ΔH_{ads}^o correlates well ($R^2 = 0.91$) with the area of the triangular facet; as the facet area increases, the predicted value of ΔH_{ads}^o decreases monotonically. We were unable to acquire data for all facet areas since some facets were inaccessible to pyridine due to steric interference by the surrounding silica. What we find is that as the area of the facet increases from 3.5 \AA^2 to 4.07 \AA^2 , the values of ΔH_{ads}^o decrease from -74 kJ/mol to -145 kJ/mol , respectively. This descriptor is reminiscent of the “accessible coordination pocket” that others have correlated with ethylene epoxidation activation energies with Nb/SiO₂ catalysts.⁷⁷

As noted in our discussion of the physical characteristics of $\equiv\text{Ti-OH}$ groups, EXAFS characterization suggests that the average Ti-O bond length is between 1.80 \AA and 1.81 \AA and that the coordination of Ti atoms with O atoms is 4.^{5,49} Assuming this geometry is tetrahedral, which is supported by the intense pre-edge XANES features, leads to the conclusion that the triangular facet area ranges from 3.74 \AA^2 to 3.78 \AA^2 ; therefore, we take 3.76 \AA^2 as the EXAFS determined Ti facet area. For this facet area the correlation presented in Figure 2.10D gives a value of $\Delta H_{ads}^o = -105 \pm 10 \text{ kJ/mol}$, which agrees remarkably well with the average experimentally determined value of $\Delta H_{ads}^o = -104 \pm 10 \text{ kJ/mol}$ observed in Figure 2.10C for pyridine coverages greater than 15%. At lower coverages, larger tetrahedral facet areas are necessary to achieve agreement between our calculations and experiments. Therefore, we propose that tetrahedral distortion of $\equiv\text{Ti-OH}$ sites can explain lower values ΔH_{ads}^o determined for coverages $<15\%$. We note this proportion of distorted sites is similar to that reported for isolated sites of Cr, W, and Mo supported on silica.^{23,87,93}

We also wish to stress that our ability to interpret the isosteric enthalpies of adsorption of pyridine is a consequence of the model for $\equiv\text{Ti-OH}$ sites on **Ti/SiO₂₋₁₀₂₃** that we have used. As indicated by the red point in Figure 2.10D, calculations of ΔH_{ads}^o determined using the T8 silsesquioxane representation of $\equiv\text{Ti-OH}$ groups under predicts the value of this parameter relative

to its experimentally determined value, as seen for $\text{SiO}_{2,1023}$, further indicating the insufficiency of the size of this model.

We conclude that only a small fraction ($\sim 15\%$) of $\equiv\text{Ti-OH}$ sites are distorted tetrahedral structures, while the rest are relatively symmetrical and consistent with the geometries determined from EXAFS data. We further propose that the observed pre-edge XANES intensity reduction relative to our tetrahedral standard results from a linear combination of distorted (weak pre-edge feature¹¹) and symmetric $\equiv\text{Ti-OH}$ structures (strong pre-edge feature).

The magnitudes of ΔH_{ads}^o measured here for $\equiv\text{Ti-OH}$ sites strongly disagree with previous researchers.^{33,48} Unfortunately, the methods of data acquisition and analysis employed by others were, in our opinion, inadequate. Firstly, the IR peaks used for coverage estimates of pyridine to the $\equiv\text{Ti-OH}$ sites overlap significantly with peaks associated with pyridine adsorption to $\equiv\text{Si-OH}$ groups of SiO_2 and no attempt was made to remove these features. Secondly, the analysis employed (Van't Hoff analysis of isobars) is only accurate in the limit of zero coverage for a theoretical Langmuir isotherm. As a result, the previously reported values of ΔH_{ads}^o lie between -10 and -30 kJ/mol, which are far lower than the enthalpies of liquefaction of pyridine ($\Delta H_{liq}^o = -40.3$ kJ/mol) and the value of ΔH_{ads}^o for pyridine adsorption on the SiO_2 support (-70 kJ/mol). We would like to note that significant underestimation of ΔH_{ads}^o and reversed trends in ΔH_{ads}^o across materials are expected from Van't Hoff isobar analysis (See SI section 2.7.27 for a full discussion).

2.4.10 Energy decomposition analysis to understand the physical origin of the effects of site distortion on ΔH_{ads}^o

To further understand the physical phenomenon governing the change in ΔH_{ads}^o with site distortion, we performed an energy decomposition analysis (EDA) using methods developed by Horn et al.⁵⁰ For this analysis, we only examined the components of the electronic energy of adsorption (ΔE_{ads}^o), as this is the largest component of the ΔH_{ads}^o .

The EDA represents ΔE_{ads}^o as the sum of five components. The overall binding energy is calculated as:

$$\Delta E_{ads}^o = \Delta E_{GD,Ti} + \Delta E_{GD,Py} + \Delta E_{FRZ} + \Delta E_{POL} + \Delta E_{CT} \quad (11)$$

where $\Delta E_{GD,x}$ captures the geometric distortion penalty of x (the $\equiv\text{Ti-OH}$ site or the pyridine molecule), or the energy difference between x in the complex geometry and its optimal geometry in vacuum; ΔE_{FRZ} is the interaction energy resulting from permanent electrostatic charges, Pauli-repulsion, and dispersion interactions (we include the MM VDW interaction in this term); ΔE_{POL} is the energy lowering due to polarization of the orbitals on each fragment in the presence of the other fragment; and ΔE_{CT} accounts for the energy lowering due to inter-fragment charge transfer (electron delocalization) between the $\equiv\text{Ti-OH}$ site and the pyridine molecule.

Interestingly, only two components of the EDA change appreciably with facet area, ΔE_{FRZ} and $\Delta E_{GD,Ti}$ (Figure 2.11). We fit linear models for each component to understand the trends quantitatively (Table 2.5). Taking the slope as the first derivative of the component in question with respect to the tetrahedral facet area suggests that the geometric distortion penalty of the $\equiv\text{Ti-OH}$ site is most strongly correlated to the ΔE_{ads}^o (the slope for this component comprises 60% of

the slope for ΔE_{ads}^o). We can take the x-intercept as the tetrahedral facet area where $\Delta E_{GD,Ti}$ is zero, which yields 4.35 \AA^2 . $\Delta E_{GD,Ti}$ must be positive semi-definite,⁵⁰ therefore this facet area also corresponds to the upper bound of the magnitude of ΔE_{ads}^o , which we estimate to be -172.5 kJ/mol based on our linear correlation. Assuming this facet area arises from a $\equiv\text{Ti-OH}$ site in perfect tetrahedral geometry implies Ti-O bond lengths of 1.94 \AA , or nearly 0.14 \AA longer than values derived from EXAFS. All attempts to locate a $\equiv\text{Ti-OH}$ site with this size facet area were unsuccessful using the amorphous silica model we employed, but sites with this level of distortion are likely to be extremely uncommon. The present analysis marks the first utilization of EDA as a means of estimating the maximum ΔE_{ads}^o of an adsorbate to a SSMC.

ΔE_{FRZ} has the second largest facet area dependence ($\sim 30\%$), and the relationship displays more scatter around our linear fit relative to $\Delta E_{GD,Ti}$ (see Figure 2.11). All other components display minimal scatter around their associated linear fits, indicating that the variation in ΔE_{ads}^o with facet area arises primarily from variation in ΔE_{FRZ} . The variability in ΔE_{FRZ} with facet area is expected since ΔE_{FRZ} includes the interaction of pyridine with the MM region of the surrounding silica support which will vary considerably for each $\equiv\text{Ti-OH}$ site in an amorphous lattice regardless of its local geometry. We note one outlier for $\Delta E_{GD,Ti}$ that occurs for a facet area of 3.66 \AA^2 (site 2, face 3 in Table 2.1). This facet exhibits a larger $\Delta E_{GD,Ti}$ relative to the linear fit because of a siloxane bridge located directly in front of the facet (can be seen in Figure 2.2, site 2). The final geometry of the $\equiv\text{Ti-OH}$ site after pyridine adsorption is more significantly distorted than would be expected since pyridine avoids steric repulsion from this siloxane bridge, leading to a more positive value of $\Delta E_{GD,Ti}$ than predicted by the linear fit.

Surprisingly, ΔE_{POL} and ΔE_{CT} remain nearly constant with facet areas. This discovery challenges previously held conjectures regarding silica-supported Zr, W, and Nb sites.²² Our results indicate that distortion does not influence the ability of the cation to accept electrons from a Lewis base, or its polarizability, but rather relieves the penalty associated with complex formation ($\Delta E_{GD,Ti}$) and enhances ΔE_{FRZ} which includes a complex interplay between permanent electrostatic charges, Pauli-repulsion, and dispersion interactions.⁵⁰ Since ΔE_{POL} and ΔE_{CT} are not dependent on facet area, this suggests that these terms depend largely on the adsorbate (for a given SSMC). Thus, we posit that shifts in the y-intercept of ΔE_{POL} and ΔE_{CT} will depend on the adsorbate polarizability and ionization energy.

Finally, we performed EDA calculations to investigate why the silsesquioxane model under binds relative to experiments and QM/MM predictions (see red datapoint on Figure 2.10D). As shown in Figure S2.32, the EDA components for the silsesquioxane-pyridine complex are all smaller in magnitude than predictions based on the $\equiv\text{Ti-OH}$ facet area. The most significant error resides in the ΔE_{FRZ} (31.7% of total absolute error), followed by ΔE_{POL} (21.1%), $\Delta E_{GD,Ti}$ (20.8%), ΔE_{CT} (18.6%), and $\Delta E_{GD,Py}$ (7.8%). Thus, the errors associated with using a small cluster model are distributed relatively evenly amongst all the components of the intermolecular interactions. This further supports the need to use more extensive representations of the silica surrounding the active site to capture all interactions present in adsorption events. Since the first step in heterogeneously catalyzed reactions involves adsorption, we believe the errors noted here for adsorption may also translate to computational catalysis studies.

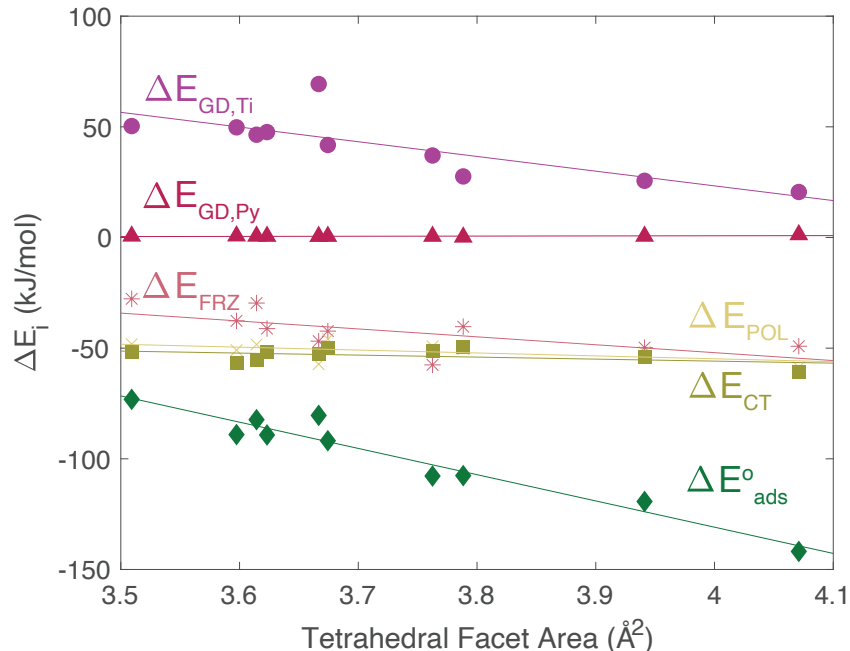


Figure 2.11: The dependence of each component of the EDA on the tetrahedral facet area.

Table 2.5: Linear fit parameters for lines in Figure 2.11

EDA Component	Slope	Intercept
$\Delta E_{GD,Ti}$	-66.5	289.2
$\Delta E_{GD,Py}$	0.7	-2.1
ΔE_{FRZ}	-35.7	78.4
ΔE_{POL}	-13.1	-2.4
ΔE_{CT}	-9.1	-19.5
ΔE_{ads}^o	-118.6	343.5

2.5 Conclusions

This study has successfully developed and validated experimental and theoretical methods for determining enthalpies of adsorption for polar molecules interacting with $\equiv\text{Si-OH}$ and $\equiv\text{Ti-OH}$ sites located on the surface of amorphous silica. We have shown that adsorbate coverage of $\equiv\text{Si-OH}$ groups can be determined accurately by IR spectroscopy, and that enthalpies of adsorption obtained by fitting a Langmuir isotherm to these data agree well with microcalorimetric measurements reported in the literature. We have also demonstrated that a silsesquioxane representation of $\equiv\text{Si-OH}$ sites is not large enough to capture non-local interactions between adsorbates and the surrounding silica support, resulting in consistent underestimation of the enthalpies of adsorption for polar molecules interacting with $\equiv\text{Si-OH}$ and $\equiv\text{Ti-OH}$ groups. By contrast, estimates of the enthalpy of adsorption on such sites that agree to within 10% of experimental measurements can be achieved using a QM/MM approach in which a given $\equiv\text{Si-OH}$ site is surrounded by amorphous silica to a radius of more than 11 Å. Extending our validated IR methods to $\equiv\text{Ti-OH}$ sites, we found that the isosteric enthalpy of adsorption of pyridine decreases with pyridine coverage for coverages up to 15% and then remains relatively constant (-105 ± 10 kJ/mol) for coverages above 15%. Using our validated QM/MM model for $\equiv\text{Si-OH}$ sites, we

generated a series of $\equiv\text{Ti-OH}$ sites differing in the degree of distortion of the tetrahedral facets (i.e., O-Ti-O triangular facets) and calculated the enthalpy of pyridine adsorption to each of them. We found that predicted enthalpy of pyridine adsorption is approximately proportional to the initial area of the $\equiv\text{Ti-OH}$ facet to which pyridine is bound. The prediction of the enthalpies of adsorption of pyridine for a tetrahedral facet area derived from experimental EXAFS measurements matches the value observed experimentally (-104 ± 10 kJ/mol). This finding and the observation of an intense XANES pre-edge feature suggest that most $\equiv\text{Ti-OH}$ sites are symmetrical tetrahedra and exhibit geometries consistent with those determined from EXAFS fitting. A small portion ($<15\%$) of $\equiv\text{Ti-OH}$ sites are described as distorted and exhibit tetrahedral facet areas larger than those measured by EXAFS. This distortion causes a decrease in intensity of the pre-edge XANES features relative to a strictly tetrahedral standard ($\text{Ti}[\text{OSiPh}_3]_4$). Energy decomposition analysis (EDA) indicates that a large initial $\equiv\text{Ti-OH}$ site facet area increases the enthalpy of pyridine adsorption by reducing the geometric distortion penalty for the $\equiv\text{Ti-OH}$ site to achieve its optimized geometry in the adsorbate-bound complex and enhances frozen interactions (a component that comprises a complex interplay between permanent electrostatics, Pauli-repulsion, and dispersion). EDA calculations suggest distorted sites could exhibit tetrahedral facet areas as large as 4.35 \AA^2 (as opposed to 3.76 \AA^2 determined from EXAFS). The identification of distorted $\equiv\text{Ti-OH}$ sites opens the need to consider the role of such sites in the promotion of reactions catalyzed by $\equiv\text{Ti-OH}$ groups, which have previously been considered to be largely minimally distorted tetrahedra, as inferred from EXAFS data.

2.6 Acknowledgments

This work was supported by the Office of Science, Office of Basic Energy Sciences of the U.S. Department of Energy under Contract No. DE-AC02-05CH11231. Work on energy decomposition analysis was supported by the U.S. National Science Foundation through Grant No. CHE-2313791. The authors thank Abraham Martinez for assistance with the acquisition of the TGA data in this work. The authors also acknowledge Dr. Yujia Ding for assistance in acquiring XAS data, and Dr. Jeremy Kropf and Dr. Jacklyn Hall for assistance setting up the in-situ XAS cube reactor. This research used resources of the Advanced Photon Source; a U.S. Department of Energy (DOE) Office of Science User Facility operated for the DOE Office of Science by Argonne National Laboratory under Contract No. DE-AC02-06CH11357. Computational resources for this work were provided by the Molecular Graphics and Computation Facility at the UC Berkeley College of Chemistry, supported by the National Institutes of Health grant NIH S10OD034382.

2.7 Supporting Information

2.7.1 TGA Characterization of SiO₂ materials

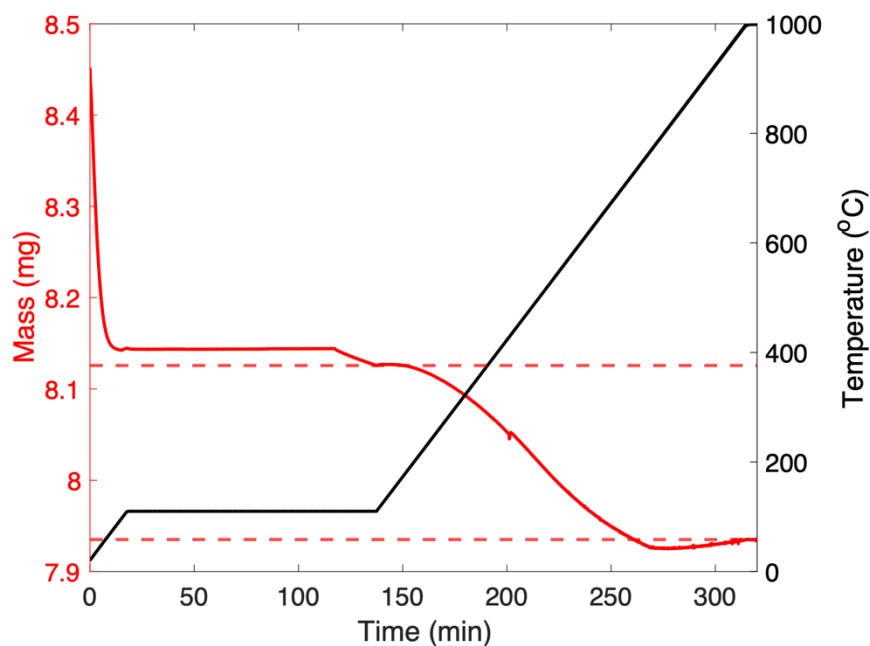


Figure S2.1: Mass thermogram of SiO_{2,Hyd}. Horizontal red dashed lines mark the mass utilized to calculate Δm_{TGA} in equation (1) of the main text.

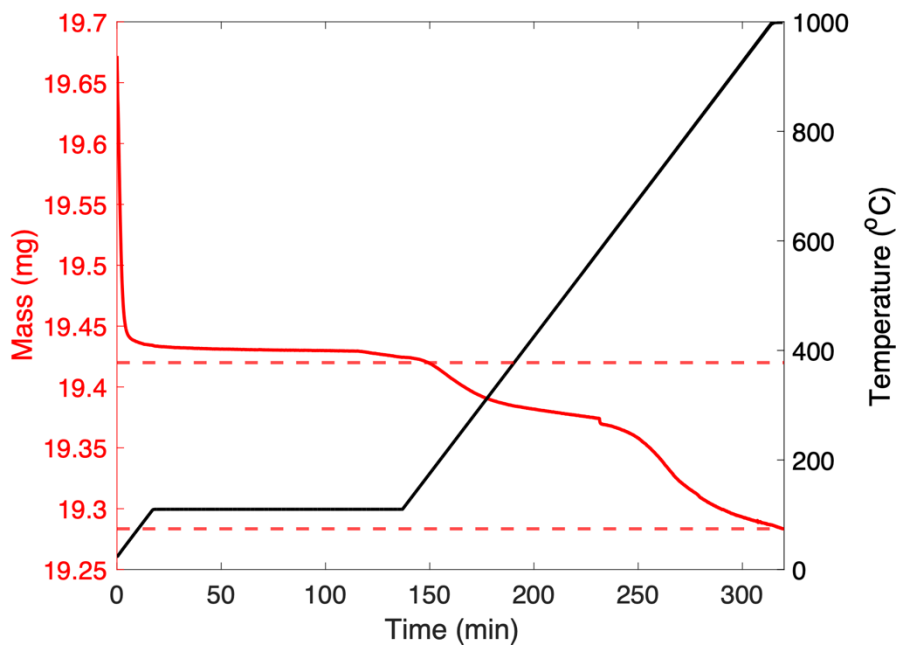


Figure S2.2: Mass thermogram of SiO_{2,1023}. Horizontal red dashed lines mark the mass utilized to calculate Δm_{TGA} in equation (1) of the main text.

2.7.2 XAS Characterization of Ti[OSiPh₃]₄

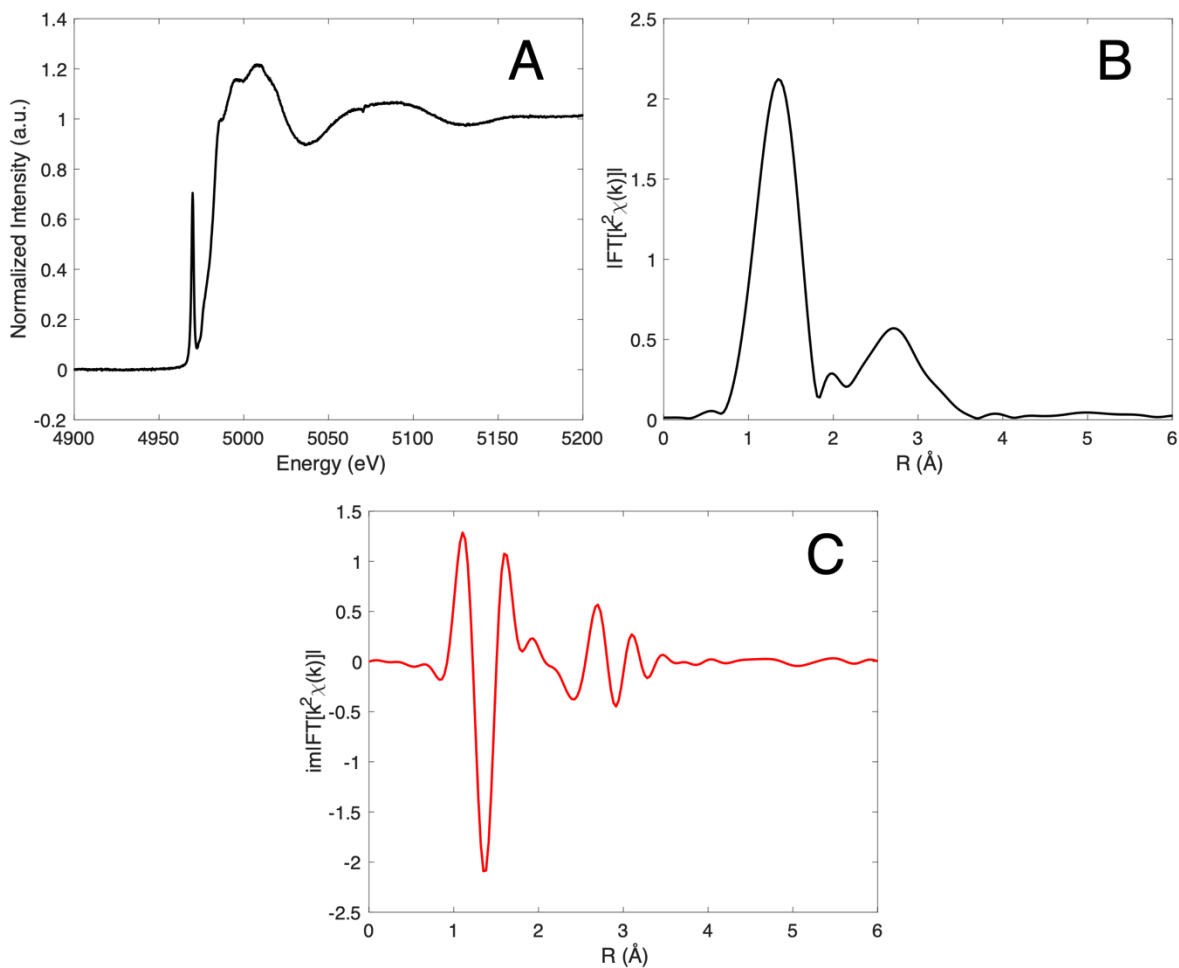


Figure S2.3: A) Normalized X-Ray Absorption Spectrum of Ti[SiOPh₃]₄ at ambient conditions. B) Magnitude and C) imaginary components of the Fourier-transformed k^2 -weighted EXAFS

Table S2.1: EXAFS fitting parameters for Ti[OSiPh₃]₄ fit from 1-2.2 Å

N	R (Å)	S_0^2	ΔE_0 (eV)	ΔR (Å)	σ^2 (Å ²)	R-factor	Ref
4 (fixed)	1.81251	0.903 ± 0.43	2.61 ± 6.3	0.026 ± 0.03	0.0018 ± 0.005	0.7%	This work
4	1.806	N/R	N/R	± 0.02	$.007 \pm 0.0007$	N/A	[⁹⁴]

2.7.3 N₂ Physisorption Characterization of SiO₂ materials

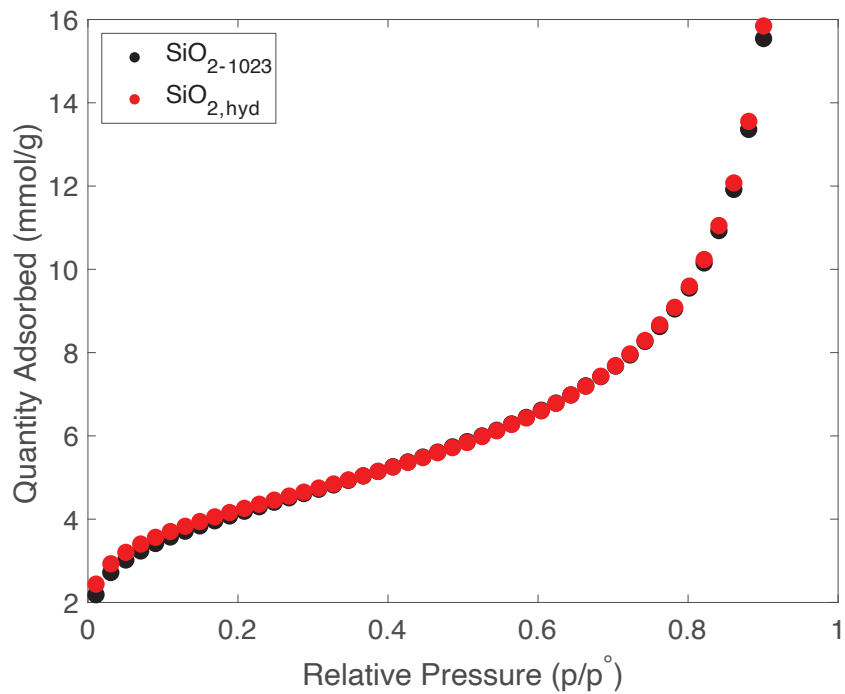


Figure S2.4: N₂ adsorption isotherms for SiO_{2,hyd} and SiO_{2,1023}

2.7.4 Infrared characterization of SiO₂ and Ti/SiO₂ materials

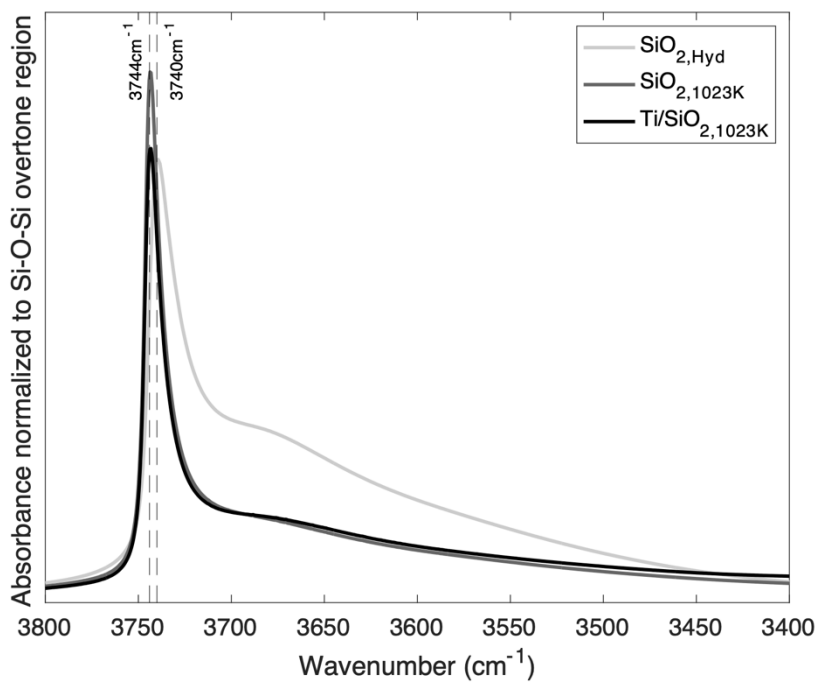


Figure S2.5: FTIR Spectra of SiO_{2,hyd}, SiO_{2,1023}, and Ti/SiO_{2,1023} (sample 2). All spectra were normalized by the integrated absorbance of the Si-O-Si overtone region from 1735 cm⁻¹ to 2000 cm⁻¹.

2.7.5 Infrared characterization of OH stretching region of $\text{SiO}_{2,1023}$ during pyridine adsorption

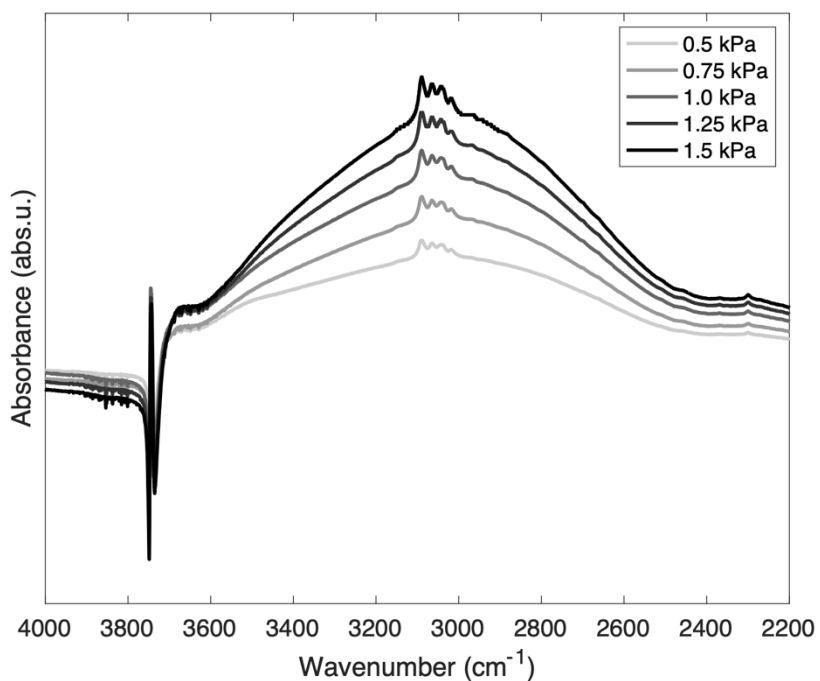


Figure S2.6: FTIR spectra of the OH stretching region of dehydroxylated fumed silica during pyridine adsorption. These spectra were acquired at 460K. In all spectra, we observed a sharp artefact near $\sim 3743\text{cm}^{-1}$ which is the same frequency of isolated silanol groups for the bare material. We attribute this artefact to low transmittance in this region, and high noise, caused by the presence and abundance of isolated silanol groups.

2.7.6 Correlation between perturbed SiO-H stretching vibration and the integrated absorbance of pyridine

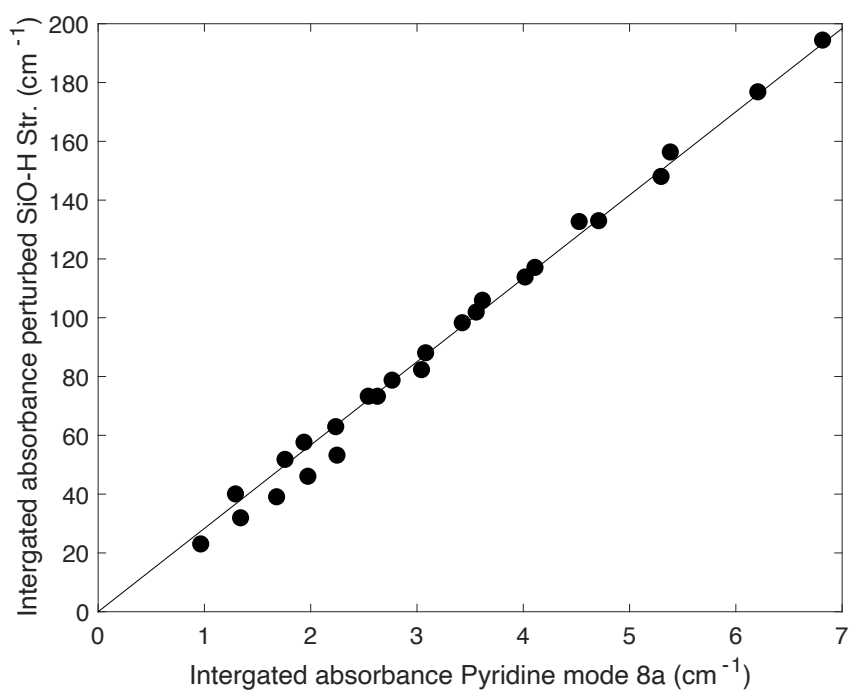


Figure S2.7: Linearly proportional relationship ($R^2 = 0.9983$) between the integrated absorbance of the perturbed SiO-H stretching vibration and the integrated absorbance of the pyridine ring-breathing vibrational mode (8a, 1594cm⁻¹) during pyridine adsorption experiments.

2.7.7 Infrared spectra and Langmuir fits during pyridine adsorption on SiO_{2,Hyd}

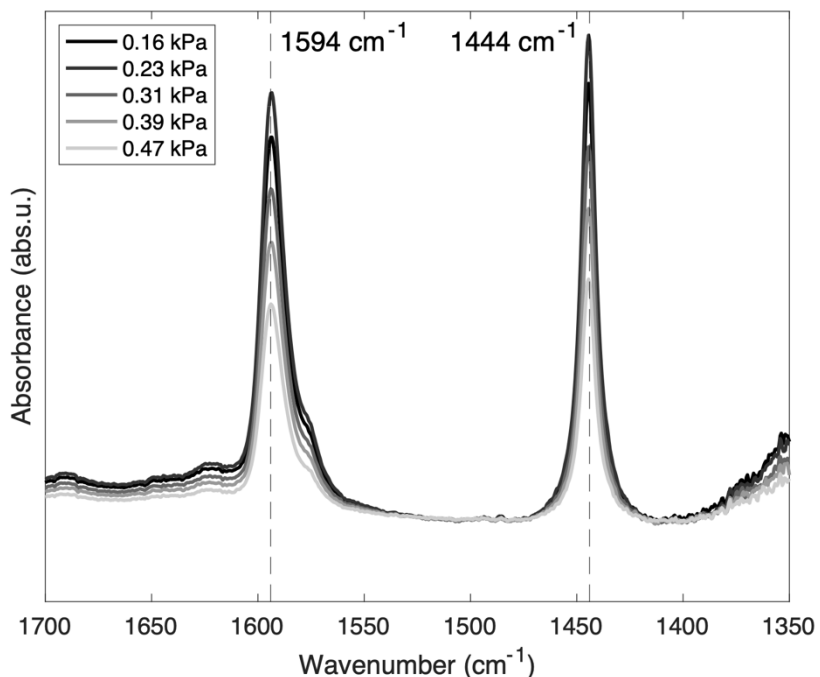


Figure S2.8: FTIR spectra of pyridine adsorbed to SiO_{2,Hyd} at T = 460 K.

Table S2.2: Assigned adsorption modes, peak centers, and Langmuir fitting parameters determined via FTIR coverage experiments for pyridine adsorbed to SiO_{2,Hyd}

Interaction	Adsorption Mode	Peak Center (cm ⁻¹)	ΔH_{ads}^o (kJ/mol)	ΔS_{ads}^o (J/molK)	Normalized* Q _{sat} x10 ²
C ₅ H ₅ N–HO–Si≡ (SiO _{2,Hyd})	19b, ring-breathing	1444	-81 ± 3.1	-134 ± 2.8	5.88 ± 0.483
C ₅ H ₅ N–HO–Si≡ (SiO _{2,Hyd})	8a, ring-breathing	1594	-78 ± 3.1	-128 ± 2.8	7.82 ± 0.608

2.7.8 Comparison between heats of adsorption of pyridine as reported in literature and measured in this work

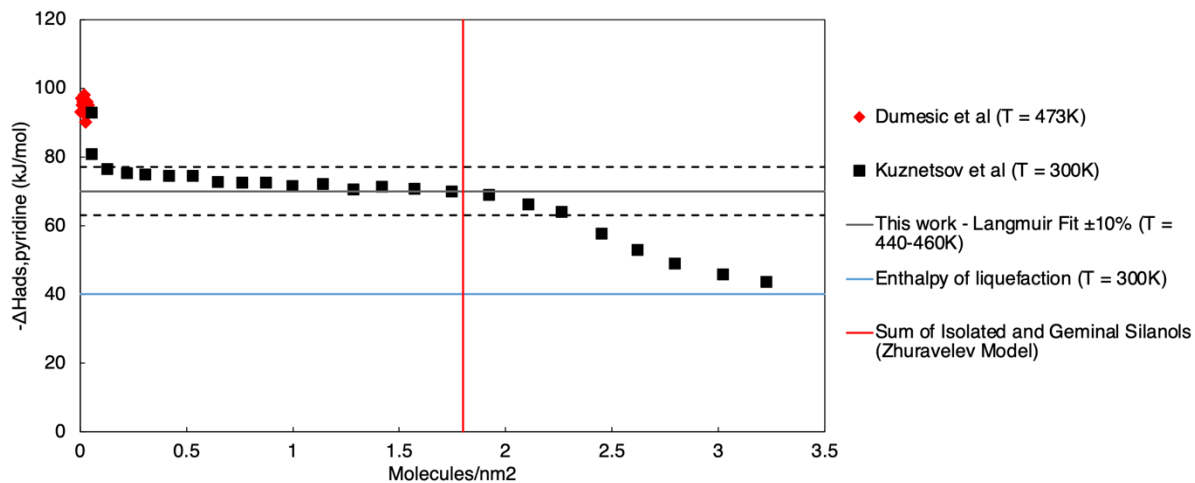


Figure S2.9: Reported heats of adsorption for pyridine adsorption to SiO₂ measured from microcalorimetry experiments. The value derived by this work using FTIR and Langmuir modeling is shown, as well as the enthalpy of liquefaction. The vertical line shows the estimated surface density of isolated and geminal silanols as estimated by the Zhuravlev model.

2.7.9 Example peak fitting procedure for CD₃CN adsorbed to SiO_{2,1023}

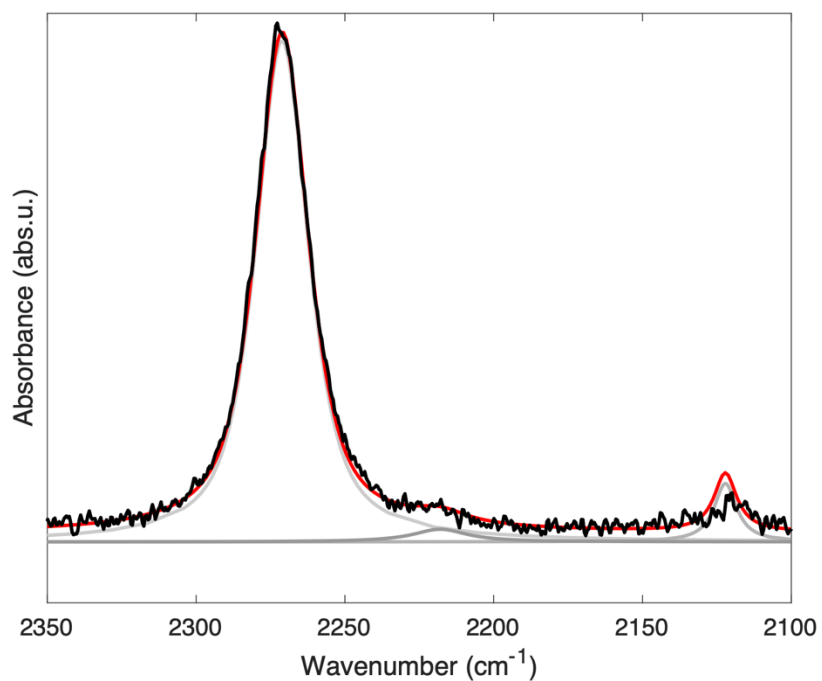


Figure S2.10: Representative peak deconvolution procedure during CD₃CN adsorption on SiO_{2,1023} (T = 460K, P_{acetone} = 0.5 kPa). Red curve is the cumulative peak fit, while black curve is the measured data. Gray curves are individual contributions. The C≡N stretching peak (2271cm⁻¹) was fit as a Gauss-Lorentz function with 80% Lorentz weight.

2.7.10 Infrared characterization of OH stretching region of $\text{SiO}_{2,1023}$ during CD_3CN adsorption

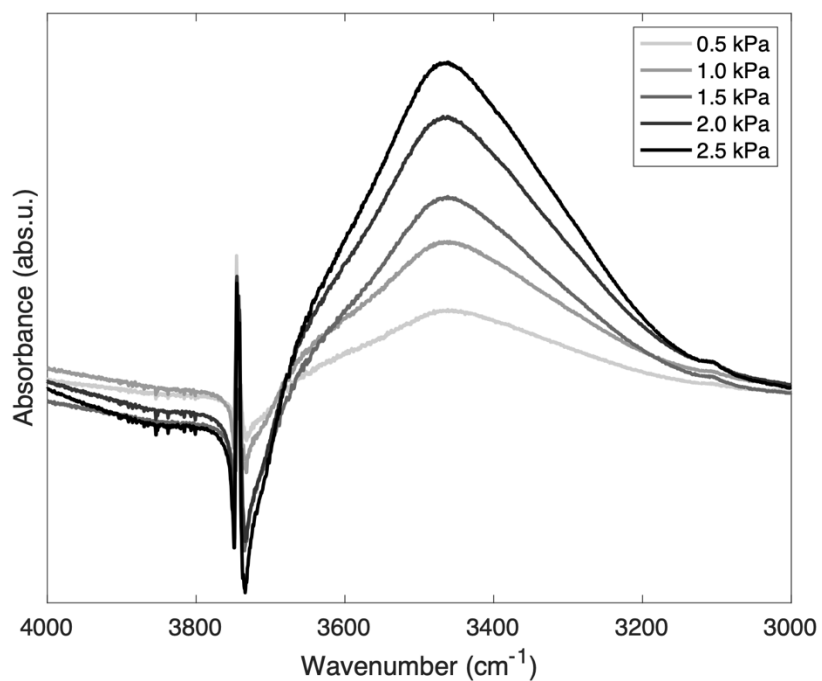


Figure S2.11: FTIR spectra of the OH stretching region of dehydroxylated fumed silica during CD_3CN adsorption. These spectra were acquired at 460K. In all spectra, we observed a sharp artefact near $\sim 3743\text{cm}^{-1}$.

2.7.11 Correlation between perturbed SiO-H stretching vibration and the integrated absorbance of CD₃CN

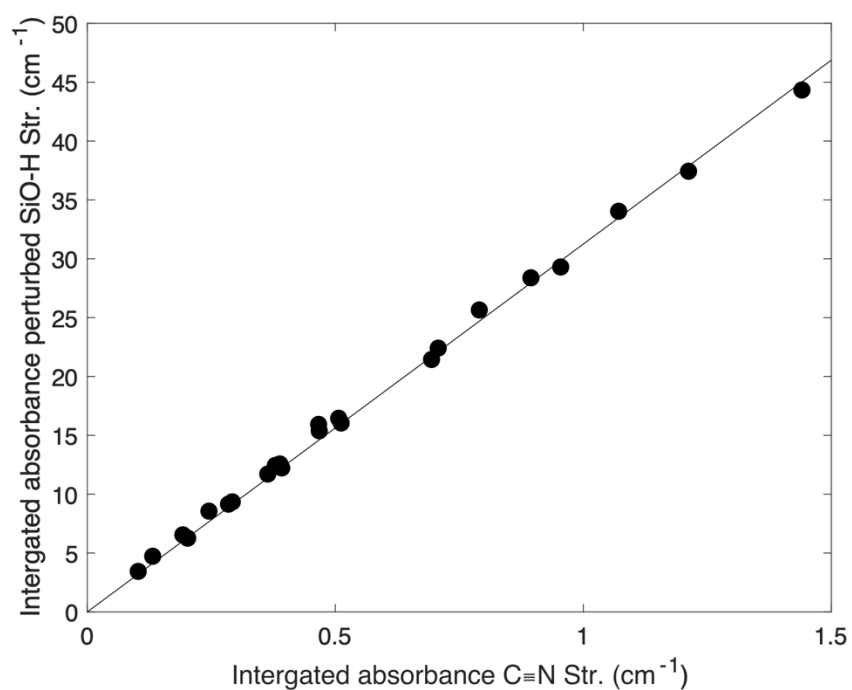


Figure S2.12: Linearly proportional relationship ($R^2 = 0.9994$) between the integrated absorbance of the perturbed SiO-H stretching vibration and the integrated absorbance of the C≡N stretching frequency during CD₃CN adsorption experiments.

2.7.12 Infrared characterization in the C=O stretching region of an empty in-situ cell

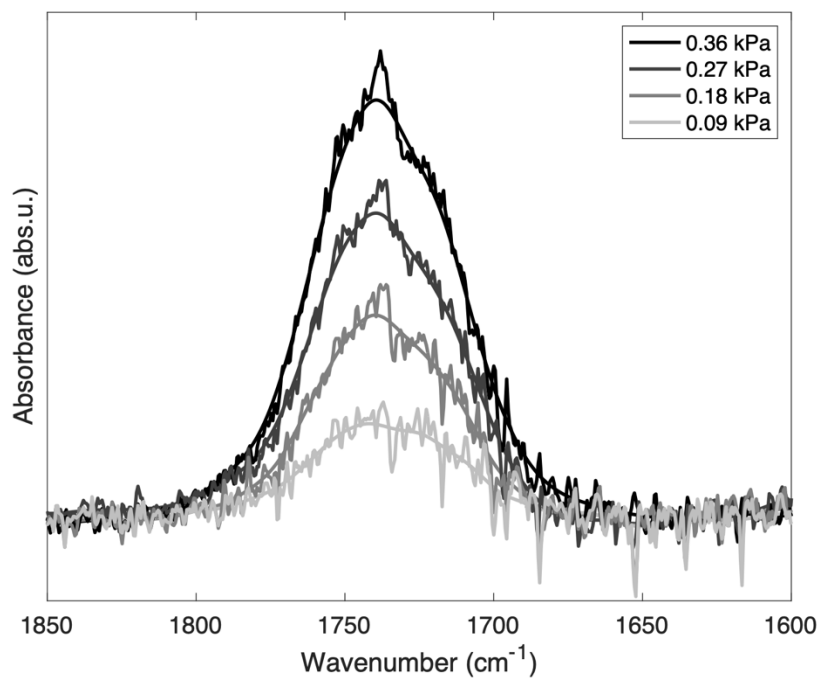


Figure S2.13: FTIR spectra of the C=O stretching region of an empty in-situ FTIR cell while flowing acetone at various partial pressures. These spectra were acquired at 460K.

2.7.13 Example peak fitting procedure for acetone adsorbed to SiO_{2,1023}

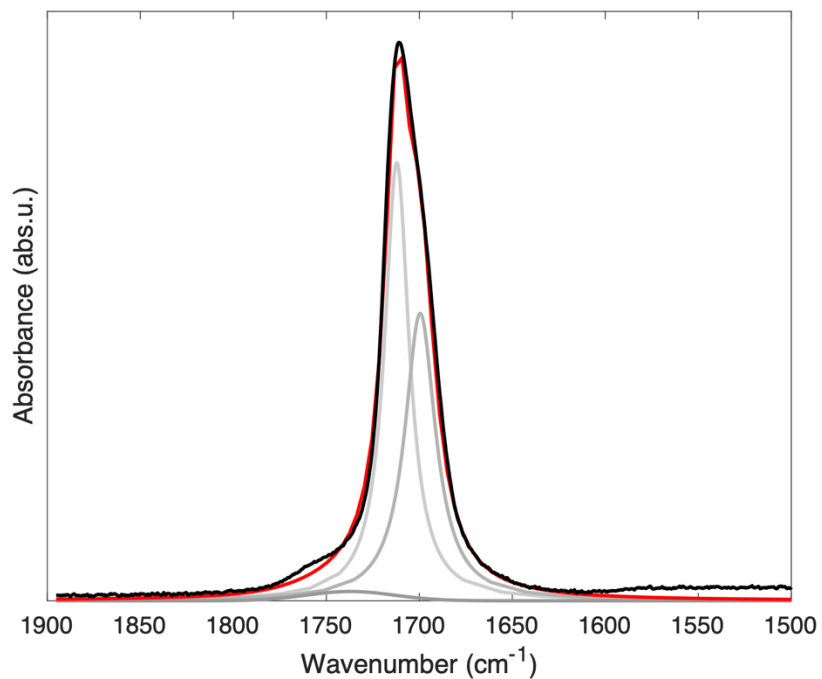


Figure S2.14: Representative peak deconvolution procedure during acetone adsorption on SiO_{2,1023} ($T = 420\text{K}$, $P_{\text{acetone}} = 0.36\text{ kPa}$). Red curve is the cumulative peak fit, while black curve is the measured data. Gray curves are individual contributions from gas-phase acetone (left), acetone adsorbed to isolated/geminal silanols (middle), and acetone adsorbed to bifurcated silanols (right). Gas-phase acetone peak is represented by a gaussian, while adsorbed acetone peaks are Lorentzian peaks.

2.7.14 Infrared characterization of OH stretching region of $\text{SiO}_{2,1023}$ during acetone adsorption

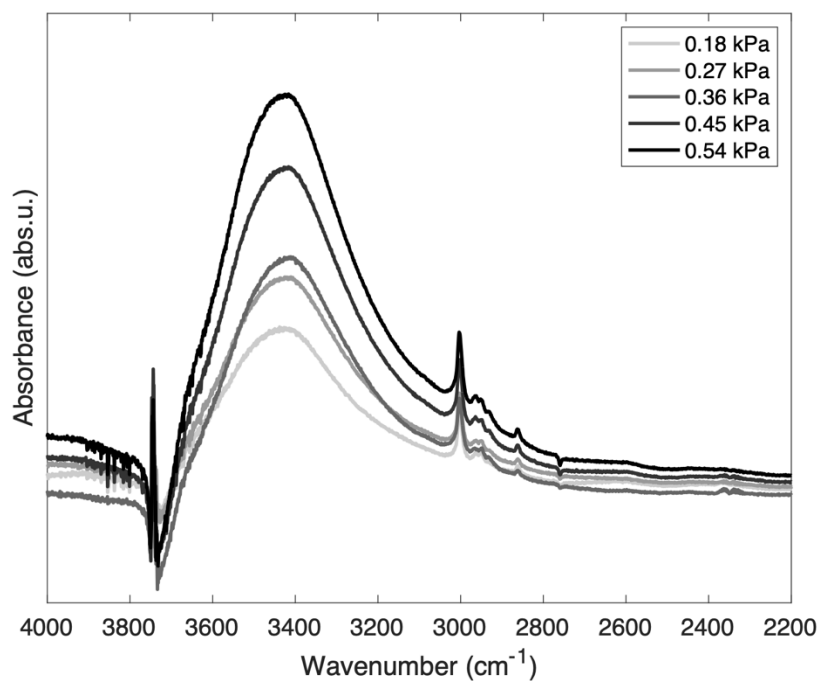


Figure S2.15: FTIR spectra of the OH stretching region of dehydroxylated fumed silica during acetone adsorption. These spectra were acquired at 460K. In all spectra, we observed a sharp artefact near $\sim 3743\text{cm}^{-1}$. We attribute this artefact to low transmittance in this region caused by the presence and abundance of isolated silanol groups (relative to the path length).

2.7.15 Correlation between perturbed SiO-H stretching vibration and the integrated absorbance of acetone

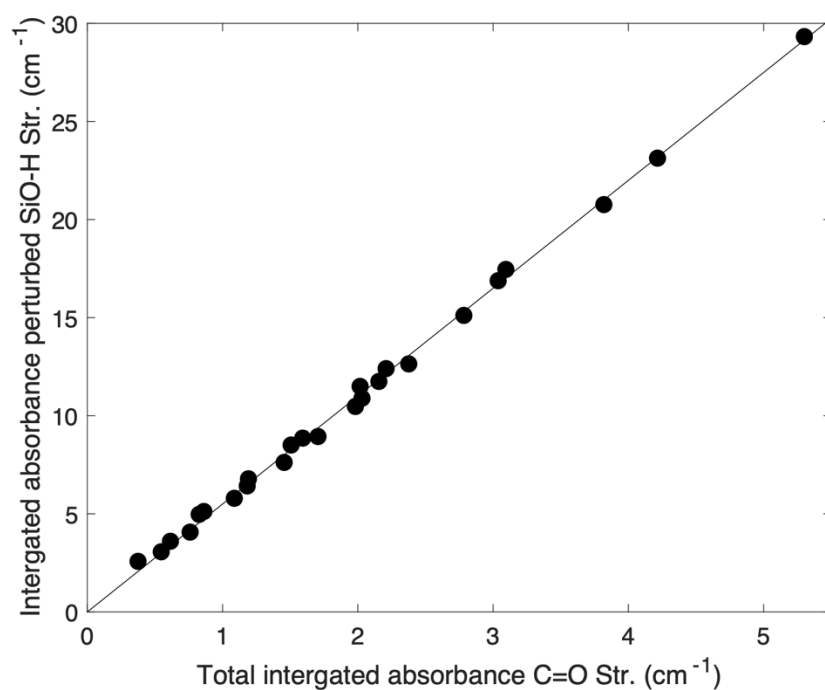


Figure S2.16: Linearly proportional relationship ($R^2 = 0.9994$) between the integrated absorbance of the perturbed SiO-H stretching vibration and the integrated absorbance of the C=O stretching frequency during acetone adsorption experiments.

2.7.16 Example peak fitting procedure for trimethylacetonitrile adsorbed to SiO_{2,1023}

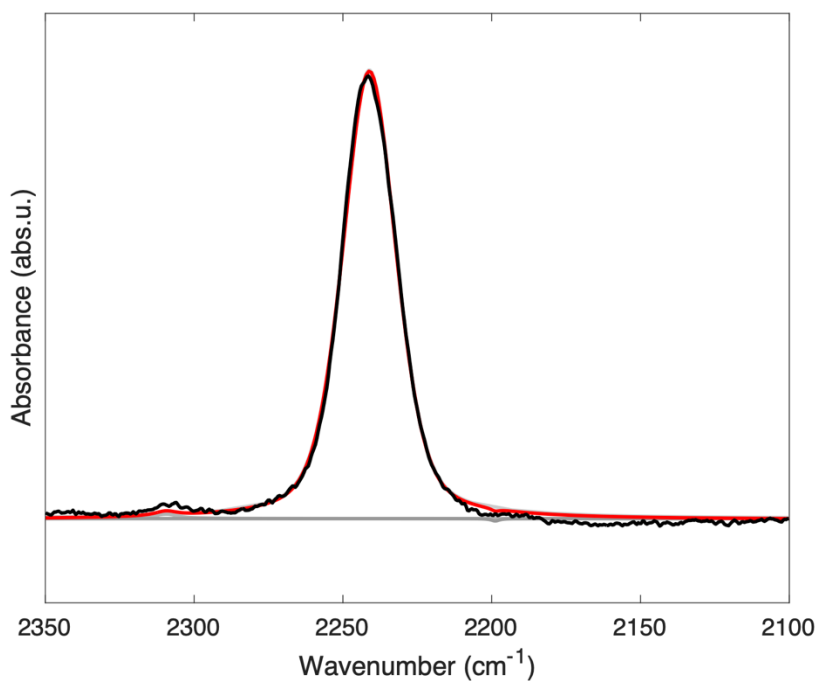


Figure S2.17: Representative peak deconvolution procedure during trimethylacetonitrile adsorption on SiO_{2,1023} (T = 460K, P_{acetone} = 0.25 kPa). Red curve is the cumulative peak fit, while black curve is the measured data. Gray curves are individual contributions. The C≡N stretching peak (2243cm⁻¹) was fit as a Gauss-Lorentz function with 50% Lorentz weight.

2.7.17 Infrared characterization of OH stretching region of $\text{SiO}_{2,1023}$ during trimethylacetonitrile adsorption

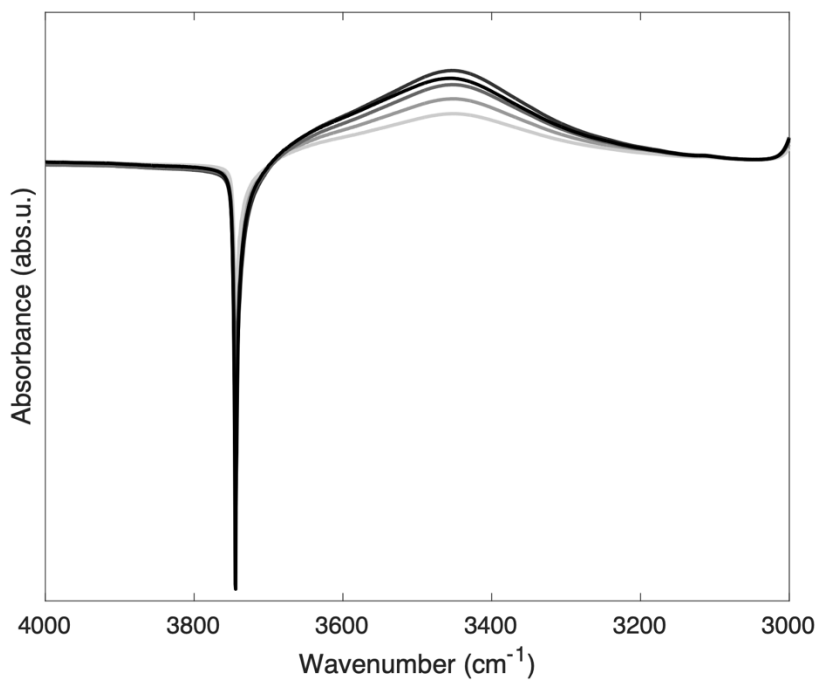


Figure S2.18: FTIR spectra of the OH stretching region of dehydroxylated fumed silica during trimethylacetonitrile adsorption. These spectra were acquired at 460K at the partial pressures shown in Figure 2.5B of the main text.

2.7.18 Correlation between perturbed SiO-H stretching vibration and the integrated absorbance of trimethylacetonitrile

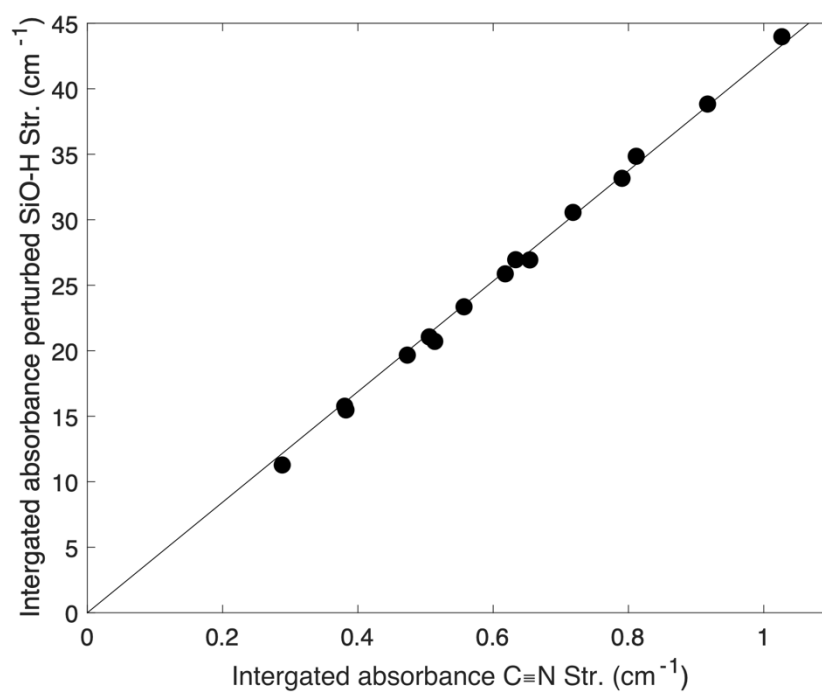


Figure S2.19: Linearly proportional relationship ($R^2 = 0.9997$) between the integrated absorbance of the perturbed SiO-H stretching vibration and the integrated absorbance of the C≡N stretching frequency during CD₃CN adsorption experiments.

2.7.19 The effect of cluster model size on ΔH_{ads}^o predictions

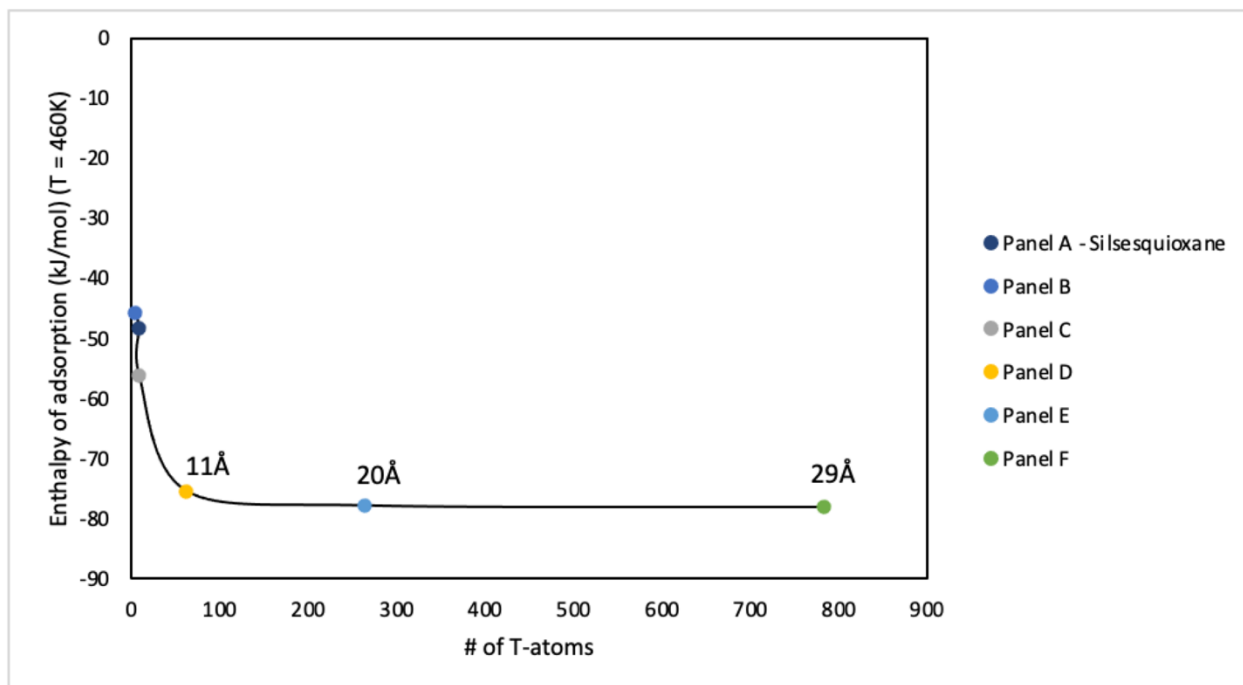


Figure S2.20: Effect of cluster model size on predicted enthalpies of adsorption. Models are listed by “Panel” as shown in Figure 2.1 of the main text. Panels D-F are QM/MM calculations that utilize Panel C as the QM region. The radii of the silica surrounding the central $\equiv\text{Si-OH}$ for Panels D-F are labeled.

2.7.20 Relationship between proton affinity, ΔH_{ads}^o , and the redshift of the SiO-H stretching frequency

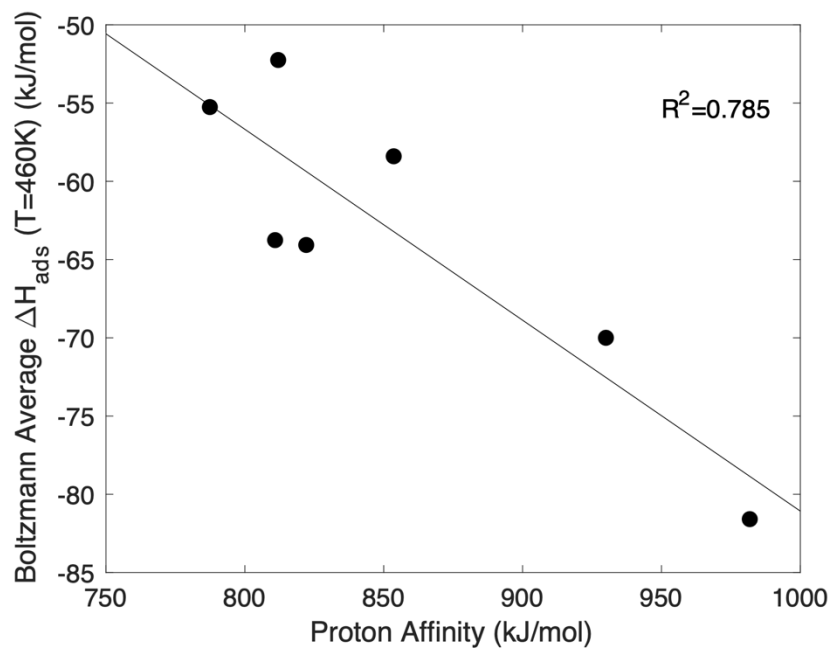


Figure S2.21: Relationship between Proton Affinity⁷⁵ and the Boltzmann averaged heat of adsorption prediction for all polar molecules in the database shown in Figure 2.8 of the main text. This includes trimethylacetonitrile, d_3 -acetonitrile, acetone, pyridine, ammonia, triethylamine, and tetrahydrofuran.

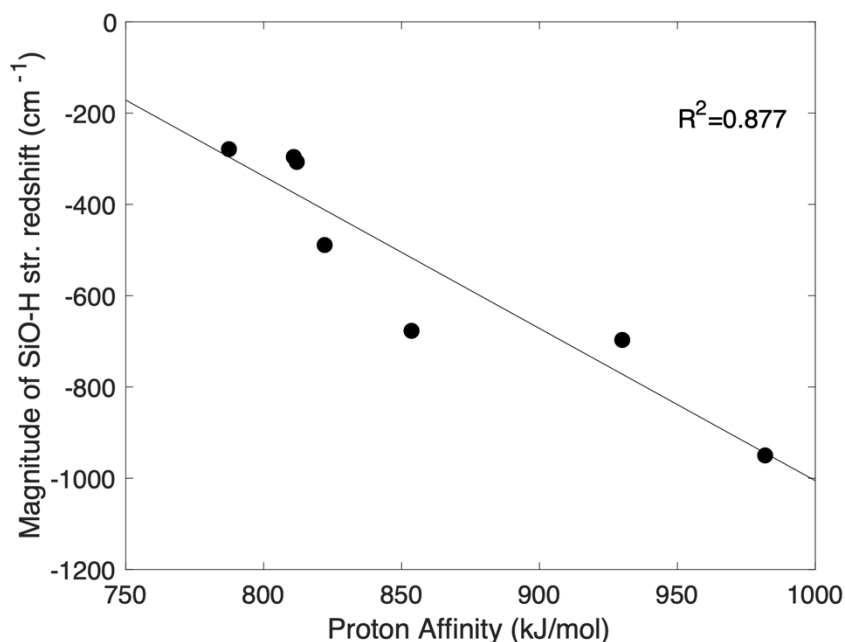


Figure S2.22: Relationship between Proton Affinity and magnitude of the SiO-H str. redshift (in cm^{-1}) for all polar molecules in the database shown in Figure 2.8 of the main text. This includes trimethylacetonitrile, d_3 -acetonitrile, acetone, pyridine, ammonia, triethylamine, and tetrahydrofuran. The magnitude of the SiO-H str. redshift was taken as the maximum, centered value of the broad peak typically located between $3000\text{-}3600\text{cm}^{-1}$. For ammonia, triethylamine, and tetrahydrofuran, the redshifted values were taken as reported in the literature.^{43,46}

2.7.21 UV/Vis spectrum of Ti/SiO_2 ,₁₀₂₃ (sample 2)

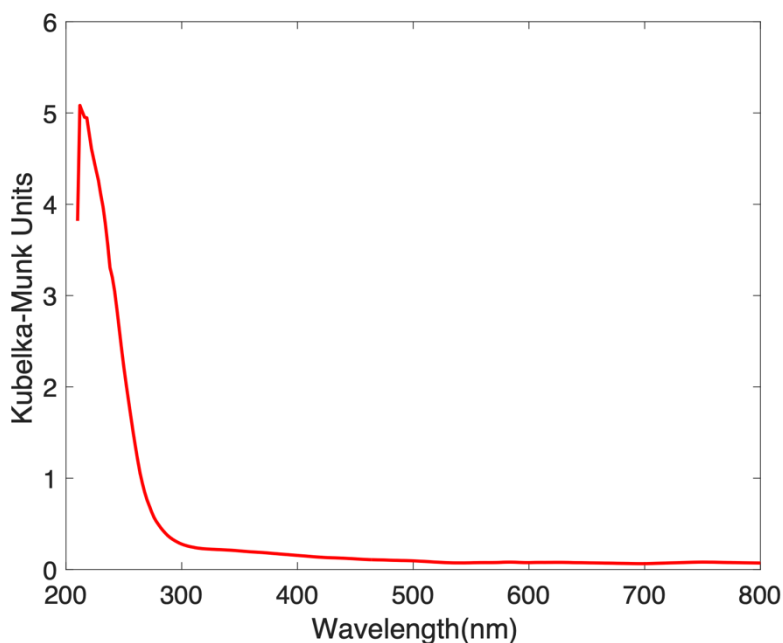


Figure S2.23: Diffuse-reflectance UV/Vis spectrum of Ti/SiO_2 ,₁₀₂₃ (**sample 2**) at 553.15K under flowing He after thermal treatment at 673K for 1h.

2.7.22 Effect of temperature on the intensity of pre-edge features

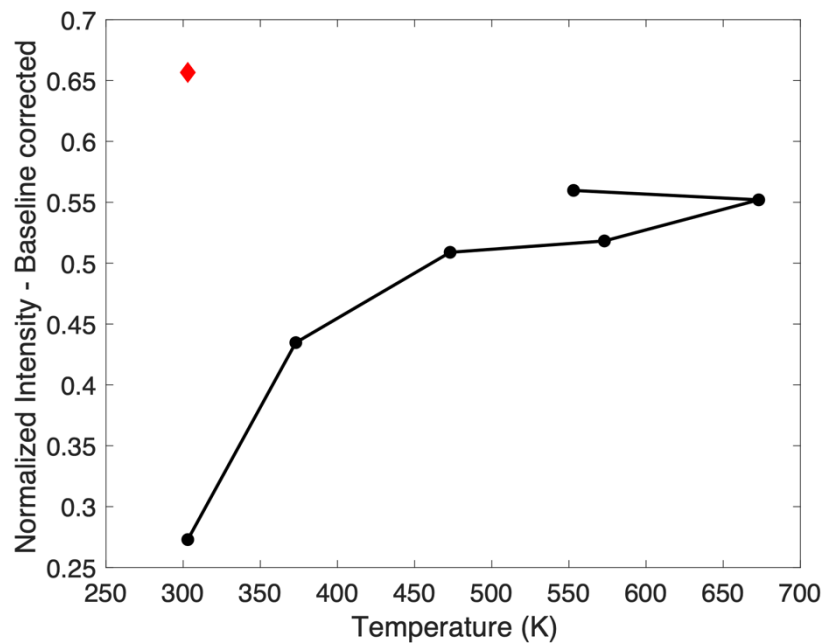


Figure S2.24: Normalized intensity (absorbance at peak center) of the pre-edge XANES feature measured for **Ti/SiO_{2,1023}** as a function of temperature under flowing He (Black) and the normalized intensity of the same feature for Ti[SiOPh₃]₄ at room temperature (red diamond).

2.7.23 Subtraction of features associated with pyridine bound to SiO₂ from the spectra of pyridine bound to Ti/SiO₂

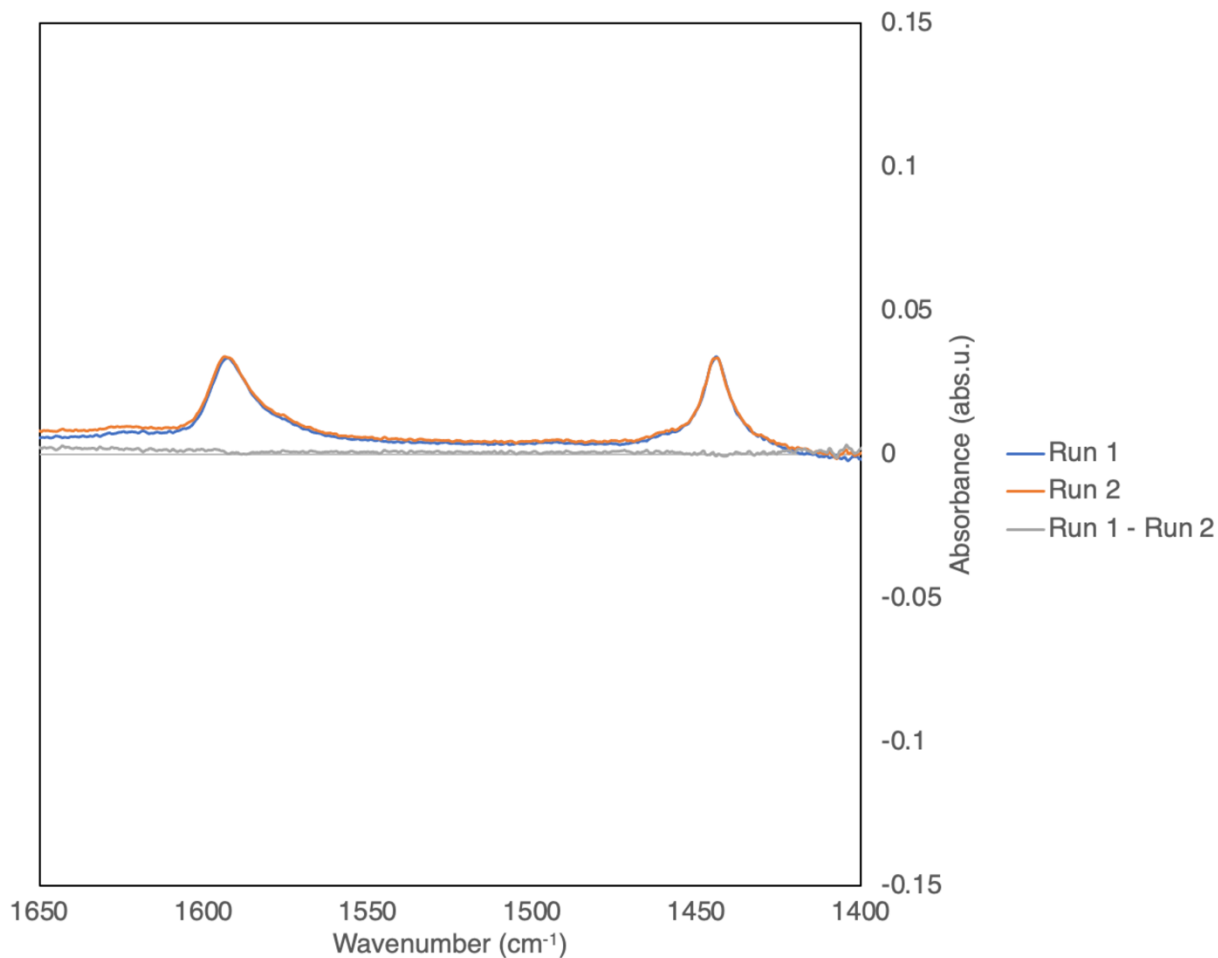


Figure S2.25: Representative FTIR spectra of two consecutive pyridine adsorption experiments (i.e., two pellets of the same material) with SiO_{2,1023} (T = 503K, P_{Pyridine} = 0.49kPa) to demonstrate subtraction procedure. This demonstrates that our experimental method is reproducible and that features associated with pyridine interacting with silanols can be effectively subtracted in this way.

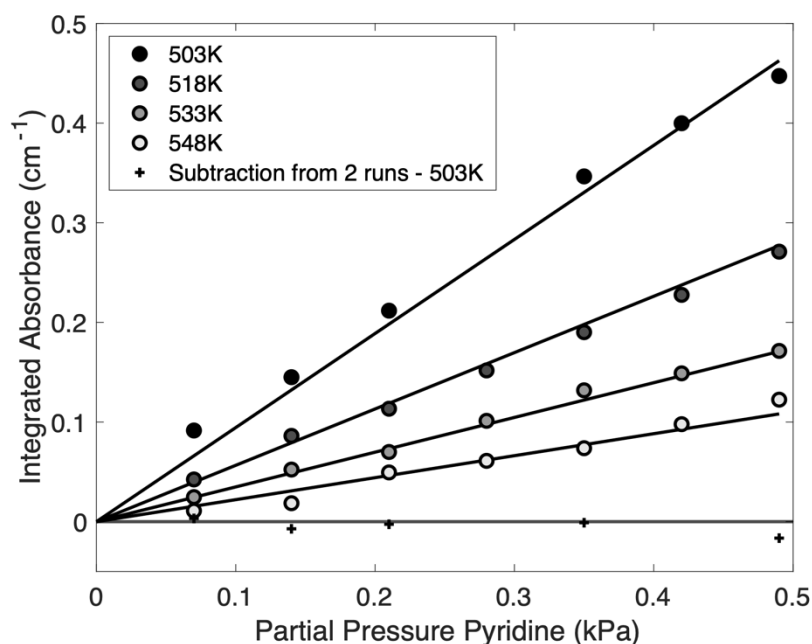


Figure S2.26: Integrated absorbance of the pyridine ring-breathing vibration (8a) as a function of partial pressure of pyridine and temperature. The circles show the integrated absorbance for one run, while the “+” show the subtracted peak areas from two consecutive runs for a representative temperature (503K). Since the “+” symbols fall on $y = 0$, this demonstrates experimental reproducibility.

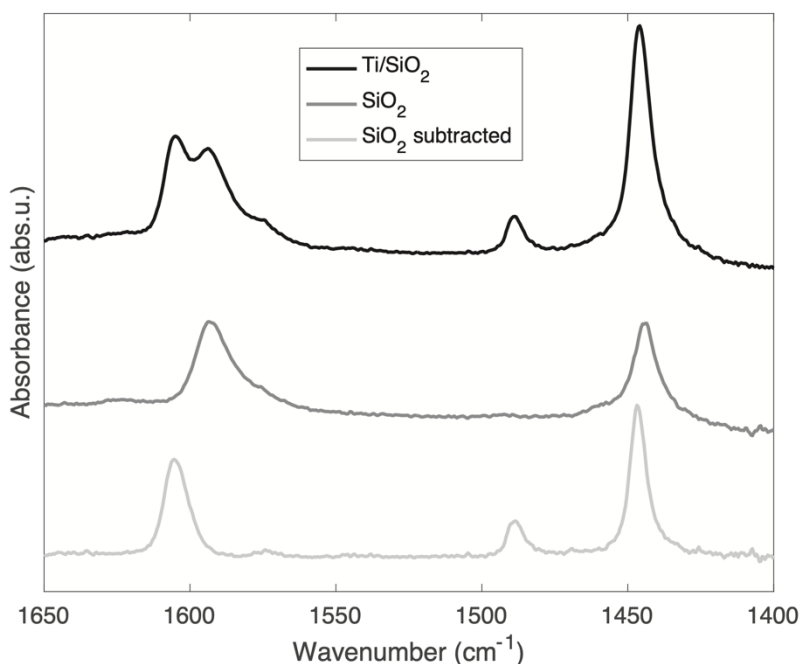


Figure S2.27: A representative example of subtraction of the overlapping features associated with pyridine adsorption to silanols ($T = 503\text{K}$, $P_{\text{py}} = 0.42\text{kPa}$). The top line shows the FTIR spectrum of pyridine interacting with $\text{Ti/SiO}_{2,1023}$ (sample 2 in this case). The middle line shows the FTIR spectrum of pyridine interacting with $\text{SiO}_{2,1023}$ at identical conditions. The bottom line shows the subtraction result, which is the same spectra shown in Figure 2.10A. The spectra are offset for clarity.

2.7.24 Attempt at fitting a Langmuir isotherm to the infrared coverage measurements of pyridine adsorbed to Ti/SiO₂

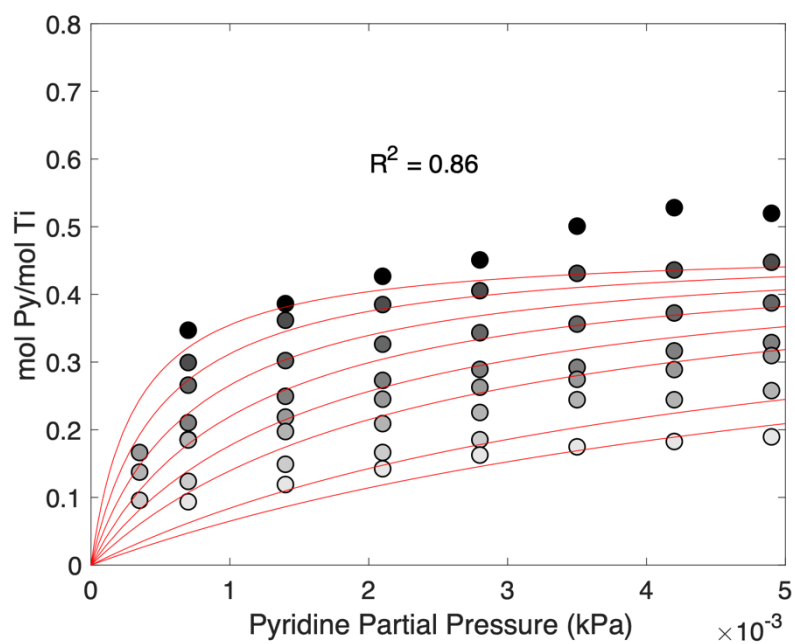


Figure S2.28: Langmuir isotherm fit attempt to the pyridine adsorption data to Ti/SiO_{2,1023} (sample 2)

2.7.25 Illustration of the effect of extrapolation percentage on isosteric heats of adsorption plots

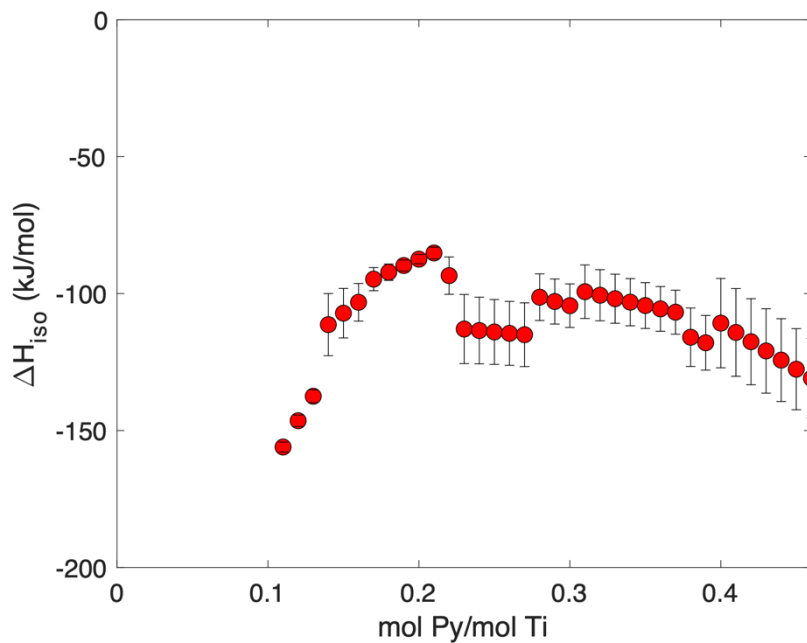


Figure S2.29: $\Delta H_{iso}^o(\theta)$ as a function of pyridine fractional coverage when extrapolation of the Langmuir-Freundlich isotherms beyond 20% of the minimum/maximum coverage for a given isostere are allowed.

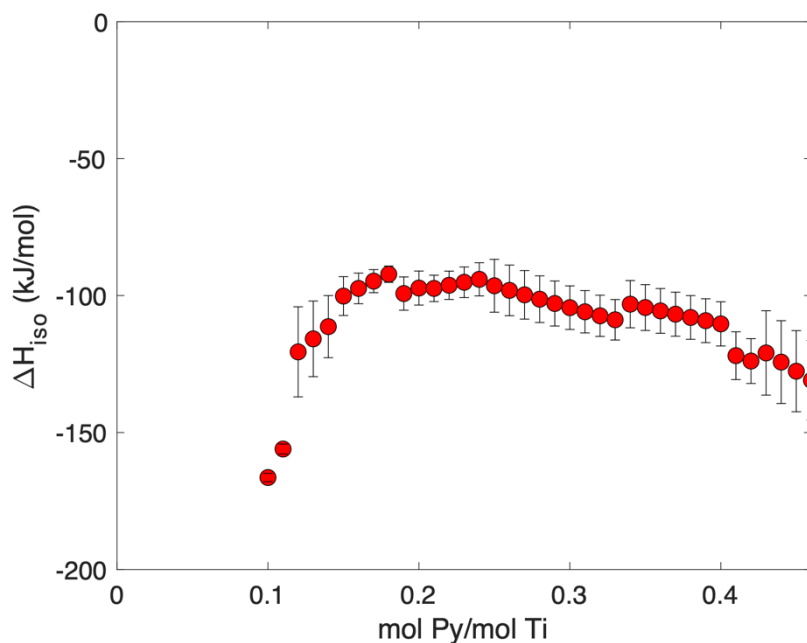


Figure S2.30: $\Delta H_{iso}^o(\theta)$ as a function of pyridine fractional coverage when extrapolation of the Langmuir-Freundlich isotherms beyond 30% of the minimum/maximum coverage for a given isostere are allowed.

2.7.26 Pyridine adsorption isotherms for Ti/SiO_{2,1023} (sample 1)

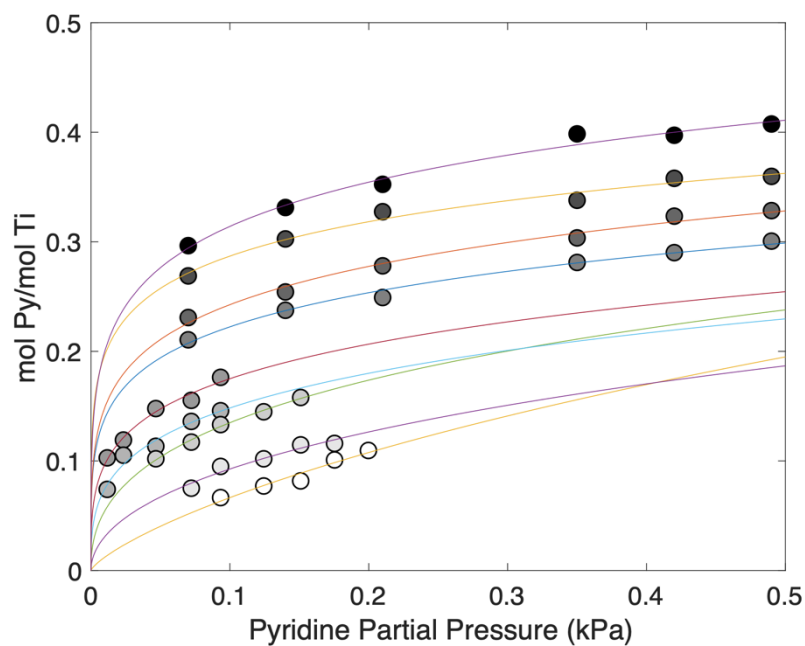


Figure S2.31: Pyridine coverage on Ti/SiO_{2,1023} (sample 1) (mol Py/mol Ti) as a function of partial pressure (kPa). Langmuir-Freundlich isotherm fits are shown as lines. Covers T-range 503.15 K through 623.15K. Langmuir-Freundlich fits for each temperature are shown as continuous lines.

2.7.27 Discussion of using isobars from FTIR coverage measurements to extract heats of adsorption

Previously reported values for the ΔH_{ads}^o of pyridine to SSMCs were derived from Van't Hoff analysis of isobars.^{33,48,95} We will now demonstrate that this methodology extracts a value for the heat of adsorption that is directly related to the coverage over which the data were collected.

We start by assuming that an adsorption phenomenon obeys Langmuir's model and that we are measuring the coverages using IR spectroscopy. In that case, we can write down equation (5) of the main text.

$$A_{py} = A_{max} \frac{K_{ads} P_{Py}}{(1 + K_{ads} P_{Py})} \quad (S1)$$

where A_{py} , K_{ads} , and P_{Py} refer to the integrated absorbance [cm^{-1}], the adsorption equilibrium constant, and the partial pressure of pyridine in the gas stream normalized by the standard pressure, 1 bar, respectively.

Again, the equilibrium constant can be described in terms of ΔH_{ads}^o and ΔS_{ads}^o , the entropy of adsorption, both of which refer to the standard-state pressure of 1 bar and a standard coverage of 0.5 monolayers:

$$K_{ads} = \exp\left(-\frac{\Delta H_{ads}^o}{RT} + \frac{\Delta S_{ads}^o}{R}\right) \quad (S2)$$

If we follow suit with the methodology proposed in the literature, we want the following derivative quantity:

$$\Delta H_{VH} = \left(\frac{d \ln(A_{py})}{d\left(\frac{1}{RT}\right)}\right)_{P_{py}} \quad (S3)$$

Where we have defined ΔH_{VH} as the heat of adsorption derived from this method.

If we plug in (S2) to (S1) and proceed to take this derivative, we get (S4)

$$\Delta H_{VH} = \left(\frac{d \ln(A_{py})}{d\left(\frac{1}{RT}\right)}\right)_{P_{py}} = \left(\frac{d \ln\left(A_{max} \frac{K_{ads} P_{Py}}{(1 + K_{ads} P_{Py})}\right)}{d\left(\frac{1}{RT}\right)}\right)_{P_{py}} \quad (S4)$$

The right hand side of this equation is equal to (S5)

$$\frac{d}{d\left(\frac{1}{RT}\right)} \left[\ln(A_{max}) + \ln(P_{Py}) + \frac{\Delta H_{ads}^o}{RT} + \frac{\Delta S_{ads}^o}{R} - \ln\left(1 + \exp\left(-\frac{\Delta H_{ads}^o}{RT} + \frac{\Delta S_{ads}^o}{R}\right) P_{Py}\right) \right] \quad (S5)$$

The first two terms, as well as the fourth term, are zero since they are constants or are being held constant. Thus, we can simplify (S5) to (S6).

$$-\Delta H_{ads}^o + \frac{d}{d\left(\frac{1}{RT}\right)} \left[-\ln \left(1 + \exp \left(-\frac{\Delta H_{ads}^o}{RT} + \frac{\Delta S_{ads}^o}{R} \right) P_{Py} \right) \right] \quad (S6)$$

Taking derivative on the right gives equation (S7)

$$-\Delta H_{ads}^o + \frac{\Delta H_{ads}^o \exp \left(-\frac{\Delta H_{ads}^o}{RT} + \frac{\Delta S_{ads}^o}{R} \right) P_{Py}}{1 + \exp \left(-\frac{\Delta H_{ads}^o}{RT} + \frac{\Delta S_{ads}^o}{R} \right) P_{Py}} \quad (S7)$$

If we plug in (S2), we can simplify (S7) to (S8) and summarize.

$$\Delta H_{VH} = \left(\frac{d \ln(A_{py})}{d\left(\frac{1}{RT}\right)} \right)_{P_{py}} = \Delta H_{ads}^o \left[-1 + \frac{K_{ads} P_{Py}}{1 + K_{ads} P_{Py}} \right] \quad (S8)$$

We can now recognize that the term on the right hand side that contains K_{ads} and P_{Py} is simply the fractional coverage for a Langmuir isotherm(Θ), leading us to equation (S9).

$$\Delta H_{VH} = \left(\frac{d \ln(A_{py})}{d\left(\frac{1}{RT}\right)} \right)_{P_{py}} = \Delta H_{ads}^o [-1 + \Theta] \quad (S9)$$

Thus, equation (S9) shows that there is a linear dependence on Θ for the apparent value (ΔH_{VH}) of the heat of adsorption when the isobar approach is utilized. As coverage increases, the ΔH_{VH} decreases proportionally. We can recover the true heat of adsorption (ΔH_{ads}^o) at the limit of zero coverage, which is unobtainable in any experiment. Thus we strongly recommend against using this method to extract ΔH_{ads}^o , especially when comparisons to theoretical calculations are desired.

As a corollary, equation (S9) also implies the great danger when using it to compare catalysts or adsorbents at the same conditions. For instance, let us assume we have two materials (A and B) that obey a Langmuir isotherm, where $\Delta H_{ads,A}^o = -65 \frac{kJ}{mol}$ and $\Delta H_{ads,B}^o = -80 \frac{kJ}{mol}$. If we take the simplest argument and assume that the entropy of adsorption (ΔS_{ads}^o) of an adsorbate to two different materials (A and B) are the same, as suggested by Campbell et al.⁷⁹, then we can perform a simple theoretical calculation of the coverage for both materials at a given temperature and partial pressure. For the sake of this example, we utilize the $\Delta S_{ads}^o = -124 \frac{J}{mol \cdot K}$, as calculated by Campbell's correlation for pyridine at 460 K. We assume the temperature and partial pressure of the experiment is 460 K and $P_{Py} = 1$ kPa. Thus, the coverages of pyridine upon material A (Θ_A) and B (Θ_B) are 0.073 and 0.799, respectively. If we used equation (S9) to calculate ΔH_{VH} one yields $\Delta H_{VH,A} = -60 \frac{kJ}{mol}$ and $\Delta H_{VH,B} = -25 \frac{kJ}{mol}$, which are not only different from the true values, but are reversed in trend. This reversal in trend will be common for this methodology because more favorable heats of adsorption generally lead to higher coverages, which results in less favorable (less negative) *apparent* ΔH_{VH} . This could lead to incorrect conclusions regarding the relative Lewis acid strength of SSMCs, which have been used to rationalize trends in catalytic activity.^{33,48,95}

2.7.28 T8 Silsesquioxane $\equiv\text{Ti-OH}$ EDA calculations

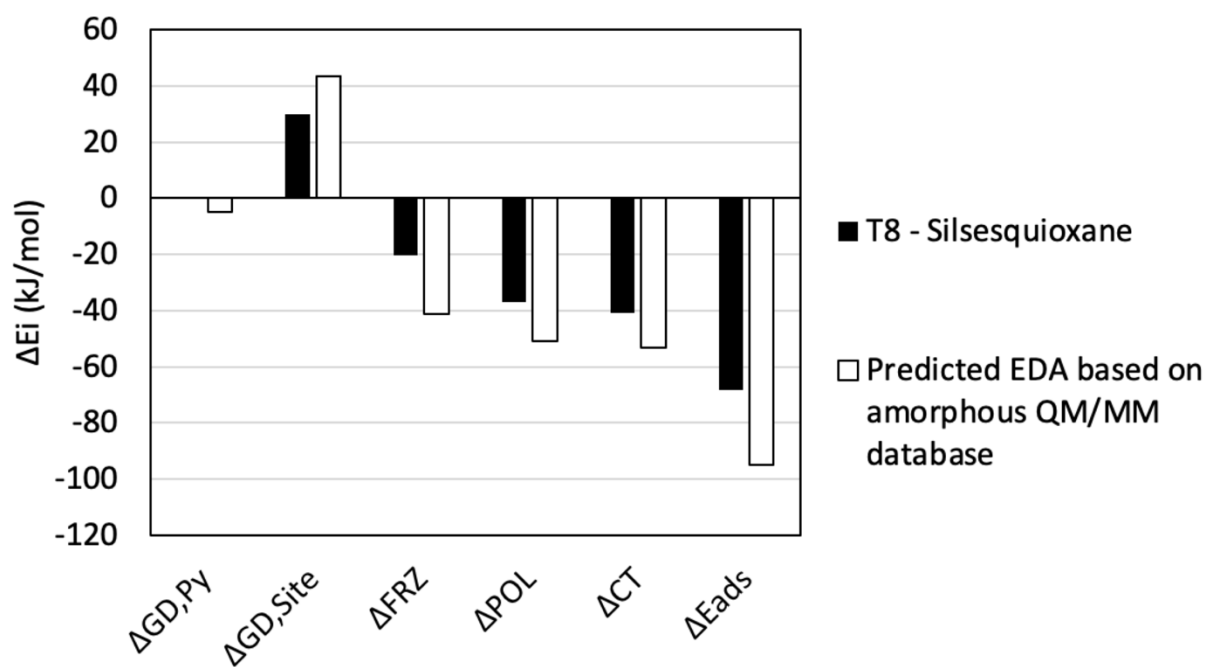


Figure S2.32: Comparison between the EDA calculation of pyridine bound to the $\equiv\text{Ti-OH}$ site of a T8 Silsesquioxane and the expected EDA based on the linear fits presented in Figure 2.11 of the main text.

3 The Effects of $\equiv\text{Ti-OH}$ Site Distortion and Product Adsorption on the Mechanism and Kinetics of Cyclohexene Epoxidation over Ti/SiO_2

3.1 Abstract

This work presents the effects of $\equiv\text{Ti-OH}$ site distortion in Ti/SiO_2 on the kinetics and mechanism of gas-phase cyclohexene (C_6H_{10}) epoxidation to form cyclohexene oxide ($\text{C}_6\text{H}_{10}\text{O}$). We utilize an experimentally validated computational method to calculate enthalpies of adsorption and transition states along a well-established mechanism for the catalytic cycle. We discover that adsorption enthalpies correlate with the facet area of the tetrahedral $\equiv\text{Ti-OH}$ group through which the adsorbate binds to Ti. In contrast, enthalpies of H_2O_2 activation and O-atom transfer are relatively insensitive. We then develop a steady-state microkinetic model (MKM) to investigate the effects of distortion on predicted kinetic observables (apparent activation energy (E_a) and reaction orders in the partial pressures of C_6H_{10} and H_2O_2), and to establish whether the mechanism is consistent with observed kinetics. Product inhibition increases with increasing facet area, greatly impacting the predicted activity. Building on our recent findings that $\equiv\text{Ti-OH}$ sites in the absence of reaction exhibit facet areas equal to, or greater than, that derived from XAS measurements ($\geq 3.76 \text{ \AA}^2$) we discover that the predicted kinetics for such sites are inconsistent with experiments. We find instead that much smaller facets are required for good agreement ($< 3.54 \text{ \AA}^2$) since $\text{C}_6\text{H}_{10}\text{O}$ does not inhibit these facets. We show that the adsorption of $\text{C}_6\text{H}_{10}\text{O}$ to one facet significantly reduces the facet area of the vacant facets on the opposite side of the same $\equiv\text{Ti-OH}$ site. $\text{C}_6\text{H}_{10}\text{O}$ adsorption also considerably narrows the area distribution of these vacant facets. We show that these reduced area facets can catalyze the epoxidation of cyclohexene while $\text{C}_6\text{H}_{10}\text{O}$ remains co-adsorbed to the other facet (Pathway B). Using our MKM with an expanded mechanism for epoxidation that includes Pathway B, we find that Pathway B dominates the net rate of production of $\text{C}_6\text{H}_{10}\text{O}$ at nearly all partial pressures of product expected along the length of a packed bed reactor. We also find that the predicted activity remains essentially constant with the level of $\equiv\text{Ti-OH}$ site distortion. This new mechanism shows quantitative agreement between experiments and our predictions for the E_a , reaction orders in the partial pressures of reactants, and the Gibbs free energy barrier. It also illustrates a key role for adsorbates in influencing the degree of distortion of $\equiv\text{Ti-OH}$ sites, in addition to the amorphous support itself.

3.2 Introduction

Isolated titanol groups supported on silica ($(\text{SiO})_3\equiv\text{Ti-OH}$ (hereafter referred to as $\equiv\text{Ti-OH}$) are known to catalyze a variety of reactions, e.g., amination of alcohols, ammoxidation of ketones, dehydration of alcohols.²⁷ Particular attention has been given to the epoxidation of alkenes (propene, cyclohexene, cyclooctene, etc.) with organic or hydrogen peroxides because of the industrial significance of these reactions.^{10,27-35}

Theoretical studies of alkene epoxidation have usually adopted a model for the geometries of $\equiv\text{Ti-OH}$ groups (Ti-O coordination numbers and bond lengths) determined from fits to Extended X-ray Absorption Fine Structure (EXAFS) data.^{6,96-101} However, recent experimental and computational studies suggest that the distribution of O-Si-O bond angles in amorphous silica can distort the tetrahedral structure of $\equiv\text{Ti-OH}$ groups in a manner similar to what has been reported for other $\equiv\text{M-OH}$ and $=\text{M}(\text{O})_2$ species ($\text{M} = \text{Cr}, \text{W}, \text{Mo}, \text{Nb}, \text{Zr}, \text{etc.}$).^{21,23,87} There have also been

reports that such geometric distortions affect the adsorptive and catalytic properties of these groups.^{22,68,70,77,87} Notably, though, recent work has shown that EXAFS cannot be used to detect distorted $\equiv\text{M-OH}$ and $=\text{M}(\text{O})_2$ groups if they occur as a minority species.¹⁰² Therefore, if distorted $\equiv\text{Ti-OH}$ sites supported on silica were present in low concentrations, they would not be detectable by EXAFS.

We have recently shown in Chapter 2 that a small fraction ($< 15\%$) of silica-supported $\equiv\text{Ti-OH}$ sites are heavily distorted. In comparison, the remaining 85% have structures consistent with those derived from analysis of EXAFS data. These conclusions were drawn from a combination of experimental and theoretical studies of pyridine adsorption on silica-supported $\equiv\text{Ti-OH}$ sites. Adsorption isotherms determined from infrared spectra of adsorbed pyridine were used to determine the isosteric heat of pyridine adsorption ΔH_{ads}^o . The value of ΔH_{ads}^o was found to increase in magnitude below 15% coverage but remained relatively constant above this coverage. This variation in ΔH_{ads}^o with pyridine coverage was analyzed using an experimentally validated theoretical approach to determine how ΔH_{ads}^o varies with the degree of $\equiv\text{Ti-OH}$ site distortion. In that work, we defined “distortion” as the deviation in each facet area of the tetrahedron defined by the 4 O atoms of a $\equiv\text{Ti-OH}$ site from that of an undistorted $\equiv\text{Ti-OH}$ tetrahedron (see Figure 3.1). Symmetrical $\equiv\text{Ti-OH}$ tetrahedra were assigned the facet areas calculated from Ti-O bond lengths determined from EXAFS data, which is about 3.76 \AA^2 . We found that the predicted values of ΔH_{ads}^o for adsorbed pyridine correlate with the facet area of the $\equiv\text{Ti-OH}$ site to which it is bound. This finding confirmed that $\equiv\text{Ti-OH}$ site distortion can impact the heat of molecular adsorption, as has been reported for other $\equiv\text{M-OH}$ groups.²² We also showed that ΔH_{ads}^o predictions for a facet area of 3.76 \AA^2 coincided with the value measured for pyridine coverages $> 15\%$. For coverages $< 15\%$, the predicted value of ΔH_{ads}^o matched the experimental values when larger facet areas were used for the prediction. Thus, we showed that a minority of increasingly distorted $\equiv\text{Ti-OH}$ sites with facet areas $> 3.76 \text{ \AA}^2$ are responsible for the strong adsorption of pyridine. Evidence for pyridine adsorption on facets with areas smaller than 3.76 \AA^2 was not found.

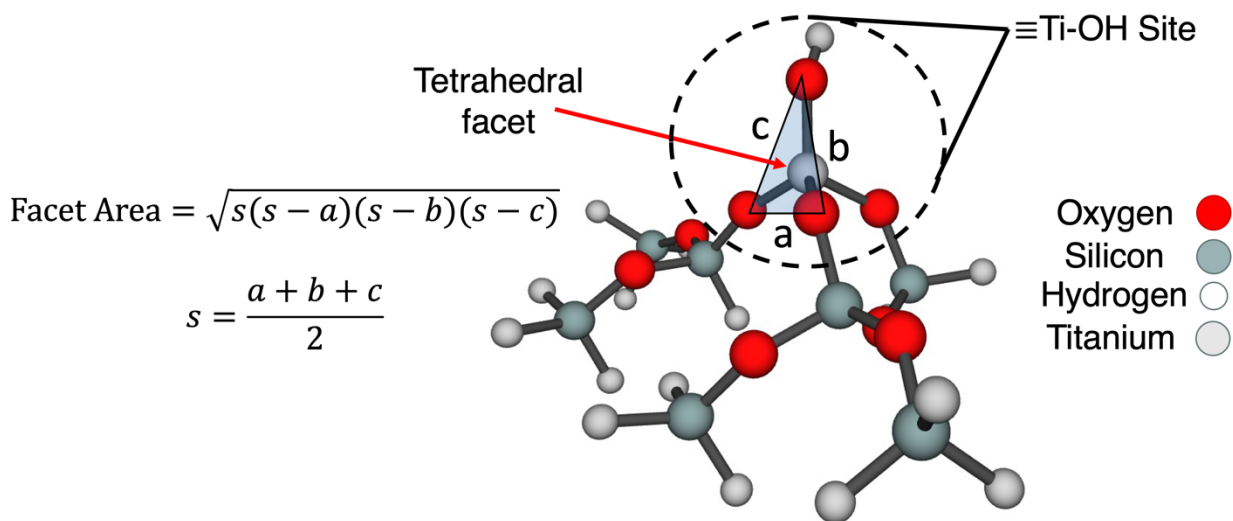


Figure 3.1: Illustration of what is meant by the “tetrahedral facet area” of a $\equiv\text{Ti-OH}$ site shown for the optimized structure of site 1 of our $\equiv\text{Ti-OH}$ site database. The equation on the left shows how the facet area is calculated, which is simply Heron’s formula for the area of a triangle. Large red spheres: oxygen, large dark grey spheres: silicon, large white spheres: titanium, small white spheres: hydrogen.

Given the strong interest in alkene epoxidation over isolated $\equiv\text{Ti-OH}$ sites for alkene epoxidation, the question is whether site distortion affects the epoxidation kinetics. We note here that this issue has been addressed recently for ethene epoxidation on $\equiv\text{Nb(-OH)}_2$.⁷⁷ While this study did find an impact of site distortion on the electronic energy barriers for O-atom transfer to ethene, its effects on H_2O_2 dissociation were not considered. Moreover, the connection to experimental findings could not be established without knowledge of the level of distortion determined experimentally for Nb/SiO_2 .⁷⁷ We also note that the effects of product adsorption on the structure of the active site were not considered. Finally, the results reported were based solely on electronic energies, valid only at zero Kelvin. For proper comparison with experiments, finite temperature effects must be considered, and microkinetic modeling is required.¹⁰³ We also note that, to the best of our knowledge, these effects have not been examined for isolated $\equiv\text{Ti-OH}$ sites.

Here, we report the results of a computational investigation of the effects of $\equiv\text{Ti-OH}$ site distortion on the mechanism and kinetics of cyclohexene (C_6H_{10}) epoxidation with H_2O_2 to form cyclohexene oxide ($\text{C}_6\text{H}_{10}\text{O}$). We aim to establish the connection between these effects and experiments by leveraging our recently acquired knowledge of the $\equiv\text{Ti-OH}$ facet area distribution from Chapter 2. We chose this particular reaction because its gas-phase kinetics have been reported recently by Notestein and co-workers, and, hence, we can use the kinetic parameters reported by these authors for comparison.³² A slightly modified version of the reaction mechanism proposed by these authors is presented in Figure 3.2 and is very similar to that proposed for liquid-phase alkene epoxidations over Ti-based catalysts.^{28–30,33,84} Prior studies have assumed that the adsorption and dissociation of H_2O_2 to produce $\equiv\text{Ti-OOH}$ species are quasi-equilibrated steps, as is the adsorption of cyclohexene to $\equiv\text{Ti-OOH}$ groups, and that the kinetically relevant step is the addition of an O-atom to the double bond of cyclohexene. Neither of the products, cyclohexene oxide and water are assumed to be strongly bound to the catalyst. These assumptions are based on the experimental observation of the reaction being 0th order and 1st order in the partial pressures of H_2O_2 and C_6H_{10} , respectively.³²

While the rates of molecular adsorption and desorption are not typically kinetically relevant at the temperatures of these experiments ($T = 410\text{-}450\text{ K}$), the question remains whether the assumption of rapid and reversible H_2O_2 dissociation is correct under all circumstances. Likewise, it is not clear whether product adsorption alters the structure of the active sites and thereby their adsorptive and catalytic properties. These are questions that we address in the present study, starting with the expanded mechanism (see Figure 3.2) proposed by Notestein and coworkers,³² which shows the adsorption and dissociation of H_2O_2 explicitly and includes two product adsorption states (C6 and C8). Hereafter we refer to this reaction pathway as Mechanism 1.

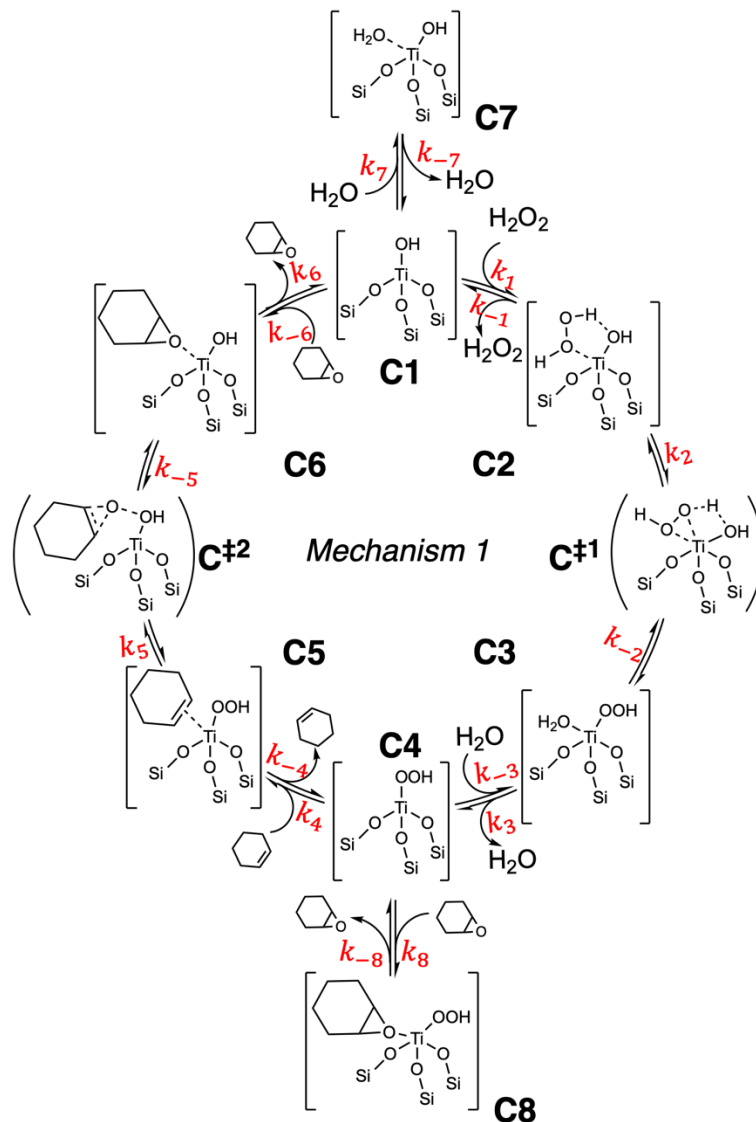


Figure 3.2: An expanded version of the literature proposed mechanism, hereafter called “Mechanism 1”. The rate constants for each elementary step are labeled, which will be discussed in detail in Methods

We begin our analysis of Mechanism 1 by computing the Gibbs free energies of each step using our validated QM/MM approach. These free energies are then used to predict the rate coefficients for each elementary step in Mechanism 1. Next, the computed rate coefficients are employed in a microkinetic model (MKM), which is used to compute the overall kinetic parameters - the apparent activation energy (E_a) and reaction orders in the partial pressures of reactants. This procedure was carried out for a sample of seven distorted $\equiv\text{Ti-OH}$ sites exhibiting a range of tetrahedral facet areas (Figure 3.1). We found that the predicted order in cyclohexene and H_2O_2 for Mechanism 1 over the tetrahedral facets with areas $\geq 3.76 \text{ \AA}^2$ are consistent with those observed experimentally, but the predicted activation energy is significantly higher than found experimentally (30 kJ/mol). We also found that the product, $\text{C}_6\text{H}_{10}\text{O}$, is strongly adsorbed, implying product inhibition. However, for areas $< 3.54 \text{ \AA}^2$ product inhibition did not occur, and the predicted activation energy agrees quantitatively with that measured experimentally. This

motivated us to identify a new mechanism for which all the predicted kinetic parameters would be consistent with those determined experimentally. We discovered that strong adsorption of the $C_6H_{10}O$ product to one of the facets of all $\equiv Ti-OH$ sites significantly reduces the facet areas of the other facets of the same $\equiv Ti-OH$ site, enabling them to become active for cyclohexene epoxidation. Our model predicts that these *in-situ* generated, reduced-area facets lead to kinetic parameters that agree quantitatively with those determined experimentally.

3.3 Methods

3.3.1 Quantum-Mechanics/Molecular Mechanics (QM/MM) Calculations

The QM/MM approach used for this study is identical to that used in Chapter 2 and is discussed there in detail. Briefly, the surface is divided into a central QM region, comprised of approximately 8-11 tetrahedral (T) atoms, surrounded by a model for the amorphous silica, described by MM, that extends 29 Å in radius from the central Ti atom. The MM region is fixed in space. All geometry optimizations and frequency calculations for all structures were performed at the $\omega B97X-D/def2-SVP$ level of theory.⁵⁷ Single-point energy calculations were performed using a larger basis set, $\omega B97M-V/def2-TZVP$, with the SG-3 quadrature grid.^{58,60} Initial guesses for transition state structures were obtained using the Freezing String Method when the optimization of guesses near the expected structure was challenging.¹⁰⁴ All enthalpy corrections at a given temperature used a quasi-rigid rotor harmonic oscillator model with a 100 cm^{-1} cutoff (qRRHO).^{61,62} For all structures involving $\equiv Ti-OH$ sites, QM/MM calculations were performed using the P2 set of MM parameters for the surrounding SiO_2 .⁶¹ All computations were performed using the Zeolite package in Q-Chem version 5.⁶⁵

3.3.2 Models for Ti/SiO_2

Our previously developed Ti/SiO_2 database was presented in Chapter 2. Briefly, seven $\equiv Ti-OH$ site geometries were generated by selecting seven isolated silanol groups ($\equiv Si-OH$) present on the surface of a model of amorphous silica.⁶⁷ The Si atom of a $\equiv Si-OH$ group was replaced with a Ti atom and then the geometry of the $\equiv Ti-OH$ was optimized in the QM region. Images of the optimized geometries of the QM regions, details of their structures, as well as their number labels (i.e., Site 1, Site 2, etc.) can be found in Section 2.3.

3.3.3 Entropy Calculations

Different methods were used to determine gas-phase, absorbed-phase, and transition-state entropies. Gas-phase entropies were calculated using standard statistical mechanics equations for fixed translational and rotational entropy, with vibrational entropy calculated with the quasi rigid-rotor harmonic-oscillator (qRRHO) approximation. As seen in Table S3.1, these calculations are accurate when compared to experimental values.

While previous studies have used the quasi rigid-rotor harmonic-oscillator (qRRHO) approximation to describe the entropy of adsorbed species, this approach has been shown to be inaccurate.⁷⁹ Consequently, we used the empirical model for entropy loss upon adsorption developed by Campbell and Sellers (hereafter denoted as the “Campbell model”), which accurately predicts the entropy for molecular (i.e. non-covalent) adsorption of non-polar and polar molecules on metal oxides, silanol groups of SiO_2 , and tetrahedral Sn sites of zeolite BEA (Sn/BEA).^{79,80}

The Campbell model provides a linear relationship between the gas-phase entropy of a species to its adsorbed-phase entropy via equation (1).

$$S_{ads,X}^o(T) = S_X^o(T) * 0.7 + 3.3R \quad (1)$$

Here, R is the ideal gas constant, S_X^o is the gas-phase entropy of X , and $S_{ads,X}^o$ is its adsorbed-phase entropy. We employ this expression to determine the entropies of all molecularly adsorbed states. When covalent interactions are involved, such as for $\equiv\text{Ti}-\text{OOH}$ sites (State C4) and for all transition states, we adopt the qRRHO model to estimate the entropy of these species. In states where a non-covalent adsorbate and a covalently bound adsorbate are both present (such as in State C8), we assume the entropy of the state can be separated and calculated as the sum of the estimate in equation (1) for the entropy of the non-covalently bound adsorbate, and the estimate using qRRHO for the entropy of the covalently bound adsorbate. The separability assumption is supported by others who have shown that equation (1) can be used to approximate the entropy of two adsorbed ethanol molecules on Sn/BEA as the sum of the estimates made for each one.⁸⁰ The estimate was within 5% of estimates made by the integration of the vibrational density of states obtained from ab-initio molecular dynamics (AIMD) trajectories.⁸⁰

3.3.4 Steady-State Microkinetic Modeling

The MKMs assume the mean-field approximation, i.e., that the catalyst surface is well-mixed and that no spatial segregation occurs.¹⁰³ With this assumption we develop the equations used to model the kinetics of cyclohexene epoxidation based on Mechanism 1, while the details for Mechanism 2 (discussed later in Results and Discussion) are given in the SI.

The rate coefficients for each elementary step in Mechanism 1 are shown in Figure 3.2. For elementary steps in which a gas phase species enters the cycle, the rate coefficient for that step is written as an apparent first-order rate coefficient that includes the partial pressure of that species. For example, for elementary step 1, H_2O_2 enters the cycle for the forward direction of this reaction. In this case, k_1 is defined as shown in equation (2).

$$k_1 = k_{1,int} \frac{P_{\text{H}_2\text{O}_2} [\text{bar}]}{1 \text{ bar}} \quad (2)$$

Where $k_{1,int}$ is the intrinsic rate coefficients calculated for $P_{\text{H}_2\text{O}_2} = 1 \text{ bar}$.

For the steps in Mechanism 1 (Figure 3.2), we can write a system of equations defining the rate of change in the fractional coverage of all intermediates. We define $\Theta_i = \frac{[Ci]}{[N_s]}$, where $[Ci]$ and $[N_s]$ are the surface concentrations of states i in Mechanism 1 (for $i = 1$ through 8) and the sum of the surface concentrations of all sites, respectively. These first-order differential equations are given by:

$$\frac{d\Theta_1}{dt} = (-k_1 - k_{-6} - k_7)\Theta_1 + k_{-1}\Theta_2 + k_6\Theta_6 + k_{-7}\Theta_7 \quad (3)$$

$$\frac{d\Theta_2}{dt} = k_1\Theta_1 + (-k_{-1} - k_2)\Theta_2 + k_{-2}\Theta_3 \quad (4)$$

$$\frac{d\Theta_3}{dt} = k_2\Theta_2 + (-k_{-2} - k_3)\Theta_3 + k_{-3}\Theta_4 \quad (5)$$

$$\frac{d\Theta_4}{dt} = k_3\Theta_3 + (-k_{-3} - k_4 - k_8)\Theta_4 + k_{-4}\Theta_1 + k_{-8}\Theta_8 \quad (6)$$

$$\frac{d\Theta_5}{dt} = k_4\Theta_4 + (-k_{-4} - k_5)\Theta_5 + k_{-5}\Theta_6 \quad (7)$$

$$\frac{d\Theta_6}{dt} = k_{-6}\Theta_1 + k_5\Theta_5 + (-k_{-5} - k_6)\Theta_6 \quad (8)$$

$$\frac{d\Theta_7}{dt} = k_7\Theta_1 - k_{-7}\Theta_7 \quad (9)$$

$$\frac{d\Theta_8}{dt} = k_8\Theta_4 - k_{-8}\Theta_8 \quad (10)$$

At steady state, Θ_i is invariant in time, so we can set the left-hand side of equations (3)-(10) to zero. Finally, we require that the sum of all intermediates is equal to unity (equation (11)).

$$\sum_i \Theta_i = 1 \quad (11)$$

When seven of the differential equations are combined with the site balance, there are eight independent, linear equations that can be solved to determine the eight unknown surface coverages (Θ_i).

These linear expressions can be rewritten in a matrix form as follows:

$$\begin{bmatrix} (-k_1 - k_{-6} - k_7) & k_{-1} & 0 & 0 & 0 & k_6 & k_{-7} & 0 \\ k_1 & (-k_{-1} - k_2) & k_{-2} & 0 & 0 & 0 & 0 & 0 \\ 0 & k_2 & (-k_{-2} - k_3) & k_{-3} & 0 & 0 & 0 & 0 \\ 0 & 0 & k_3 & (-k_{-3} - k_4 - k_8) & k_{-4} & 0 & 0 & k_{-8} \\ 0 & 0 & 0 & k_4 & (-k_{-4} - k_5) & k_{-5} & 0 & 0 \\ k_{-6} & 0 & 0 & 0 & k_5 & (-k_{-5} - k_6) & 0 & 0 \\ k_7 & 0 & 0 & 0 & 0 & 0 & -k_{-7} & 0 \\ 1 & 1 & 1 & 1 & 1 & 1 & 1 & 1 \end{bmatrix} \begin{bmatrix} \Theta_1 \\ \Theta_2 \\ \Theta_3 \\ \Theta_4 \\ \Theta_5 \\ \Theta_6 \\ \Theta_7 \\ \Theta_8 \end{bmatrix} = \begin{bmatrix} 0 \\ 0 \\ 0 \\ 0 \\ 0 \\ 0 \\ 0 \\ 1 \end{bmatrix} \quad (12)$$

Equation (12) is solved in MATLAB using the backslash operator to determine Θ_i in terms of the rate coefficients. Then, the turnover frequency can be calculated from the site-normalized net rate of $C_6H_{10}O$ desorption as shown in equation (13).

$$TOF = (k_6\Theta_6 - k_{-6}\Theta_1) + (k_{-8}\Theta_8 - k_8\Theta_4) \quad (13)$$

To connect the Gibbs free energy estimates obtained from our QM/MM calculations to the rate coefficients, we assume that each rate coefficient can be described by harmonic transition state theory, equation (14).¹⁰³

$$k_j = \left(\frac{k_B T}{h}\right) \exp\left(\frac{-\left(G_{|j|}^{\ddagger,o} - G_{reactant,k_j}^o\right)}{RT}\right) \quad (14)$$

Where k_B , h , and R are the Boltzmann, Planck, and ideal gas constants, respectively. $G_{|j|}^{\ddagger,o} - G_{reactant,k_j}^o$ is the difference in the Gibbs free energy between the transition state for reaction j and the reactant state associated with k_j in Figure 3.2. We note for clarity that the transition state for k_j is the same as for k_{-j} , but the reactant states are different depending on the direction.

Transition state Gibbs free energies for all molecular adsorption and desorption steps (such as steps 1, 3, 4, 6, 7, and 8 in Mechanism 1) are the same as those assumed by Campbell and coworkers in the development of equation (1) for adsorbate entropies.⁷⁹ Briefly, the transition state for adsorption and desorption is the molecule on a two-dimensional plane parallel to the surface. The molecules on this plane are located far enough from the surface to experience no enthalpic stabilization from their interaction with the surface, even when rotating.⁷⁹ Thus the transition state for molecular adsorption and desorption has a Gibbs free energy equal to the three-dimensional gas-phase Gibbs free energy minus one degree of translational freedom (normal to the surface):⁷⁹

$$G_n^{\ddagger,o} = G_{gas}^o - G_{gas,1D-trans}^o \quad (15)$$

Or, in terms of the enthalpy and the entropy:

$$H_n^{\ddagger,0} = H_{gas}^o - \frac{1}{2}RT \quad (16)$$

$$S_n^{\ddagger,0} = S_{gas}^o - S_{gas,1D-trans}^o \quad (17)$$

Note we have invoked the equipartition theorem in equation (16) for the enthalpy of one degree of translational freedom. The index n is a positive integer that runs over all molecular adsorption and desorption reactions (in Figure 3.2, $n=1, 3, 4, 6, 7,$ and 8). We note that these expressions lead to predictions of adsorbate entropies that are in close agreement with those determined from equilibrium adsorption isotherm measurements, and to predictions of desorption pre-factors that agree well with experiments.⁷⁹ When we estimate the desorption prefactor for H₂O at 300 K using these expressions, we calculate $4.4 \times 10^{14} \text{ s}^{-1}$, which agrees with the range of experimental values reported for H₂O desorption from Ti (IV) sites of TiO₂ (101), TiO₂ (110), and TiO₂ (100) ($3.15\text{-}5.0 \times 10^{14} \text{ s}^{-1}$).¹⁰⁵

The apparent activation energy (E_a) was calculated by fitting a straight line to a plot of $\ln(\text{TOF})$ versus $1/RT$, the slope of which is equal to $-E_a$. For these calculations, the temperature was varied between 383.15 K and 423.15 K in 5 equal increments while holding $P_{\text{H}_2\text{O}_2} = 3 \text{ kPa}$, and $P_{\text{C}_6\text{H}_{10}} = 3 \text{ kPa}$. The product partial pressures were fixed at $P_{\text{H}_2\text{O}} = 30 \text{ Pa}$ and $P_{\text{C}_6\text{H}_{10}\text{O}} = 30 \text{ Pa}$, corresponding to approximately 1% product yield, as seen experimentally.³²

The reaction order in $P_{\text{H}_2\text{O}_2}$ was calculated by fitting a straight line to a plot of $\ln(\text{TOF})$ vs. $\ln(P_{\text{H}_2\text{O}_2})$ over five equal increments from 0.6 to 3 kPa, with $P_{\text{C}_6\text{H}_{10}} = 3 \text{ kPa}$, $P_{\text{H}_2\text{O}} = 30 \text{ Pa}$, and $P_{\text{C}_6\text{H}_{10}\text{O}} = 30 \text{ Pa}$, at $T = 403.15 \text{ K}$. The reaction order in $P_{\text{C}_6\text{H}_{10}}$ was calculated by fitting a straight line to a plot of $\ln(\text{TOF})$ vs. $\ln(P_{\text{C}_6\text{H}_{10}})$ over five equal increments from 0.6 to 3 kPa, with $P = 3 \text{ kPa}$, $P_{\text{H}_2\text{O}} = 30 \text{ Pa}$, and $P_{\text{C}_6\text{H}_{10}\text{O}} = 30 \text{ Pa}$, at $T = 403.15 \text{ K}$.

The kinetically relevant transition states were determined using the degree of rate control.¹⁰⁶

3.4 Results and Discussion

3.4.1 Correlations of Enthalpies of Adsorption with Tetrahedral Facet Area

Our first objective was to understand how enthalpies of adsorption (ΔH_{ads}^o) for the steps in Mechanism 1 (presented in Figure 3.2) correlate with the tetrahedral facet area of $\equiv\text{Ti-OH}$ groups (defined in Figure 3.1). The states along the cycle that correspond to molecular adsorption events are states C2 (H₂O₂ adsorption), C3 & C7 (H₂O adsorption), C5 (C₆H₁₀ adsorption), and C6 & C8 (C₆H₁₀O adsorption). We note that state C8 corresponds to C₆H₁₀O adsorption to the metal center of a $\equiv\text{Ti-OOH}$ group, not a $\equiv\text{Ti-OH}$ group. However, we have found that the difference in the values of ΔH_{ads}^o for C₆H₁₀O adsorption to the metal center in these two groups is not large over a collection of sites in our database (Figure S3.1). Therefore, we estimate the value for ΔH_{ads}^o to a $\equiv\text{Ti-OOH}$ group using these correlations which greatly reduces the computational burden by reducing the number of DFT calculations required.

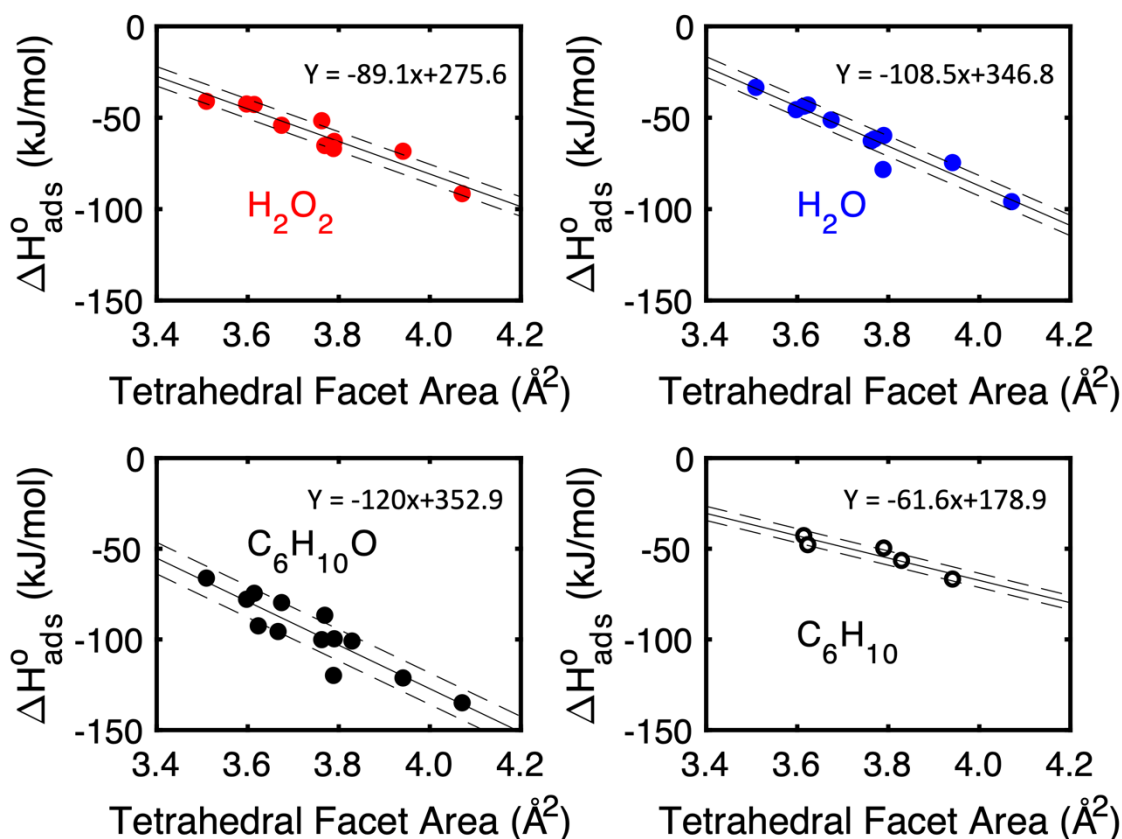


Figure 3.3: Effect of the tetrahedral facet area on ΔH_{ads}° ($T = 403.15$ K) for multiple polar molecules present within the reactor during C_6H_{10} epoxidation. Reference states are one vacant $\equiv Ti-OH$ site and one gas-phase molecule. Lines shown linear models with the equation representing that line shown in the inset. The dashed lines show one standard error of the y-estimate.

Figure 3.3 shows that the values of ΔH_{ads}° for molecularly bound H_2O_2 , H_2O , $C_6H_{10}O$, and C_6H_{10} correlate linearly with the tetrahedral facet area to which the molecule is adsorbed, identical to what we found for pyridine adsorption in Chapter 2. These correlations are the result of two dominant phenomena, previously deduced from an energy decomposition analysis of pyridine adsorption (EDA). As the $\equiv Ti-OH$ site facet area increases, the $\equiv Ti-OH$ site has less geometric distortion penalties to form the adsorbate-bound complex, and “frozen” interactions (the complex interplay of permanent electrostatic, Pauli repulsion, and dispersion interactions) become increasingly favorable.

The optimal geometry for adsorbed H_2O_2 is shown in Figure 3.4. It involves the simultaneous formation of a hydrogen bond and Lewis acid-base adduct with the $O^{\alpha}-O^{\beta}$ bond axis oriented parallel to the $\equiv Ti-OH$ bond. This structure is similar to that reported previously for H_2O_2 dissociation using a small $Ti(OH)_4$ tetrahedral cluster model for the $\equiv Ti-OH$ site at the B3LYP/LANL2DZ(Ti)/6-311+G(d,p) level of theory.¹⁰⁰ H_2O forms a Lewis acid-base adduct with the Ti metal center with the hydrogens oriented along the Ti-O bonds (Figure S3.2). For C_6H_{10} , most geometry optimizations starting from initial structures in which the C=C pi bond interacts with the Ti cation resulted in the departure of C_6H_{10} from the $\equiv Ti-OH$ site towards the surrounding

silica, indicating very weak bonding. We only report the ΔH_{ads}^o values for stable C=C pi-Ti bonding complexes in Figure 3.3. The fact that these interactions are weak supports the experimentally observed 1st order dependence on the pressure of C₆H₁₀ which suggested low coverage of kinetically relevant C₆H₁₀ adsorbed species.³²

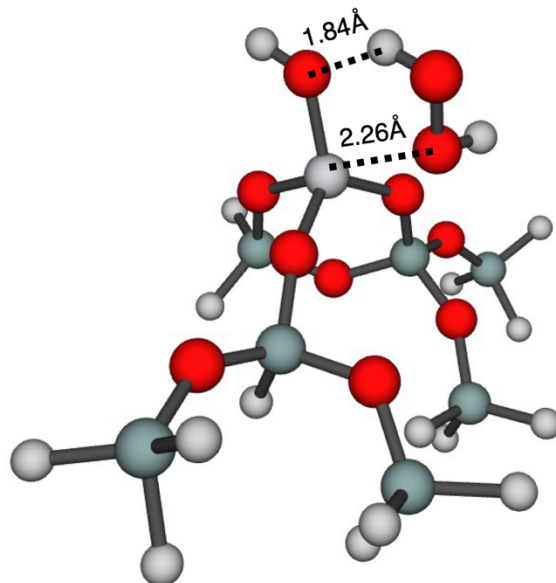


Figure 3.4: Optimized geometry of H₂O₂ molecularly bound to site 1 of our ≡Ti-OH site database. Large red spheres: oxygen, large dark grey spheres: silicon, large white spheres: titanium, small white spheres: hydrogen.

For C₆H₁₀O, two binding geometries were considered. In the first geometry, C₆H₁₀O binds with the vector normal to the C-O-C triangle of the epoxide nearly perpendicular to the ≡Ti-OH bond, as seen in Figure 3.5A. In the second geometry shown in Figure 3.5B, the vector normal to the C-O-C ring of the epoxide is nearly parallel to the ≡Ti-OH bond. The perpendicular configuration was more favorable for nearly all ≡Ti-OH sites (Figure S3.3). The data points used to define the linear correlation shown in Figure 3.3 were the most favorable configurations for each facet.

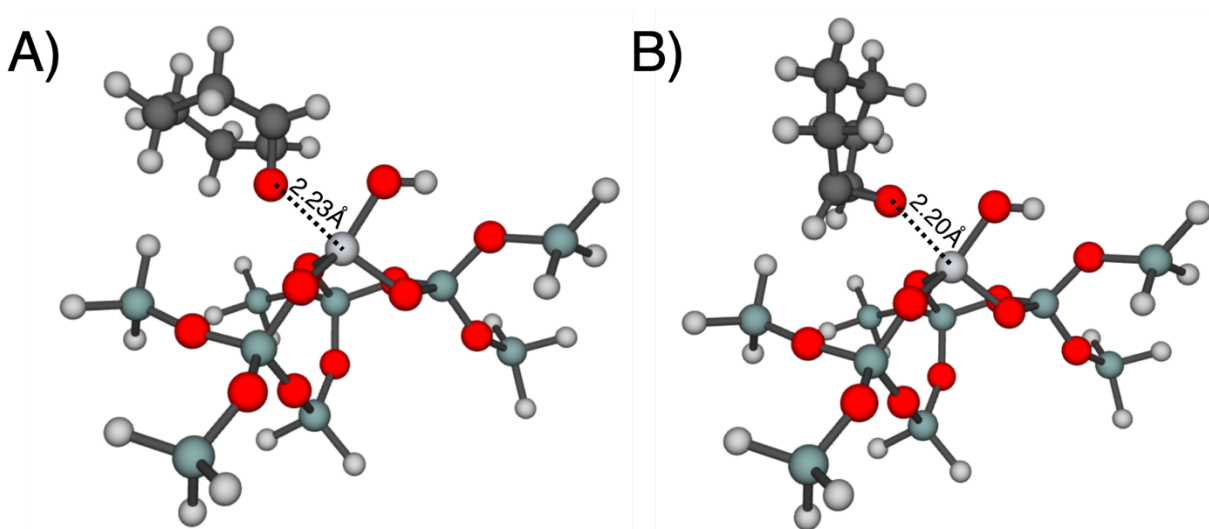


Figure 3.5: Optimized geometries of $C_6H_{10}O$ to site 2, facet 2. A) the vector normal to the C-O-C triangle of the epoxide is nearly perpendicular to the $\equiv Ti-OH$ bond B) the vector normal to the C-O-C triangle of the epoxide is nearly parallel to the $\equiv Ti-OH$ bond. Large red spheres: oxygen, large dark grey spheres: silicon, large white spheres: titanium, small white spheres: hydrogen, large black spheres: carbon.

We also sought to understand how distortion impacts the enthalpies of formation of $\equiv Ti-OOH$ groups (state C4). In general, the OH group of the $\equiv Ti(\eta^2-OOH)$ complex was found to sit normal to a tetrahedral facet in its optimal geometry, as illustrated in Figure 3.6. In contrast to molecular adsorbates, there was no apparent correlation between the enthalpies of $\equiv Ti-OOH$ groups (formation of state C4) and the tetrahedral facet area. Across the seven sites we examined, the enthalpy of reaction (ΔH_{rxn}^o) for $\equiv Ti-OOH$ formation from H_2O_2 only varied from -13.3 to -25.4 kJ/mol, with an average of -17 kJ/mol and a standard deviation of 3.8 kJ/mol (Table S3.2), which is similar to ΔE_{rxn}^o reported by others for small cluster models of $\equiv Ti-OH$ (-19 kJ/mol).⁶ The entropy of reaction was also narrowly distributed with an average of $-32.2 \pm 9 J/(mol \cdot K)$. The similarity in enthalpies across our database, and the agreement of our calculations with others utilizing much smaller clusters indicates that the enthalpy of this state is relatively insensitive to the surrounding environment.

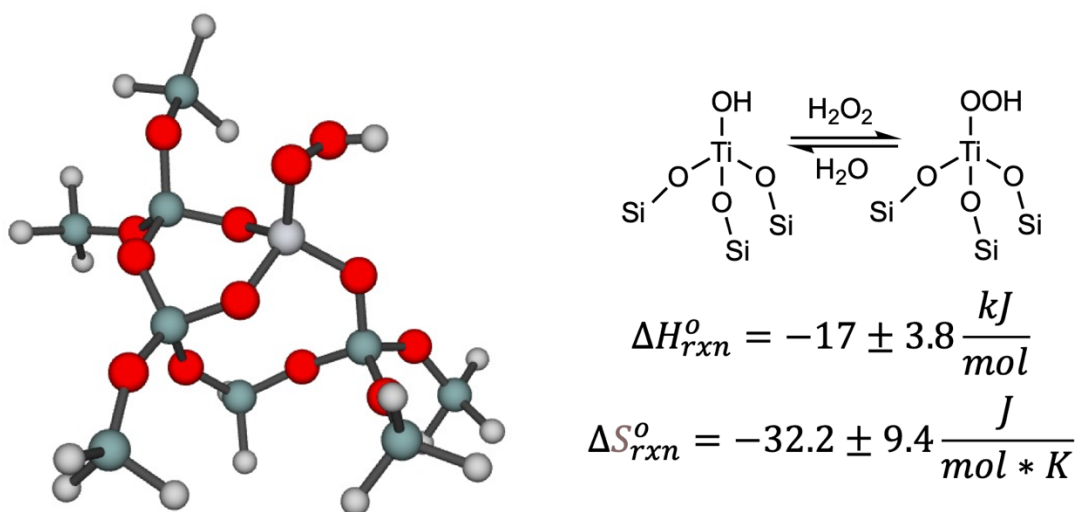


Figure 3.6: Representative optimized geometry of the $\equiv Ti-OOH$ structure for Site 2 (left) and schematic representing the formation of $\equiv Ti(\eta^2-OOH)$ sites and the calculated average enthalpy and entropy change (right). Calculations are relative to a vacant site and gas-phase H_2O_2 . Large red spheres: oxygen, large dark grey spheres: silicon, large white spheres: titanium, small white spheres: hydrogen.

3.4.2 Correlations of Enthalpies of Activation with Tetrahedral Facet Area

Next, we wish to understand how transition state enthalpies correlate with the tetrahedral facet area of $\equiv Ti-OH$ groups. The optimal geometry for the H_2O_2 dissociation transition state (state $C^{\ddagger 1}$ in Mechanism 1) is shown in Figure 3.7 for Site 1 – Facet 1 of our database. Images of all H_2O_2 dissociation transition state structures can be found in section 3.7.6 of the SI. In this geometry, the Ti-O-Si bond is straddled by the $O^{\alpha}-O^{\beta}$ bond of H_2O_2 with H^{α} being abstracted by the Ti hydroxyl group to form H_2O , and H^{β} directed axially such that the $HOOH$ dihedral angle is near 180° .

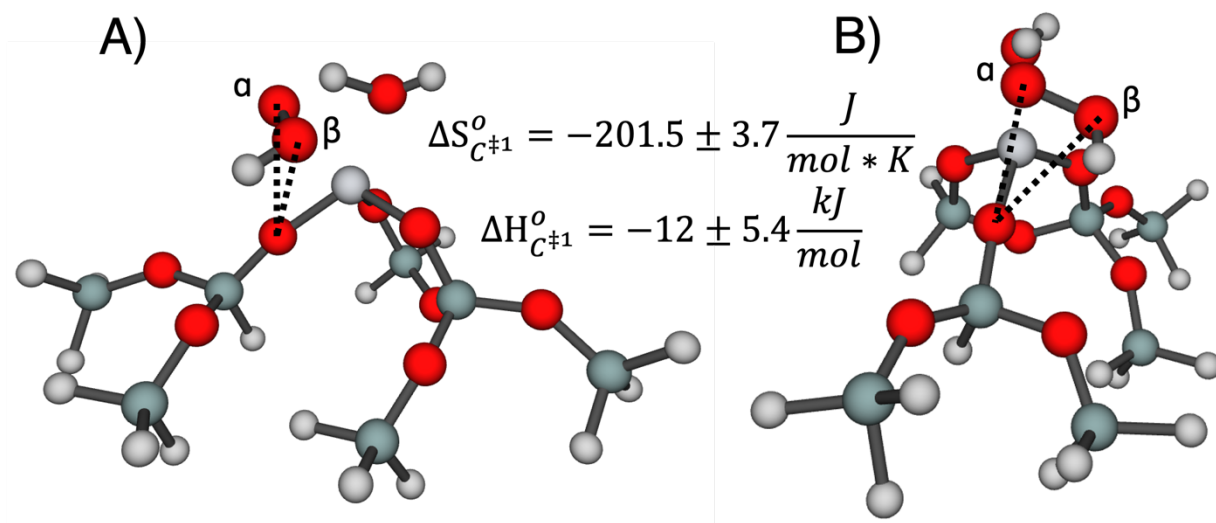


Figure 3.7: Two angles of view (A and B are the same structure) of the optimized geometry for the H_2O_2 dissociation transition state (state $C^{\ddagger 1}$) for Site 1 – Facet 1 of our database. The average enthalpy and entropy, with the standard deviations, are displayed in the center of the figure (relative to a vacant site and gas-phase H_2O_2). Large red spheres: oxygen, large dark grey spheres: silicon, large white spheres: titanium, small white spheres: hydrogen.

The enthalpies for these transition states are relatively constant across our $\equiv Ti-OH$ database with an average of -12 kJ/mol (relative to gas phase reactants) and a standard deviation of ± 5.4 kJ/mol (Table S3.3). Likewise, the entropies are similar, with an average of -201.5 ± 3.7 J/(mol·K). Thus, there was little correlation between the tetrahedral facet area (i.e., distortion) and the transition state enthalpy because the H_2O_2 molecule no longer forms a Lewis acid-base adduct with the metal center during H_2O_2 dissociation.

We found two structures for the transition state involved in oxygen transfer from the $\equiv Ti-OOH$ to C_6H_{10} to form $C_6H_{10}O$ (state $C^{\ddagger 2}$ in Mechanism 1). In one form, the $C=C$ bond of C_6H_{10} is in-plane with the tetrahedral facet, as shown in Figure 3.8. The enthalpy of the in-plane state correlates roughly with the facet area. In the other structure, the C -backbone is inverted, and the $C=C$ bond straddles the neighboring $Ti-O-Si$ bond during oxygen transfer (Figure 3.8). As for the straddled H_2O_2 transition state, the geometries are nearly isenthalpic, likely because these structures are not simultaneously coordinated to a Ti facet during oxygen transfer. Therefore, unlike the values of ΔH_{ads}^o where a single linear correlation is observed (Figure 3.3), the enthalpy of the transition state must be estimated by a piecewise linear function considering both geometries, as shown in the inset of Figure 3.8. The straddled geometry is more favorable for facet areas less than 3.925 \AA^2 , whereas the in-plane geometry is more favorable above this value. Since most $\equiv Ti-OH$ sites in Ti/SiO_2 exhibit facet areas smaller than 3.925 \AA^2 , as shown in Chapter 2, the straddled configuration is likely the more common one. However, the minority of in-plane transition states for facets larger than 3.925 \AA^2 are relatively stable. This could imply high specific activity for a small proportion of the $\equiv Ti-OH$ sites exhibiting such large facet areas; however, as shown in Figure 3.3, product adsorption states also become more favorable, which could lead to

product inhibition. A complete microkinetic modeling analysis is necessary to answer this question and is provided in the following section. We note that entropies of all geometries were quite similar, with averages of -236 ± 6.3 J/(mol·K) and -234 ± 3.4 J/(mol·K) for in-plane and straddled geometries, respectively (Table S3.4 and Table S3.5).

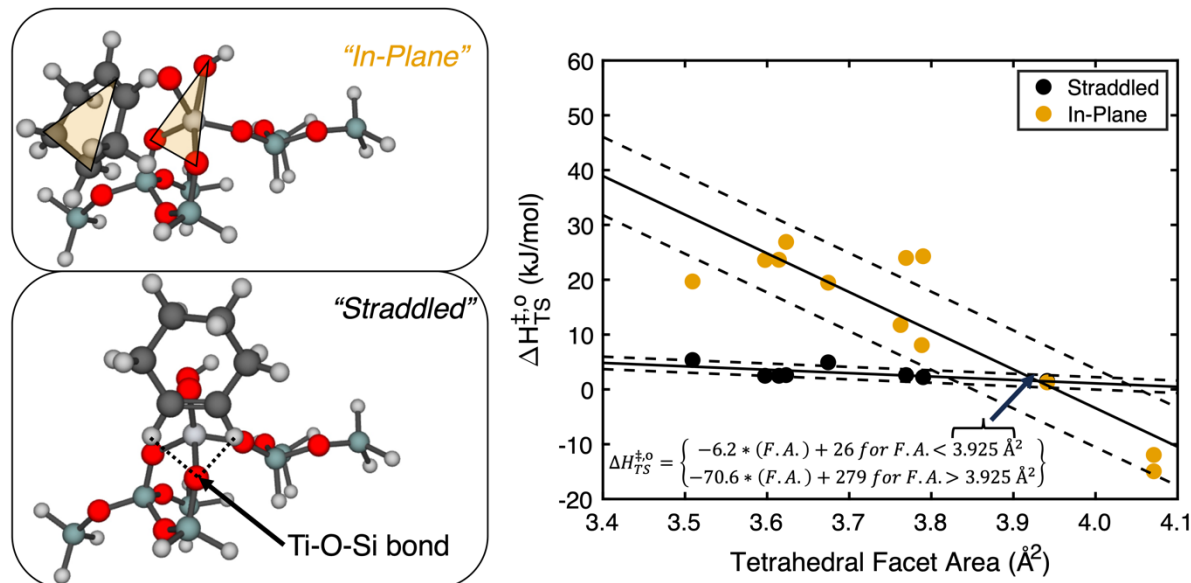


Figure 3.8: Representative images of “In-Plane” and “Straddled” transition state geometries for epoxidation by site 1 of our database (left). The “In-Plane” transition structure shows two shaded triangles describing the meaning of “In-Plane.” Both triangles are in-plane with one another. Large red spheres: oxygen, large dark grey spheres: silicon, large white spheres: titanium, small white spheres: hydrogen, large black spheres: carbon. The effect of facet area on the enthalpies (relative to a vacant site and gas-phase H_2O_2 and C_6H_{10}) of transition states (right). The piecewise function in the inset shows the equations for both linear correlations. Dashed lines show one standard error in the estimated enthalpies from each correlation.

The findings noted above agree qualitatively with those reported recently in a study of ethylene epoxidation over Nb/SiO₂, which found multiple transition state structures for the same elementary reaction with different energies.⁷⁷ While we also find that the energies of *some* structures correlate with a geometric descriptor representing the undercoordination of the metal cation, we also find that some transition state geometries are isenthalpic across distorted $\equiv\text{Ti-OH}$ sites. The relative enthalpies for these two classes of transition states depend on the facet area of the $\equiv\text{Ti-OH}$ site in question.

In summary, distortions in the tetrahedral geometry of $\equiv\text{Ti-OH}$ sites primarily influence ΔH_{ads}^0 of reactants and products. By contrast, transition state enthalpies for H_2O_2 dissociation and O-atom transfer are relatively insensitive to tetrahedral facet area since the most favorable geometries straddle Ti-O-Si bonds and do not simultaneously coordinate with Ti facets.

3.4.3 Microkinetic Modeling of Cyclohexene Epoxidation over Ti/SiO₂

Having established estimates of the enthalpies for all states involved in Mechanism 1, we now have a means for estimating the rate coefficients for each elementary step as a function of the tetrahedral facet area. Thus, we utilized the calculated enthalpies of adsorption and activation, presented in the previous section, in a microkinetic model (MKM) based on Mechanism 1 to allow

direct comparison between theoretically predicted reaction rate parameters and experimental results.³²

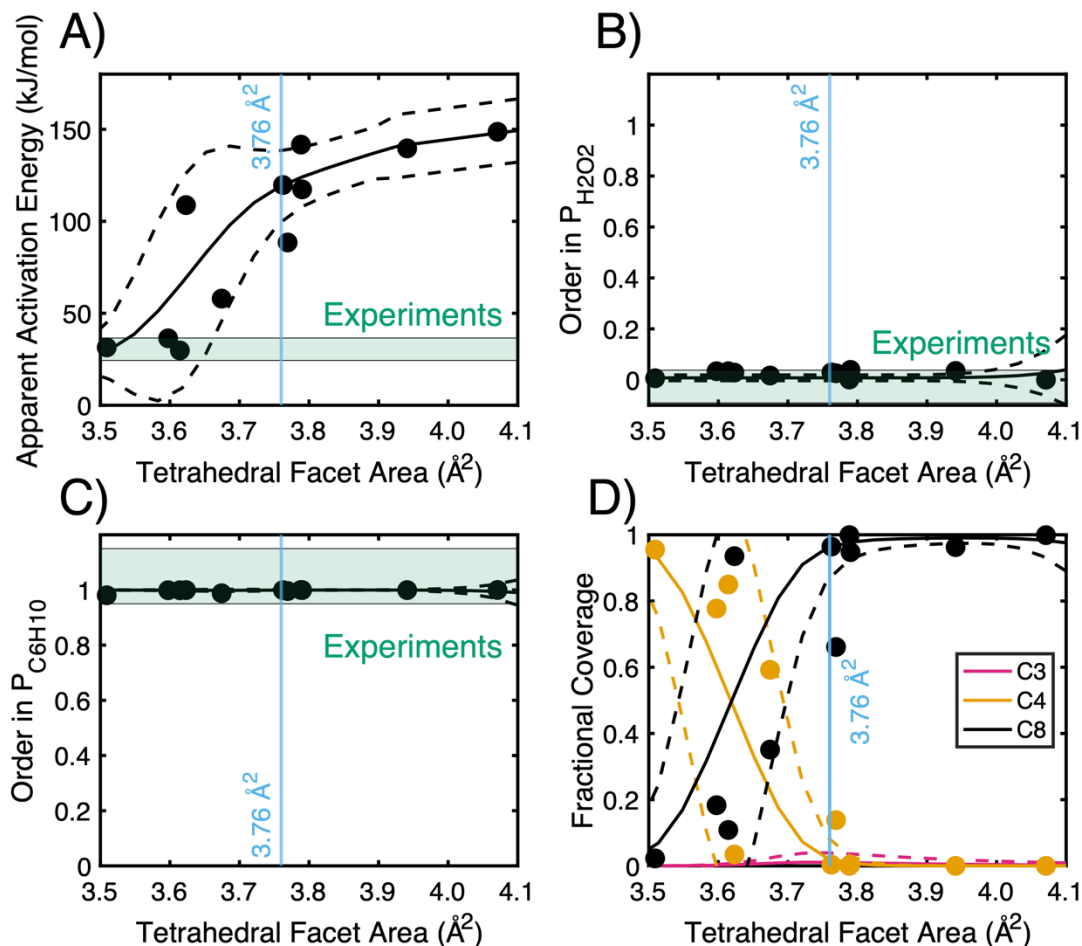


Figure 3.9: MKM results for Mechanism 1 as a function of the tetrahedral facet area. Panels plot A) the apparent activation energy (E_a), B) reaction order in $P_{\text{H}_2\text{O}_2}$, C) reaction order in $P_{\text{C}_6\text{H}_{10}}$, and D) the fractional coverage of significant intermediates at $T = 403.15 \text{ K}$, $P_{\text{H}_2\text{O}_2} = 3 \text{ kPa}$, $P_{\text{C}_6\text{H}_{10}} = 3 \text{ kPa}$, $P_{\text{C}_6\text{H}_{10}\text{O}} = 30 \text{ Pa}$, and $P_{\text{H}_2\text{O}} = 30 \text{ Pa}$. The data points utilize DFT-calculated (thermally corrected to 403.15 K) enthalpies from structures specific to each site in our database - in situations where the energy of a state was not calculated for a specific facet, it was estimated from the linear correlations and averages presented in the previous section. The solid lines are the predicted values of the parameter in question for a given facet area calculated only using enthalpies from the linear correlations and averages presented in the previous section. The dashed lines show \pm two times the standard deviation of the parameter in question when the standard errors in the linear correlations presented in Figure 3.3 and the standard deviations in the averages used for transition state enthalpies are propagated. The results from Notestein and coworkers³² are displayed as the shaded region and take into account one standard error in the parameter measured. A vertical blue line shows the facet area of a tetrahedral $\equiv\text{Ti-OH}$ site constructed from EXAFS measurements (3.76 \AA^2) which represent the majority of $\equiv\text{Ti-OH}$ sites in the as-synthesized material.

Figure 3.9 illustrates the predicted apparent activation energy (E_a) and reaction orders in the partial pressures of H_2O_2 and C_6H_{10} as a function of the tetrahedral facet area to which molecular adsorbates bind. These results are also compared with the experimental values, which are shown in the light green shaded bands. Figure 3.9B and Figure 3.9C show that our model agrees with the experimentally observed orders in C_6H_{10} and H_2O_2 , 1st and 0th order, respectively,

irrespective of the facet area of different $\equiv\text{Ti-OH}$ sites. On the other hand, Figure 3.9A shows that the E_a increases from 24 kJ/mol to 150 kJ/mol as the facet area increases, leading to a decrease in catalytic activity (see Figure S3.4 for ΔG_{app}^\ddagger vs. facet area). Quantitative agreement with experiments is achieved only when the tetrahedral facet area is less than 3.54 \AA^2 (or 3.65 \AA^2 if we take a more conservative stance and utilize the dashed lines in Figure 3.9A). As seen in Figure 3.9D, our model indicates this is due to a change in the catalyst resting state from C4 ($\equiv\text{Ti-OOH}$) to C8 ($\text{C}_6\text{H}_{10}\text{O}$ adsorbed to $\equiv\text{Ti-OOH}$ site), indicating strong product inhibition. It is important to note that state C8 in Mechanism 1 is an intermediate that is not involved in the formation of products, and consequently, is often left out of proposed mechanisms in studies of epoxidation.³² Figure 3.9D demonstrates that this state is quite important since it dominates the catalyst resting state for a majority of the facet areas. Analysis of the degree of rate control for transition states involved in Mechanism 1 is shown in Figure S3.5, where it is seen that the kinetically relevant step is O-atom transfer to cyclohexene. It is also observed that H_2O_2 dissociation is rapid relative to O-atom transfer, consistent with the assumption made in the experimental study of this system.³²

To this point, we have established that $\equiv\text{Ti-OH}$ site distortion significantly impacts the apparent activation energy for cyclohexene epoxidation by $\equiv\text{Ti-OH}$ sites, if the reaction occurs via Mechanism 1 (Figure 3.2). We also see that agreement with the experimental value of E_a is only attained when tetrahedral facet areas of $\equiv\text{Ti-OH}$ sites are smaller than 3.54 \AA^2 , at which point adsorbed $\text{C}_6\text{H}_{10}\text{O}$ is not the resting state.

We next explore whether $\equiv\text{Ti-OH}$ site modification occurs under reaction conditions so as to create O-Ti-O facet areas smaller than those observed prior to the reaction. $\equiv\text{Ti-OH}$ sites are three-dimensional structures that can bind adsorbates to more than one of their facets simultaneously if steric constraints allow (i.e., the silica support does not block access to a facet). It is helpful to note that $\equiv\text{Ti-OH}$ sites supported on amorphous silica may only have one accessible facet, while others could have two or three accessible facets. The largest facet of the accessible facets for a given $\equiv\text{Ti-OH}$ site will adsorb polar molecules preferentially due to its more negative value of ΔH_{ads}^o , and, subsequently, more negative value of ΔG_{ads}^o since we consider all ΔS_{ads}^o for molecular adsorptions to be the same (see Entropy Calculations – Campbell Model). By examining the geometries of $\text{C}_6\text{H}_{10}\text{O}$ bound to $\equiv\text{Ti-OH}$ sites with more than one accessible facet, we discovered that the facets opposite to the facet to which $\text{C}_6\text{H}_{10}\text{O}$ is bound become even smaller, as seen in Figure 3.10. Interestingly, the facet area range for the accessible, vacant facets of $\text{C}_6\text{H}_{10}\text{O}$ bound $\equiv\text{Ti-OH}$ sites is narrow (3.47 \AA^2 to 3.53 \AA^2) relative to the original $\equiv\text{Ti-OH}$ site facet area range (3.5 \AA^2 to 4.07 \AA^2). Importantly, we note that facets that are 3.76 \AA^2 , which are consistent with a majority of sites, are still reduced to 3.53 \AA^2 after $\text{C}_6\text{H}_{10}\text{O}$ adsorption to Facet 1 indicating this effect would apply for most sites in Ti/SiO_2 . Facet areas in the range of 3.47 \AA^2 to 3.53 \AA^2 are too small to adsorb $\text{C}_6\text{H}_{10}\text{O}$ and exhibit E_a consistent with experimental values, as shown previously in Figure 3.9. Therefore, if the co-adsorbed $\text{C}_6\text{H}_{10}\text{O}$ influences the energetics of epoxidation negligibly, then it is possible that small facets generated *in situ* by $\text{C}_6\text{H}_{10}\text{O}$ adsorption could still be active and exhibit kinetics consistent with experimental observation.

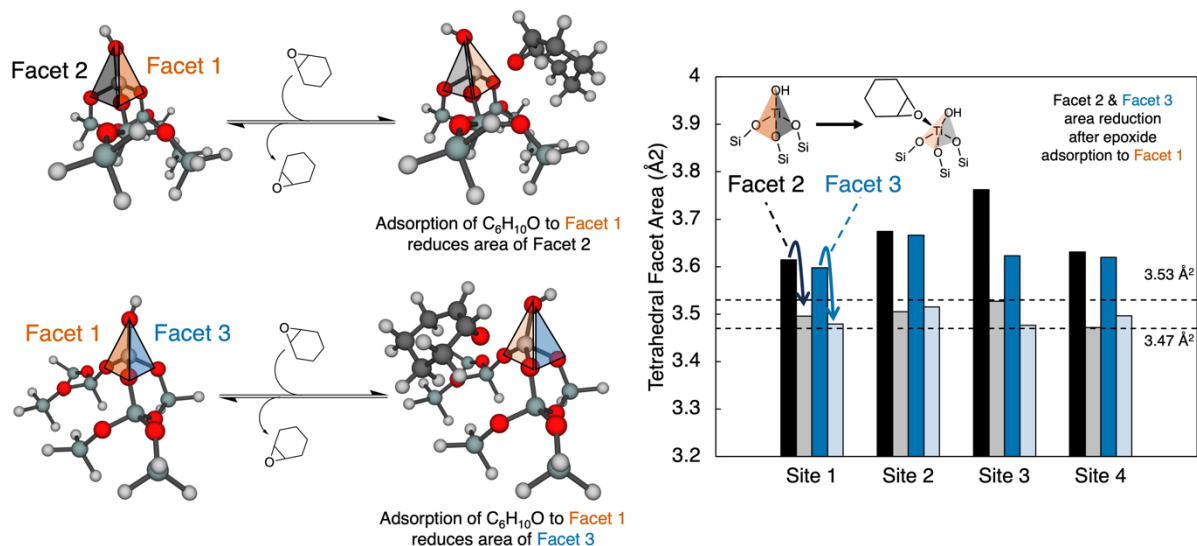


Figure 3.10: Effects of C₆H₁₀O adsorption on the tetrahedral facet area of the vacant facets opposite the facet to which C₆H₁₀O adsorbs. Sites 1-4 are the only sites in our database with more than one accessible facet. The horizontal dashed lines show the range of facet areas for Facet 2 and 3 after C₆H₁₀O adsorption to Facet 1. Large red spheres: oxygen, large dark grey spheres: silicon, large white spheres: titanium, small white spheres: hydrogen, large black spheres: carbon.

To assess this possibility, we simulated the epoxidation pathway over a smaller facet (Facet 2) of Site 1 when C₆H₁₀O remains bound to Facet 1 of the ≡Ti-OH site (Figure 3.11, Pathway B). We also considered the epoxidation reaction over Facet 1 and Facet 2 in isolation. The combination of all pathways presented in Figure 3.11 is called Mechanism 2.

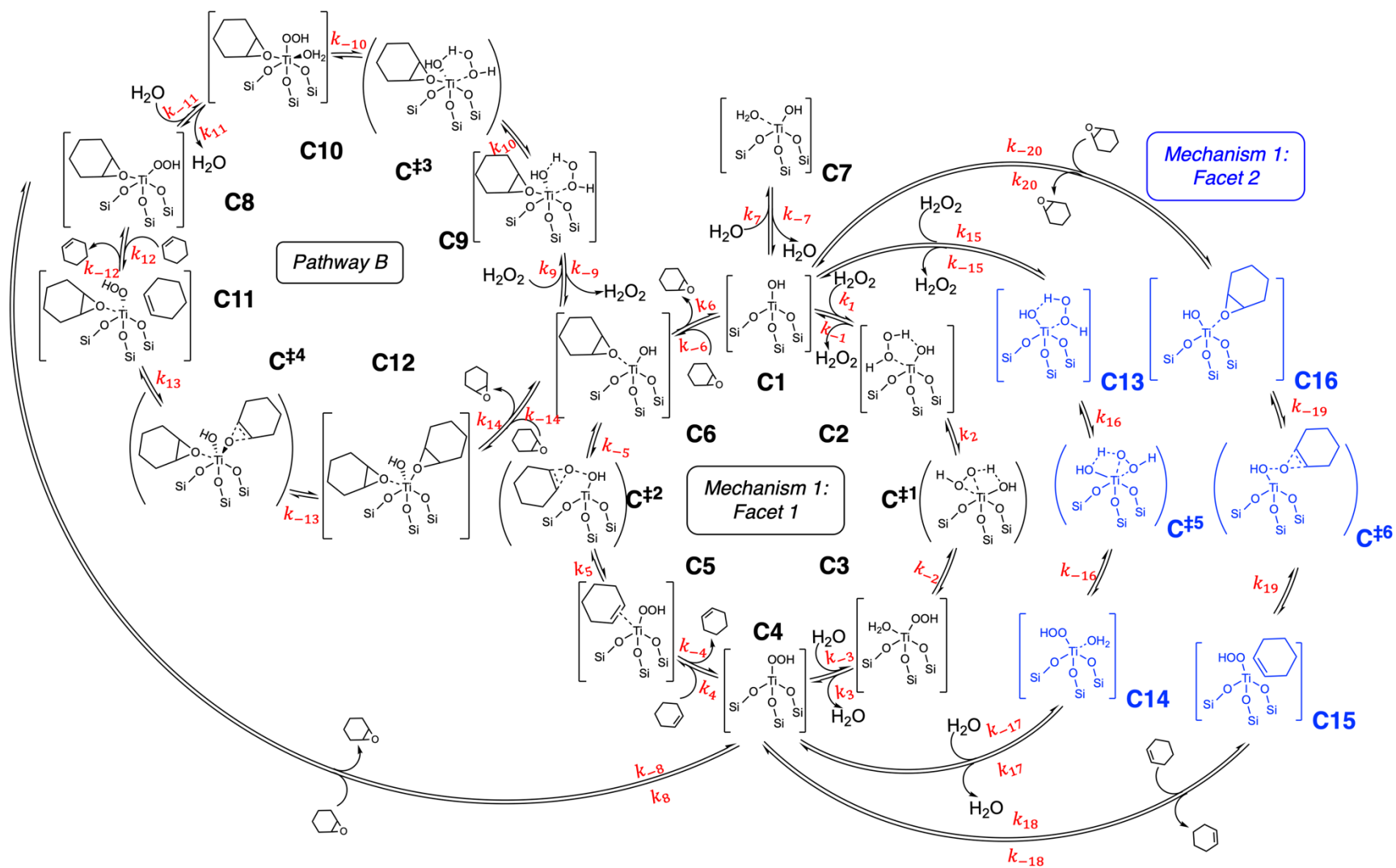


Figure 3.11: Mechanism 2, which includes the possibility of Facet 2 epoxidation catalysis with (Pathway B) and without (Mechanism 1-Facet 2) a $C_6H_{10}O$ co-adsorbed to Facet 1.

Figure 3.12A displays the enthalpy landscape for all three epoxidation pathways within Mechanism 2 computed for Site 1. In Figure 3.12A, we have modified the reference state for Pathway B to facilitate visual comparison with the other pathways. Adsorption of $C_6H_{10}O$ on Facet 1 causes Facet 2 to contract from 3.61 \AA^2 to 3.49 \AA^2 (Figure 3.10). Figure 3.12B shows the enthalpies along Pathway B (with co-adsorbed $C_6H_{10}O$) and the expected enthalpies for a facet area of 3.49 \AA^2 based on our linear correlations or average values developed from a scenario without co-adsorbed $C_6H_{10}O$. In Figure 3.12B, a perfect overlap of the dashed line with the solid line would indicate that co-adsorbed $C_6H_{10}O$ has a negligible effect on the energetics of epoxidation.

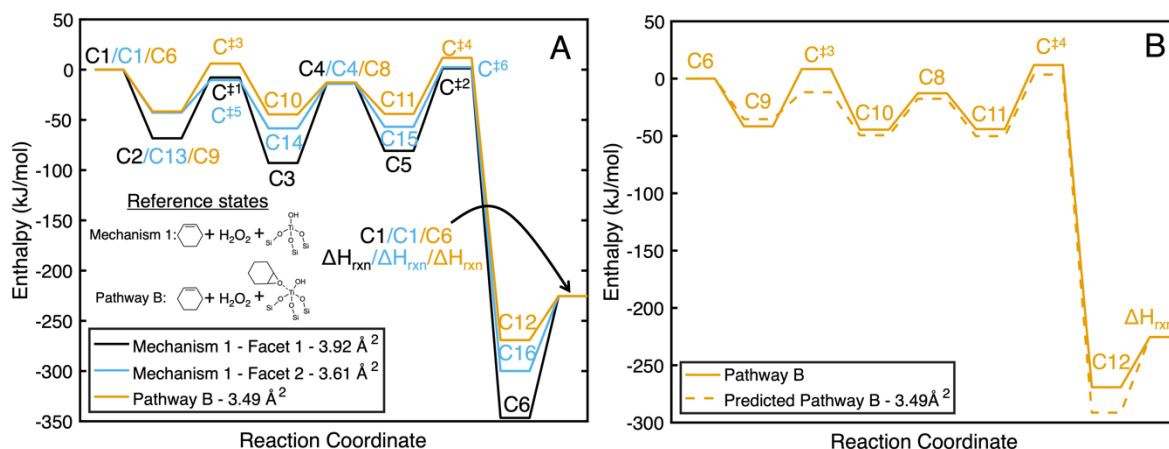


Figure 3.12: A) Enthalpy landscapes for all pathways in Mechanism 2 computed over Site 1. The reference state for Pathway B is adjusted to allow for easier visual comparison. B) Pathway B enthalpy landscape computed using DFT methods (solid line) and estimated Pathway B enthalpies using linear correlations and averages for a tetrahedral facet area equal to 3.49 \AA^2 . This facet area is the size of Facet 2 after the adsorption of $C_6H_{10}O$ to Facet 1.

We will first discuss the effects of co-adsorbed $C_6H_{10}O$ on the values of ΔH_{ads}^o for H_2O_2 , C_6H_{10} , and $C_6H_{10}O$. The value of ΔH_{ads}^o for H_2O_2 (States C2/C9/C13) is largest for Facet 1 (State C2) due to its significantly larger facet area (3.94 \AA^2) relative to Facet 2 (3.61 \AA^2 in State C13 of Mechanism 1 - Facet 2, 3.49 \AA^2 in C9 of Pathway B). Interestingly, the ΔH_{ads}^o for H_2O_2 to Facet 2 is the same without and with co-adsorbed $C_6H_{10}O$, even though its facet area has been reduced in the former case. By contrast, the ΔH_{ads}^o for C_6H_{10} and $C_6H_{10}O$ to Facet 2 with co-adsorbed $C_6H_{10}O$ becomes less favorable by 6 and 22 kJ/mol, respectively, even after correcting for Facet 2 area reduction. (see solid vs. dashed lines in Figure 3.12B for State C9 vs. States C11 and C12).

Thus, the presence of $C_6H_{10}O$ bound to Facet 1 can affect the adsorptive ability of Facet 2 in ways that depend on the type of adsorbate. When adsorbates form predominantly Lewis acid-base adducts with the Ti metal center, as is the case for C_6H_{10} and $C_6H_{10}O$, these interactions will be reduced when a co-adsorbed Lewis base is already present. However, in cases where the adsorbate can form a simultaneous Lewis acid-base adduct and a hydrogen bond with the $\equiv Ti-OH$ hydroxyl (such as for H_2O_2), the effects of a co-adsorbate involve an interplay between reduced Lewis acid-base interactions and enhanced H-bonding. Natural Bonding Orbital (NBO) calculations for Ti (IV) cations in zeolites have revealed that the coordination of Lewis bases reduces the positive charge of the metal center and slightly increases the negative charge on the

surrounding O atoms, which supports our findings.¹⁰⁷ Ultimately, this implies that the correlations in Figure 3.3 are only valid for polar molecule adsorption to an initially vacant $\equiv\text{Ti-OH}$ site.

The ΔH_{rxn}^o for the formation of $\equiv\text{Ti-OOH} + \text{H}_2\text{O}(\text{g})$ from H_2O_2 and a $\equiv\text{Ti-OH}$ site are nearly the same with (-12.7 kJ/mol) and without (-14 kJ/mol) co-adsorbed $\text{C}_6\text{H}_{10}\text{O}$ for all pathways (Figure 3.12A, States C4 and C8). This also implies that the value of ΔH_{ads}^o for $\text{C}_6\text{H}_{10}\text{O}$ adsorbed on $\equiv\text{Ti-OOH}$ is similar to the value of ΔH_{ads}^o for $\text{C}_6\text{H}_{10}\text{O}$ adsorbed to a $\equiv\text{Ti-OH}$ site, a conclusion that we confirmed previously for two other sites in our database (see Figure S3.1). We remind the reader that we did not compute the enthalpy of states C3/C10/C14 (H_2O adsorption to a $\equiv\text{Ti-OOH}$ site). Instead, we opted to estimate the enthalpy as a sum of ΔH_{rxn}^o for $\equiv\text{Ti-OOH}$ formation and ΔH_{ads}^o for H_2O adsorbed to a $\equiv\text{Ti-OH}$ site since we found this to be accurate for $\text{C}_6\text{H}_{10}\text{O}$. Thus, a direct comparison between these states was not attempted.

The enthalpy of the transition state for H_2O_2 dissociation (States $\text{C}^{\ddagger 1}$, $\text{C}^{\ddagger 3}$, and $\text{C}^{\ddagger 5}$) relative to gas-phase reactants was previously found to be insensitive to facet area due to its straddled configuration (see Figure 3.7). The average value across our database was calculated to be -12 ± 5.4 kJ/mol, which encompasses the values calculated for the transition states for Site 1 - Facet 1 (-8 kJ/mol) and Site 1 - Facet 2 (-10 kJ/mol). When $\text{C}_6\text{H}_{10}\text{O}$ is co-adsorbed, however, the transition state enthalpy (relative to State C6) is 6 kJ/mol, or approximately 18 kJ/mol higher than our average value derived from calculations without co-adsorbed $\text{C}_6\text{H}_{10}\text{O}$ (See Figure S3.6 for the geometry of this structure). Since the value of ΔH_{ads}^o for H_2O_2 is unchanged in the presence of co-adsorbed $\text{C}_6\text{H}_{10}\text{O}$, this also increases the intrinsic enthalpy barrier by 18 kJ/mol.

For O-atom transfer to C_6H_{10} , we find that the straddled transition state geometry is more favorable than the in-plane geometry for Facet 2 with co-adsorbed $\text{C}_6\text{H}_{10}\text{O}$ by 11 kJ/mol (See Figure S3.7 for the geometry of this structure). Interestingly, the presence of co-adsorbed $\text{C}_6\text{H}_{10}\text{O}$ on Facet 1 does not strongly influence the intrinsic enthalpy barrier for O-atom transfer (difference in enthalpy between states C11 and $\text{C}^{\ddagger 4}$) that we expected from the combination of linear correlations shown in Figure 3.3 and Figure 3.8 (an error of only 1.9 kJ/mol). This indicates that the destabilization in ΔH_{ads}^o (about 6 kJ/mol) is equally applied to the O-atom transfer transition state.

In summary, our findings from this section are:

1. The presence of $\text{C}_6\text{H}_{10}\text{O}$ adsorbed to Facet 1 does not significantly modify the value of ΔH_{rxn}^o for $\equiv\text{Ti-OOH}$ formation.
2. The value of ΔH_{ads}^o for Lewis acid-base adducts is reduced to a greater extent than what can be attributed to a reduction in facet area alone. This includes the adsorption of C_6H_{10} , $\text{C}_6\text{H}_{10}\text{O}$, and likely also H_2O (this was not explored).
3. The value of ΔH_{ads}^o of H_2O_2 remains unchanged.
4. The intrinsic enthalpy of activation for O-atom transfer to cyclohexene is not significantly modified.
5. The intrinsic enthalpy barrier for H_2O_2 dissociation is increased by 18 kJ/mol when $\text{C}_6\text{H}_{10}\text{O}$ is co-adsorbed.

The matrix representation of the set of differential equations describing the rates of change of the coverages of each intermediate in Mechanism 2 is displayed in section 3.7.11 of the SI. Analysis of the kinetics for cyclohexene epoxidation via Mechanism 2 over Site 1 reveals that state C8 is the dominant resting state (97% coverage), i.e., $\text{C}_6\text{H}_{10}\text{O}$ bound to the large facet of a $\equiv\text{Ti-}$

OOH site (Table 3.1). The kinetically relevant transition state is $C^{\ddagger 4}$, corresponding to O-atom transfer to C_6H_{10} while $C_6H_{10}O$ remains co-adsorbed, indicating Pathway B is now the dominant reaction pathway and determines steady-state epoxidation turnovers. This means that epoxidation on Site 1 occurs on the smaller of its facets, concurrently with $C_6H_{10}O$ bound to the largest facet. The results in Table 3.1 demonstrate that the predicted rate parameters for cyclohexene epoxidation via Mechanism 2 over Site 1 agree satisfactorily with those reported experimentally. The agreement seen for $\Delta G_{app}^{\ddagger}$ and $\Delta S_{app}^{\ddagger}$ suggests that our initial assumption of a qRRHO-like transition state (see ‘‘Entropy Corrections’’ in Methods) was reasonable.

Table 3.1: Predicted rate parameters for cyclohexene epoxidation via Mechanism 2 over Site 1 compared with those determined experimentally.

Parameter	MKM – Mechanism 2	Experiment ³²
E_a (kJ/mol)	27.5	30.4 ± 6.1
Ord($P_{cyclohexene}$)	0.99	1.05 ± 0.1
Ord($P_{H_2O_2}$)	0.05	-0.027 ± 0.064
$\Delta G_{app}^{\ddagger}$ (kJ/mol)*	113.1	119.6
$\Delta S_{app}^{\ddagger}$ (J/mol*K)	-220.6	-229.4
Resting State	C8 (97%), C6 (3%)	-
Degree of Rate Control	$C^{\ddagger 4}$ (99.7%)	-

*calculated as $\Delta G_{app}^{\ddagger} = \left(\ln(TOF [s^{-1}]) - \ln\left(\frac{k_B T}{h}\right) \right) * -R(403.15 K)$. Conditions for the experiment were $T = 403 K$, $P_{H_2O_2} = 3$ kPa, and $P_{C_6H_{10}} = 3$ kPa. Conditions for calculations were $T = 403 K$, $P_{H_2O_2} = 3$ kPa, $P_{C_6H_{10}} = 3$ kPa, $P_{C_6H_{10}O} = 30$ Pa, and $P_{H_2O} = 30$ Pa.

Remarkably, the entirety of Mechanism 2 reduces to a well-defined resting state (C8) and a single transition state requiring the adsorption and reaction of cyclohexene ($C^{\ddagger 4}$) within a single pathway (Pathway B). Thus, we concur with the experimental literature that H_2O_2 dissociation can be assumed to be rapid and equilibrated at the reaction conditions used experimentally, that O-atom transfer is kinetically relevant, and that the most abundant surface species is a form of $\equiv Ti-OOH$ species.³² Consequently, we demonstrate that all the kinetic parameters predicted from Mechanism 2 for Site 1 reproduce those determined by Notestein and coworkers in their experiments:

$$r_{epox} = k_{app} P_{C_6H_{10}} \quad (18)$$

The crucial difference between the mechanism proposed here is the presence of strongly bound $C_6H_{10}O$ adsorbed to Ti sites throughout the catalytic cycle. This conclusion could not have been drawn from experimental kinetics alone.

What remains to be determined is the effect of site distortion on the prevalence of state C8 and Pathway B. The question is whether this issue can be addressed without computing the mechanism for all $\equiv\text{Ti-OH}$ sites in our database, a process that would be very resource-intensive. For this reason, we opted for a series of carefully chosen assumptions in an attempt to model Mechanism 2 as a function of facet area.

These assumptions are as follows:

- 1) For simplicity, we only consider a two-facet mechanism, i.e., Mechanism 2, shown in Figure 3.11. We contend that a three-facet mechanism equivalent to Pathway B would be unlikely because this would require *two* co-adsorbed $\text{C}_6\text{H}_{10}\text{O}$ molecules during catalysis, resulting in greater-than-6-fold (octahedral) coordination for Ti(IV) for other intermediates and transition states along the mechanism. Greater-than-6-fold coordination is generally quite rare for Ti(IV) cations.¹⁰⁸
- 2) We assume that the area of Facet 1 > Facet 2.
- 3) We assume that Facet 2 has an initial facet area of 3.75 \AA^2 which reduces to 3.5 \AA^2 if $\text{C}_6\text{H}_{10}\text{O}$ adsorbs to Facet 1 (Figure 3.10).
- 4) In estimating the enthalpies of States C9, C11, and C12, we adopt the conclusions drawn from our previous calculations for Site 1. For example, to estimate ΔH_{ads}^o for $\text{C}_6\text{H}_{10}\text{O}$ adsorption to Facet 2 of a site with co-adsorbed $\text{C}_6\text{H}_{10}\text{O}$ on Facet 1 (State C12), we use the linear correlations presented in Figure 3.3 to make this prediction for a facet area of 3.5 \AA^2 but apply a penalty of 22 kJ/mol which is equal to the error in our linear correlations that we calculated in the previous section for Site 1. We repeat the same process for States C9 and C11 but with a penalty of 0 kJ/mol and 6 kJ/mol, respectively, as calculated for Site 1. These penalties represent second-order corrections to the linear correlations presented in Figure 3.3. Although these second-order corrections may not be the same across all Facet 2 areas with co-adsorbed $\text{C}_6\text{H}_{10}\text{O}$, we recall that the distribution is relatively narrow (3.47\AA^2 to 3.53\AA^2); therefore, we contend that our assumptions are reasonable due to the limited range of facets we are dealing with.
- 5) The enthalpy of State C10 (adsorption of H_2O to a $\equiv\text{Ti-OOH}$ site with a co-adsorbed $\text{C}_6\text{H}_{10}\text{O}$) is estimated from the linear correlations with no second-order correction. As shown in the previous section, not including a second-order correction implies that we are likely predicting a value of ΔH_{ads}^o that is more negative than the actual value. Therefore, if the coverage of State C10 is predicted to be very small with this assumption applied, it is likely even smaller if the actual value were known and used accordingly. The results below demonstrate that the predicted coverage of State C10 is negligible, supporting this assumption.
- 6) For H_2O_2 dissociation (State $\text{C}^{\ddagger 3}$), we adopt the learnings from Site 1 and apply an 18 kJ/mol penalty to the estimated value using our linear correlations and averages.
- 7) The intrinsic enthalpy barrier for O-atom transfer (State $\text{C}^{\ddagger 4}$) can be estimated by the difference in the enthalpies of States C11 and $\text{C}^{\ddagger 4}$ predicted by the linear correlations shown in Figures 1 and 6, which was accurate for the enthalpies of Pathway B over Site 1 (Figure 3.12).

For this analysis, we focused on the experimentally observed distribution of $\equiv\text{Ti-OH}$ facet areas ($\geq 3.76\text{\AA}^2$) and only varied the initial area of Facet 1 as a parameter.

Figure 3.13 compares the predicted kinetics for Mechanisms 1 and 2 as a function of Facet 1 area. The leftmost side of the plots in Figure 3.13 is the prediction for sites whose structures are based on EXAFS measurements, which comprise the majority of sites in Ti/SiO₂ (~85%). The results for Mechanism 2 reveal several significant findings: 1) As seen in Figure 3.13D, State C^{‡4}, representing O-atom transfer to C₆H₁₀ in Pathway B, remains the kinetically relevant transition state. 2) State C8 remains the resting state, as shown in Figure S3.8. 3) the E_a and reaction orders agree quantitatively with experiments for all facets as shown in Figure 3.13A through Figure 3.13C, and 4) the effects of facet area on these parameters are minor. In other words, *all sites have similar activity* (see Figure S3.9 for plot of $\Delta G_{app}^{\ddagger}$ vs. facet area). This is a direct consequence of the strong adsorption of C₆H₁₀O which reduces the distribution of available facets for catalysis to a narrow range of small facet areas - from 3.47 Å² to 3.53 Å². C₆H₁₀O does not inhibit these *in-situ* generated facets, and ΔH_{ads}^o does not vary over such a small range. This finding contrasts with the results for Mechanism 1, which show that the facet area significantly impacts the catalytic activity due to product inhibition (Figure S3.9).

Thus, the assumption that site distortion leads to a significant variation in catalytic activity is an artefact of not considering a complete mechanism. A series of computational studies contend that silica-supported metal sites should express a distribution of activities (i.e., all sites are not the same) due to distortion imposed on the metal site geometry by the amorphous silica support to which it is grafted.^{18,23,24,77} These propositions are challenged by experimental literature on cyclooctene epoxidation in the liquid phase. Some studies have demonstrated, through ≡Ti-OH site poisoning experiments with phenyl phosphonic acid, a linear decrease in activity with the amount of poison introduced, leading to the conclusion that all active sites are kinetically similar.²⁹⁻³¹ Our work connects these studies because it confirms that while site geometries identified in the absence of reaction exhibit a range of adsorptive and catalytic properties (pyridine adsorption and cyclohexene epoxidation via Mechanism 1), modifications of the active site under reaction conditions through the adsorption of C₆H₁₀O, or any polar adsorbate in principle, can generate a new distribution of active sites with a narrow range of activities (Figure 3.10 and Figure 3.13). Notably, experimental evidence for Pathway B in the aqueous phase has been established, where the co-adsorbate has been proposed to be H₂O based on EXAFS data.⁹⁷

Experimental evidence for gas-phase cyclohexene epoxidation via Pathway B (where our calculations apply) could be obtained via *in-situ* EXAFS or the observation of adsorbed C₆H₁₀O by *in-situ* IR spectroscopy. While such experiments, to the best of our knowledge, have not been reported, IR spectra of adsorbed propene oxide formed during the epoxidation of propene on Au/Ti/SiO₂ from a gas-phase mixture of H₂/O₂/propene has been reported. The spectra obtained are similar to those recorded by exposing the catalyst to pure propene oxide.¹⁰⁹

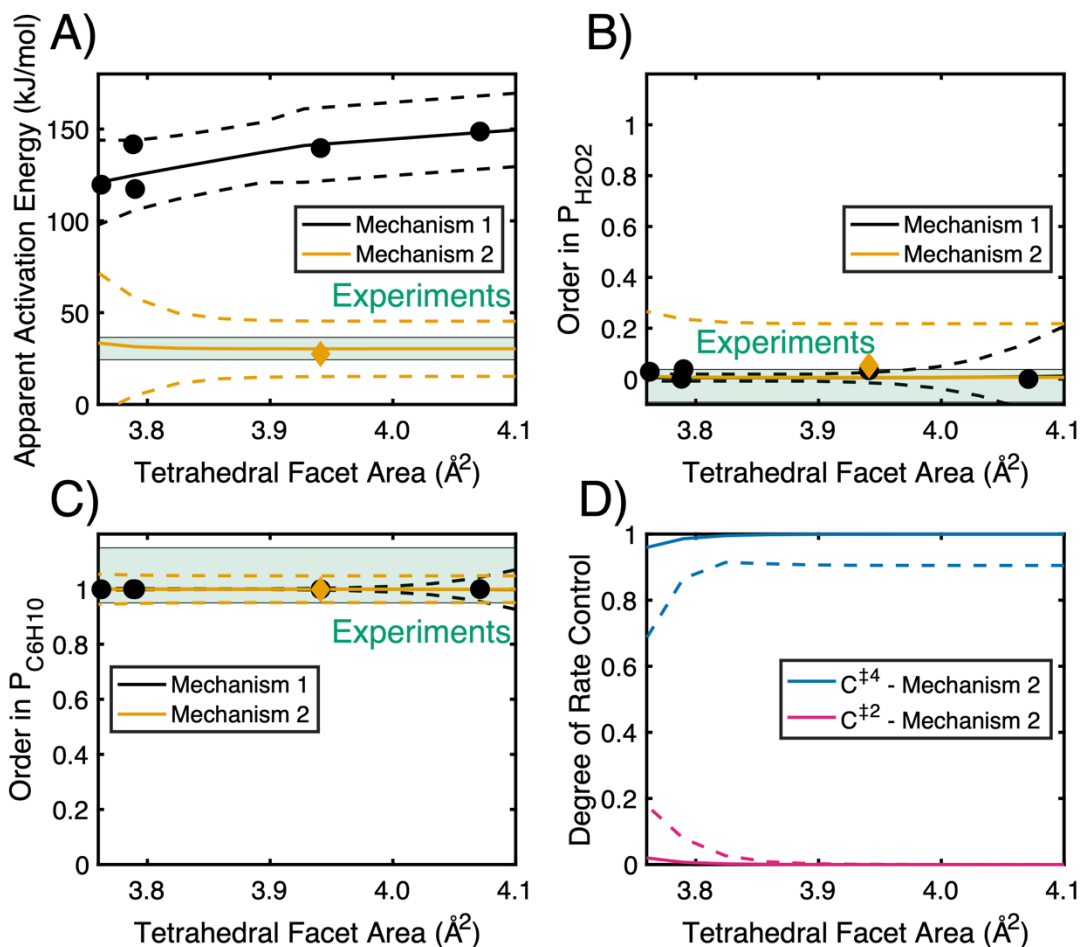


Figure 3.13: Comparison of kinetic predictions for Mechanisms 1 and 2 as a function of facet area for the A) apparent activation energy, B) reaction order in H_2O_2 (top right), C) reaction order in C_6H_{10} (bottom left), and D) the degree of rate control for Mechanism 2 (bottom right). Conditions are $T = 403$ K, $P_{H_2O_2} = 3$ kPa, $P_{C_6H_{10}} = 3$ kPa, $P_{C_6H_{10}O} = 30$ Pa, $P_{H_2O} = 30$ Pa. For Mechanism 2, the modified facet area is the largest of the two facets (Facet 1), with the Facet 2 area equal to 3.75 \AA^2 . The experimental results are displayed as the shaded region and take into account one standard error in the parameter measured. Black data points are the MKM results using the Gibbs free energies calculated for specific sites undergoing Mechanism 1. The yellow data point shows the MKM results for Mechanism 2 over Site 1. Black lines show the MKM results when the linear correlations in Figure 1 are used to estimate the enthalpies of states for Mechanism 1. Yellow lines show the MKM results for Mechanism 2 as a function of the Facet 1 area, the assumptions of which are outlined in the text. The dashed lines show \pm two times the standard deviation of the parameter in question when the standard errors in the linear correlations presented in Figure 3.3 and the standard deviations in the averages used for transition state enthalpies are propagated.

Pathway B in Mechanism 2 only applies to $\equiv Ti-OH$ sites with two or more accessible facets. As mentioned previously, $\equiv Ti-OH$ sites supported on amorphous silica can, in principle, exhibit only one accessible facet if the surrounding silica blocks access to the other facets. In that case, Mechanism 1 will apply to such $\equiv Ti-OH$ sites and the predicted kinetics will be equal to what is shown in Figure 3.9. It is worth noting that when these $\equiv Ti-OH$ sites with only one accessible facet expose a facet area of 3.76 \AA^2 , consistent with the majority of facets in Ti/SiO_2 , such sites are inhibited by $C_6H_{10}O$ and have a low TOF, as shown in Figure S3.4. In other words, these sites

would be deactivated as $C_6H_{10}O$ is produced. Deactivation was observed in the experimental study of this system.³²

To this point, we have determined the kinetics of cyclohexene epoxidation for a fixed set of reactant and product partial pressures ($P_{H_2O_2} = 3$ kPa, $P_{C_6H_{10}} = 3$ kPa, $P_{C_6H_{10}O} = 30$ Pa, $P_{H_2O} = 30$ Pa). These conditions correspond to approximately 1% product yield, observed experimentally at the reactor outlet.³² In reality, the concentration of products varies along the length of the catalyst bed as reactants are converted into products.¹¹⁰ Therefore, the question arises as to whether our calculations shown in Figure 3.13 are directly comparable to the experimental results, which reflect apparent kinetic parameters derived from integrals of rates over the length of the catalyst bed. A related question is whether Pathway B, which requires the co-adsorption of $C_6H_{10}O$, remains the dominant pathway over this length.

To determine the sensitivity of our results to product partial pressure, we computed the kinetics over a wide range of expected product partial pressures along the catalyst bed (1-30 Pa). In Figure 3.14, we plot the kinetic parameters for Mechanism 2 as a function of the partial pressure of products when Facet 1 is equal to 3.76 \AA^2 (representing the majority of sites in Ti/SiO_2) and 3.82 \AA^2 to investigate the impact of facet area. Facet 2 was fixed at 3.75 \AA^2 , so it was always smaller or nearly equal to Facet 1.

Figure 3.14D shows that State $C^{\ddagger 4}$, O-atom transfer to C_6H_{10} via Pathway B, remains the dominant transition state (> 0.5) above ~ 1 Pa, corresponding to approximately 0.033% yield. The reaction orders in the partial pressure of H_2O_2 and C_6H_{10} remain 0th and 1st, respectively, across all product partial pressures (Figure 3.14B and 11C). Interestingly, E_a shows a small dependence at low product partial pressures (Figure 3.14A). The distribution of most-abundant surface intermediates (C4 and C8, mainly, see Figure S3.10) and transition states with non-zero degrees of rate (Figure 3.14D) results in the subtle E_a changes seen in Figure 3.14A. Figure 3.14D also demonstrates that multiple transition states can be kinetically relevant simultaneously, however, only over a small range of conditions near the inlet of the reactor. As the tetrahedral facet area of Facet 1 increases from 3.76 \AA^2 to 3.82 \AA^2 , States $C^{\ddagger 4}$ and C8 become increasingly dominant, resulting in predicted kinetic parameters that are firmly within the experimental values. In summary, Pathway B remains the dominant pathway, even at very low product yields in the reactor. This conclusion becomes stronger for relatively large Facet 1 areas ($> 3.76 \text{ \AA}^2$).

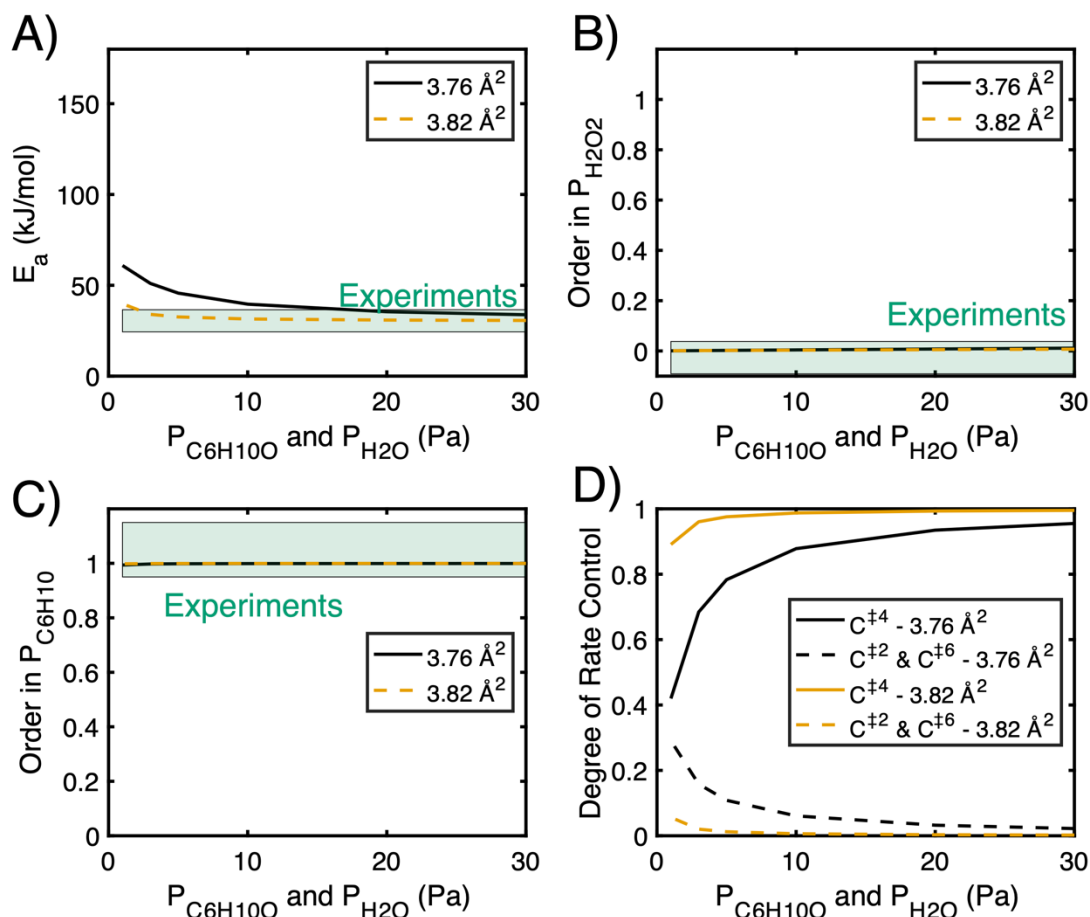


Figure 3.14: A) The apparent activation energy, B) Reaction order in $P_{H_2O_2}$, C) Reaction order in $P_{C_6H_{10}O}$, and D) the degree of rate control for each transition state in Mechanism 2 as a function of the partial pressure of $C_6H_{10}O$ and H_2O_2 . Conditions are $T = 403 \text{ K}$, $P_{H_2O_2} = 3 \text{ kPa}$, and $P_{C_6H_{10}O} = 3 \text{ kPa}$. The Facet 1 area is varied parametrically from 3.76 \AA^2 to 3.82 \AA^2 . The Facet 2 area is equal to 3.75 \AA^2 . Error bars for model calculations were omitted for clarity.

3.5 Conclusions

In this study, we investigated the effects of $\equiv Ti-OH$ site distortion on the properties of the site for the mechanism and kinetics of gas-phase cyclohexene epoxidation with H_2O_2 . We show a general correlation between our descriptor for distortion, the tetrahedral facet area to which polar adsorbates bind, and the value of ΔH_{ads}^o for all reactants and products. We also show that the enthalpies of transition states for H_2O_2 activation and O-atom transfer to cyclohexene are relatively insensitive to facet area. Estimates of the Gibbs free energies of molecular adsorption and activation, based on our calculations of the enthalpies of adsorption and activation together with estimates of the associated entropies, were used to determine the rate coefficients for each step of a mechanism for cyclohexene epoxidation previously proposed in the literature. We then used a microkinetic model to predict the apparent activation energy and reaction orders in the partial pressures of cyclohexene and H_2O_2 . These calculations predict the correct reaction orders but reveal that the apparent activation energy deviates strongly from that observed experimentally for all but the smallest facet areas because of strong product inhibition. Further analysis revealed that

significantly smaller facet areas than those present prior to reaction are required to prevent product inhibition and obtain agreement between theory and experiment.

An alternative mechanistic pathway must therefore be operative. We discovered that when $C_6H_{10}O$ adsorbs to the largest facet, the vacant facets of the same $\equiv Ti-OH$ site contract to a narrow range of facet areas (3.47 - 3.53 \AA^2). These *in-situ* generated, contracted facets become active for epoxidation, while $C_6H_{10}O$ remains bound to the larger facet of the same $\equiv Ti-OH$ site. We predict that all the kinetic parameters for this newly proposed mechanism agree quantitatively with those reported from experiments. We also find that the activity of each $\equiv Ti-OH$ site proceeding by this new mechanism is virtually identical because of the narrow range of *in-situ* generated small-area facets. These new findings demonstrate that the distortion of $\equiv Ti-OH$ sites, caused by the amorphous support and adsorbed species (products, reactants, or spectators), should be considered in analyzing the kinetics of reactions catalyzed by such sites.

3.6 Acknowledgments

This work was supported by the Office of Science, Office of Basic Energy Sciences of the U.S. Department of Energy under Contract No. DE-AC02-05CH11231. Calculations were performed at the Molecular Computing Graphics Facility at UC Berkeley.

3.7 Supporting Information

3.7.1 Gas phase entropy predictions

Table S3.1: Gas phase entropies ($T = 298.15 \text{ K}$, $P^{\circ} = 1 \text{ bar}$) – comparison between qRRHO predictions and literature

Species	$S_{gas,1 \text{ bar}}^{\circ} \left(\frac{\text{J}}{\text{mol}\cdot\text{K}} \right) - \text{Literature}$	$S_{gas,1 \text{ bar}}^{\circ} \left(\frac{\text{J}}{\text{mol}\cdot\text{K}} \right) - \text{qRRHO}$
H ₂ O ₂	232.95 ⁸¹	232.964
C ₆ H ₁₀	310.45 ⁸¹	302.534
H ₂ O	188.835 ⁸¹	188.778
C ₆ H ₁₀ O	-	319.751

3.7.2 Equivalence of $\Delta H_{\text{ads}}^{\circ}$ for cyclohexene oxide to $\equiv\text{Ti-OH}$ and $\equiv\text{Ti-OOH}$ sites

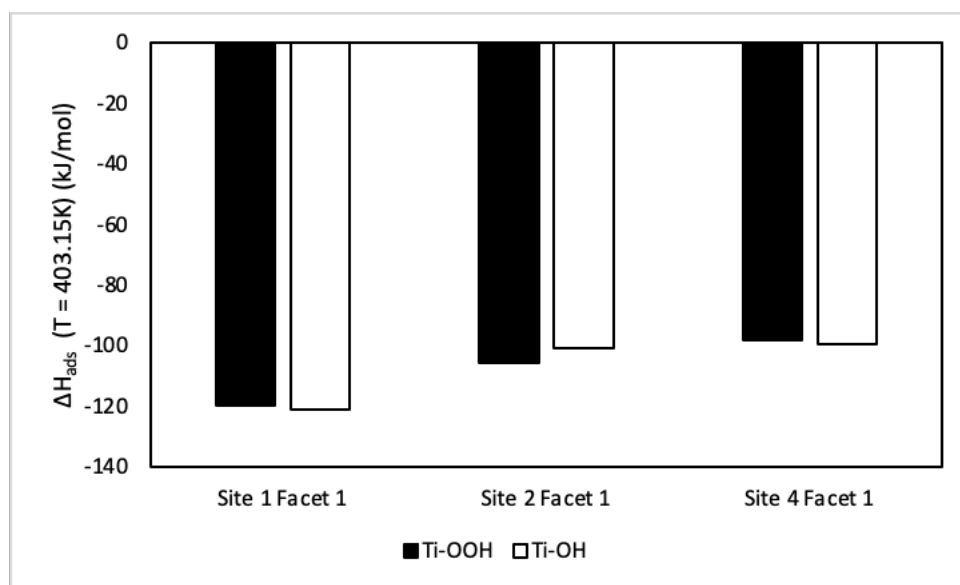


Figure S3.1

3.7.3 Representative optimized geometry of H₂O molecularly bound to Site 1 of our ≡Ti-OH database

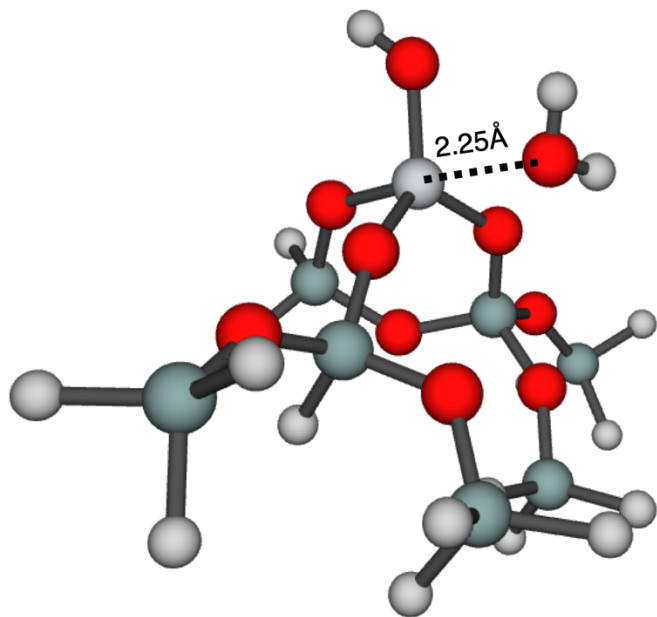


Figure S3.2: Representative optimized geometry of H₂O molecularly bound to Site 1 of our ≡Ti-OH database. Large red spheres: oxygen, large dark grey spheres: silicon, large white spheres: titanium, small white spheres: hydrogen.

3.7.4 Comparison of ΔH_{ads}° of cyclohexene oxide to $\equiv\text{Ti-OH}$ sites with the vector normal to the COC bond parallel or perpendicular to the $\equiv\text{Ti-OH}$ bond

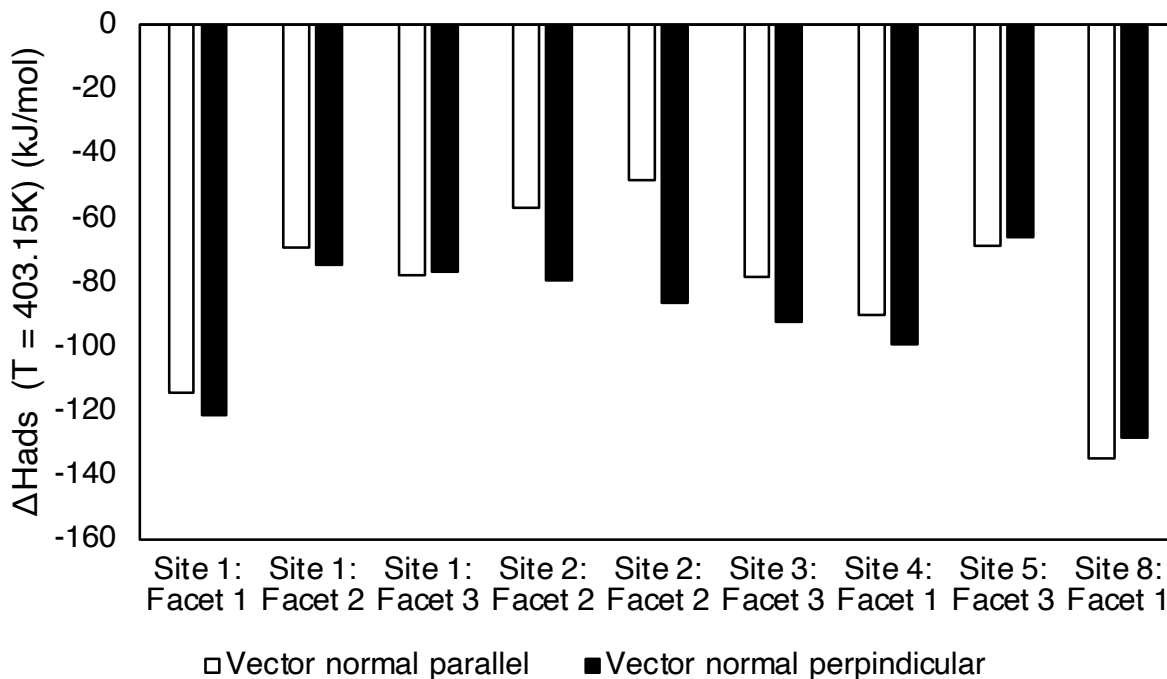


Figure S3.3: Comparison of ΔH_{ads}° of cyclohexene oxide to $\equiv\text{Ti-OH}$ sites with the vector normal to the COC bond parallel or perpendicular to the $\equiv\text{Ti-OH}$ bond.

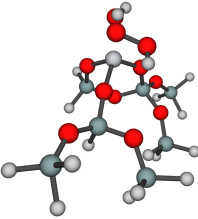
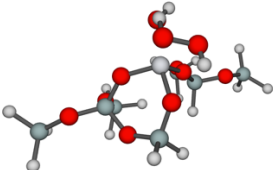
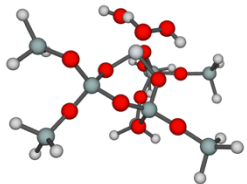
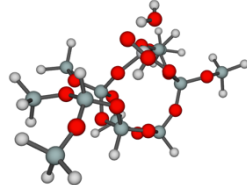
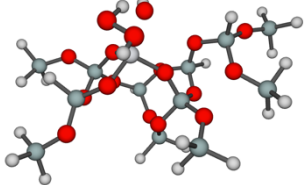
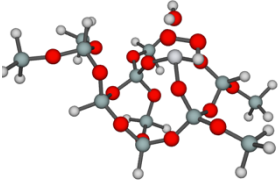
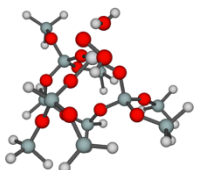
3.7.5 Enthalpies and entropies of $\equiv\text{Ti-OOH}$ formation

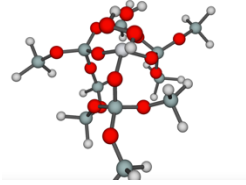
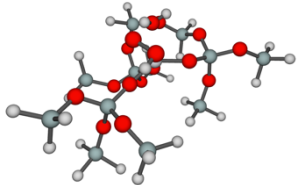
Table S3.2: Enthalpies and entropies of formation of $\equiv\text{Ti-OOH}$ sites + $\text{H}_2\text{O}(\text{g})$ (state C4 in Mechanism 1) from H_2O_2 and $\equiv\text{Ti-OH}$ sites

Site	ΔH_{rxn}° (T = 403.15 K)	ΔS_{rxn}° (T = 403.15 K)
1	-14.10	-38.75
2	-17.43	-41.49
3	-14.44	-37.85
4	-13.32	-36.77
5	-18.73	-34.97
6	-16.52	-14.28
7	-25.36	-21.59

3.7.6 H₂O₂ activation enthalpies and entropies

Table S3.3: Enthalpies and entropies of activation (T = 403.15 K) of ≡Ti-OOH sites + H₂O(g) (state C[‡]₁ in Mechanism 1&2) from H₂O₂ and ≡Ti-OH sites

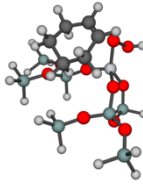
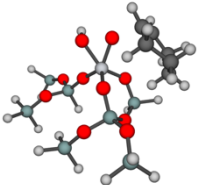
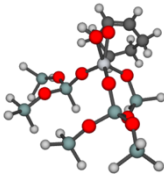
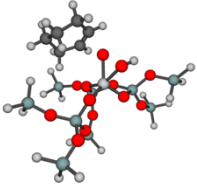
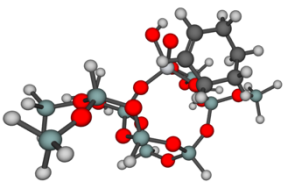
Site	Facet area	Image**	$\Delta H_{C^{\ddagger}1}^o$ (kJ/mol)*	$\Delta S_{C^{\ddagger}1}^o$ (J/molK)*
1 – Facet 1	3.94		-7.79	-203.05
1 – Facet 2	3.61		-10.41	-199.32
1 – Facet 3	3.60	Same as Site 1 -Facet 2		
2 – Facet 2	3.67		-12.55	-201.98
3 – Facet 1	3.77		-14.43	-205.81
3 – Facet 2	3.76		-8.96	-203.90
3 – Facet 3	3.62		-9.78	-198.30
4 – Facet 1	3.79		-10.18	-203.86

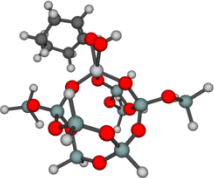
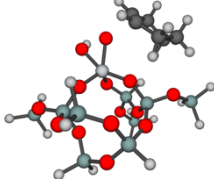
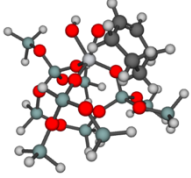
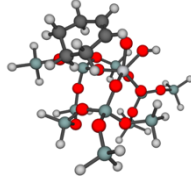
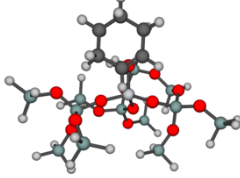
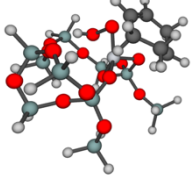
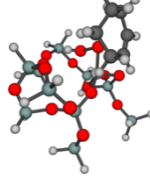
5 – Facet 3	3.51		-7.56	-193.64
7 – Facet 1	4.07		-25.02	-203.22
Average			-12	-201.45
Standard Deviation			5.4	3.75

*Relative to gas-phase H₂O₂ and isolated ≡Ti-OH sites. **Large red spheres: oxygen, large dark grey spheres: silicon, large white spheres: titanium, small white spheres: hydrogen.

3.7.7 O-atom transfer activation enthalpies and entropies

Table S3.4: Enthalpies and entropies of activation (T = 403.15 K) of O-atom transfer to cyclohexene (state C[‡]₂ in Mechanism 1&2) for in-plane geometries

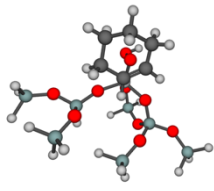
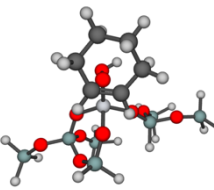
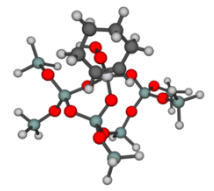
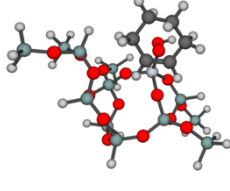
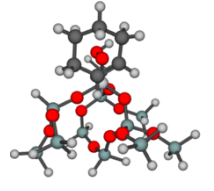
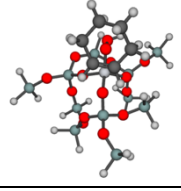
Site – Facet	Facet area	Image**	$\Delta H_{C^{\ddagger}2}^o$ (kJ/mol)*	$\Delta S_{C^{\ddagger}1}^o$ (J/molK)*
1 – Facet 1	3.94		1.27	-242.66
1 – Facet 2	3.61		23.64	-238.49
1 – Facet 3	3.60		23.61	-239.55
2 – Facet 2	3.67		19.47	-243.16
3 – Facet 1	3.77		23.98	-239.26

3 – Facet 2	3.76		11.75	-235.09
3 – Facet 3	3.62		26.90	-233.74
4 – Facet 1	3.79		24.29	-244.57
5 – Facet 3	3.51		19.69	-237.328
6 – Facet 1	3.79		8.07	-224.93
7 – Facet 1	4.07		-14.94	-226.76
7 – Facet 1 – 2 nd geometry	4.07		-11.95	-227.55
Average			-	-236.63
Standard Deviation			-	6.32

*Relative to gas-phase H₂O₂ and isolated ≡Ti-OH sites. **Large red spheres: oxygen, large dark grey spheres: silicon, large white spheres: titanium, small white spheres: hydrogen, large black spheres: carbon.

Table S3.5: Enthalpies and entropies of activation (T = 403.15 K) of O-atom transfer to cyclohexene (state C^{‡2} in Mechanism 1&2) for straddled geometries

Site – Facet	Facet area	Image**	$\Delta H_{C^{\ddagger 2}}^{\circ}$ (kJ/mol)*	$\Delta S_{C^{\ddagger 1}}^{\circ}$ (J/molK)*
--------------	------------	---------	-----------------------------------------------	-----------------------------------------------

1 – Facet 1	3.94		1.55	-233.76
1 – Facet 2	3.61		2.48	-232.47
1 – Facet 3	3.60	Same as Site 1 -Facet 2		
2 – Facet 2	3.67		4.93	-238.46
3 – Facet 1	3.77		2.60	-235.09
3 – Facet 3	3.62	Same as Site 3 -Facet 3		
4 – Facet 1	3.79		2.22	-234.99
5 – Facet 3	3.51		5.35	-226.87
Average			-	-234.09
Standard Deviation			-	3.39

*Relative to gas-phase H₂O₂ and isolated ≡Ti-OH sites **Large red spheres: oxygen, large dark grey spheres: silicon, large white spheres: titanium, small white spheres: hydrogen, large black spheres: carbon.

3.7.8 Effect of tetrahedral facet area on ΔG_{app}^\ddagger for Mechanism 1

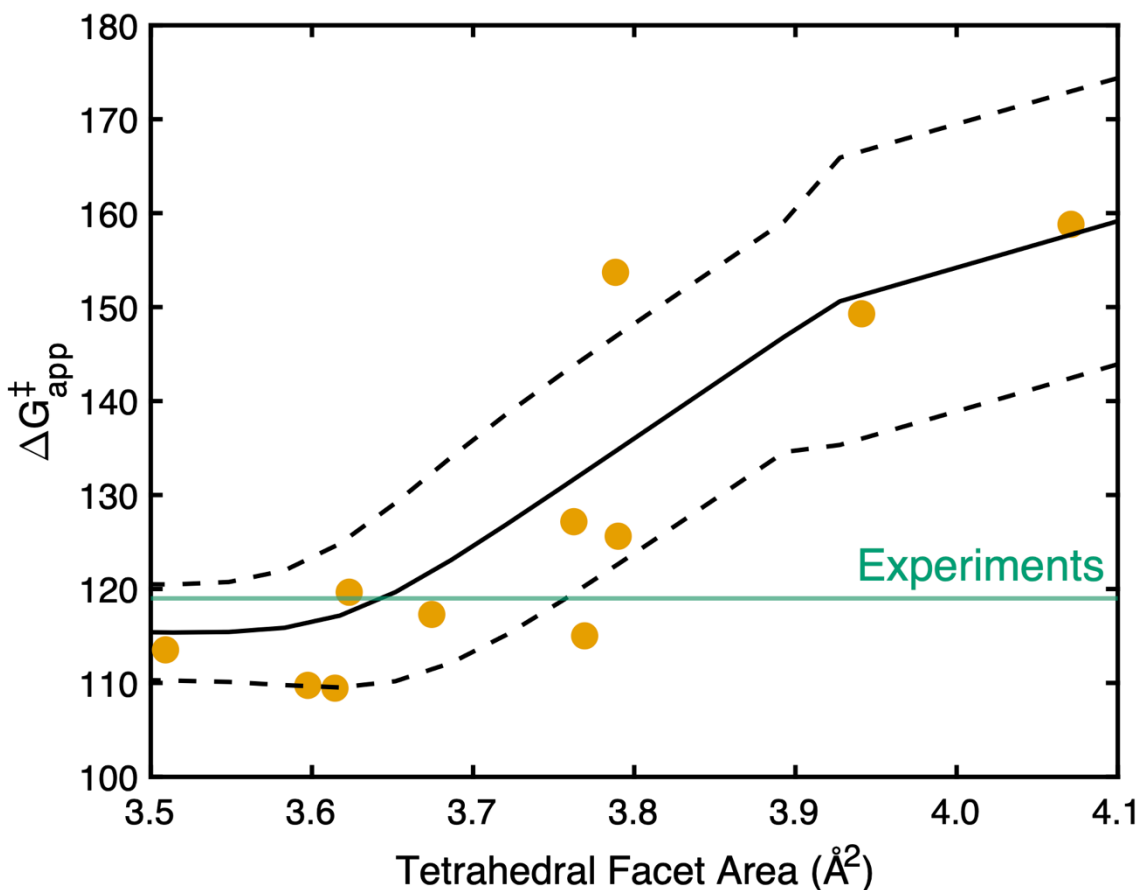


Figure S3.4: Effect of tetrahedral facet area on ΔG_{app}^\ddagger for Mechanism 1. $\Delta G_{app}^\ddagger = \left(\ln(TOF[s^{-1}]) - \ln\left(\frac{k_B T}{h}\right) \right) * -R(403.15 K)$. Conditions are $T = 403.15 K$, $P_{H_2O_2} = 3 kPa$, $P_{C_6H_{10}} = 3 kPa$, $P_{C_6H_{10}O} = 30 Pa$, and $P_{H_2O} = 30 Pa$. The experimental value is shown as a horizontal green line.³² The orange data points utilize DFT-calculated (thermally corrected to 403.15 K) enthalpies from structures specific to each site in our database - in situations where the energy of a state was not calculated for a specific facet, it was estimated from the linear correlations and averages presented in the previous section. The solid lines are the predicted values of the parameter in question for a given facet area calculated only using enthalpies from the linear correlations and averages presented in the previous section. The dashed lines show \pm two times the standard deviation of the parameter in question when the standard errors in the linear correlations presented in Figure 3.3 and the standard deviations in the averages used for transition state enthalpies are propagated.

3.7.9 Effect of tetrahedral facet area on the degree of rate control for Mechanism 1

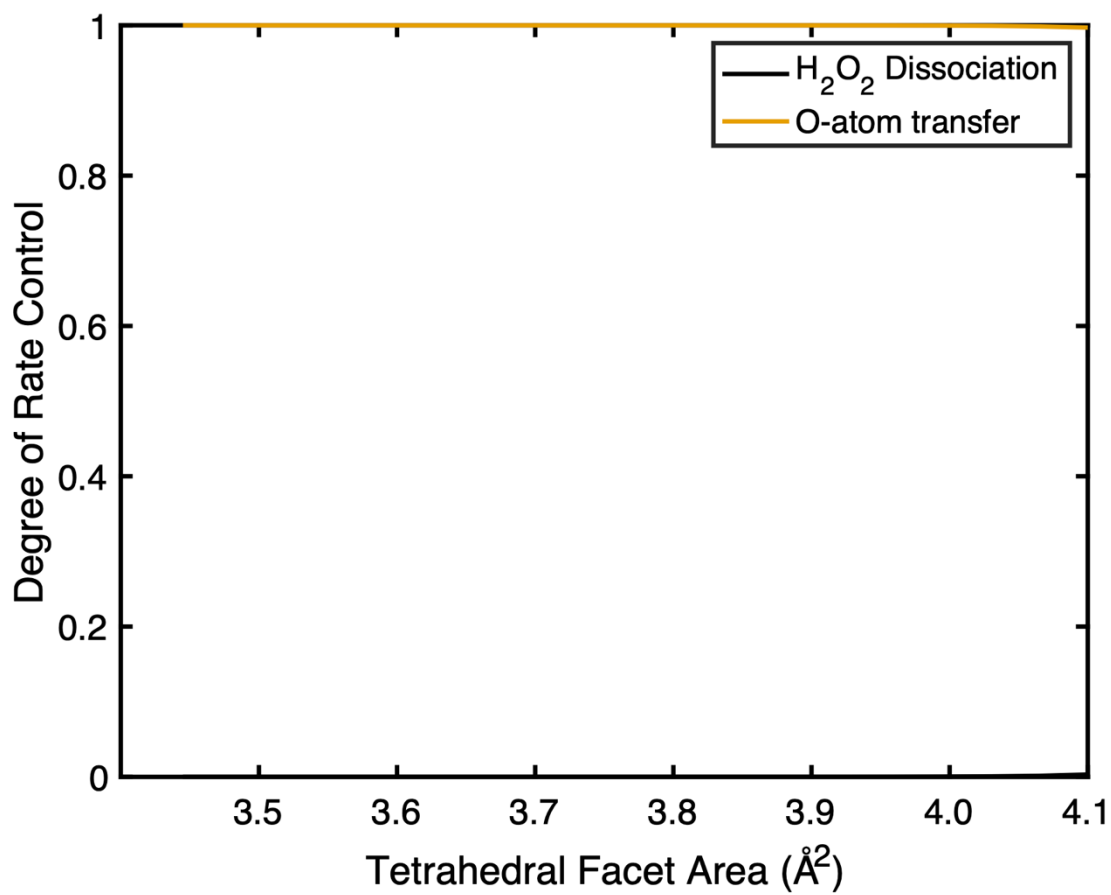


Figure S3.5: Effect of tetrahedral facet area on the degree of rate control for Mechanism 1. Conditions are $T = 403.15$ K, $P_{\text{H}_2\text{O}_2} = 3$ kPa, $P_{\text{C}_6\text{H}_{10}} = 3$ kPa, $P_{\text{C}_6\text{H}_{100}} = 30$ Pa, and $P_{\text{H}_2\text{O}} = 30$ Pa.

3.7.10 Geometries of transition states for Pathway B over Site 1

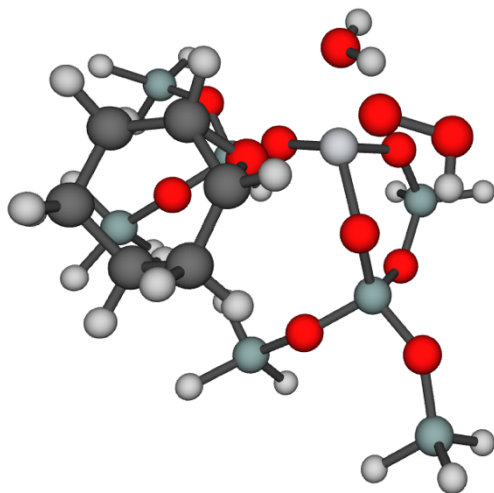


Figure S3.6: Optimized geometry of State C^{‡3}, H₂O₂ dissociation over Facet 2 with C₆H₁₀O co-adsorbed to Facet 1 over Site 1. Large red spheres: oxygen, large dark grey spheres: silicon, large white spheres: titanium, small

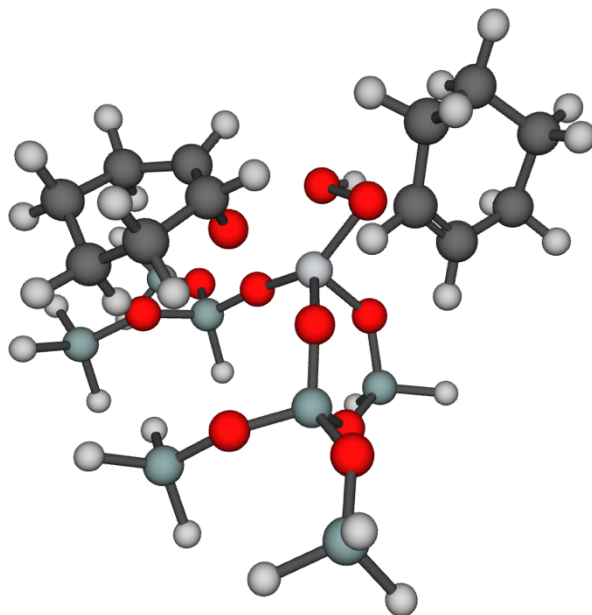


Figure S3.7: Optimized geometry of State C^{‡4}, O-atom transfer to cyclohexene over Facet 2 with C₆H₁₀O co-adsorbed to Facet 1 over Site 1. The C-backbone of cyclohexene is pointed away from the surface and the C=C bond is straddling the Ti-O-Si bond. Large red spheres: oxygen, large dark grey spheres: silicon, large white spheres: titanium, small white spheres: hydrogen, large black spheres: carbon

3.7.11 Matrix representation of the set of differential equations describing the steady-state rates of change of coverages in Mechanism 2

Here, we display the matrix representation of the set of differential equations describing the steady-state rates of change of the coverages of intermediates in Mechanism 2. This was utilized to solve for the steady-state coverages of the intermediates in Figure 3.11.

$$\begin{bmatrix}
 (-k_1 - k_{-6} - k_7 - k_{15} - k_{-20}) & k_{-1} & 0 & 0 & 0 & k_6 & k_{-7} & 0 & 0 & 0 & 0 & 0 & k_{-15} & 0 & 0 & k_{20} \\
 k_1 & (-k_{-1} - k_2) & k_{-2} & 0 & 0 & 0 & 0 & 0 & 0 & 0 & 0 & 0 & 0 & 0 & 0 & 0 \\
 0 & k_2 & (-k_{-2} - k_3) & k_{-3} & 0 & 0 & 0 & 0 & 0 & 0 & 0 & 0 & 0 & 0 & 0 & 0 \\
 0 & 0 & k_3 & (-k_{-3} - k_4 - k_8 - k_{-17} - k_{18}) & k_{-4} & 0 & 0 & k_{-8} & 0 & 0 & 0 & 0 & 0 & k_{17} & k_{-18} & 0 \\
 k_{-6} & 0 & 0 & k_4 & (-k_{-4} - k_5) & k_{-5} & 0 & 0 & 0 & 0 & 0 & 0 & 0 & 0 & 0 & 0 \\
 k_7 & 0 & 0 & 0 & k_5 & (-k_{-5} - k_6 - k_9 - k_{-14}) & 0 & 0 & k_{-9} & 0 & k_{14} & 0 & 0 & 0 & 0 & 0 \\
 0 & 0 & 0 & 0 & 0 & 0 & (-k_{-8} - k_{12} - k_{-11}) & 0 & 0 & k_{11} & k_{-12} & 0 & 0 & 0 & 0 & 0 \\
 0 & 0 & 0 & 0 & 0 & 0 & 0 & 0 & (-k_9 - k_{10}) & k_{-10} & 0 & 0 & 0 & 0 & 0 & 0 \\
 0 & 0 & 0 & 0 & 0 & 0 & 0 & k_{-11} & k_{10} & (-k_{-10} - k_{11}) & 0 & 0 & 0 & 0 & 0 & 0 \\
 0 & 0 & 0 & 0 & 0 & 0 & 0 & 0 & k_{12} & 0 & (-k_{-12} - k_{13}) & k_{-13} & 0 & 0 & 0 & 0 \\
 k_{15} & 0 & 0 & 0 & 0 & k_{-14} & 0 & 0 & 0 & 0 & k_{13} & (-k_{-13} - k_{14}) & 0 & 0 & 0 & 0 \\
 0 & 0 & 0 & 0 & 0 & 0 & 0 & 0 & 0 & 0 & 0 & 0 & (-k_{-15} - k_{16}) & k_{-16} & 0 & 0 \\
 0 & 0 & 0 & k_{-17} & 0 & 0 & 0 & 0 & 0 & 0 & 0 & 0 & k_{16} & (-k_{-16} - k_{17}) & 0 & 0 \\
 0 & 0 & 0 & k_{18} & 0 & 0 & 0 & 0 & 0 & 0 & 0 & 0 & 0 & 0 & (-k_{-18} - k_{19})k_{-19} & 0 \\
 1 & 1 & 1 & 1 & 1 & 1 & 1 & 1 & 1 & 1 & 1 & 1 & 1 & 1 & 1 & 1
 \end{bmatrix}
 \begin{bmatrix}
 \Theta_1 \\
 \Theta_2 \\
 \Theta_3 \\
 \Theta_4 \\
 \Theta_5 \\
 \Theta_6 \\
 \Theta_7 \\
 \Theta_8 \\
 \Theta_9 \\
 \Theta_{10} \\
 \Theta_{11} \\
 \Theta_{12} \\
 \Theta_{13} \\
 \Theta_{14} \\
 \Theta_{15} \\
 \Theta_{16}
 \end{bmatrix}
 =
 \begin{bmatrix}
 0 \\
 0 \\
 0 \\
 0 \\
 0 \\
 0 \\
 0 \\
 0 \\
 0 \\
 0 \\
 0 \\
 0 \\
 0 \\
 0 \\
 0 \\
 1
 \end{bmatrix}$$

The coverage vector is a 16x1 vector containing the steady-state coverages of each intermediate in Mechanism 2. Then, the TOF can be calculated as the sum of the net rates of desorption of cyclohexene oxide:

$$TOF = k_6\Theta_6 - k_{-6}\Theta_1 + k_{14}\Theta_{12} - k_{-14}\Theta_6 + k_{-8}\Theta_8 - k_8\Theta_4 + k_{20}\Theta_{16} - k_{-20}\Theta_1$$

With the TOF in hand, one can vary the temperature and partial pressures to extract apparent activation energies and reaction orders

3.7.12 Effect of tetrahedral facet area on the fractional coverage of relevant intermediates for Mechanism 1 and 2

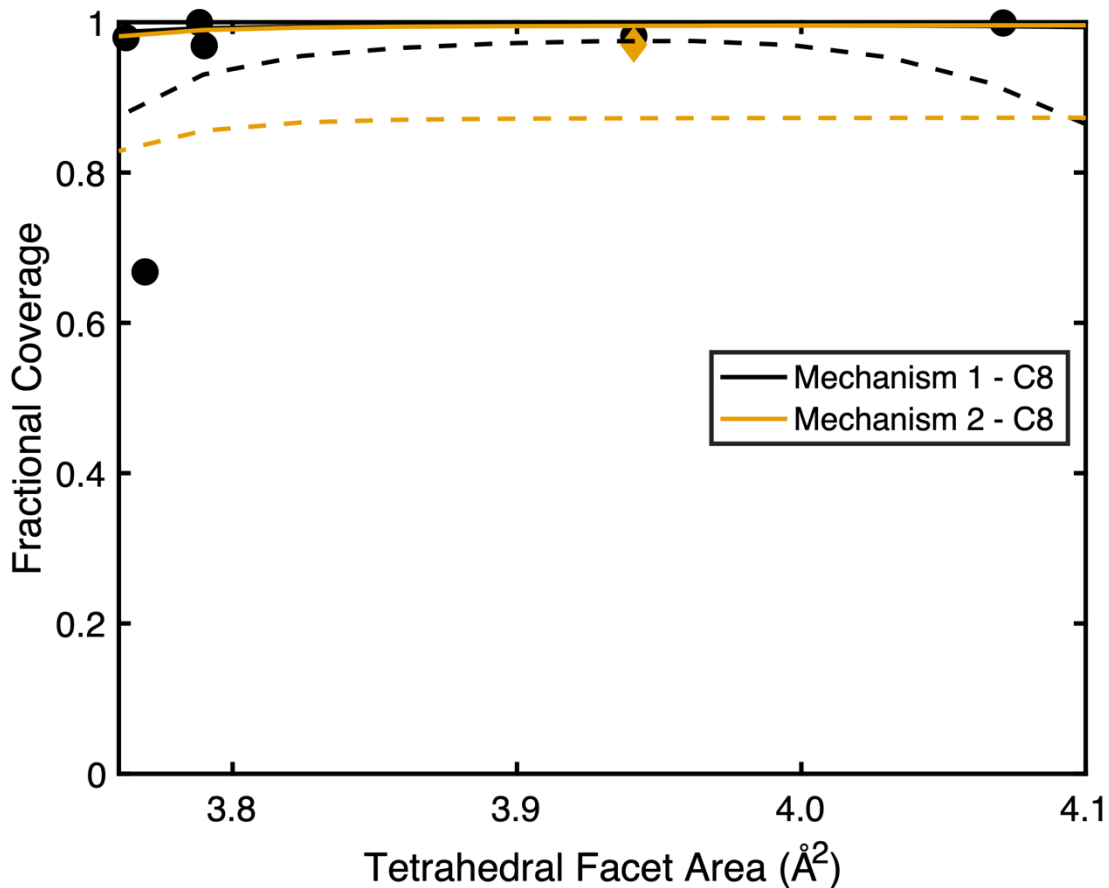


Figure S3.8: Effect of the tetrahedral facet area on the fractional coverage of relevant intermediates for Mechanism 1 and 2. For Mechanism 2, the Facet 1 area is varied with Facet 2 = 3.75 Å². Conditions are T = 403 K, P_{H₂O₂} = 3 kPa, P_{C₆H₁₀} = 3 kPa, P_{C₆H₁₀O} = 30 Pa, P_{H₂O} = 30 Pa. The dashed lines show ± two times the standard deviation of the parameter in question when the standard errors in the linear correlations presented in Figure 3.3 of the main text and the standard deviations in the averages used for transition state enthalpies are propagated.

3.7.13 Effect of tetrahedral facet area on ΔG_{app}^\ddagger for Mechanism 1 and 2

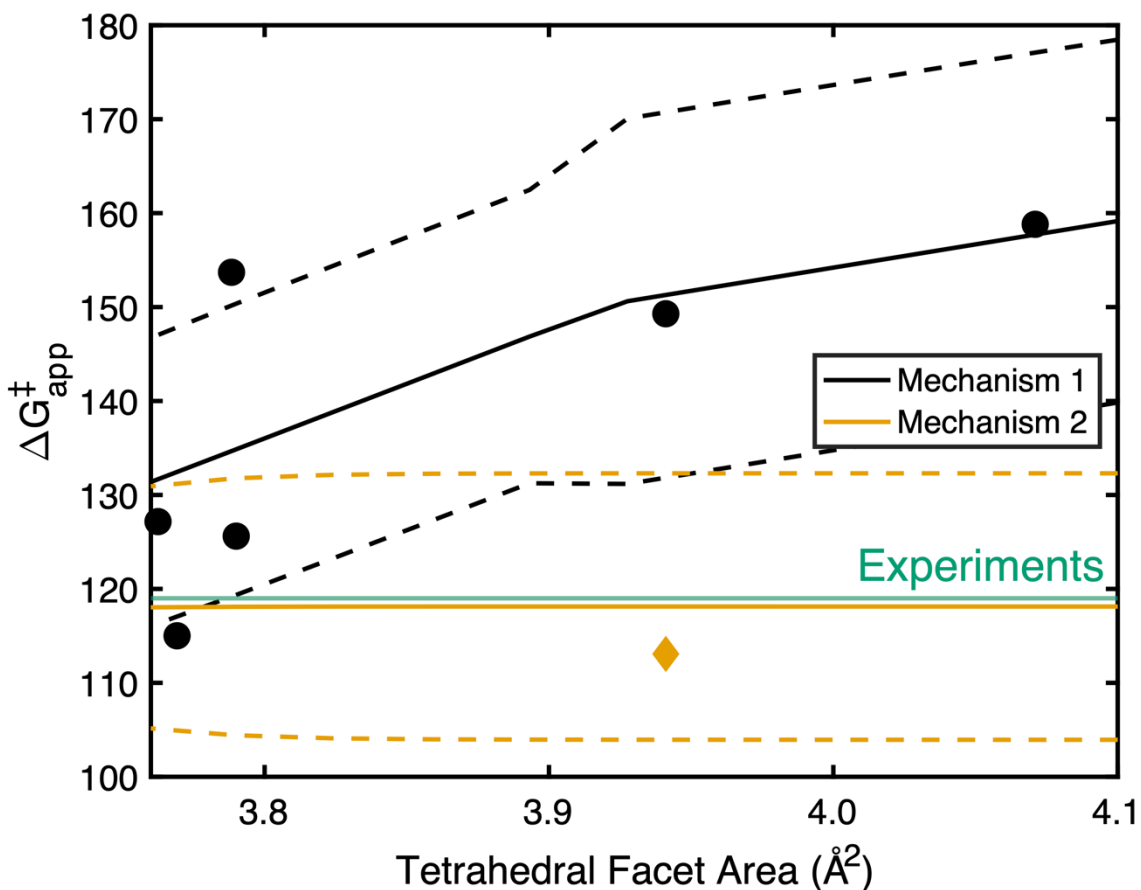


Figure S3.9: Effect of the tetrahedral facet area on ΔG_{app}^\ddagger for Mechanism 1 and 2. For Mechanism 2, the Facet 1 area is varied with Facet 2 = 3.75 \AA^2 . Conditions are T = 403 K, $P_{\text{H}_2\text{O}_2}$ = 3 kPa, $P_{\text{C}_6\text{H}_{10}}$ = 3 kPa, $P_{\text{C}_6\text{H}_{10}\text{O}}$ = 30 Pa, $P_{\text{H}_2\text{O}}$ = 30 Pa. The dashed lines show \pm two times the standard deviation of the parameter in question when the standard errors in the linear correlations presented in Figure 3.3 of the main text and the standard deviations in the averages used for transition state enthalpies are propagated. The experimental value is shown as a horizontal green line.³²

3.7.14 Effect of product partial pressure and facet area on the fractional coverage of kinetically relevant intermediates calculated from the MKM based on Mechanism 2

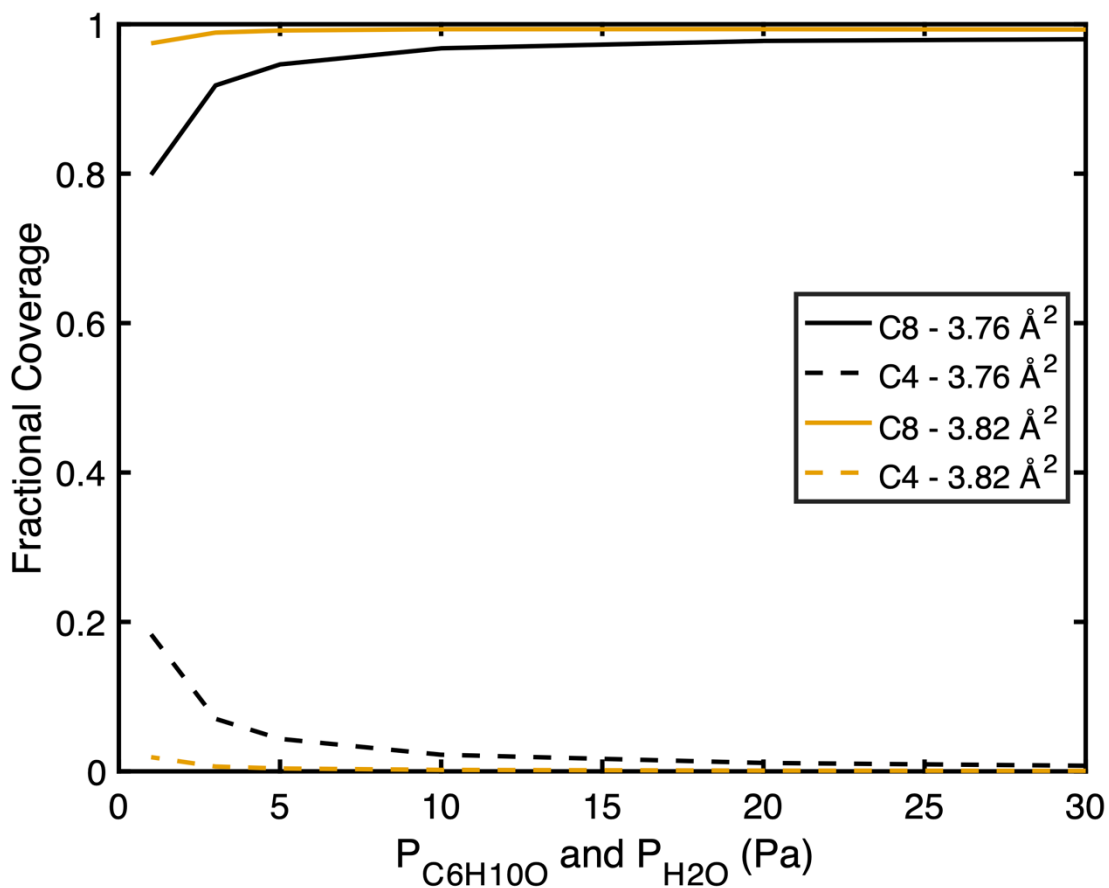


Figure S3.10: Effect of product partial pressure and facet area on the fractional coverage of kinetically relevant intermediates calculated from the MKM based on Mechanism 2. Conditions are $T = 403$ K, $P_{\text{H}_2\text{O}_2} = 3$ kPa, and $P_{\text{C}_6\text{H}_{10}} = 3$ kPa. The Facet 1 area is varied parametrically from 3.76 \AA^2 to 3.82 \AA^2 . The Facet 2 area is equal to 3.75 \AA^2 .

4 Preliminary Experimental and Theoretical Study of Unimolecular Isopropanol Dehydration over Ti/SiO₂

4.1 Introduction

Isolated titanol groups supported on silica ((SiO)₃≡Ti-OH (hereafter referred to as ≡Ti-OH) are known to catalyze a variety of reactions, e.g., amination of alcohols, ammoxidation of ketones, epoxidation of alkenes.^{10,27–35} We have recently shown in Chapter 2 that a small fraction (<15%) of silica-supported ≡Ti-OH sites are heavily distorted. In comparison, the remaining 85% have structures consistent with those derived from analysis of EXAFS data.

In Chapter 3, we explored how ≡Ti-OH site distortion impacts the kinetic predictions of cyclohexene epoxidation, a well-known industrial reaction, catalyzed by such sites. We found that distortion of ≡Ti-OH sites, caused by the amorphous support *and* adsorbed species (products, reactants, or spectators), should be considered in analyzing the kinetics of epoxidation catalyzed by such sites. The question naturally arises as to whether the reported effects of ≡Ti-OH site distortion on epoxidation are general, or if they depend on the reaction being studied.

To address this question, we conducted a preliminary investigation of the kinetics of isopropanol (IPA) dehydration to form propene and water catalyzed by ≡Ti-OH sites. Isopropanol dehydration, shown in Figure 4.1, was selected due to its high selectivity for the unimolecular pathway over metal oxides which greatly simplifies kinetic measurements.^{111,112} In contrast to Chapter 3, for which the epoxidation kinetics were already published, the kinetics of IPA dehydration have not, to the best of our knowledge, been reported over this catalyst. Therefore, we measured the kinetics of IPA dehydration over ≡Ti-OH sites on silica and we report them here.

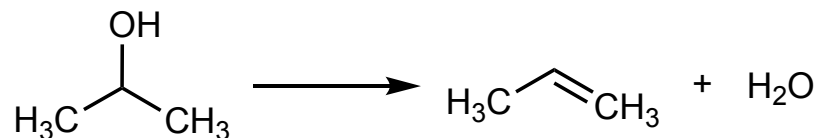


Figure 4.1: Overall stoichiometry for unimolecular dehydration of isopropanol to form propene and water.

The present work reports the kinetics of IPA dehydration over ≡Ti-OH sites, and also preliminary *in-situ* UV/Vis, pre-edge XANES, and FTIR spectroscopy results during reaction conditions. Additionally, we reveal, through the combination of results from pyridine co-feeding *in-situ* FTIR and kinetic experiments, that the active form of Ti sites is a minority species representing less than 6% of Ti sites in the reactor bed. Kinetic isotope effect experiments suggest that the mechanism proceeds through an E2 mechanism with mostly C-H bond-breaking character. Finally, we report a preliminary computational investigation that shows that the majority of ≡Ti-OH sites would form titanium isopropoxides (≡Ti-OiPr) that do not lead to propene formation. We then report additional calculations in an attempt to align the predictions of theory with experimentally measured kinetic parameters.

4.2 Methods

Many of the catalyst preparation methods can be found in detail in Chapter 2.

4.2.1 Silica Preparation

Fumed silica, an amorphous, non-porous material was obtained from Sigma Aldrich (surface area = $395 \text{ m}^2/\text{g} \pm 25 \text{ m}^2/\text{g}$). First, the raw material was dispersed in boiling water (1:1 by volume) for 24 h (with constant stirring), cooled, and filtered. The silica cake was dried in an oven at 353 K under nitrogen overnight to form silica chips. The chips were ground in a mortar and pestle and sieved to a consistent particle size ($250 \text{ }\mu\text{m} < \phi_d < 500 \text{ }\mu\text{m}$). This sample is referred to as **SiO_{2,Hyd}**. To dehydroxylate **SiO_{2,Hyd}**, it was heated in 100 mL/min of Praxair Extra Dry air at 1023 K (3 K/min ramp rate) for 8 h and cooled to room temperature. The resulting material is referred to as **SiO₂₋₁₀₂₃**.

4.2.2 Wet impregnation of SiO₂₋₁₀₂₃ with Cp₂TiCl₂ and calcination to form Ti/SiO₂₋₁₀₂₃

Ti was grafted onto the surface of **SiO₂₋₁₀₂₃** using Cp₂TiCl₂ (Strem Chemicals) as the Ti precursor. This step was conducted under air-free conditions utilizing an N₂ Schlenk line.⁵ At the end of synthesis, the samples were exposed to ambient conditions and immediately calcined in air (Praxair Extra Dry) at 823 K (3 K/min ramp rate) for 8 h producing a bright white powder (**Ti/SiO₂₋₁₀₂₃**). Ti weight loadings were determined by ICP-OES at Galbraith laboratories.

4.2.3 Synthesis of Ti[SiOPh₃]₄

The synthesis of **Ti[SiOPh₃]₄** was carried out following the procedure of Johnson et al. and was presented in detail in Chapter 2.⁵²

4.2.4 Diffuse Reflectance UV/Visible Spectroscopy (UV/Vis)

UV/Vis spectra were acquired using a Thermo Scientific Evolution 3000 UV/Vis spectrophotometer equipped with a Harrick Praying Mantis Diffuse Reflectance accessory. Reference spectra were acquired with BaSO₄ and transformations of percent reflectance to absorbance were calculated with the Kubelka-Munk function. Samples were heated under 100 ml/min of flowing He (Praxair UHP grade) to 673 K (6.25 K/min ramp rate), held at 673 K for 1h, then cooled to the conditions of interest. The UV/Vis spectrum of **SiO₂₋₁₀₂₃** was subtracted from that of **Ti/SiO₂₋₁₀₂₃**. To make a quantitative comparison with the literature, Tauc plots were constructed assuming direct transitions, and the direct edge energy was calculated using a sigmoidal fitting procedure as in previous work.⁵³

4.2.5 X-ray absorption spectroscopy (XAS)

XAS spectra at the Ti K-edge were acquired on beamline 10-BM at the Advanced Photon Source at Argonne National Laboratory. The energy was referenced to Ti foil (4966 eV) taken in transmission mode. Before measurement, **Ti[SiOPh₃]₄** was diluted with boron nitride. The XAS of **Ti/SiO₂₋₁₀₂₃** was acquired in fluorescence mode using a Vortex detector and an in-situ cube cell under flowing He. Multiple spectra were merged to improve the signal-to-noise ratio as much as reasonably possible. Data were collected from 4780 eV to 5767 eV with a step size of 0.1 eV in the pre-edge region. Due to the low loadings of Ti in **Ti/SiO₂₋₁₀₂₃**, the EXAFS region of the XAS

yielded low signal, so only pre-edge data was acquired. All data workup and analysis were conducted using Athena and Artemis software.⁵⁶ After background subtraction, all spectra were normalized to the absorbance in the region 150-400 eV above the edge. Pre-edge features were baseline corrected using an arctan function, as reported previously.⁴⁹ An EXAFS fit for **Ti[SiOPh₃]₄** was performed in the range 1.2-2.2 Å in R-space. Initial guesses for Ti-O scattering paths were calculated from the crystal structures of **Ti[SiOPh₃]₄** using the FEFF6 plug-in within Artemis.^{52,56}

4.2.6 Fourier-Transform Infrared Spectroscopy (FTIR)

Catalyst samples (~30 mg) were pressed into self-supporting pellets and loaded into a stainless-steel sample holder that was then placed in a home-built in-situ transmission IR cell. The cell was connected to heated stainless-steel gas transfer lines. A septum adapter was placed upstream of the cell, allowing for continuous liquid injection (Legato 100 syringe pump) into the heated gas stream. The *in-situ* cell was equipped with a cylindrical heater, and the temperature was measured using a K-type thermocouple (Omega) in direct physical contact with the stainless-steel sample holder. The temperature was controlled using an Omega CS8DPT controller. Spectra were acquired using a Thermo Scientific Nicolet 6700 FTIR spectrometer with a liquid-nitrogen-cooled MCT detector.

All FTIR measurements followed the same sample pretreatment conditions. Samples were heated under 100 ml/min of flowing He (Praxair UHP grade) to 673 K (6.25 K/min ramp rate), held at 673 K for 1h, then cooled to the conditions of interest. All spectra were collected as an average of 64 scans with 1 cm⁻¹ resolution.

4.2.7 Isopropanol Dehydration Catalysis

Reactions were performed in a quartz-tube, packed-bed reactor (10 mm inner diameter) with a glass frit to hold the catalyst in place. The reactor was connected to heated stainless-steel gas transfer lines. A septum adapter was placed upstream of the reactor, allowing for continuous liquid injection (Legato 100 syringe pump) of IPA (Fisher Scientific) and water (Milli-Q) into the heated gas stream. The temperature of the reactor was monitored with a K-type (omega) thermocouple with the tip in physical contact with the glass reactor walls at the same level as the catalyst. The temperature was controlled using an Omega CS8DPT temperature controller. Propene partial pressures in the effluent stream were measured using a calibrated Agilent 6890 gas chromatograph. These partial pressures were converted to propene flow rates and divided by the total moles of Ti in the reactor bed to calculate the Turnover Frequency (TOF). The conversion of IPA to products reported in all kinetics experiments was always less than 2%.

4.2.8 Quantum-Mechanics/Molecular Mechanics (QM/MM) Calculations

The QM/MM approach used for this study is identical to that used in Chapter 2 and is discussed there in detail. Briefly, the surface is divided into a central QM region, comprised of approximately 8-11 tetrahedral (T) atoms, surrounded by a model for the amorphous silica, described by MM, that extends 29 Å in radius from the central Ti atom. The MM region is fixed in space. All geometry optimizations and frequency calculations for all structures were performed with ωB97X-D/def2-SVP.⁵⁷ Single-point energy calculations were performed with ωB97M-

V/def2-TZVP with the SG-3 quadrature grid.^{58,60} Initial guesses for transition state structures were obtained using the Freezing String Method when the optimization of guesses near the expected structure was challenging.¹⁰⁴ All enthalpy corrections at a given temperature used a quasi-rigid rotor harmonic oscillator model with a 100 cm⁻¹ cutoff (qRRHO).^{61,62} For all structures involving ≡Ti-OH sites, QM/MM calculations were performed using the P2 set of MM parameters for the surrounding SiO₂.⁶¹ All computations were performed using the Zeolite package in Q-Chem version 5.⁶⁵

4.2.9 Models for Ti/SiO₂

The Ti/SiO₂ database reported in Chapter 2 was used to select representative ≡Ti-OH site geometries. Briefly, seven ≡Ti-OH site geometries were generated by selecting seven isolated silanol groups (≡Si-OH) present on the surface of a model of amorphous silica.⁶⁷ The Si atom of a ≡Si-OH group was replaced with a Ti atom and then the geometry of the ≡Ti-OH was optimized in the QM region. Images of the optimized geometries of the QM regions, details of their structures, as well as their number labels (i.e., Site 1, Site 2, etc.) can be found in Section 2.3.

4.2.10 Entropy Calculations

Different methods were used to determine gas-phase, adsorbed-phase, and transition-state entropies. Gas-phase entropies were calculated using standard statistical mechanics equations for fixed translational and rotational entropy, with vibrational entropy calculated with the quasi rigid-rotor harmonic-oscillator (qRRHO) approximation.^{61,62}

While previous studies have used the quasi rigid-rotor harmonic-oscillator (qRRHO) approximation to describe the entropy of adsorbed species, this approach has been shown to be inaccurate.⁷⁹ Consequently, we used the empirical model for entropy loss upon adsorption developed by Campbell and Sellers (hereafter denoted as the “Campbell model”), which accurately predicts the entropy for molecular (i.e. non-covalent) adsorption of non-polar and polar molecules on metal oxides, silanol groups of SiO₂, and tetrahedral Sn sites of zeolite BEA (Sn/BEA).^{79,80}

The Campbell model provides a linear relationship between the gas-phase entropy of a species to its adsorbed-phase entropy via equation (1).

$$S_{ads,X}^o(T) = S_X^o(T) * 0.7 + 3.3R \quad (1)$$

Here, R is the ideal gas constant, S_X^o is the gas-phase entropy of X, and $S_{ads,X}^o$ is its adsorbed-phase entropy. We employ this expression to determine the entropies of all molecularly adsorbed states. When covalent interactions are involved, such as for ≡Ti-OiPr sites, and for all transition states, we adopt the qRRHO model to estimate the entropy of these species.

4.3 Results and Discussion

4.3.1 Diffuse Reflectance UV/Vis spectroscopy

UV/Vis spectra were acquired to investigate the local coordination of $\equiv\text{Ti-OH}$ sites under ambient, dehydrated, and reaction conditions, as shown in Figure 1A. Under ambient conditions, the UV/Vis spectrum displays a broad peak centered at 222 nm. This peak corresponds to ligand-to-metal charge transfer (LMCT) transitions of isolated, tetrahedral Ti sites.⁸⁴ This spectrum was used to construct a direct-transition Tauc plot, from which the band-edge energy was calculated. The band-edge energy for ambient $\text{Ti/SiO}_2\text{-1023}$ was 4.46 eV. Dehydration of the sample increases the intensity at low wavelengths and blue-shifts the corresponding band-edge energy from 4.46 eV to 4.84 eV. This effect has been observed previously and is known to result from the desorption of adsorbates from the metal centers of $\equiv\text{Ti-OH}$ sites.⁴ The value for the band-edge energy for dehydrated $\text{Ti/SiO}_2\text{-1023}$ is in good agreement with those previously reported for $\text{Ti/SiO}_2\text{-1023}$ samples containing very low loadings of Ti (Chapter 2).

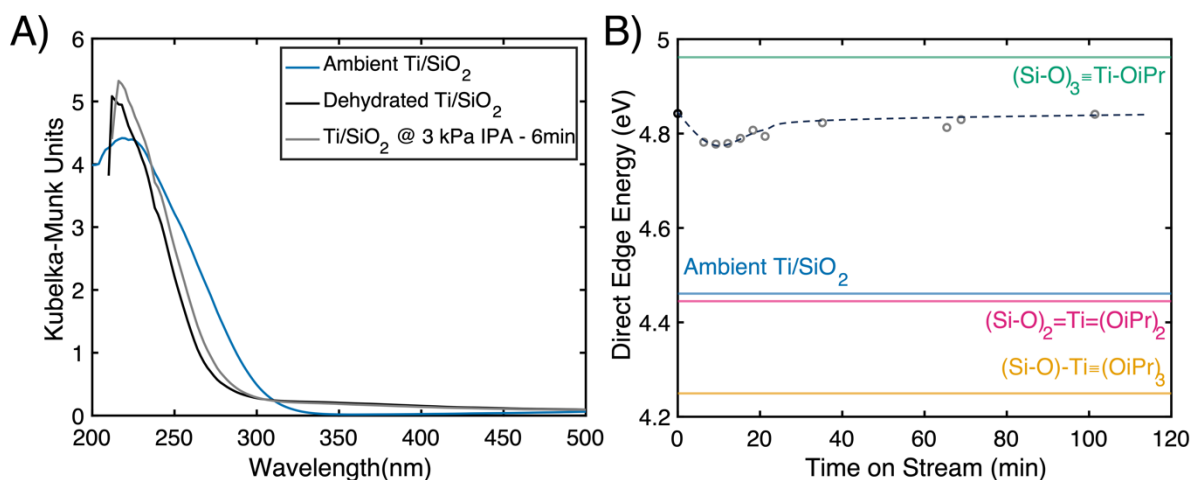


Figure 4.2: A) Diffuse-Reflectance UV/Vis spectra of $\text{Ti/SiO}_2\text{-1023}$ under ambient (300 K, 100 mL/min He), dehydrated ($T = 553.15$ K, He, sample was pre-treated at 673 K for 1 h under flowing He) and reaction conditions ($T = 553.15$ K, 3 kPa IPA/He). B) Direct band-edge energies determined from Tauc plots for $\text{Ti/SiO}_2\text{-1023}$ (open circles) under dehydrated conditions ($t = 0$ min), and under 3 kPa IPA/He as a function of time. Also shown is the band-edge energy determined for $\text{Ti/SiO}_2\text{-1023}$ at ambient conditions (blue line), and the edge energies of various Ti isopropoxide silsesquioxane structures taken from ref.¹¹³ The dashed line is a guide for the eye.

Under reaction conditions ($P_{\text{IPA}} = 3$ kPa), subtle changes are observed in the UV-Vis spectrum, as shown in the gray spectrum of Figure 1A. Figure 1B shows how the band-edge energy changes under exposure to IPA over time. Initially, the band-edge energy sharply decreases from 4.84 eV to 4.78 eV, consistent with the coordination of adsorbates to Ti sites.⁴ Over 1 hour, the band-edge energy slowly returns to the value observed under dehydrated conditions, 4.84 eV. The reported band-edge energy for a titanium monoisopropoxide ($\equiv\text{Ti-OiPr}$) grafted to the corner of a silsesquioxane is similar to the value for our catalyst after exposure to IPA.¹¹³ Given that the band-edge energies for titanium diisopropoxides and triisopropoxides are much lower than the value for our sample, we can rule out their presence.

4.3.2 Ti K-edge XAS in the pre-edge region

We also acquired Ti K-edge XAS spectra in the pre-edge region to complement the findings from our UV/Vis measurements. We note that these spectra were acquired for a different batch of $\text{Ti/SiO}_2\text{-1023}$. However, the same experimental procedure was used to prepare this batch of $\text{Ti/SiO}_2\text{-1023}$, and it exhibits a nearly identical Ti loading and UV/Vis spectrum (which is shown in Figure 2.9 of this thesis).

The pre-edge XAS peak corresponds to $1s \rightarrow 3d$ electronic transitions that become dipole-allowed due to $3d/4p$ mixing as a result of tetrahedral geometry.⁸⁵ Deviations from perfect tetrahedral geometry ($\angle\text{O-Ti-O} \neq 109.5^\circ$) caused by the coordination of adsorbates or due to tetrahedral distortion caused by the silica support will decrease the intensity of and red-shift this peak.¹¹ Figure 4.3 shows that when $\text{Ti/SiO}_2\text{-1023}$ is dehydrated under He at 673 K followed by cooling to 553 K, the pre-edge peak increases intensity two-fold and blue-shifts by 0.3 eV. These changes are consistent with the desorption of water, a phenomenon also supported previously by our UV/Vis measurements. Even after the desorption of water, the feature for dehydrated $\text{Ti/SiO}_2\text{-1023}$ remains weaker in intensity than the feature measured for a material known to contain tetrahedral Ti centers, $\text{Ti}[\text{OSiPh}_3]_4$ (which we confirmed from EXAFS fitting in Chapter 2). This difference was attributed to the fact that a small fraction ($>15\%$) of Ti centers exist as distorted tetrahedra, which contribute only weakly to the pre-edge peak.

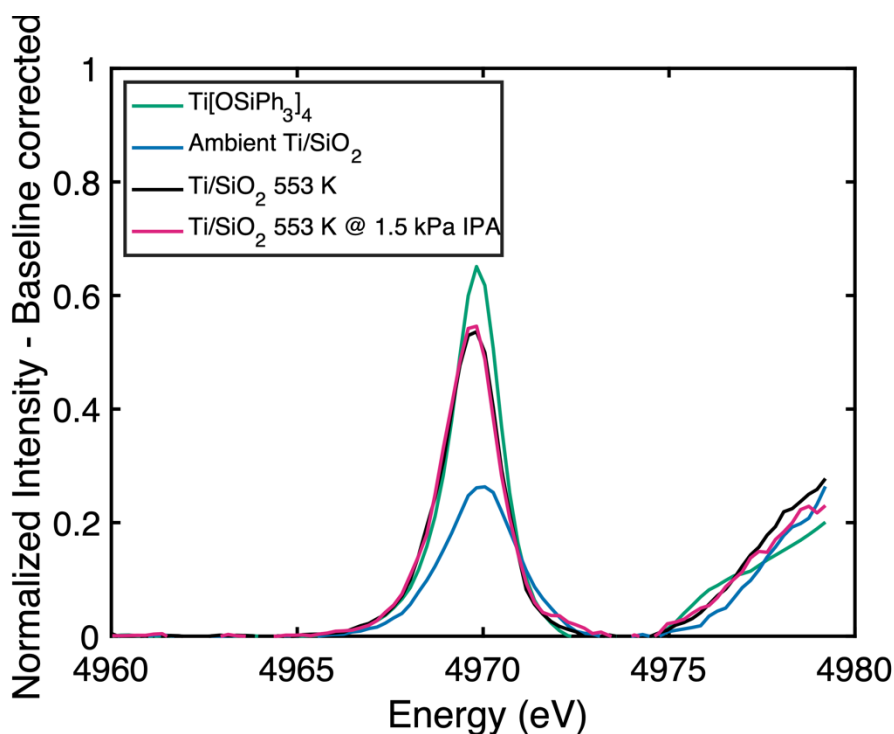


Figure 4.3: Pre-edge XANES spectra of $\text{Ti/SiO}_2\text{-1023}$ at ambient ($T = 300$ K, He), dehydrated (spectra recorded at $T = 553.15$ K, He). The sample was pre-treated at 673 K for 1 h under flowing He before cooling to 553.15 K), and under 1.5 kPa of IPA/He. The pre-edge spectra for $\text{Ti}[\text{OSiPh}_3]_4$, a Ti tetrahedral standard, was previously measured in ref. X is reproduced above (green line).

The pre-edge feature was then measured after 1 h of exposure to a flowing stream of IPA (1.5 kPa)/He. Remarkably, very few changes were observed in the spectrum. This indicates that

most Ti centers in **Ti/SiO₂₋₁₀₂₃** do not coordinate IPA directly to the metal center at these conditions. These spectra are consistent with either, 1) unaffected $\equiv\text{Ti-OH}$ sites, or 2) the formation of $\equiv\text{Ti-OiPr}$ species since these both exhibit tetrahedral geometry. We will show later that theoretical calculations strongly support the formation of $\equiv\text{Ti-OiPr}$ over $\equiv\text{Ti-OH}$ sites at these conditions.

4.3.3 *In-situ* FTIR of SiO₂₋₁₀₂₃ and Ti/SiO₂₋₁₀₂₃

We utilized *in-situ* FTIR to monitor the presence of adsorbed intermediates during IPA dehydration. Figure 4.4 shows the FTIR spectra of **Ti/SiO₂₋₁₀₂₃**, and the SiO₂ support (**SiO₂₋₁₀₂₃**), after 1 h of exposure to 3 kPa of IPA/He at 553 K in the C-H stretching region. Characteristic C-H stretching peaks corresponding to adsorbed alkanols can be observed on both samples in the region of 2800-3050 cm⁻¹.¹¹⁴ These peaks grow very rapidly at early times on stream and continue to grow at a slower rate at longer times. These peaks persist when the system is purged with He, indicating the formation of covalently bound isopropoxides. We note that a subtle 1 cm⁻¹ redshift is observed in going from **SiO₂₋₁₀₂₃** to **Ti/SiO₂₋₁₀₂₃** for the peaks centered at 2981 and 2940 cm⁻¹, potentially evidencing a different form of adsorbed IPA due to the presence of Ti in the sample. FTIR spectra of IPA adsorbed on single-facet dominant TiO₂ crystals have been measured, and their peaks occur at 2973 and 2936 cm⁻¹.¹¹⁵ If we assume that similar peaks would be formed in the formation of $\equiv\text{Ti-OiPr}$ sites, this would be consistent with the redshift we have observed. Unfortunately, the peaks in Figure 4.4 for both materials appear similar, so we are unable to identify a clear peak corresponding to $\equiv\text{Ti-OiPr}$.

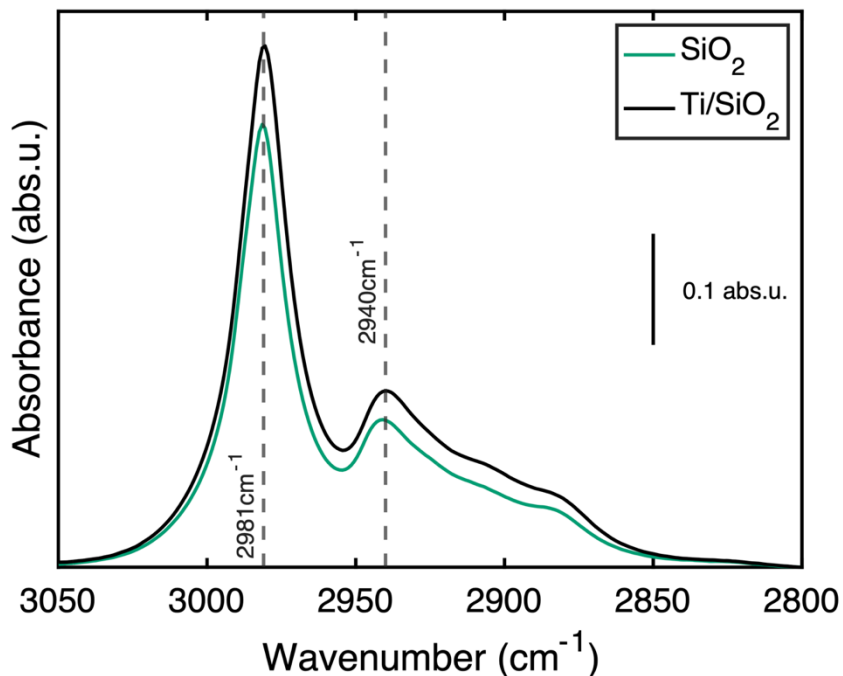


Figure 4.4: In-situ FTIR spectra of **Ti/SiO₂₋₁₀₂₃** and **SiO₂₋₁₀₂₃** under 3 kPa IPA/He taken after 1 h. T = 553.15 K. Both spectra were baseline-subtracted.

4.3.4 IPA Dehydration Kinetics

Figure 4.5A shows the observed TOF for the formation of propene as a function of time on stream over **Ti/SiO₂-1023**. No propene was produced when the reactor was charged with the SiO₂ support at the same mass, indicating Ti is required for dehydration catalysis. Deactivation of the catalyst is initially severe but attenuates over time. This deactivation is thought to be caused by the formation of titanium isopropoxides, which are intermediates that do not lead to IPA dehydration (see later in QM/MM calculations).

To account for deactivation, we fit an expression to the full range of data collected at 553 K, as shown in the inset of Figure 4.5A. This deactivation expression fits the data satisfactorily. Our deactivation model predicts that the TOF at $t > 1000$ min is about 20% of its value at $t = 0$ minutes. We can then use our model to subtract the effects of deactivation from all our data, as shown in Figure 4.5B. Since we still observe some deactivation for the high-temperature data in Figure 4.5B ($T = 568$ K), the deactivation is mildly dependent on the temperature.

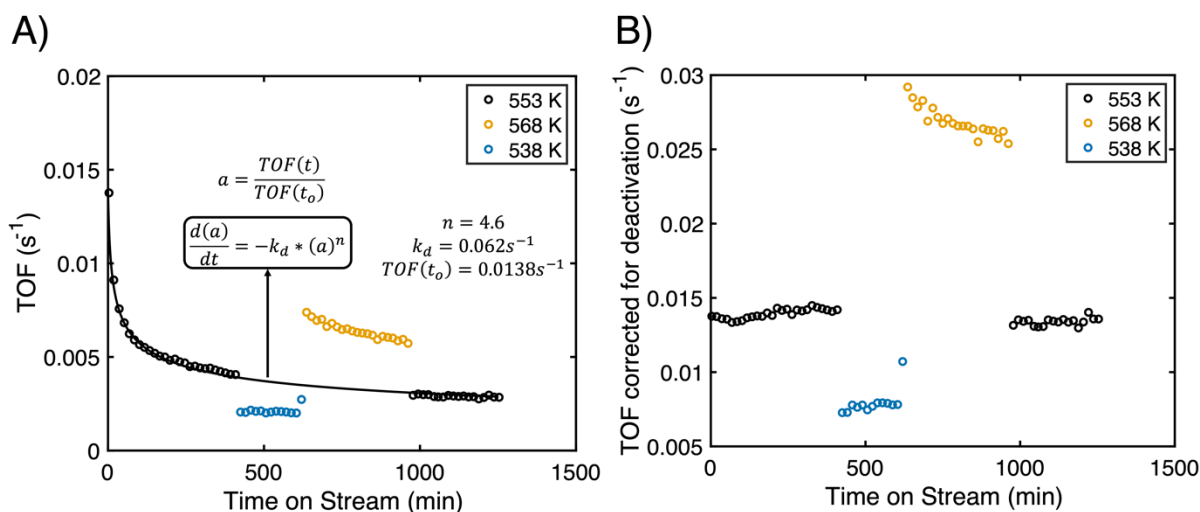


Figure 4.5: A) IPA dehydration activity over **Ti/SiO₂-1023** as a function of time on stream (mass = 25 mg, $P_{IPA} = 3$ kPa, total flow = 51 mL/min). The inset shows the deactivation equation and fit parameters that give the best fit (in a least-squares sense) B) Deactivation subtracted IPA dehydration activity as a function of time on stream.

We can use the deactivation-corrected average TOF measurements at the three temperatures to construct an Arrhenius plot, as shown in Figure 4.6A. The apparent activation energy (E_a) is 103.3 ± 15 ($\pm 2\sigma$) kJ/mol. If we had used either the early or late time data point for $T = 568$ K when constructing our Arrhenius plot, we would have obtained activation energies of 112 kJ/mol and 100 kJ/mol, respectively. These values suggest that the deactivation process is not significantly altering our calculated activation energy, so we maintain that the E_a is 103.3 ± 15 ($\pm 2\sigma$) kJ/mol. Figure 4.6B shows the dependence of the TOF on the partial pressures of IPA and water, respectively. The data shown in Figure 4.6B was measured just after the data presented in Figure 4.5A and Figure 4.5B, during the same experiment.

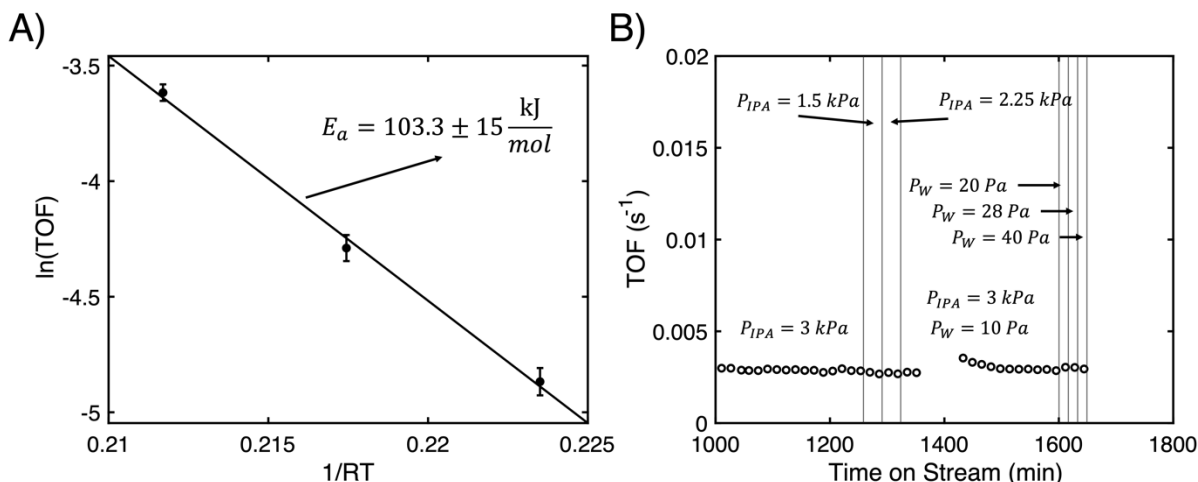


Figure 4.6: A) Arrhenius plot of the average TOF value for each temperature derived from the data in Figure 4B. B) Effect of IPA and water partial pressures on the TOF over $\text{Ti/SiO}_2\text{-1023}$. We note the TOF was not corrected for deactivation.

The TOF is insensitive to the partial pressures of IPA and water (P_{IPA} and P_{W} , resp.) for partial pressures range from 1.5-3 kPa and 10-40 Pa, respectively, as shown in Figure 4.6B. This indicates that the TOF is 0th-order in the partial pressures of both species at these conditions.

Also, the negligible impact of P_{W} on the TOF, and under the assumption that the partial pressure of propene has a negligible impact on the TOF, indicates that the TOF is constant over the reactor bed. A rate expression consistent with all the above kinetic observations is, simply:

$$TOF = k_{int} \quad (2)$$

Where k_{int} is a 0th-order rate coefficient with an activation energy of $103.3 \pm 15 \text{ kJ/mol}$.

To investigate whether the rate-limiting step involves the cleavage of O-H or C-H bonds, we conducted the reaction with perdeuterated IPA, as shown in Figure 4.7. As was seen for perhydrogenated IPA, a steep deactivation period is also observed at early times on stream. We fit the same deactivation expression to this phenomenon to estimate the deactivation-corrected TOF at later times on stream. We then switched the feed from 3 kPa of perdeuterated IPA to 3 kPa of perhydrogenated IPA (Figure 4.7A) and observed an increase in activity. Using our deactivation expression to estimate the future time perdeuterated TOF, we compared this to the perhydrogenated TOF as a function of time on steam, as shown in Figure 4.7B. Across 1000 min, the ratio of the TOF for perhydrogenated IPA dehydration to perdeuterated IPA dehydration was ~ 2.3 . If we assume that the 0th order dependence in the partial pressure of IPA holds true for perdeuterated IPA, then this TOF ratio reflects the ratio of their respective 0th order rate coefficients. The observation of a KIE > 1 strongly suggests that the cleavage of a C-H or O-H bond is involved in the kinetically relevant step for IPA dehydration over $\text{Ti/SiO}_2\text{-1023}$. This KIE is higher than the KIE observed for IPA dehydration over single-facet dominant TiO_2 crystals at similar temperatures (1.4, $T = 533 \text{ K}$, $\sim 0^{\text{th}}$ order in P_{IPA}) suggesting that the transition state for IPA dehydration reported here more closely resembles a C-H or O-H bend-cleavage step.¹¹⁵

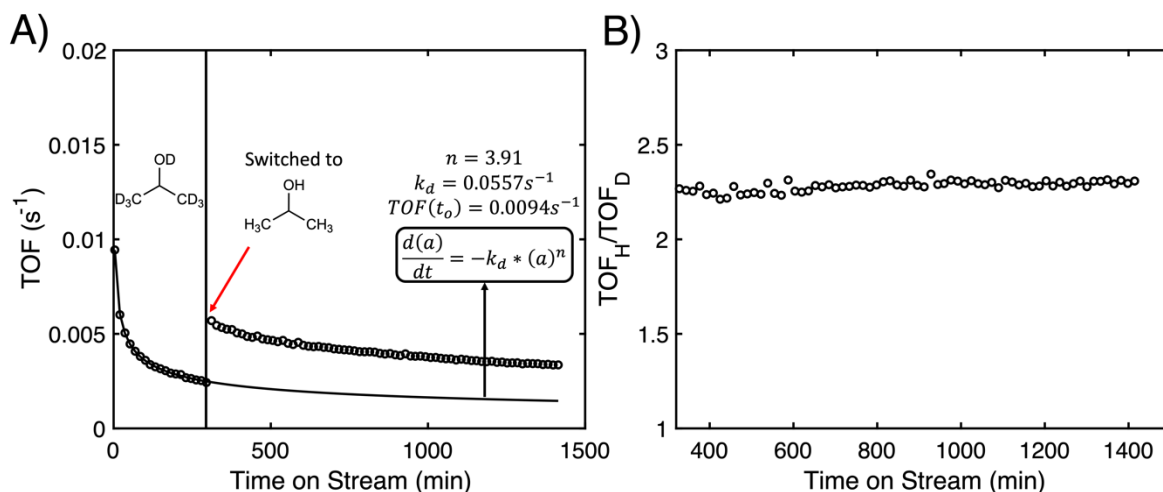


Figure 4.7: A) IPA dehydration activity over $\text{Ti/SiO}_2\text{-1023}$ as a function of time on stream (mass = 25 mg, $P_{\text{d-IPA}} = 3$ kPa, total flow = 51 mL/min) using perdeuterated IPA initially, followed by switching to perhydrogenated IPA ($P_{\text{IPA}} = 3$ kPa). The inset shows the deactivation equation and fit parameters that give the best fit (in a least-squares sense) to the perdeuterated TOF data before switching to perhydrogenated IPA B) Ratio of the TOF measured using perhydrogenated IPA to the deactivation model extrapolated TOF fit to the TOF data collected with perdeuterated IPA at early times on stream.

To interpret the magnitude of this KIE, we calculated the maximum non-tunneling (semi-classical) kinetic isotope effect when breaking C-H and O-H bonds, which yields values of 2.7 and 3.03, respectively.¹¹⁶ For the KIE for the cleavage of a C-H bond, this calculation assumes that the vibrational frequencies of C-H and C-D stretches are 2900 and 2150 cm^{-1} , respectively, and that the KIE is controlled by the difference in the zero-point energy of these bonds in the reactant state (before cleavage).¹¹⁶ Let us assume that the observed KIE is due to a rate-limiting C-H bond cleavage, rather than an O-H bond cleavage because previous work has shown that the deuteration of the OH group does not influence the kinetics for unimolecular dehydration over alumina or titania.^{115,117} If this is true for the $\text{Ti/SiO}_2\text{-1023}$ system, then the KIE we have observed is 85% of the maximum (2.3/2.7). To interpret this percentage, we remind ourselves that the mechanism of unimolecular alkanol dehydration is known to proceed through one of four general mechanisms: E1, E1_{cb,irr}, E1_{cb,rev}, and E2 as shown in Figure 4.8.¹¹⁸ We note that the kinetically relevant transition state for each mechanism is different. As one goes from E1 and E1_{cb,rev} \rightarrow E2 \rightarrow E1_{cb,irr}, the kinetically relevant transition state becomes more characteristic of a C-H bond-breaking step, and less like a C-O bond-breaking step. For any real process, the true transition state sits on a continuum between these extremes.¹¹⁸ On the E1 and E1_{cb,rev} extreme, the slow step involves the cleavage of a C-O bond. This would imply a KIE near 1, which is not observed for IPA dehydration over $\text{Ti/SiO}_2\text{-1023}$, so we rule out these mechanisms. If the mechanism follows E1_{cb,irr}, then the KIE is expected to be near the maximum, which is 2.7 at these conditions.¹¹⁶ An E2-type mechanism should exhibit a KIE between 1 and 2.7 - we observed a value of 2.3. Therefore, we propose that dehydration of IPA over $\text{Ti/SiO}_2\text{-1023}$ occurs through an E2 transition state with a higher degree of C-H bond-breaking character compared to C-O bond-breaking character.

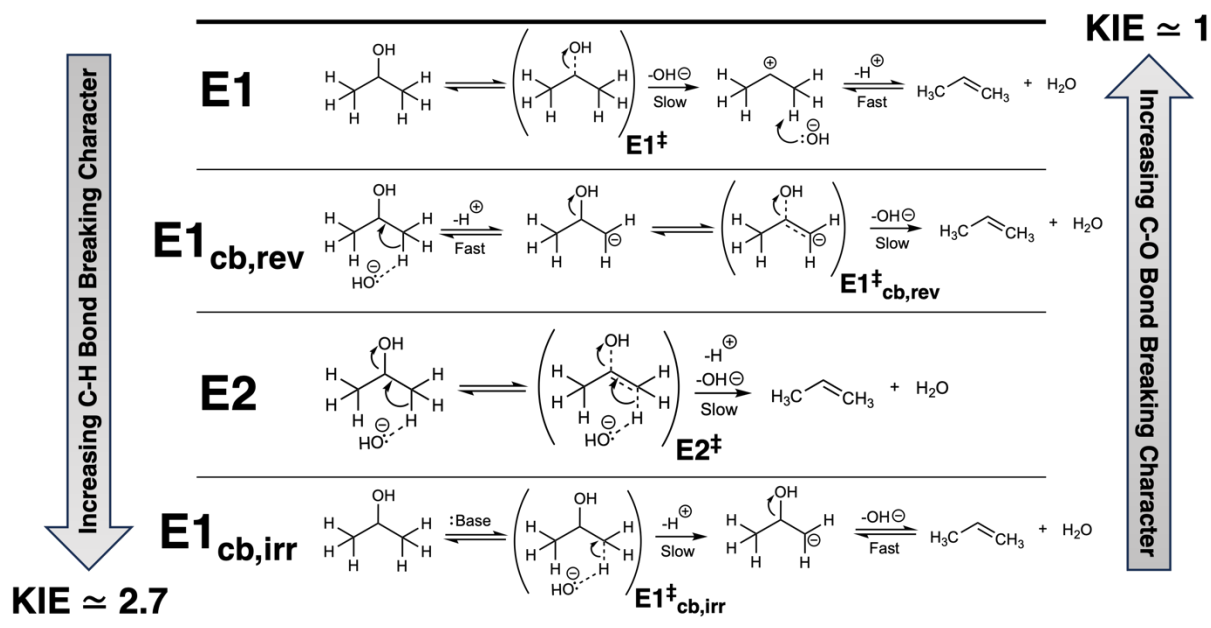


Figure 4.8: Illustration of the continuum of possible dehydration mechanisms and their expected KIEs for $T = 553.15$ K.^{116,118}

To estimate the fraction of Ti sites that participate in the reaction, we combined the results of kinetic and *in-situ* FTIR measurements when the catalyst is exposed to pyridine. Figure 4.9A and Figure 4.9B show how the TOF is influenced by the presence of pyridine at different partial pressures.

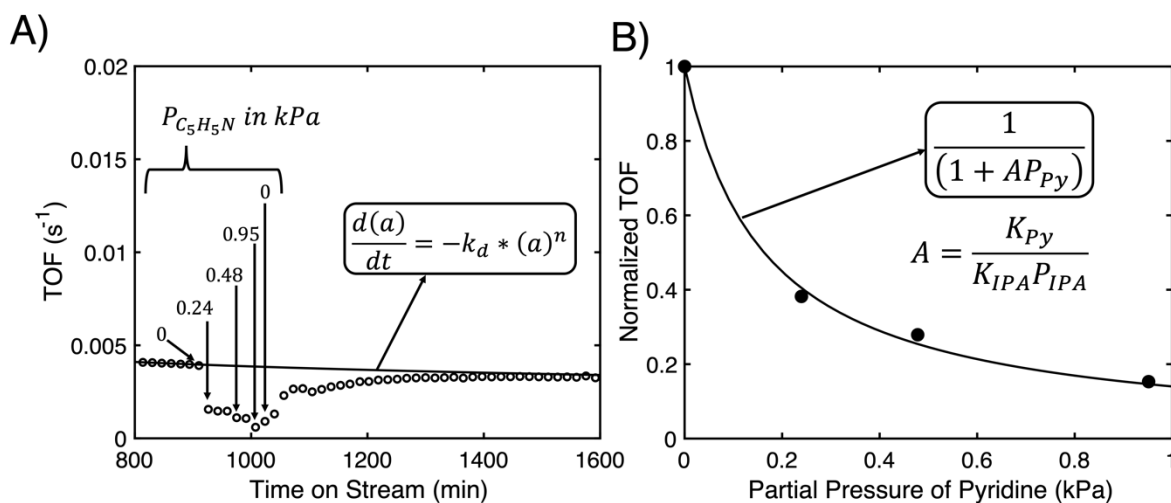


Figure 4.9: A) The effect of pyridine cofeeding at multiple partial pressures as a function of time on stream ($T = 553.15$ K). The TOF values were not deactivation subtracted. The deactivation function is shown as a solid line. B) Normalized TOF as a function of the partial pressure of pyridine. The TOF values were normalized to the initial TOF just before pyridine injection. For pyridine partial pressures in which multiple TOF values were collected, the average was used. The line shows the fit function in the inset.

Introducing 0.24 kPa of pyridine reduces the normalized activity (normalized to the TOF prior to pyridine injection) to 0.39. In other words, the TOF is reduced by 61%. Increasing the

partial pressure of pyridine to 0.48 kPa and 0.95 kPa further reduces the normalized activity to 0.28 and 0.153, respectively. After pyridine is removed from the feed, the activity slowly returns to the values prior to pyridine injection, suggesting the adsorption of pyridine is reversible. To interpret the effects of pyridine partial pressure on the TOF, we developed kinetic expressions that account for a reversibly adsorbed poison that blocks access to active sites, as shown below.

When pyridine is not present, the rate expression for IPA dehydration is assumed to take on the following, Langmuirian form:

$$TOF(s^{-1}) = \frac{K_{IPA}k_{int}[s^{-1}] \left(\frac{P_{IPA}}{P^o}\right)}{\left(1 + K_{IPA} \left(\frac{P_{IPA}}{P^o}\right)\right)} \quad (3)$$

Here K_{IPA} is the dimensionless adsorption equilibrium constant for the adsorption of IPA. As previously shown, the kinetics are 0th order in P_{IPA} , meaning that $K_{IPA} \left(\frac{P_{IPA}}{P^o}\right) \gg 1$ in the denominator, so it cancels out in the numerator. Doing so recovers equation (2). If a reversible poison is present, then the rate expression now becomes:

$$TOF_{py}(s^{-1}) = \frac{K_{IPA}k_{int}[s^{-1}] \left(\frac{P_{IPA}}{P^o}\right)}{\left(1 + K_{IPA} \left(\frac{P_{IPA}}{P^o}\right) + K_{Py} \left(\frac{P_{Py}}{P^o}\right)\right)} \quad (4)$$

Here K_{Py} is the dimensionless adsorption equilibrium constant for pyridine adsorption. The data in Figure 4.8B is normalized with respect to the TOF before pyridine injection, so we divide equation (4) by equation (3) to get equation (5):

$$\frac{TOF_{py}(s^{-1})}{TOF(s^{-1})} = \frac{\left(\frac{K_{IPA}k_{int}[s^{-1}] \left(\frac{P_{IPA}}{P^o}\right)}{\left(1 + K_{IPA} \left(\frac{P_{IPA}}{P^o}\right) + K_{Py} \left(\frac{P_{Py}}{P^o}\right)\right)}\right)}{\left(\frac{K_{IPA}k_{int}[s^{-1}] \left(\frac{P_{IPA}}{P^o}\right)}{\left(1 + K_{IPA} \left(\frac{P_{IPA}}{P^o}\right)\right)}\right)} \quad (5)$$

Simplifying equation (5) gives equation (6):

$$\frac{TOF_{py}(s^{-1})}{TOF(s^{-1})} = \frac{\left(1 + K_{IPA} \left(\frac{P_{IPA}}{P^o}\right)\right)}{\left(1 + K_{IPA} \left(\frac{P_{IPA}}{P^o}\right) + K_{Py} \left(\frac{P_{Py}}{P^o}\right)\right)} \quad (6)$$

As mentioned previously, $K_{IPA} \left(\frac{P_{IPA}}{P^o}\right) \gg 1$ for the conditions prior to pyridine injection, which leads to the observed 0th order dependence on P_{IPA} (Figure 4.6B). We assume that upon feeding pyridine, a reversible exchange is taking place such that $K_{IPA} \left(\frac{P_{IPA}}{P^o}\right) + K_{Py} \left(\frac{P_{Py}}{P^o}\right) \gg 1$ at all pyridine partial pressures. In other words, the introduction of pyridine does not increase the coverage of vacant Ti sites, represented by the value of 1 in equation (6). If this is the case, then equation (6) can be approximated by equation (7):

$$\frac{TOF_{py}(s^{-1})}{TOF(s^{-1})} = \frac{\left(K_{IPA} \left(\frac{P_{IPA}}{P^o}\right)\right)}{\left(K_{IPA} \left(\frac{P_{IPA}}{P^o}\right) + K_{Py} \left(\frac{P_{Py}}{P^o}\right)\right)} \quad (7)$$

Further rearrangement of equation (7) gives equation (8):

$$\frac{TOF_{py}(s^{-1})}{TOF(s^{-1})} = \frac{1}{\left(1 + \frac{K_{Py}P_{Py}}{K_{IPA}P_{IPA}}\right)} = \frac{1}{(1 + AP_{Py})} \quad (8)$$

This is the same expression shown in the inset of Figure 4.9B, which adequately fits the data. Thus, we conclude the pyridine adsorbs reversibly and displaces adsorbed IPA which reduces the dehydration rate. The fitted value of A is about 614 bar^{-1} , which corresponds to a ratio of adsorption equilibrium constants $\left(\frac{K_{Py}}{K_{IPA}}\right)$ equal to 18.4, indicating that the adsorption of pyridine to active Ti sites is more favorable than IPA. This is consistent with our calculations below, which show that ΔH_{ads}^o for pyridine adsorbed to the metal centers of Ti sites is typically $\sim 20 \text{ kJ/mol}$ more negative than those calculated for IPA. The fact that only a single adsorption equilibrium constant ratio is required to fit the data suggests that the adsorption sites exhibit relatively homogeneous values of ΔH_{ads}^o for pyridine and IPA.

To monitor the coverage of pyridine to Ti sites during the conditions of the experiments shown in Figure 4.9, we collected *in-situ* FTIR spectra at similar conditions. Figure 4.10A shows the FTIR spectra of **Ti/SiO₂-1023** under three conditions: 1) $P_{Py} = 0.24$ kPa, 2) $P_{Py} = 0.24$ kPa and $P_{IPA} = 3$ kPa, and 3) $P_{Py} = 0.09$ kPa and $P_{IPA} = 3$ kPa at 553 K. We focused on the IR region that shows absorption due to the ring-breathing vibrational mode 8a, which is indicative of pyridine directly adsorbed to Ti metal centers.

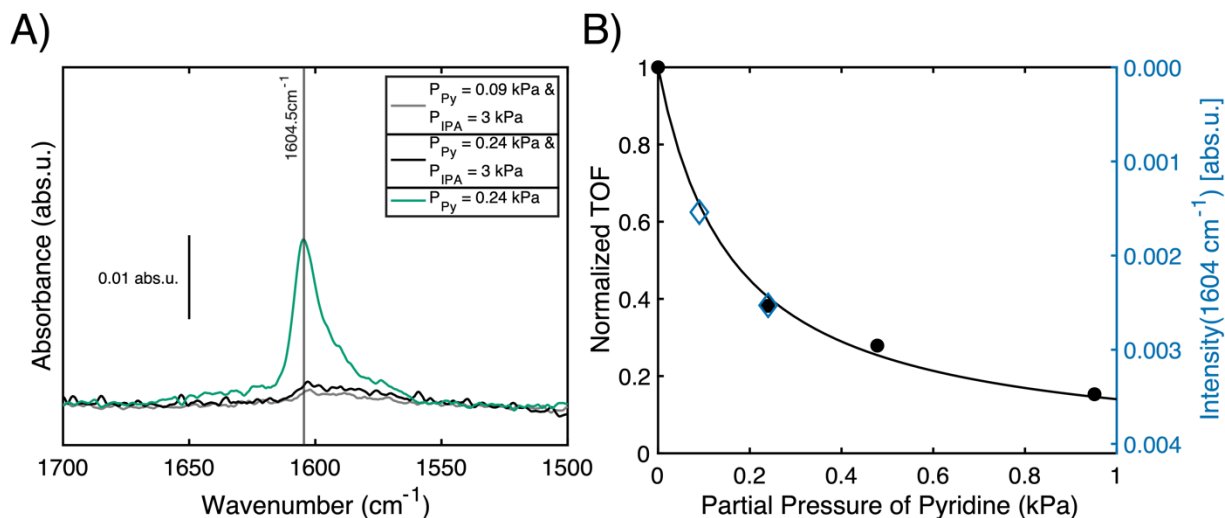


Figure 4.10: A) *in-situ* FTIR spectra of pyridine adsorbed to **Ti/SiO₂-1023** at multiple pyridine partial pressures and in the presence of 3 kPa IPA ($T = 553$ K). B) Normalized TOF as a function of pyridine partial pressure (reproduced from Figure 4.9B), and the intensity of the peak centered near 1604 cm^{-1} as a function of pyridine partial pressure. The second y-axis describing the intensity was scaled such that 0.000 abs.u. equaled a normalized TOF of 1, and $2.52 \times 10^{-3}\text{ abs.u.}$ equaled a normalized TOF of 0.39 (see text). The line shows the fit function in the inset.

The green spectrum in Figure 4.10A corresponds to adsorbed pyridine in the absence of IPA. This system has already been analyzed in Chapter 2. The peak is centered at 1604.5 cm^{-1} , with an intensity of 1.96×10^{-2} absorbance units, is indicative of pyridine adsorbed to the metal centers of $\equiv\text{Ti-OH}$ sites. In Chapter 2, we utilized the extinction coefficient for this feature, along with the known Ti loading in the sample, to establish that the ratio of the moles of pyridine to the moles of Ti was equal to 0.29 under these conditions.

The black and gray spectra show the absorbance of mode 8a after introducing pyridine at fixed partial pressures ($P_{Py} = 0.24$ kPa and $P_{Py} = 0.09$ kPa, respectively) in the presence of flowing IPA at $P_{IPA} = 3$ kPa. Before introducing pyridine, IPA was allowed to flow over the catalyst for one hour. The intensities of both peaks are significantly reduced relative to the peak observed in the absence of IPA, indicative of the competition between IPA and pyridine for adsorption sites. The black spectrum ($P_{Py} = 0.24$ kPa and $P_{IPA} = 3$ kPa), is most similar to the conditions employed in our kinetic experiments presented in Figure 4.9, which are reproduced in Figure 4.10B. This feature exhibits an intensity of 2.52×10^{-3} absorbance units. In our kinetics experiments, it was found that the TOF decreased by 61% after introducing pyridine at the same conditions. Therefore, an intensity of 2.52×10^{-3} absorbance units is required for a 61% reduction in the TOF, and an intensity of 0 absorbance units is required to reduce the TOF by 0%. We have visualized this statement graphically in Figure 4.10B by overlaying the two data points at a normalized TOF =

0.39 and an intensity of 2.52×10^{-3} absorbance units. Then, we plotted the intensity of mode 8a when $P_{py} = 0.09$ kPa, which is 1.59×10^{-3} absorbance units. Remarkably, the data point falls directly on the model prediction, suggesting that when $P_{py} = 0.09$ kPa, the TOF would be reduced by ~40%. The question now becomes: what intensity of mode 8a of adsorbed pyridine is required to completely extinguish the TOF? From examining the bottom of the y-axis of Figure 4.10B, the intensity required when the TOF is equal to zero is 4.1×10^{-3} absorbance units. Previously, we stated that the intensity of mode 8a in the absence of IPA is 1.96×10^{-2} absorbance units, which had been found to be equal to 0.29 moles of pyridine/moles of Ti (green spectrum of Figure 4.10A). Therefore:

$$\frac{4.1 * 10^{-3}}{1.96 * 10^{-2}} [abs. u.] = \frac{x}{0.29 \frac{mol Py}{mol Ti}}$$

Solving for x yields 0.06 mol Py/mol Ti. This indicates only 6% of $\equiv Ti-OH$ sites, at most, are participating in the dehydration reaction after 1 h of reaction. As previously shown in Figure 4A, the deactivation continues well past one hour, suggesting the percentage of active Ti is even lower at longer times on stream.

In summary, we have obtained evidence that the fraction of active $\equiv Ti-OH$ sites for isopropanol dehydration is very low (<6%). In other words, the active site is a minority species of the **Ti/SiO₂₋₁₀₂₃** material. However, this is in stark contrast to what has been found from $\equiv Ti-OH$ site poisoning experiments with phenyl phosphonic acid during cyclooctene epoxidation, which showed that around 60% of $\equiv Ti-OH$ sites at low Ti loadings are active.³⁰ Therefore, the fraction of active Ti may depend on the reaction and conditions (temperature, phase, etc.) employed.

4.3.5 Preliminary investigation of IPA dehydration utilizing QM/MM calculations

The main findings from the experimental section were:

1. *In-situ* UV/Vis and pre-edge XANES suggest that the majority of $\equiv Ti-OH$ sites do not coordinate adsorbates and remain tetrahedral.
2. The fraction of Ti sites that are active for IPA dehydration is very low (<6%).

We will now show the results of a set of preliminary QM/MM DFT calculations that were conducted to explain the experimental findings.

Starting with experimental observation #1: We propose that the subtle changes, or lack thereof, in the UV/Vis and pre-edge XANES spectra when IPA is present are consistent with the formation of $\equiv Ti-OiPr$ species that retain the tetrahedral structures of the Ti atoms. The formation of $\equiv Ti-OiPr$ might be supported by *in-situ* FTIR, but very similar peaks corresponding to $\equiv Si-OiPr$ make it difficult to determine their presence unequivocally. To test whether the formation of $\equiv Ti-OiPr$ groups is favorable under our reaction conditions, we performed DFT calculations using an experimentally validated method to estimate equilibrium constants for their formation. For these calculations, we considered four possible intermediates, 1) vacant, unchanged $\equiv Ti-OH$ sites (State

C1), 2) $\equiv\text{Ti-OiPr}$ (State C2), 3) IPA adsorbed molecularly to Ti sites (State C3), and 4) water adsorbed molecularly to Ti sites (State C4), as shown in Figure 4.11.

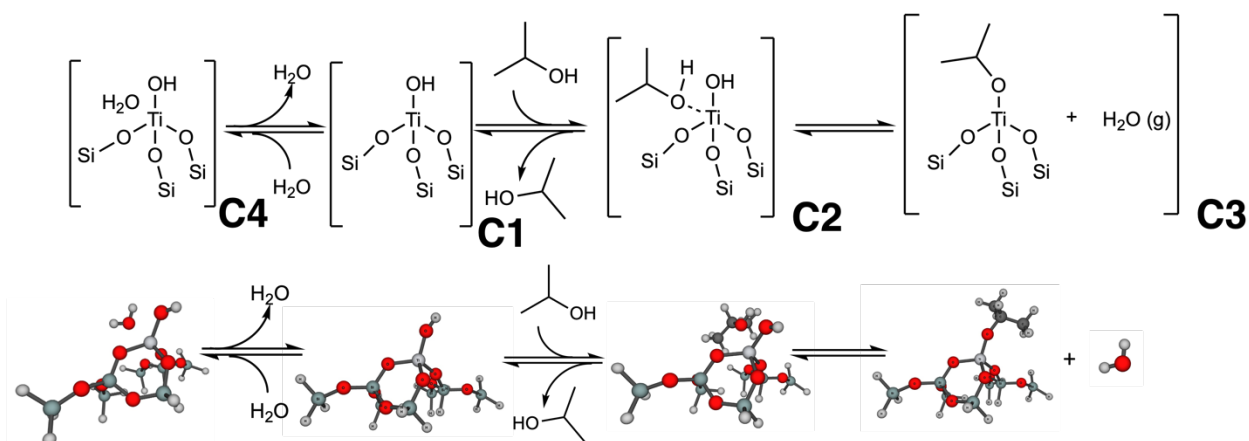


Figure 4.11: Optimized geometries for the adsorption of IPA (State C2) and the formation of a $\equiv\text{Ti-OiPr}$ (State C3), optimized at the $\omega\text{B97X-D/def2-SVP}$ level of theory. The MM region extends 29Å in radius from the central Ti atom, but it is not shown for clarity.

To estimate the equilibrium constants for each intermediate, we need to calculate their enthalpies and entropies. The entropy estimates for these states were described in the Methods section. For the enthalpies, we must consider the effects of tetrahedral distortion on State C2 and State C4. States C2 and C4 are molecular adsorption events, and previous studies have shown that the ΔH_{ads}^o for molecular adsorption to O-Ti-O facets correlates linearly with the areas of the facet. Figure 4.12A demonstrates from a small collection of calculations that this is true for IPA adsorption, while in Chapter 3, we showed this to be true for water adsorption. This correlation results from two dominant phenomena, as found from an Energy Decomposition Analysis (EDA) for pyridine adsorption in Chapter 2. As the facet area increases, 1) there is less of a geometric distortion energetic penalty in forming the adsorbate-bound geometry, and 2) “frozen” interactions (which comprise a complex interplay between permanent electrostatic, Pauli-repulsion, and dispersion interactions) become more favorable.

On the other hand, State C3 is a titanium hydroxyl substitution reaction with no adsorbates coordinated directly to a facet. We previously found such states to be relatively insensitive to the facet area in the context of titanium hydroperoxide formation from H_2O_2 . Therefore, we make only one estimate of its enthalpy and assume it is also insensitive to the facet area. This is shown as the green horizontal line in Figure 4.12A. Using the enthalpies, and estimates for their entropies, we can calculate the equilibrium constants in equations (9)-(12) to determine their fractional coverages assuming equilibrium between all species is reached:

$$\Theta_{C1} = \frac{1}{\left(1 + K_{C2}P_{IPA} + \frac{K_{C3}P_{IPA}}{P_W} + K_{C4}P_W\right)} \quad (9)$$

$$\Theta_{C2} = \frac{K_{C2}P_{IPA}}{\left(1 + K_{C2}P_{IPA} + \frac{K_{C3}P_{IPA}}{P_W} + K_{C4}P_W\right)} \quad (10)$$

$$\Theta_{C3} = \frac{\frac{K_{C3}P_{IPA}}{P_W}}{\left(1 + K_{C2}P_{IPA} + \frac{K_{C3}P_{IPA}}{P_W} + K_{C4}P_W\right)} \quad (11)$$

$$\Theta_{C4} = \frac{K_{C4}P_W}{\left(1 + K_{C2}P_{IPA} + \frac{K_{C3}P_{IPA}}{P_W} + K_{C4}P_W\right)} \quad (12)$$

In the above equations, Θ_X , K_X , and P_X correspond to the fractional coverage, equilibrium constant, and partial pressure of X , respectively. We note that P_W is the partial pressure of water, which is set to 0.013 kPa for the remaining calculations. This term comes from the fact that water is a product in the formation of State C3. This partial pressure corresponds to its estimated value at the outlet of the reactor based on the conversion of IPA (Figure 4).

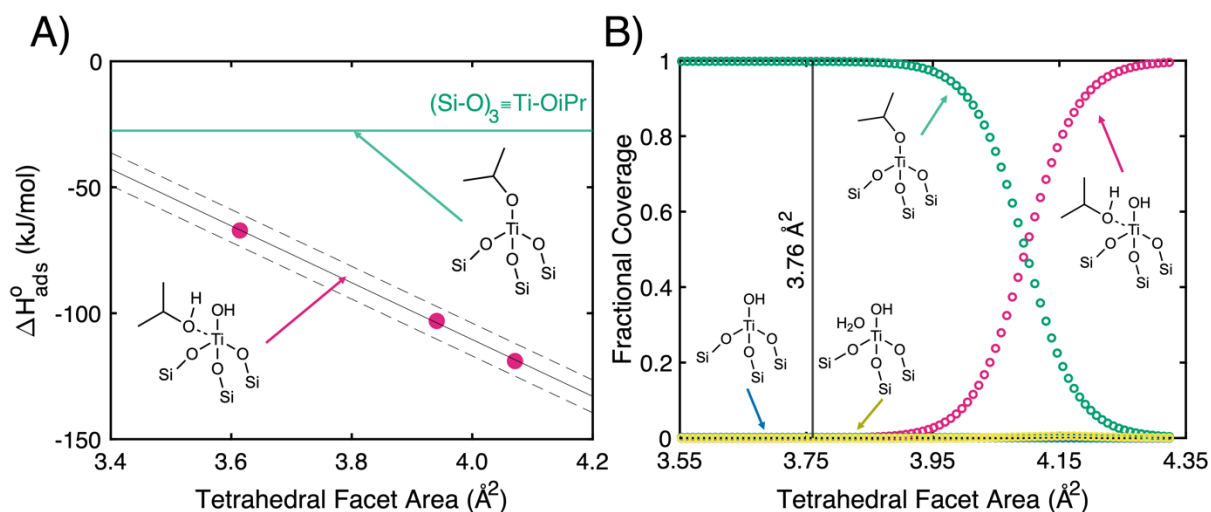


Figure 4.12: A) QM/MM calculations of ΔH_{ads}° ($T = 553.15$ K) as a function of the tetrahedral facet area of the \equiv Ti-OH site to which IPA is bound). The solid line is the linear fit, while the dashed lines are one standard error of the estimated value of ΔH_{ads}° adopted from Chapter 2 for the same correlation derived from enthalpies of pyridine adsorption to \equiv Ti-OH sites. B) The fractional coverage of states C1, C2, C3, and C4 as a function of the tetrahedral facet area. $P_{IPA} = 3$ kPa, $P_W = 13$ Pa, $T = 553.15$ K.

Figure 4.12B plots the fractional coverages of States C1-C4 as a function of the tetrahedral facet area. We note that the largest facet area physically possible was estimated in Chapter 2 to be 4.35 Å². Figure 4.12B shows that \equiv Ti-OiPr groups dominate the population of possible intermediates until the facet area reaches ~ 4.1 Å². The majority of \equiv Ti-OH sites in the **Ti/SiO₂-1023** material exhibit facet areas equal to 3.76 Å², shown as a vertical black line in Figure 4.12B. Thus, our calculations predict that the majority of \equiv Ti-OH sites in **Ti/SiO₂-1023** will form \equiv Ti-OiPr groups

at these conditions. Interestingly, the fractional coverage of State C2 (molecularly adsorbed IPA), only has dominating coverages (>0.9) above $\sim 4.2 \text{ \AA}^2$. Regardless of whether State C3 or State C2 is the most abundant surface intermediate, this shows that a form of adsorbed IPA will be present which is consistent with the experimentally observed 0th order dependence in the partial pressure of IPA.

Finally, we note that the fraction of vacant sites and the fraction of sites binding water (States C1 and C4) are predicted to be near zero for all facet areas. This final point supports the experimentally observed 0th order dependence on the partial pressure of IPA, indicating saturation of the kinetically relevant form of adsorbed IPA.

Now we examine experimental observation #2: “The fraction of Ti sites that are active for IPA dehydration is very low ($<6\%$).” This implies that the majority of $\equiv\text{Ti-OH}$ sites, which form $\equiv\text{Ti-OiPr}$ groups, are *not* active for IPA dehydration. To confirm this, we performed DFT calculations attempting to form propene from State C3 ($\equiv\text{Ti-OiPr}$). Figure 4.13 displays a schematic of this transformation, as well as the structures we optimized for Site 1 of our database. This reaction is an intra-molecular H shift from the methyl group to the O-atom of the isopropoxide. The transition state (State C[‡]1) is a 4-membered ring.

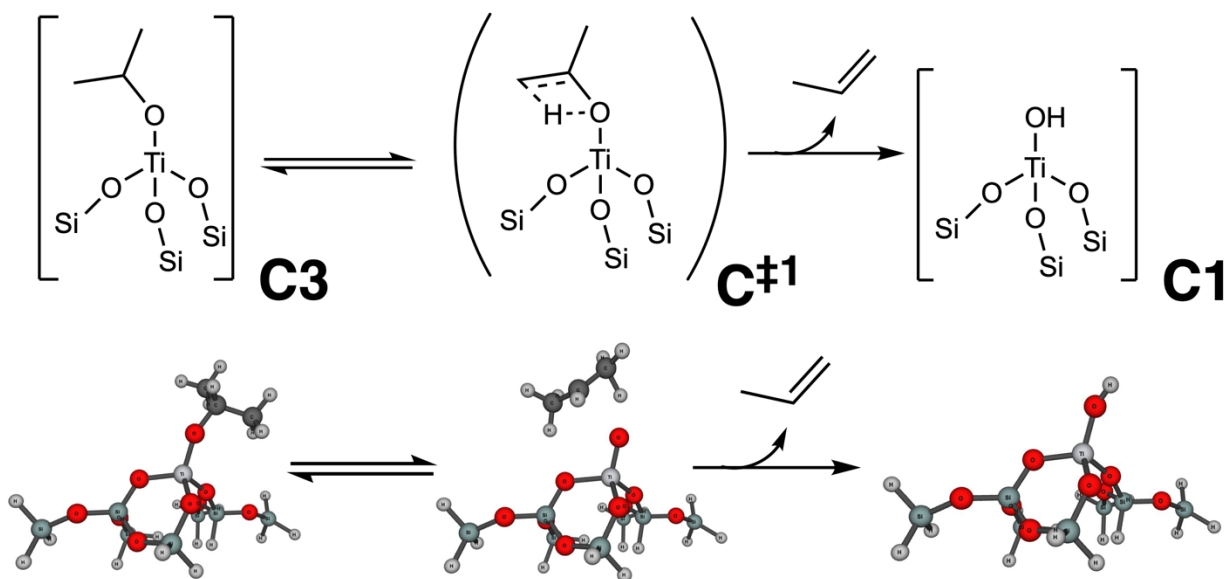


Figure 4.13: Optimized geometries of a $\equiv\text{Ti-OiPr}$ (State C3) and the intra-molecular H shift to form propene (State C[‡]1). All structures were optimized at the $\omega\text{B97X-D/def2-SVP}$ level of theory. The MM region extends 29 \AA in radius from the central Ti atom, but it is not shown for clarity.

Table 4.1: Enthalpy, entropy and Gibbs free energy estimates for States C3 and C^{‡1}

Thermodynamic parameter*	State C3	State C ^{‡1}	Δ^{**}
H° (kJ/mol)	-28.61	170.10	198.71
S° (J/molK)	-41.58	-42.21	-0.63
G° (kJ/mol)	-5.61	193.44	199.06

*Conditions are T = 553.15 K, P° = 1 bar. The thermodynamic reference state is State C1, which includes one gas-phase IPA molecule. **Denotes the change in enthalpy, entropy or Gibbs free energy from State C1 to C^{‡1}

Under the assumption that State C3 (\equiv Ti-OiPr) is the most abundant surface intermediate, as is supported by our previous calculations for facet areas smaller than 4 Å², and the rate-determining step is the intra-molecular H shift (C^{‡1}), the *forward* rate of propene formation can be calculated using transition state theory as:

$$\text{forward rate (s}^{-1}\text{)} = \frac{k_b T}{h} \exp\left(\frac{-\Delta G^{\ddagger,0}}{RT}\right) \quad (13)$$

where $\Delta G^{\ddagger,0}$ is the difference in Gibbs free energy between State C^{‡1} and State C3.

The activation enthalpy ($\Delta H^{\ddagger,0}$) for this reaction is nearly 200 kJ/mol, as shown in Table 4.1. At T = 553.15 K, the forward rate is calculated to be 1.8 x 10⁻⁶ s⁻¹. This rate is slow relative to the rates of propene formation we observed, which were O(10⁻² s⁻¹) as shown in Figure 4.5.

The mechanism proposed in Figure 4.13 is not the only possible mechanism for propene formation from \equiv Ti-OiPr. Figure 4.14 displays another possible pathway for propene formation by H abstraction by a Ti-O-Si support bond through a 6-membered ring transition state (C^{‡2}).

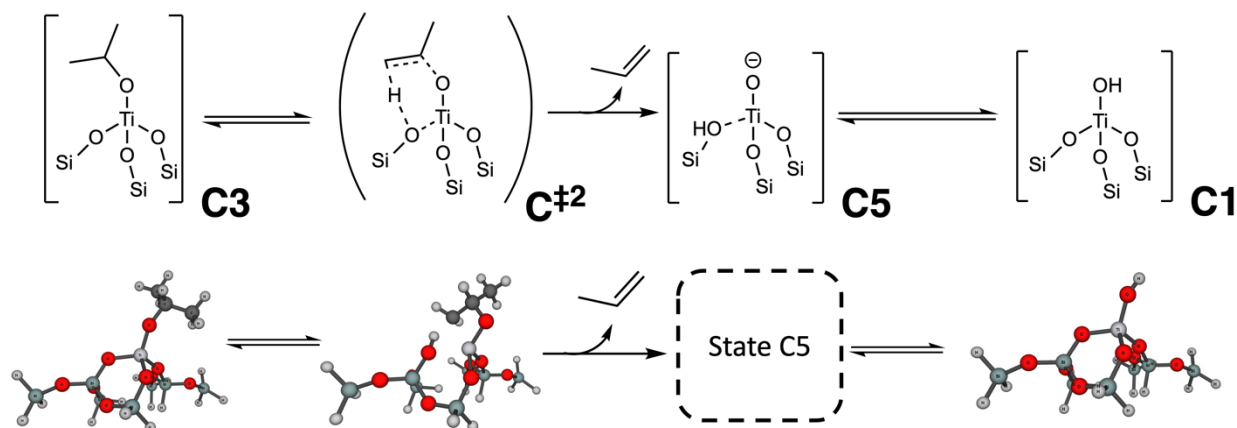


Figure 4.14: Optimized geometries of a \equiv Ti-OiPr (State C3) and the H shift to a Ti-O-Si bond to form propene (State C^{‡2}). All structures were optimized at the ω B97X-D/def2-SVP level of theory. We note that State C4 was not computed since it was not needed to assess the forward rate of propene formation from C3 through transition state C^{‡2}. The MM region extends 29Å in radius from the central Ti atom, but it is not shown for clarity.

Table 4.2: Enthalpy, entropy, and Gibbs free energy estimates for States C3 and C^{‡2}

Thermodynamic parameter*	State C3	State C ^{‡2}	Δ^{**}
H ^o (kJ/mol)	-28.61	174.21	202.83
S ^o (J/molK)	-41.58	-70.09	-28.52
G ^o (kJ/mol)	-5.61	212.99	218.60

*Conditions are T = 553.15 K, P^o = 1 bar. The thermodynamic reference state is State C1 (vacant site) and one gas-phase IPA molecule. **Denotes the change in enthalpy, entropy or Gibbs free energy from State C3 to C^{‡2}

Again, under the assumption that State C3 is the most abundant surface intermediate, as is supported by our previous calculations for facet areas smaller than 4 Å², and the rate-determining step is now C^{‡2}, the *forward* rate of propene formation can be calculated as before using transition state theory using the value for $\Delta G^{\ddagger,0}$ in Table 4.2 between State C^{‡2} and State C3. This yields 2.62 x 10⁻⁸ s⁻¹, even slower than the forward rate calculated from the intramolecular H shift mechanism (Figure 4.13).

Therefore, the findings presented in Tables 4.1 and 4.2 indicate that the formation of ≡Ti-OiPr does not lead to appreciable rates of propene formation. Since most Ti-OH sites are predicted to form ≡Ti-OiPr, most ≡Ti-OH sites will not be active for IPA dehydration.

Figure 4.12B demonstrates that ≡Ti-OH sites with facet areas larger than ~4.2 Å² do not form ≡Ti-OiPr but instead coordinate IPA as a molecule. Thus, we continue our analysis by proposing that the active Ti sites are the minority that exhibit large tetrahedral facet areas. To test this hypothesis, we only need to compute the Gibbs free energies of states along a mechanism for dehydration conducted on such a site.

Site 7 exhibits a facet area of 4.07 Å², the largest tetrahedral facet area in our database, as shown in Figure 4.15. Attempts to locate another ≡Ti-OH site with an even larger facet area proved challenging, and we were not successful. At the conditions employed in the calculations shown in Figure 4.12B, 37% of ≡Ti-OH sites with such facet areas will molecularly adsorb IPA (State C2), indicating that this site could be a candidate for the active site observed experimentally.

Site 7 is also distinctive in that it shares two Ti-O-Si bonds with one Si atom, as shown in Figure 4.15. As a result, the tetrahedra formed by both the Si and the Ti and their four O atoms are heavily distorted. This partially causes the large facet area of 4.07 Å².

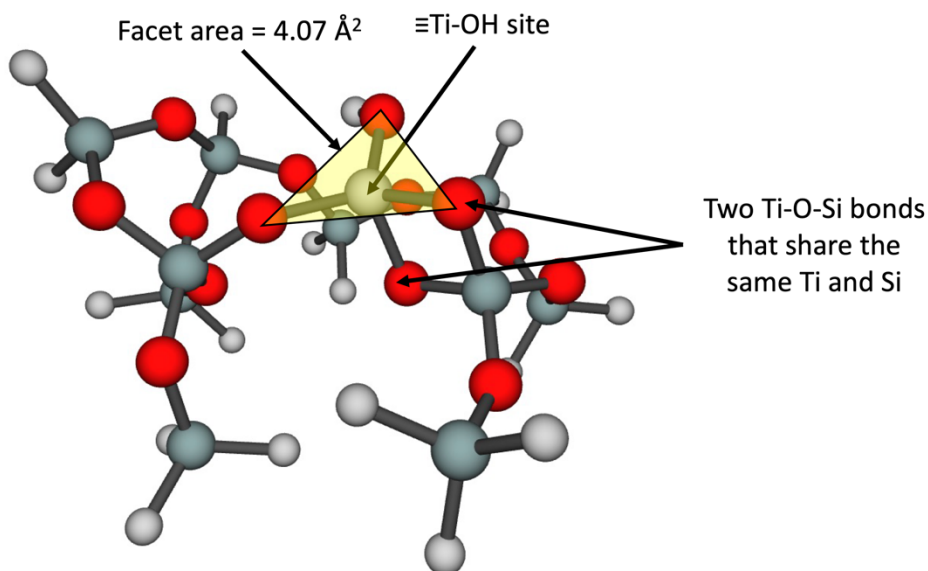


Figure 4.15: Optimized geometry of State C1 (vacant site) using Site 7 of our database. The MM region extends 29Å in radius from the central Ti atom, but it is not shown for clarity. The tetrahedral facet with an area of 4.07 Å² is highlighted using a yellow triangle.

As shown previously for calculations with Site 1, the formation of $\equiv\text{Ti-OiPr}$ did not lead to predictions of propene formation rates that agreed with the experimental rate. Therefore, we do not examine pathways starting from $\equiv\text{Ti-OiPr}$. Instead, we begin at State C2 (molecularly adsorbed IPA) and attempt to form propene. To form propene, a β -H must be abstracted. We considered β -H abstraction from the titanium hydroxyl group or the highly strained Ti-O-Si bridge, as shown in Figure 4.16.

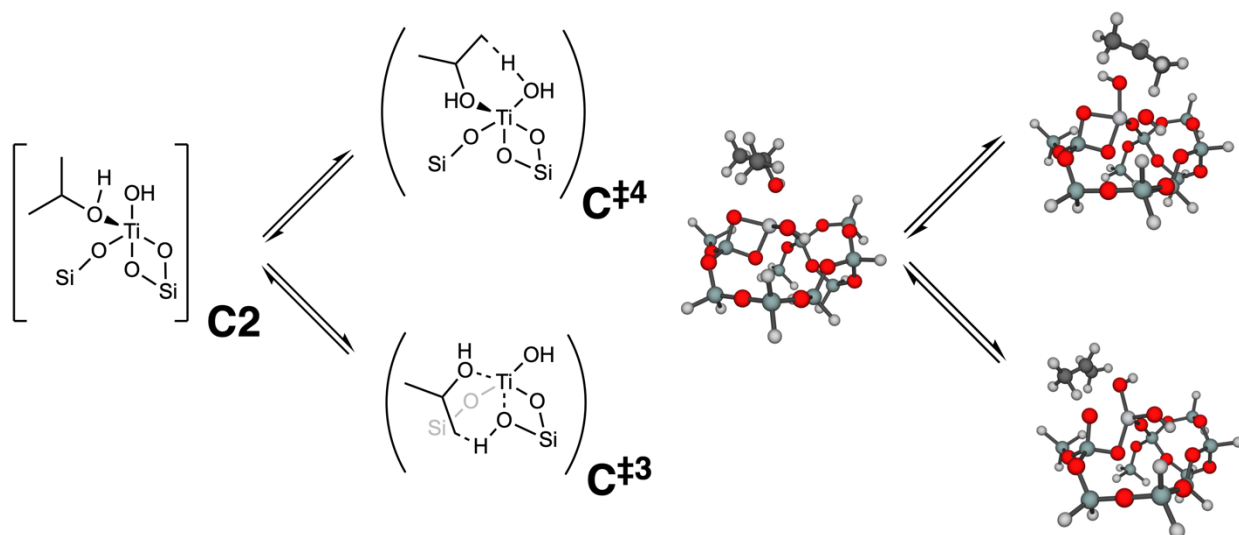


Figure 4.16: Optimized geometries of a molecularly adsorbed IPA molecule to Site 7 (State C2) and E2 (concerted) transition states for propene formation where the β -H is abstracted by the Ti-O-Si bond (State C^{‡3}) or by the titanium hydroxyl (State C^{‡4}). All structures were optimized at the $\omega\text{B97X-D/def2-SVP}$ level of theory. The MM region extends 29Å in radius from the central Ti atom, but it is not shown for clarity.

Table 4.3: Enthalpy, entropy, and Gibbs free energy estimates for States C2, C^{3‡}, and C^{4‡}

Thermodynamic parameter*	State C2	State C ^{3‡}	Δ^{**}	State C ^{4‡}	Δ^{***}
H° (kJ/mol)	-118.98	161.07	161.07	56.45	175.44
S° (J/molK)	-136.74	-183.34	-46.59	-183.90	-47.15
G° (kJ/mol)	-43.34	138.00	181.34	152.66	196.00

*Conditions are T = 553.15 K, P° = 1 bar. The thermodynamic reference state is State C1 (vacant site) and one gas-phase IPA molecule. **Denotes the change in enthalpy, entropy or Gibbs free energy from State C2 to C^{3‡}. ***Denotes the change in enthalpy, entropy or Gibbs free energy from State C2 to C^{4‡}.

In both cases, the optimized transition state structures exhibit the simultaneous (concerted) cleavage of the C-OH and C-H bonds. This is known as the E2 dehydration pathway (Figure 4.5).¹¹⁸ The enthalpy barrier for going from State C2 to C^{3‡} and C^{4‡} are 161 and 175 kJ/mol, respectively (Table 4.3). Therefore, the pathway in which the highly-strained Ti-O-Si bond performs the abstraction has a lower barrier than the relatively free-to-move titanium hydroxyl. We believe this is because upon H-atom abstraction, the Ti-O-Si bond is cleaved, and both the Ti and Si atoms are allowed to form less distorted tetrahedral geometries. While this barrier is still not close to that observed experimentally (103±15 kJ/mol), but it is more consistent than the pathways we have examined starting from ≡Ti-OiPr. This also demonstrates that there can be significant differences in calculated enthalpy barriers for E2 IPA dehydration depending on the H-acceptor.

Having established that the calculated enthalpy barriers for both E2 dehydration pathways over Site 7 are closer to experimental results, we decided to examine two orthogonal modifications of the active site structure. In the first modification, we investigate the effects on the energetics of the E2 dehydration pathway when the β-H is abstracted by a Ti-O-Ti bond, rather than a Ti-O-Si bond. This requires starting from a Ti dimer structure and recalculating the thermodynamic parameters for States C2 and C^{3‡}. In the second modification, we investigate the effects of an H-bonding interaction between the titanium hydroxyl and a nearby silanol (≡Si-OH) group on the thermodynamics of the E2 dehydration pathway through state C^{4‡}. We generated this site by adding water across a neighboring Si-O-Si bridge and replacing one of the silanol groups with a terminating H-atom. Both vacant site structures are shown in Figure 4.17. As shown in Figure 4.17B, the H-bond distance is 1.85 Å, which is 0.17 Å shorter than the previous TiOH---O-Si bond distance in Site 7, which is clear evidence of a stronger H-bonding interaction. Additionally, the harmonic vibrational frequency of the TiO—H bond is redshifted by 122 cm⁻¹ after this modification, which also suggests that this Ti-OH group is participating in a stronger H-bonding interaction by interacting with a silanol, rather than a siloxane bridge.

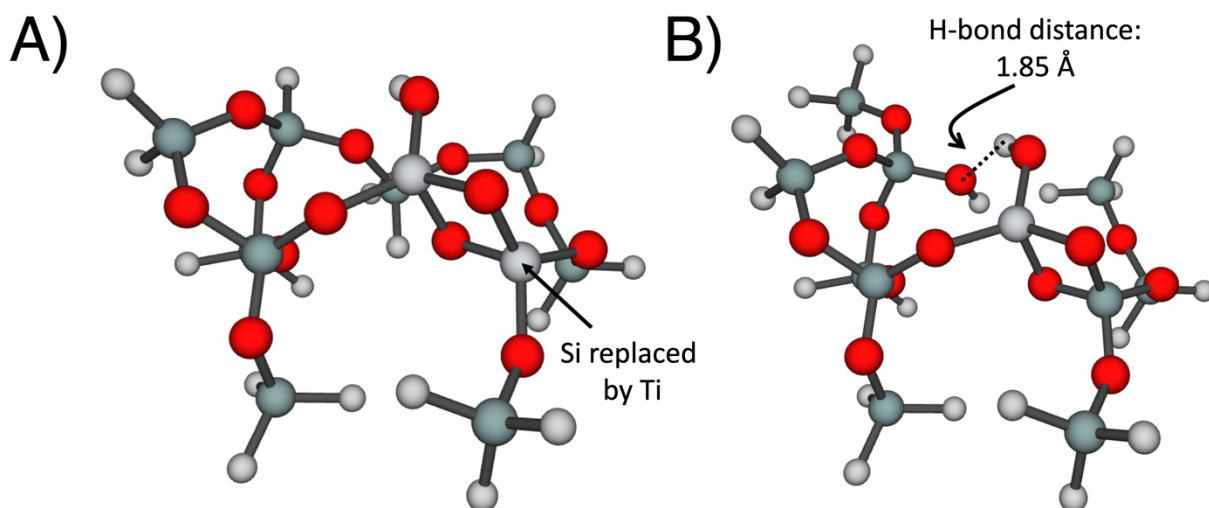


Figure 4.17: Modified Ti sites structures all based on Site 7. A) Optimized geometry of a Ti dimer which was generated by replacing the Si that formed two Si-O-Ti bonds with the central Ti in Site 7. B) Optimized geometry of the \equiv Ti-OH site from Site 7 that now forms a H-bond with a neighboring silanol group. The H-bond distance is shown.

Figure 4.18 shows the E2 dehydration pathways that we calculated over each of these sites. The values of ΔH_{ads}° for IPA adsorption to the dimer and H-bonded \equiv Ti-OH sites are slightly less favorable by 4 kJ/mol and 7.5 kJ/mol, respectively (Table 4.4). The enthalpy barriers for E2 dehydration over the dimer and H-bonded \equiv Ti-OH sites are 170.45 and 171.45, respectively. The former barrier shows that the E2 dehydration enthalpy barrier *increased* by 9 kJ/mol when the β -H was abstracted by a Ti-O-Ti bond, rather than by a Si-O-Ti bond. The energetic penalty to distort a Si tetrahedron have been calculated to be relatively high.¹¹⁹ It is also very rare for silicon oxygen compounds to adopt anything other than tetrahedral coordination.¹²⁰ Therefore, it is our belief that the lower barrier for E2 dehydration over the Si-O-Ti bond in comparison to the Ti-O-Ti bond can be attributed to the greater energetic stabilization resulting from the relaxation of the distorted tetrahedral geometry of Si during the transition state. On the other hand, the enthalpy barrier for E2 dehydration when the β -H is abstracted by the titanium hydroxyl *decreased* by 4 kJ/mol when a H-bonding interaction is present. Therefore, the titanium hydroxyl group appears to become more basic when the same hydroxyl is participating in an H-bond as an H-donor.

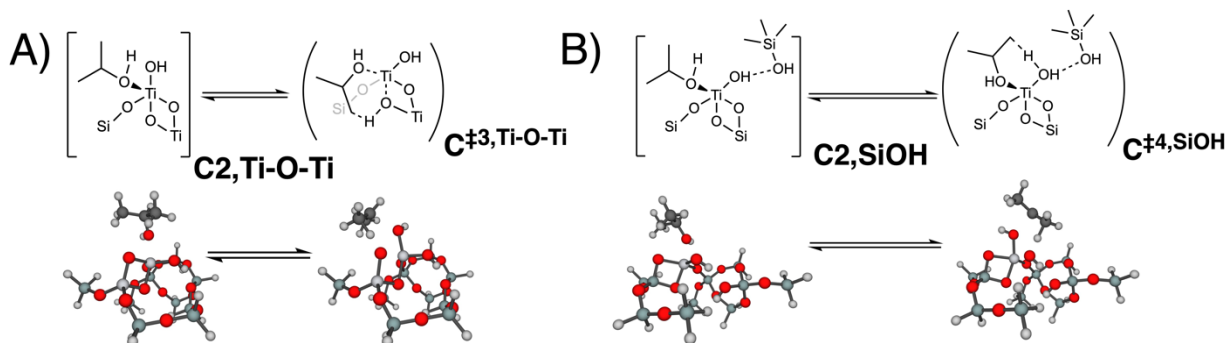


Figure 4.18: A) Optimized geometries of a molecularly adsorbed IPA molecule to the dimer form of Site 7 (State C2,Ti-O-Ti) and E2 (concerted) transition states for propene formation where the β -H is abstracted by the Ti-O-Ti bond (State C‡3,Ti-O-Ti). B) Optimized geometries of a molecularly adsorbed IPA molecule to the H-bonded form of Site 7 (State C2,SiOH) and E2 (concerted) transition states for propene formation where the β -H is abstracted by

the titanium hydroxyl (State C^{‡4,SiOH}). All structures were optimized at the ωB97X-D/def2-SVP level of theory. The MM region extends 29Å in radius from the central Ti atom, but it is not shown for clarity.

Table 4.4: Enthalpy, entropy, and Gibbs free energy estimates for E2 dehydration over Ti-O-Ti and H-bonded ≡Ti-OH sites

Thermodynamic parameter*	State C2, Ti-O-Ti	State C ^{‡3,Ti-O-Ti}	Δ**	State C2, SiOHC ^{‡4,SiOH}	State C ^{‡4,SiOH}	Δ***
H° (kJ/mol)	-115.53	54.93	170.45	-111.51	56.45	171.45
S° (J/molK)	-136.74	-182.00	-45.26	-136.74	-189.00	-52.26
G° (kJ/mol)	-39.89	150.14	190.03	-35.87	158.82	194.69

*Conditions are T = 553.15 K, P° = 1 bar. The thermodynamic reference state is State C1 (vacant site) and one gas-phase IPA molecule. **Denotes the change in enthalpy, entropy or Gibbs free energy from State C2,Ti-O-Ti to C^{‡3,Ti-O-Ti}.***Denotes the change in enthalpy, entropy or Gibbs free energy from State C2,SiOH to C^{‡4,SiOH}.

Despite these findings, all of the calculated enthalpy and Gibbs free energy barriers are far from experimental values. Up to now, we have assumed that Site 7 was a potential candidate for the active site since it would exhibit an appreciable coverage (~37%) of molecularly adsorbed IPA (State C2). We remind the reader that we have assumed State C2 to be the true resting state for IPA dehydration, given that ≡Ti-OiPr groups do not lead to appreciable rates of propene formation. However, we have neglected to consider how the partial pressure of water would change the relative coverage of State C2 for Site 7. Experiments show that the reaction order in the partial pressure of water is 0th order (Figure 5B). If we continue to assume that State C2 is the true resting state, then the fractional coverage of State C2 should be constant with respect to the partial pressure of water. This qualitative reasoning can be expressed mathematically as:

$$\frac{d\ln(P_w)}{d\ln(\Theta_{C2})} \approx 0 \quad (14)$$

To test if equation (14) holds for Site 7, we increased the partial pressure of water from 13-40 Pa, the range we studied experimentally (Figure 5B), and recalculated the fractional coverage of State C2 as a function of the facet area. Figure 4.19 shows the results of equation (14) as a function of the tetrahedral facet area. The apparent order in P_w peaks near the facet area for Site 7, 4.07 Å², and exhibits a value of ~0.23. This is not 0th order, as seen experimentally, therefore, we should reject Site 7 as a candidate for the active site. To the left and right of the peak, the coverage of ≡Ti-OiPr and molecularly adsorbed IPA dominate (Figure 4.12B). As a result, changes in the partial pressure of water only have an observable effect when the surface has appreciable concentrations of *both* species, which is true for Site 7. Thus, if State C2 is the true resting state, then a site most consistent with the experimental kinetics would need to exhibit a facet area >4.2Å², where the apparent order would be > 0.03 – effectively 0th order within experimental error. Our previous study in Chapter 2 of the facet area distribution of this material

revealed that facet areas larger than 4.2 \AA^2 represent less than 8% of the total $\equiv\text{Ti-OH}$ sites, which is consistent with the very low fraction of active Ti measured experimentally for IPA dehydration using our pyridine reversible site blocking technique ($> 6\%$, Figure 4.10B). As mentioned previously, all attempts to locate a facet area greater than 4.07 \AA^2 in our database were unsuccessful since such facets are likely to be rare.

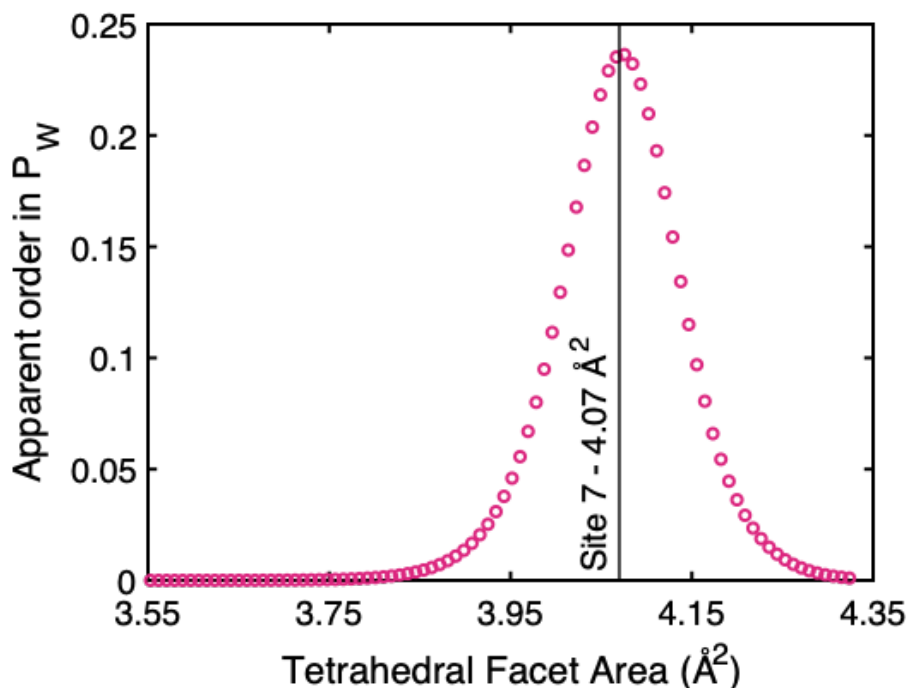


Figure 4.19: The apparent order in the partial pressure of water (P_W) as a function of the tetrahedral facet area assuming State C2 is the true resting state for IPA dehydration. $T = 553.15 \text{ K}$, $P_{\text{IPA}} = 3 \text{ kPa}$.

4.4 Conclusions

In this study, the kinetics of Isopropanol (IPA) dehydration to form propene and water were explored through kinetic measurements, *in-situ* FTIR, XANES, and UV/Vis spectroscopy, and theoretical computations using an experimentally validated Quantum-Mechanics Molecular Mechanics (QM/MM) method. Turnover frequencies (TOF) for propene formation decreased rapidly initially, then moderately thereafter. The TOF was 0th order in the partial pressures of IPA and water and exhibited an apparent activation energy of $103 \pm 15 \text{ kJ/mol}$. A primary kinetic isotope effect of 2.3 ($\text{TOF}_H/\text{TOF}_D$) was observed when perdeuterated IPA was exchanged for hydrogenated IPA in the reactor inlet, indicating the kinetic relevance in cleaving a C-H or O-H bond. Under the assumption that O-H bond cleavage is not relevant, we conclude that IPA dehydration occurs through an E2 (concerted) mechanism with a higher degree of C-H bond-breaking character compared to C-O bond-breaking character. *In-situ* FTIR, XANES, and UV/Vis spectroscopy suggest that isopropoxide groups are formed under reaction conditions and that the majority of $\equiv\text{Ti-OH}$ sites exhibit tetrahedral geometries. The most significant finding of the present study is that the fraction of active Ti sites is, at most, 6%. This finding was determined by combining the results of kinetic site-blocking measurements and *in-situ* FTIR spectroscopy. QM/MM calculations revealed that $\equiv\text{Ti-OH}$ sites that exhibit tetrahedral facet areas less than 4.1

\AA^2 , which constitute the majority of $\equiv\text{Ti-OH}$ sites on Ti/SiO_2 , favor the formation of $\equiv\text{Ti-OiPr}$ groups over molecularly adsorbed IPA and vacant $\equiv\text{Ti-OH}$ sites. Further calculations revealed that the enthalpy barriers for the formation of propene starting from these groups are high, which supports the observation that the majority of $\equiv\text{Ti-OH}$ sites are not active for IPA dehydration. Additional calculations were then performed starting from molecularly adsorbed IPA. We utilized the $\equiv\text{Ti-OH}$ site from our database that exhibited the largest tetrahedral facet (4.07 \AA^2) and found that E2 (concerted C-O and C-H bond cleavage) dehydration transition states are possible. Predictions of the apparent activation energies for these transition states overestimated the experimentally observed activation energy by, at best, 60 kJ/mol. Calculations of the apparent order in the partial pressure of water revealed that Site 7 would exhibit an order of 0.23 which is inconsistent with experiments (0^{th} order) and rules out this site as a candidate for the true active site. By contrast, facet areas $> 4.2 \text{ \AA}^2$ would exhibit orders consistent with experiments. The fraction of active Ti ($> 6\%$) is similar to the fraction of Ti with facets $> 4.2 \text{ \AA}^2$ ($> 8\%$). The present results demonstrate that bulk spectroscopic techniques cannot identify the active sites for IPA dehydration on isolated $\equiv\text{Ti-OH}$ sites present on the surface of Ti/SiO_2 since the active sites are a minority species. Further work is needed to determine the active sites for this reaction.

4.5 Acknowledgments

This work was supported by the Office of Science, Office of Basic Energy Sciences of the U.S. Department of Energy under Contract No. DE-AC02-05CH11231. Calculations were performed at the Molecular Computing Graphics Facility at UC Berkeley. The authors also acknowledge Dr. Yujia Ding for assistance in acquiring XAS data, and Dr. Jeremy Kropf and Dr. Jacklyn Hall for assistance setting up the in-situ XAS cube reactor. This research used resources of the Advanced Photon Source; a U.S. Department of Energy (DOE) Office of Science User Facility operated for the DOE Office of Science by Argonne National Laboratory under Contract No. DE-AC02-06CH11357.

5 Conclusions and Future Work

This thesis has successfully developed and validated experimental and theoretical methods for determining enthalpies of adsorption for polar molecules interacting with $\equiv\text{Si-OH}$ and $\equiv\text{Ti-OH}$ sites located on the surface of amorphous silica. We have done this utilizing *in-situ* IR spectroscopy, developed in Chapter 2. The enthalpies of adsorption measured in this way agree well with available microcalorimetry literature. We have also demonstrated that utilizing silsesquioxane models for $\equiv\text{Si-OH}$ groups results in consistent underestimation of the enthalpies of adsorption for polar molecules. By contrast, agreement to within 10% of experimental measurements can be achieved using a QM/MM approach in which a given $\equiv\text{Si-OH}$ or $\equiv\text{Ti-OH}$ site is surrounded by amorphous silica to a radius of more than 11 Å.

Chapter 2 found that the enthalpy of pyridine adsorption decreases with increasing pyridine coverage until 15% and then remains constant thereafter. The enthalpy of adsorption is directly proportional to the initial area of the $\equiv\text{Ti-OH}$ facet to which pyridine is bound. The majority of $\equiv\text{Ti-OH}$ sites are symmetrical tetrahedra, while a small portion (<15%) are distorted. These distorted sites could exhibit tetrahedral facet areas as large as 4.35 Å². Energy decomposition analysis (EDA) indicates that an increasing $\equiv\text{Ti-OH}$ site facet area increases the enthalpy of pyridine adsorption by enhancing frozen interactions and reducing the geometric distortion penalty that the $\equiv\text{Ti-OH}$ site experiences. Our findings suggest that we need to consider the role of distorted $\equiv\text{Ti-OH}$ sites in catalyzing reactions. Previously, these sites were largely considered to be minimally distorted tetrahedra.

In Chapter 3, we studied the effects of $\equiv\text{Ti-OH}$ site distortion on gas-phase cyclohexene epoxidation with H₂O₂. A general correlation was found between the tetrahedral facet area and the value of ΔH_{ads}° for all reactants and products. The enthalpies of transition states for H₂O₂ activation and O-atom transfer to cyclohexene were relatively insensitive to the facet area. Our calculations were used to determine rate coefficients for each step of a previously proposed mechanism. Further analysis revealed that smaller facet areas are required to prevent product inhibition and obtain agreement between theory and experiment. We discovered that when C₆H₁₀O adsorbs to the largest facet, the vacant facets of the same $\equiv\text{Ti-OH}$ site contract to a narrow range of facet areas (3.47 - 3.53 Å²). These *in-situ* generated, contracted facets become active for epoxidation, while C₆H₁₀O remains bound to the larger facet of the same $\equiv\text{Ti-OH}$ site. These findings demonstrate that analyzing the kinetics of reactions catalyzed by $\equiv\text{Ti-OH}$ sites should consider the distortion caused by the amorphous support and adsorbed species.

In Chapter 4, we found that isopropanol (IPA) dehydration to propene and water occurs through an E2 (concerted) mechanism with more C-H bond-breaking character than C-O bond-breaking character. The chapter used *in-situ* FTIR, XANES, and UV/Vis spectroscopy, revealing that under reaction conditions, isopropoxide groups are formed, and most $\equiv\text{Ti-OH}$ sites exhibit tetrahedral geometries. The study found that only 6% of active Ti sites are present, which was determined by combining the results of kinetic site-blocking measurements and *in-situ* FTIR spectroscopy. Preliminary QM/MM DFT calculations indicate that most $\equiv\text{Ti-OH}$ sites on Ti/SiO₂ favor the formation of $\equiv\text{Ti-OiPr}$ groups over molecularly adsorbed IPA and vacant $\equiv\text{Ti-OH}$ sites. The enthalpy barriers for the formation of propene from these groups are high, supporting the

observation that most $\equiv\text{Ti-OH}$ sites are not active for IPA dehydration. Transition states for E2 (concerted C-O and C-H bond cleavage) dehydration were also analyzed, which overestimated the experimentally observed activation energy. This chapter revealed that bulk spectroscopic techniques cannot identify the active sites for IPA dehydration since they are a minority species. Further research is needed to determine the active sites for this reaction.

There are several important avenues for future work:

1. We have established a method for measuring isosteric enthalpies of adsorption of pyridine bound exclusively to $\equiv\text{Ti-OH}$ sites. Scott and coworkers have demonstrated for Cr/SiO₂ that the silica pretreatment temperature prior to Cr deposition can affect the ability of the catalyst to initiate ethylene polymerization.⁸⁷ The ethylene polymerization induction period decreased as the silica support was pretreated at higher temperatures (from 200 °C to 800 °C). The authors propose that this was due to the generation of distorted Cr centers only for silica pretreated at high temperatures. Thus, future work could explore how the facet area distribution, interpreted from *in-situ* FTIR measured isosteric enthalpies of adsorption of pyridine bound to $\equiv\text{Ti-OH}$ sites, changes as a function of silica support pretreatment temperatures. A subsequent question would then be, how does this affect the catalytic activity of each material for a given reaction?
2. We leveraged a qualitative understanding of XANES pre-edge features to conclude that a diminution of absorbance results from Ti tetrahedral distortion. While V/SiO₂ time-dependent DFT calculations support these conclusions, further scrutiny of that work reveals that oscillator strengths are only sometimes adequately captured.¹¹ Therefore, future work is needed to develop better predictions of pre-edge XANES features from first principles DFT calculations based on a given structure of a $\equiv\text{Ti-OH}$ site. When this is established, simultaneous prediction of pre-edge XANES features, UV/Vis spectra, and isosteric enthalpies of adsorption of pyridine can be conducted based on an assumed distribution of distorted and undistorted $\equiv\text{Ti-OH}$ sites. If all experimental observables are well-described by the assumed distribution, this distribution of $\equiv\text{Ti-OH}$ sites should be utilized to calculate the kinetics of a reaction of interest using a microkinetic model.
3. As we reviewed in the introduction of this thesis, many metals can be used as SSMCs. The question is, how does the fraction of distorted metal sites changes as a function of the metal employed. Therefore, it would be interesting to utilize our experimental methodology for other SSMCs.
4. The last three points focus on the material after calcination but pre-reaction. As shown in Chapter 3, the facet area distribution can change under reaction conditions. Therefore, it would be interesting to investigate how measured isosteric enthalpies of adsorption change for a material pre and post-reaction.
5. In this thesis, we utilized empirical estimates for entropies of adsorbed species in our microkinetic models. A significant need is the ability to calculate entropies of adsorption from a small number of first-principles calculations. This would allow for the development of the rate coefficients used microkinetic models developed from first principles with a minimum amount empiricism. Good experimental benchmark data to compare calculations is a significant holdup for developing this field. Our *in-situ* FTIR method, developed in Chapter 2, can measure entropies of adsorption and enthalpies of adsorption. Therefore, we strongly recommend further employment of this method to establish an experimental

database of entropies of pyridine adsorption to multiple SSMCs and then developing methods for entropy of adsorption predictions using this database as a benchmark.

6. Chapter 3 concludes with a significant mechanistic proposition for cyclohexene epoxidation. To prove or disprove our proposal, future experimental work, such as in-situ FTIR and XAS, is needed to identify the presence of coadsorbed cyclohexene oxide.
7. We have established in Chapter 4 that IPA dehydration occurs on only a small fraction of Ti sites (<6%). Future work is needed to identify the structure of this active site.

6 References

- (1) *Spectroscopy of Transition Metal Ions on Surfaces*; Weckhuysen, B. M., Voort, P. van der, Catana, G., Eds.; Leuven University Press: Leuven, Belgium, 2000.
- (2) Hanna, D. G.; Shylesh, S.; Li, Y.-P.; Krishna, S.; Head-Gordon, M.; Bell, A. T. Experimental and Theoretical Study of *n*-Butanal Self-Condensation over Ti Species Supported on Silica. *ACS Catal.* **2014**, *4* (9), 2908–2916. <https://doi.org/10.1021/cs500704b>.
- (3) Marchese, L.; Maschmeyer, T.; Gianotti, E.; Coluccia, S.; Thomas, J. M. Probing the Titanium Sites in Ti–MCM41 by Diffuse Reflectance and Photoluminescence UV–Vis Spectroscopies. *J. Phys. Chem. B* **1997**, *101* (44), 8836–8838. <https://doi.org/10.1021/jp971963w>.
- (4) Gianotti, E.; Dellarocca, V.; Marchese, L.; Martra, G.; Coluccia, S.; Maschmeyer, T. NH₃ Adsorption on MCM-41 and Ti-Grafted MCM-41. FTIR, DR UV–Vis–NIR and Photoluminescence Studies. *Phys. Chem. Chem. Phys.* **2002**, *4* (24), 6109–6115. <https://doi.org/10.1039/B207231A>.
- (5) Maschmeyer, T.; Rey, F.; Sankar, G.; Thomas, J. M. Heterogeneous Catalysts Obtained by Grafting Metallocene Complexes onto Mesoporous Silica. *Nature* **1995**, *378* (6553), 159–162. <https://doi.org/10.1038/378159a0>.
- (6) Barker, C. M.; Gleeson, D.; Kaltsoyannis, N.; Catlow, C. R. A.; Sankar, G.; Thomas, J. M. On the Structure and Coordination of the Oxygen-Donating Species in Ti↑MCM-41/TBHP Oxidation Catalysts: A Density Functional Theory and EXAFS Study. *Phys. Chem. Chem. Phys.* **2002**, *4* (7), 1228–1240. <https://doi.org/10.1039/b104735n>.
- (7) Jarupatrakorn, J.; Tilley, T. D. Silica-Supported, Single-Site Titanium Catalysts for Olefin Epoxidation. A Molecular Precursor Strategy for Control of Catalyst Structure. *J. Am. Chem. Soc.* **2002**, *124* (28), 8380–8388. <https://doi.org/10.1021/ja0202208>.
- (8) Shylesh, S.; Bettinson, L. A.; Aljahri, A.; Head-Gordon, M.; Bell, A. T. Experimental and Computational Studies of Carbon–Carbon Bond Formation via Ketonization and Aldol Condensation over Site-Isolated Zirconium Catalysts. *ACS Catal.* **2020**, *10* (8), 4566–4579. <https://doi.org/10.1021/acscatal.9b05176>.
- (9) Conrad, S.; Verel, R.; Hammond, C.; Wolf, P.; Göttl, F.; Hermans, I. Cover Picture: Silica-Grafted Sn^{IV} Catalysts in Hydrogen-Transfer Reactions (ChemCatChem 20/2015). *ChemCatChem* **2015**, *7* (20), 3188–3188. <https://doi.org/10.1002/cctc.201501018>.
- (10) Thornburg, N. E.; Nauert, S. L.; Thompson, A. B.; Notestein, J. M. Synthesis–Structure–Function Relationships of Silica-Supported Niobium(V) Catalysts for Alkene Epoxidation with H₂O₂. *ACS Catal.* **2016**, *6* (9), 6124–6134. <https://doi.org/10.1021/acscatal.6b01796>.
- (11) Patel, P.; Lu, Z.; Jafari, M. G.; Hernández-Prieto, C.; Zatssep, P.; Mindiola, D. J.; Kaphan, D. M.; Delferro, M.; Kropf, A. J.; Liu, C. Integrated Experimental and Computational K-Edge X-Ray Absorption Near-Edge Structure Analysis of Vanadium Catalysts. *J. Phys. Chem. C* **2022**, *126* (29), 11949–11962. <https://doi.org/10.1021/acs.jpcc.2c02049>.
- (12) Patel, P.; Wells, R. H.; Kaphan, D. M.; Delferro, M.; Skodje, R. T.; Liu, C. Computational Investigation of the Role of Active Site Heterogeneity for a Supported Organovanadium(III) Hydrogenation Catalyst. *ACS Catal.* **2021**, *11* (12), 7257–7269. <https://doi.org/10.1021/acscatal.1c00688>.

- (13) Wells, R. H.; An, S.; Patel, P.; Liu, C.; Skodje, R. T. Single-Molecule Kinetics of Styrene Hydrogenation on Silica-Supported Vanadium: The Role of Disorder for Single-Atom Catalysts. *J. Phys. Chem. C* **2021**, *125* (37), 20286–20300. <https://doi.org/10.1021/acs.jpcc.1c04759>.
- (14) Wachs, I. E. Catalysis Science of Supported Vanadium Oxide Catalysts. *Dalton Trans.* **2013**, *42* (33), 11762. <https://doi.org/10.1039/c3dt50692d>.
- (15) Thornburg, N. E.; Thompson, A. B.; Notestein, J. M. Periodic Trends in Highly Dispersed Groups IV and V Supported Metal Oxide Catalysts for Alkene Epoxidation with H₂O₂. *ACS Catal.* **2015**, *5* (9), 5077–5088. <https://doi.org/10.1021/acscatal.5b01105>.
- (16) Chen, Y.; Fierro, J. L. G.; Tanaka, T.; Wachs, I. E. Supported Tantalum Oxide Catalysts: Synthesis, Physical Characterization, and Methanol Oxidation Chemical Probe Reaction. *J. Phys. Chem. B* **2003**, *107* (22), 5243–5250. <https://doi.org/10.1021/jp0276451>.
- (17) McDaniel, M. P. A Review of the Phillips Supported Chromium Catalyst and Its Commercial Use for Ethylene Polymerization. In *Advances in Catalysis*; Elsevier, 2010; Vol. 53, pp 123–606. [https://doi.org/10.1016/S0360-0564\(10\)53003-7](https://doi.org/10.1016/S0360-0564(10)53003-7).
- (18) Ewing, C. S.; Bagussety, A.; Patriarca, E. G.; Lambrecht, D. S.; Vesper, G.; Johnson, J. K. Impact of Support Interactions for Single-Atom Molybdenum Catalysts on Amorphous Silica. *Ind. Eng. Chem. Res.* **2016**, *55* (48), 12350–12357. <https://doi.org/10.1021/acs.iecr.6b03558>.
- (19) Ohler, N.; Bell, A. T. A Study of the Redox Properties of MoO_x/SiO₂. *J. Phys. Chem. B* **2005**, *109* (49), 23419–23429. <https://doi.org/10.1021/jp058230t>.
- (20) Ohler, N.; Bell, A. Selective Oxidation of Methane over MoO/SiO: Isolation of the Kinetics of Reactions Occurring in the Gas Phase and on the Surfaces of SiO and MoO. *Journal of Catalysis* **2005**, *231* (1), 115–130. <https://doi.org/10.1016/j.jcat.2004.12.024>.
- (21) Howell, J. G.; Li, Y.-P.; Bell, A. T. Propene Metathesis over Supported Tungsten Oxide Catalysts: A Study of Active Site Formation. *ACS Catal.* **2016**, *6* (11), 7728–7738. <https://doi.org/10.1021/acscatal.6b01842>.
- (22) Caricato, M. Cluster Model Simulations of Metal-Doped Amorphous Silicates for Heterogeneous Catalysis. *J. Phys. Chem. C* **2021**, *125* (50), 27509–27519. <https://doi.org/10.1021/acs.jpcc.1c07524>.
- (23) Goldsmith, B. R.; Peters, B.; Johnson, J. K.; Gates, B. C.; Scott, S. L. Beyond Ordered Materials: Understanding Catalytic Sites on Amorphous Solids. *ACS Catal.* **2017**, *7* (11), 7543–7557. <https://doi.org/10.1021/acscatal.7b01767>.
- (24) Peters, B.; Scott, S. L. Single Atom Catalysts on Amorphous Supports: A Quenched Disorder Perspective. *The Journal of Chemical Physics* **2015**, *142* (10), 104708. <https://doi.org/10.1063/1.4914145>.
- (25) Lichtenstein, L.; Büchner, C.; Yang, B.; Shaikhutdinov, S.; Heyde, M.; Sierka, M.; Włodarczyk, R.; Sauer, J.; Freund, H.-J. The Atomic Structure of a Metal-Supported Vitreous Thin Silica Film. *Angew. Chem. Int. Ed.* **2012**, *51* (2), 404–407. <https://doi.org/10.1002/anie.201107097>.
- (26) Liu, C.; Camacho-Bunquin, J.; Ferrandon, M.; Savara, A.; Sohn, H.; Yang, D.; Kaphan, D. M.; Langeslay, R. R.; Ignacio-de Leon, P. A.; Liu, S.; Das, U.; Yang, B.; Hock, A. S.; Stair, P. C.; Curtiss, L. A.; Delferro, M. Development of Activity–Descriptor Relationships for Supported Metal Ion Hydrogenation Catalysts on Silica. *Polyhedron* **2018**, *152*, 73–83. <https://doi.org/10.1016/j.poly.2018.06.006>.

- (27) Gao, X.; Wachs, I. E. Titania–Silica as Catalysts: Molecular Structural Characteristics and Physico–Chemical Properties. *Catalysis Today* **1999**, *51* (2), 233–254. [https://doi.org/10.1016/S0920-5861\(99\)00048-6](https://doi.org/10.1016/S0920-5861(99)00048-6).
- (28) Smeets, V.; Gaigneaux, E. M.; Debecker, D. P. Titanosilicate Epoxidation Catalysts: A Review of Challenges and Opportunities. *ChemCatChem* **2022**, *14* (1), e202101132. <https://doi.org/10.1002/cctc.202101132>.
- (29) Eaton, T. R.; Campos, M. P.; Gray, K. A.; Notestein, J. M. Quantifying Accessible Sites and Reactivity on Titania–Silica (Photo)Catalysts: Refining TOF Calculations. *Journal of Catalysis* **2014**, *309*, 156–165. <https://doi.org/10.1016/j.jcat.2013.09.015>.
- (30) Eaton, T. R.; Boston, A. M.; Thompson, A. B.; Gray, K. A.; Notestein, J. M. Counting Active Sites on Titanium Oxide–Silica Catalysts for Hydrogen Peroxide Activation through In Situ Poisoning with Phenylphosphonic Acid. *ChemCatChem* **2014**, *6* (11), 3215–3222. <https://doi.org/10.1002/cctc.201402611>.
- (31) Ardagh, M. A.; Bregante, D. T.; Flaherty, D. W.; Notestein, J. M. Controlled Deposition of Silica on Titania–Silica to Alter the Active Site Surroundings on Epoxidation Catalysts. *ACS Catal.* **2020**, *10* (21), 13008–13018. <https://doi.org/10.1021/acscatal.0c02937>.
- (32) Ahn, S.; Nauert, S. L.; Hicks, K. E.; Ardagh, M. A.; Schweitzer, N. M.; Farha, O. K.; Notestein, J. M. Demonstrating the Critical Role of Solvation in Supported Ti and Nb Epoxidation Catalysts via Vapor-Phase Kinetics. *ACS Catal.* **2020**, *10* (4), 2817–2825. <https://doi.org/10.1021/acscatal.9b04906>.
- (33) Bregante, D. T.; Thornburg, N. E.; Notestein, J. M.; Flaherty, D. W. Consequences of Confinement for Alkene Epoxidation with Hydrogen Peroxide on Highly Dispersed Group 4 and 5 Metal Oxide Catalysts. *ACS Catal.* **2018**, *8* (4), 2995–3010. <https://doi.org/10.1021/acscatal.7b03986>.
- (34) Notestein, J. M.; Andriani, L. R.; Kalchenko, V. I.; Requejo, F. G.; Katz, A.; Iglesia, E. Structural Assessment and Catalytic Consequences of the Oxygen Coordination Environment in Grafted Ti–Calixarenes. *J. Am. Chem. Soc.* **2007**, *129* (5), 1122–1131. <https://doi.org/10.1021/ja065830c>.
- (35) Kwon, O.; Ayla, E. Z.; Potts, D. S.; Flaherty, D. W. Effects of Solvent–Pore Interaction on Rates and Barriers for Vapor Phase Alkene Epoxidation with Gaseous H₂O₂ in Ti-BEA Catalysts. *ACS Catal.* **2023**, *13* (9), 6430–6444. <https://doi.org/10.1021/acscatal.3c00730>.
- (36) McDaniel, M. P. A Review of the Phillips Chromium Catalyst for Ethylene Polymerization. In *Handbook of Transition Metal Polymerization Catalysts*; Hoff, R., Ed.; John Wiley & Sons, Inc.: Hoboken, NJ, USA, 2018; pp 401–571. <https://doi.org/10.1002/9781119242277.ch13>.
- (37) Gani, T. Z. H.; Berkson, Z. J.; Zhu, R.; Kang, J. H.; Di Iorio, J. R.; Chan, K. W.; Consoli, D. F.; Shaikh, S. K.; Copéret, C.; Román-Leshkov, Y. Promoting Active Site Renewal in Heterogeneous Olefin Metathesis Catalysts. *Nature* **2023**, *617* (7961), 524–528. <https://doi.org/10.1038/s41586-023-05897-w>.
- (38) Tiozzo, C.; Bisio, C.; Carniato, F.; Gallo, A.; Scott, S. L.; Psaro, R.; Guidotti, M. Niobium–Silica Catalysts for the Selective Epoxidation of Cyclic Alkenes: The Generation of the Active Site by Grafting Niobocene Dichloride. *Phys. Chem. Chem. Phys.* **2013**, *15* (32), 13354. <https://doi.org/10.1039/c3cp51570b>.
- (39) Van der Mynsbrugge, J.; Bell, A. T. Challenges for the Theoretical Description of the Mechanism and Kinetics of Reactions Catalyzed by Zeolites. *Journal of Catalysis* **2021**, *404*, 832–849. <https://doi.org/10.1016/j.jcat.2021.08.048>.

- (40) Mansoor, E.; Van Der Mynsbrugge, J.; Head-Gordon, M.; Bell, A. T. Impact of Long-Range Electrostatic and Dispersive Interactions on Theoretical Predictions of Adsorption and Catalysis in Zeolites. *Catalysis Today* **2018**, *312*, 51–65. <https://doi.org/10.1016/j.cattod.2018.02.007>.
- (41) Kiselev, A. V.; Kuznetsov, B. V.; Lanin, S. N. Adsorption of Triethylamine and Water Vapor and the Modification of Silica Surface by Gaseous Trimethylchlorosilane. *Journal of Colloid and Interface Science* **1979**, *69* (1), 148–156. [https://doi.org/10.1016/0021-9797\(79\)90089-4](https://doi.org/10.1016/0021-9797(79)90089-4).
- (42) Kuznetsov, B. V.; Tuan, N. A.; Rachmanova, T. A. Calorimetric and Isosteric Heats of Adsorption of Substances with Molecules of Different Electronic Structure. *Adsorption Science & Technology* **1989**, *6* (1), 27–34. <https://doi.org/10.1177/026361748900600104>.
- (43) Curthoys, G.; Davydov, V. Y.; Kiselev, A. V.; Kiselev, S. A.; Kuznetsov, B. V. Hydrogen Bonding in Adsorption on Silica. *Journal of Colloid and Interface Science* **1974**, *48* (1), 58–72. [https://doi.org/10.1016/0021-9797\(74\)90328-2](https://doi.org/10.1016/0021-9797(74)90328-2).
- (44) Cardonamartinez, N. Acid Strength of Silica-Alumina and Silica Studied by Microcalorimetric Measurements of Pyridine Adsorption. *Journal of Catalysis* **1990**, *125* (2), 427–444. [https://doi.org/10.1016/0021-9517\(90\)90316-C](https://doi.org/10.1016/0021-9517(90)90316-C).
- (45) Hertl, W.; Hair, M. L. Hydrogen Bonding between Adsorbed Gases and Surface Hydroxyl Groups on Silica. *J. Phys. Chem.* **1968**, *72* (13), 4676–4682. <https://doi.org/10.1021/j100859a053>.
- (46) Armandi, M.; Bolis, V.; Bonelli, B.; Otero Areán, C.; Ugliengo, P.; Garrone, E. Silanol-Related and Unspecific Adsorption of Molecular Ammonia on Highly Dehydrated Silica. *J. Phys. Chem. C* **2011**, *115* (47), 23344–23353. <https://doi.org/10.1021/jp206301c>.
- (47) Day, R. E.; Kiselev, A. V.; Kuznetsov, B. V. Non-Specific, Specific Molecular and Chemical Adsorption of Tetrahydrofuran on Progressively Dehydroxylated Aerosilgel. *Trans. Faraday Soc.* **1969**, *65*, 1386. <https://doi.org/10.1039/tf9696501386>.
- (48) Noh, G.; Lam, E.; Bregante, D. T.; Meyet, J.; Šot, P.; Flaherty, D. W.; Copéret, C. Lewis Acid Strength of Interfacial Metal Sites Drives CH₃OH Selectivity and Formation Rates on Cu-Based CO₂ Hydrogenation Catalysts. *Angew. Chem.* **2021**, *133* (17), 9736–9745. <https://doi.org/10.1002/ange.202100672>.
- (49) Grosso-Giordano, N. A.; Hoffman, A. S.; Boubnov, A.; Small, D. W.; Bare, S. R.; Zones, S. I.; Katz, A. Dynamic Reorganization and Confinement of Ti^{IV} Active Sites Controls Olefin Epoxidation Catalysis on Two-Dimensional Zeotypes. *J. Am. Chem. Soc.* **2019**, *141* (17), 7090–7106. <https://doi.org/10.1021/jacs.9b02160>.
- (50) Horn, P. R.; Mao, Y.; Head-Gordon, M. Probing Non-Covalent Interactions with a Second Generation Energy Decomposition Analysis Using Absolutely Localized Molecular Orbitals. *Phys. Chem. Chem. Phys.* **2016**, *18* (33), 23067–23079. <https://doi.org/10.1039/C6CP03784D>.
- (51) Zhuravlev, L. T. The Surface Chemistry of Amorphous Silica. Zhuravlev Model. *Colloids and Surfaces A: Physicochemical and Engineering Aspects* **2000**, *173* (1–3), 1–38. [https://doi.org/10.1016/S0927-7757\(00\)00556-2](https://doi.org/10.1016/S0927-7757(00)00556-2).
- (52) Johnson, B. F. G.; Klunduk, M. C.; Martin, C. M.; Sankar, G.; Teate, S. J.; Meurig Thomas, J. The Preparation, Molecular Structure and Catalytic Relevance of Ti(OSiPh₃)₄ and Ti(OGepH₃)₄. *Journal of Organometallic Chemistry* **2000**, *596* (1–2), 221–225. [https://doi.org/10.1016/S0022-328X\(99\)00744-5](https://doi.org/10.1016/S0022-328X(99)00744-5).

- (53) Getsoian, A. “Bean”; Zhai, Z.; Bell, A. T. Band-Gap Energy as a Descriptor of Catalytic Activity for Propene Oxidation over Mixed Metal Oxide Catalysts. *J. Am. Chem. Soc.* **2014**, *136* (39), 13684–13697. <https://doi.org/10.1021/ja5051555>.
- (54) Harris, J. W.; Cordon, M. J.; Di Iorio, J. R.; Vega-Vila, J. C.; Ribeiro, F. H.; Gounder, R. Titration and Quantification of Open and Closed Lewis Acid Sites in Sn-Beta Zeolites That Catalyze Glucose Isomerization. *Journal of Catalysis* **2016**, *335*, 141–154. <https://doi.org/10.1016/j.jcat.2015.12.024>.
- (55) Crocellà, V.; Cerrato, G.; Magnacca, G.; Morterra, C. Adsorption of Acetone on Nonporous and Mesoporous Silica. *J. Phys. Chem. C* **2009**, *113* (37), 16517–16529. <https://doi.org/10.1021/jp903910n>.
- (56) Ravel, B.; Newville, M. *ATHENA*, *ARTEMIS*, *HEPHAESTUS*: Data Analysis for X-Ray Absorption Spectroscopy Using *IFEFFIT*. *J. Synchrotron Rad* **2005**, *12* (4), 537–541. <https://doi.org/10.1107/S0909049505012719>.
- (57) Chai, J.-D.; Head-Gordon, M. Long-Range Corrected Hybrid Density Functionals with Damped Atom–Atom Dispersion Corrections. *Phys. Chem. Chem. Phys.* **2008**, *10* (44), 6615–6620. <https://doi.org/10.1039/B810189B>.
- (58) Mardirossian, N.; Head-Gordon, M. ω B97M-V: A Combinatorially Optimized, Range-Separated Hybrid, Meta-GGA Density Functional with VV10 Nonlocal Correlation. *J. Chem. Phys.* **2016**, *144* (21), 214110. <https://doi.org/10.1063/1.4952647>.
- (59) Mardirossian, N.; Head-Gordon, M. Thirty Years of Density Functional Theory in Computational Chemistry: An Overview and Extensive Assessment of 200 Density Functionals. *Molecular Physics* **2017**, *115* (19), 2315–2372. <https://doi.org/10.1080/00268976.2017.1333644>.
- (60) Dasgupta, S.; Herbert, J. M. Standard Grids for High-precision Integration of Modern Density Functionals: SG-2 and SG-3. *J. Comput. Chem.* **2017**, *38* (12), 869–882. <https://doi.org/10.1002/jcc.24761>.
- (61) Li, Y.-P.; Gomes, J.; Mallikarjun Sharada, S.; Bell, A. T.; Head-Gordon, M. Improved Force-Field Parameters for QM/MM Simulations of the Energies of Adsorption for Molecules in Zeolites and a Free Rotor Correction to the Rigid Rotor Harmonic Oscillator Model for Adsorption Enthalpies. *J. Phys. Chem. C* **2015**, *119* (4), 1840–1850. <https://doi.org/10.1021/jp509921r>.
- (62) Grimme, S. Supramolecular Binding Thermodynamics by Dispersion-Corrected Density Functional Theory. *Chem. Eur. J.* **2012**, *18* (32), 9955–9964. <https://doi.org/10.1002/chem.201200497>.
- (63) Zimmerman, P. M.; Head-Gordon, M.; Bell, A. T. Selection and Validation of Charge and Lennard-Jones Parameters for QM/MM Simulations of Hydrocarbon Interactions with Zeolites. *J. Chem. Theory Comput.* **2011**, *7* (6), 1695–1703. <https://doi.org/10.1021/ct2001655>.
- (64) Vandervelden, C.; Jystad, A.; Peters, B.; Caricato, M. Predicted Properties of Active Catalyst Sites on Amorphous Silica: Impact of Silica Preoptimization Protocol. *Ind. Eng. Chem. Res.* **2021**, *60* (35), 12834–12846. <https://doi.org/10.1021/acs.iecr.1c01849>.
- (65) Epifanovsky, E.; Gilbert, A. T. B.; Feng, X.; Lee, J.; Mao, Y.; Mardirossian, N.; Pokhilko, P.; White, A. F.; Coons, M. P.; Dempwolff, A. L.; Gan, Z.; Hait, D.; Horn, P. R.; Jacobson, L. D.; Kaliman, I.; Kussmann, J.; Lange, A. W.; Lao, K. U.; Levine, D. S.; Liu, J.; McKenzie, S. C.; Morrison, A. F.; Nanda, K. D.; Plasser, F.; Rehn, D. R.; Vidal, M. L.; You, Z.-Q.; Zhu, Y.; Alam, B.; Albrecht, B. J.; Aldossary, A.; Alguire, E.; Andersen, J.

- H.; Athavale, V.; Barton, D.; Begam, K.; Behn, A.; Bellonzi, N.; Bernard, Y. A.; Berquist, E. J.; Burton, H. G. A.; Carreras, A.; Carter-Fenk, K.; Chakraborty, R.; Chien, A. D.; Closser, K. D.; Cofer-Shabica, V.; Dasgupta, S.; de Wergifosse, M.; Deng, J.; Diedenhofen, M.; Do, H.; Ehlert, S.; Fang, P.-T.; Fatehi, S.; Feng, Q.; Friedhoff, T.; Gayvert, J.; Ge, Q.; Gidofalvi, G.; Goldey, M.; Gomes, J.; González-Espinoza, C. E.; Gulania, S.; Gunina, A. O.; Hanson-Heine, M. W. D.; Harbach, P. H. P.; Hauser, A.; Herbst, M. F.; Hernández Vera, M.; Hodecker, M.; Holden, Z. C.; Houck, S.; Huang, X.; Hui, K.; Huynh, B. C.; Ivanov, M.; Jász, Á.; Ji, H.; Jiang, H.; Kaduk, B.; Kähler, S.; Khistyayev, K.; Kim, J.; Kis, G.; Klunzinger, P.; Koczor-Benda, Z.; Koh, J. H.; Kosenkov, D.; Koulias, L.; Kowalczyk, T.; Krauter, C. M.; Kue, K.; Kunitsa, A.; Kus, T.; Ladjánszki, I.; Landau, A.; Lawler, K. V.; Lefrancois, D.; Lehtola, S.; Li, R. R.; Li, Y.-P.; Liang, J.; Liebenthal, M.; Lin, H.-H.; Lin, Y.-S.; Liu, F.; Liu, K.-Y.; Loipersberger, M.; Luenser, A.; Manjanath, A.; Manohar, P.; Mansoor, E.; Manzer, S. F.; Mao, S.-P.; Marenich, A. V.; Markovich, T.; Mason, S.; Maurer, S. A.; McLaughlin, P. F.; Menger, M. F. S. J.; Mewes, J.-M.; Mewes, S. A.; Morgante, P.; Mullinax, J. W.; Oosterbaan, K. J.; Paran, G.; Paul, A. C.; Paul, S. K.; Pavošević, F.; Pei, Z.; Prager, S.; Proynov, E. I.; Rák, Á.; Ramos-Cordoba, E.; Rana, B.; Rask, A. E.; Rettig, A.; Richard, R. M.; Rob, F.; Rossomme, E.; Scheele, T.; Scheurer, M.; Schneider, M.; Sergueev, N.; Sharada, S. M.; Skomorowski, W.; Small, D. W.; Stein, C. J.; Su, Y.-C.; Sundstrom, E. J.; Tao, Z.; Thirman, J.; Tornai, G. J.; Tsuchimochi, T.; Tubman, N. M.; Veccham, S. P.; Vydrov, O.; Wenzel, J.; Witte, J.; Yamada, A.; Yao, K.; Yeganeh, S.; Yost, S. R.; Zech, A.; Zhang, I. Y.; Zhang, X.; Zhang, Y.; Zuev, D.; Aspuru-Guzik, A.; Bell, A. T.; Besley, N. A.; Bravaya, K. B.; Brooks, B. R.; Casanova, D.; Chai, J.-D.; Coriani, S.; Cramer, C. J.; Cserey, G.; DePrince, A. E.; DiStasio, R. A.; Dreuw, A.; Dunietz, B. D.; Furlani, T. R.; Goddard, W. A.; Hammes-Schiffer, S.; Head-Gordon, T.; Hehre, W. J.; Hsu, C.-P.; Jagau, T.-C.; Jung, Y.; Klamt, A.; Kong, J.; Lambrecht, D. S.; Liang, W.; Mayhall, N. J.; McCurdy, C. W.; Neaton, J. B.; Ochsenfeld, C.; Parkhill, J. A.; Peverati, R.; Rassolov, V. A.; Shao, Y.; Slipchenko, L. V.; Stauch, T.; Steele, R. P.; Subotnik, J. E.; Thom, A. J. W.; Tkatchenko, A.; Truhlar, D. G.; Van Voorhis, T.; Wesolowski, T. A.; Whaley, K. B.; Woodcock, H. L.; Zimmerman, P. M.; Faraji, S.; Gill, P. M. W.; Head-Gordon, M.; Herbert, J. M.; Krylov, A. I. Software for the Frontiers of Quantum Chemistry: An Overview of Developments in the Q-Chem 5 Package. *J. Chem. Phys.* **2021**, *155* (8), 084801. <https://doi.org/10.1063/5.0055522>.
- (66) Schweitzer, N. M.; Hu, B.; Das, U.; Kim, H.; Greeley, J.; Curtiss, L. A.; Stair, P. C.; Miller, J. T.; Hock, A. S. Propylene Hydrogenation and Propane Dehydrogenation by a Single-Site Zn²⁺ on Silica Catalyst. *ACS Catal.* **2014**, *4* (4), 1091–1098. <https://doi.org/10.1021/cs401116p>.
- (67) Gierada, M.; Petit, I.; Handzlik, J.; Tielens, F. Hydration in Silica Based Mesoporous Materials: A DFT Model. *Phys. Chem. Chem. Phys.* **2016**, *18* (48), 32962–32972. <https://doi.org/10.1039/C6CP05460A>.
- (68) Tielens, F.; Gierada, M.; Handzlik, J.; Calatayud, M. Characterization of Amorphous Silica Based Catalysts Using DFT Computational Methods. *Catalysis Today* **2020**, *354*, 3–18. <https://doi.org/10.1016/j.cattod.2019.03.062>.
- (69) Parry, E. An Infrared Study of Pyridine Adsorbed on Acidic Solids. Characterization of Surface Acidity. *Journal of Catalysis* **1963**, *2* (5), 371–379. [https://doi.org/10.1016/0021-9517\(63\)90102-7](https://doi.org/10.1016/0021-9517(63)90102-7).

- (70) Jystad, A.; Leblanc, H.; Caricato, M. Surface Acidity Characterization of Metal-Doped Amorphous Silicates via Py-FTIR and ^{15}N NMR Simulations. *J. Phys. Chem. C* **2020**, *124* (28), 15231–15240. <https://doi.org/10.1021/acs.jpcc.0c03292>.
- (71) Suib, S. L.; Přeč, J.; Szaniawska, E.; Čejka, J. Recent Advances in Tetra- (Ti, Sn, Zr, Hf) and Pentavalent (Nb, V, Ta) Metal-Substituted Molecular Sieve Catalysis. *Chem. Rev.* **2023**, *123* (3), 877–917. <https://doi.org/10.1021/acs.chemrev.2c00509>.
- (72) Child, M. J.; Heywood, M. J.; Pulton, S. K.; Vicary, G. A.; Geok Hua Yong; Rochester, C. H. Infrared Studies of the Adsorption of Triethylamine on Silica at the Solid/Vapor and Solid/Liquid Interfaces. *Journal of Colloid and Interface Science* **1982**, *89* (1), 202–208. [https://doi.org/10.1016/0021-9797\(82\)90133-3](https://doi.org/10.1016/0021-9797(82)90133-3).
- (73) Bregante, D. T.; Johnson, A. M.; Patel, A. Y.; Ayla, E. Z.; Cordon, M. J.; Bukowski, B. C.; Greeley, J.; Gounder, R.; Flaherty, D. W. Cooperative Effects between Hydrophilic Pores and Solvents: Catalytic Consequences of Hydrogen Bonding on Alkene Epoxidation in Zeolites. *J. Am. Chem. Soc.* **2019**, *141* (18), 7302–7319. <https://doi.org/10.1021/jacs.8b12861>.
- (74) Sushkevich, V. L.; Vimont, A.; Travert, A.; Ivanova, I. I. Spectroscopic Evidence for Open and Closed Lewis Acid Sites in ZrBEA Zeolites. *J. Phys. Chem. C* **2015**, *119* (31), 17633–17639. <https://doi.org/10.1021/acs.jpcc.5b02745>.
- (75) Linstrom, P. NIST Chemistry WebBook, NIST Standard Reference Database 69, 1997. <https://doi.org/10.18434/T4D303>.
- (76) Kachurovskaya, N. A.; Zhidomirov, G. M.; Aristov, Y. I. On the Problem of Differentiation of Acetone Adsorption Species on the Silica Gel: Molecular Models of Adsorption Complexes. *Journal of Molecular Catalysis A: Chemical* **2000**, *158* (1), 281–285. [https://doi.org/10.1016/S1381-1169\(00\)00091-1](https://doi.org/10.1016/S1381-1169(00)00091-1).
- (77) Zhang, K.; Caricato, M. Modeling Catalyzed Reactions on Metal-Doped Amorphous Silicates: The Case of Niobium-Catalyzed Ethylene Epoxidation. *J. Phys. Chem. C* **2023**, *127* (10), 4984–4997. <https://doi.org/10.1021/acs.jpcc.3c00213>.
- (78) DiVerdi, J. A.; Kobayashi, T.; Maciel, G. E. Molecular Dynamics of Pyridine Adsorbed on the Silica Surface. *J. Phys. Chem. C* **2007**, *111* (16), 5982–5989. <https://doi.org/10.1021/jp067353q>.
- (79) Campbell, C. T.; Sellers, J. R. V. The Entropies of Adsorbed Molecules. *J. Am. Chem. Soc.* **2012**, *134* (43), 18109–18115. <https://doi.org/10.1021/ja3080117>.
- (80) Bukowski, B. C.; Bates, J. S.; Gounder, R.; Greeley, J. First Principles, Microkinetic, and Experimental Analysis of Lewis Acid Site Speciation during Ethanol Dehydration on Sn-Beta Zeolites. *Journal of Catalysis* **2018**, *365*, 261–276. <https://doi.org/10.1016/j.jcat.2018.07.012>.
- (81) Johnson, R. Computational Chemistry Comparison and Benchmark Database, NIST Standard Reference Database 101, 2002. <https://doi.org/10.18434/T47C7Z>.
- (82) Putnam, W. E.; McEachern, D. M.; Kilpatrick, J. E. Entropy and Related Thermodynamic Properties of Acetonitrile (Methyl Cyanide). *The Journal of Chemical Physics* **1965**, *42* (2), 749–755. <https://doi.org/10.1063/1.1696002>.
- (83) Westrum, E. F.; Ribner, A. Trimethylacetone. Low-Temperature Heat Capacity, Vapor Pressure, and Chemical Thermodynamics of the Crystalline, Liquid, and Gaseous Phases. *J. Phys. Chem.* **1967**, *71* (5), 1216–1224. <https://doi.org/10.1021/j100864a006>.

- (84) Ratnasamy, P.; Srinivas, D.; Knözinger, H. Active Sites and Reactive Intermediates in Titanium Silicate Molecular Sieves. In *Advances in Catalysis*; Elsevier, 2004; Vol. 48, pp 1–169. [https://doi.org/10.1016/S0360-0564\(04\)48001-8](https://doi.org/10.1016/S0360-0564(04)48001-8).
- (85) Yamamoto, T. Assignment of Pre-Edge Peaks in K-Edge x-Ray Absorption Spectra of 3d Transition Metal Compounds: Electric Dipole or Quadrupole? *X-Ray Spectrom.* **2008**, *37* (6), 572–584. <https://doi.org/10.1002/xrs.1103>.
- (86) Farges, F.; Brown, G. E.; Rehr, J. J. Ti K -Edge XANES Studies of Ti Coordination and Disorder in Oxide Compounds: Comparison between Theory and Experiment. *Phys. Rev. B* **1997**, *56* (4), 1809–1819. <https://doi.org/10.1103/PhysRevB.56.1809>.
- (87) Demmelmaier, C. A.; White, R. E.; Van Bokhoven, J. A.; Scott, S. L. Evidence for a Chromasiloxane Ring Size Effect in Phillips (Cr/SiO₂) Polymerization Catalysts. *Journal of Catalysis* **2009**, *262* (1), 44–56. <https://doi.org/10.1016/j.jcat.2008.11.024>.
- (88) De Clercq, R.; Dusselier, M.; Poleunis, C.; Debecker, D. P.; Giebler, L.; Oswald, S.; Makshina, E.; Sels, B. F. Titania-Silica Catalysts for Lactide Production from Renewable Alkyl Lactates: Structure–Activity Relations. *ACS Catal.* **2018**, *8* (9), 8130–8139. <https://doi.org/10.1021/acscatal.8b02216>.
- (89) Gao, X.; Bare, S. R.; Fierro, J. L. G.; Banares, M. A.; Wachs, I. E. Preparation and In-Situ Spectroscopic Characterization of Molecularly Dispersed Titanium Oxide on Silica. *J. Phys. Chem. B* **1998**, *102* (29), 5653–5666. <https://doi.org/10.1021/jp981423e>.
- (90) Zaki, M. I.; Hasan, M. A.; Al-Sagheer, F. A.; Pasupulety, L. In Situ FTIR Spectra of Pyridine Adsorbed on SiO₂–Al₂O₃, TiO₂, ZrO₂ and CeO₂: General Considerations for the Identification of Acid Sites on Surfaces of Finely Divided Metal Oxides. *Colloids and Surfaces A: Physicochemical and Engineering Aspects* **2001**, *190* (3), 261–274. [https://doi.org/10.1016/S0927-7757\(01\)00690-2](https://doi.org/10.1016/S0927-7757(01)00690-2).
- (91) Cordon, M. J.; Harris, J. W.; Vega-Vila, J. C.; Bates, J. S.; Kaur, S.; Gupta, M.; Witzke, M. E.; Wegener, E. C.; Miller, J. T.; Flaherty, D. W.; Hibbitts, D. D.; Gounder, R. Dominant Role of Entropy in Stabilizing Sugar Isomerization Transition States within Hydrophobic Zeolite Pores. *J. Am. Chem. Soc.* **2018**, *140* (43), 14244–14266. <https://doi.org/10.1021/jacs.8b08336>.
- (92) Zholobenko, V.; Freitas, C.; Jendrlin, M.; Bazin, P.; Travert, A.; Thibault-Starzyk, F. Probing the Acid Sites of Zeolites with Pyridine: Quantitative AGIR Measurements of the Molar Absorption Coefficients. *Journal of Catalysis* **2020**, *385*, 52–60. <https://doi.org/10.1016/j.jcat.2020.03.003>.
- (93) Grosso-Giordano, N. A.; Zones, S. I.; Katz, A. Opportunities for Controlling Catalysis by Designing Molecular Environments around Active Sites: Cations Supported on Amorphous versus Crystalline Zeolitic Silicate Supports. In *Catalysis*; Spivey, J., Han, Y.-F., Shekhawat, D., Eds.; Royal Society of Chemistry: Cambridge, 2019; Vol. 31, pp 72–126. <https://doi.org/10.1039/9781788016971-00072>.
- (94) Gleeson, D.; Sankar, G.; Richard A. Catlow, C.; Meurig Thomas, J.; Spanó, G.; Bordiga, S.; Zecchina, A.; Lamberti, C. The Architecture of Catalytically Active Centers in Titanosilicate (TS-1) and Related Selective-Oxidation Catalysts. *Phys. Chem. Chem. Phys.* **2000**, *2* (20), 4812–4817. <https://doi.org/10.1039/b005780k>.
- (95) Bregante, D. T.; Flaherty, D. W. Periodic Trends in Olefin Epoxidation over Group IV and V Framework-Substituted Zeolite Catalysts: A Kinetic and Spectroscopic Study. *J. Am. Chem. Soc.* **2017**, *139* (20), 6888–6898. <https://doi.org/10.1021/jacs.7b01422>.

- (96) Thomas, J. M.; Sankar, G. The Role of Synchrotron-Based Studies in the Elucidation and Design of Active Sites in Titanium–Silica Epoxidation Catalysts. *Acc. Chem. Res.* **2001**, *34* (7), 571–581. <https://doi.org/10.1021/ar010003w>.
- (97) Sankar, G.; Thomas, J. M.; Catlow, C. R. A.; Barker, C. M.; Gleeson, D.; Kaltsoyannis, N. The Three-Dimensional Structure of the Titanium-Centered Active Site during Steady-State Catalytic Epoxidation of Alkenes. *J. Phys. Chem. B* **2001**, *105* (38), 9028–9030. <https://doi.org/10.1021/jp011979t>.
- (98) Yoon, C. W.; Hirsekorn, K. F.; Neidig, M. L.; Yang, X.; Tilley, T. D. Mechanism of the Decomposition of Aqueous Hydrogen Peroxide over Heterogeneous TiSBA15 and TS-1 Selective Oxidation Catalysts: Insights from Spectroscopic and Density Functional Theory Studies. *ACS Catal.* **2011**, *1* (12), 1665–1678. <https://doi.org/10.1021/cs2003774>.
- (99) Lu, Z.; Liu, X.; Zhang, B.; Gan, Z.; Tang, S.; Ma, L.; Wu, T.; Nelson, G. J.; Qin, Y.; Turner, C. H.; Lei, Y. Structure and Reactivity of Single Site Ti Catalysts for Propylene Epoxidation. *Journal of Catalysis* **2019**, *377*, 419–428. <https://doi.org/10.1016/j.jcat.2019.07.051>.
- (100) Sever, R. R.; Root, T. W. DFT Study of Solvent Coordination Effects on Titanium-Based Epoxidation Catalysts. Part One: Formation of the Titanium Hydroperoxo Intermediate. *J. Phys. Chem. B* **2003**, *107* (17), 4080–4089. <https://doi.org/10.1021/jp026056s>.
- (101) Sever, R. R.; Root, T. W. DFT Study of Solvent Coordination Effects on Titanium-Based Epoxidation Catalysts. Part Two: Reactivity of Titanium Hydroperoxo Complexes in Ethylene Epoxidation. *J. Phys. Chem. B* **2003**, *107* (17), 4090–4099. <https://doi.org/10.1021/jp026057k>.
- (102) Finzel, J.; Sanroman Gutierrez, K. M.; Hoffman, A. S.; Resasco, J.; Christopher, P.; Bare, S. R. Limits of Detection for EXAFS Characterization of Heterogeneous Single-Atom Catalysts. *ACS Catal.* **2023**, *13* (9), 6462–6473. <https://doi.org/10.1021/acscatal.3c01116>.
- (103) Motagamwala, A. H.; Dumesic, J. A. Microkinetic Modeling: A Tool for Rational Catalyst Design. *Chem. Rev.* **2021**, *121* (2), 1049–1076. <https://doi.org/10.1021/acs.chemrev.0c00394>.
- (104) Behn, A.; Zimmerman, P. M.; Bell, A. T.; Head-Gordon, M. Efficient Exploration of Reaction Paths via a Freezing String Method. *The Journal of Chemical Physics* **2011**, *135* (22), 224108. <https://doi.org/10.1063/1.3664901>.
- (105) Campbell, C. T.; Sellers, J. R. V. Enthalpies and Entropies of Adsorption on Well-Defined Oxide Surfaces: Experimental Measurements. *Chem. Rev.* **2013**, *113* (6), 4106–4135. <https://doi.org/10.1021/cr300329s>.
- (106) Campbell, C. T. The Degree of Rate Control: A Powerful Tool for Catalysis Research. *ACS Catal.* **2017**, *7* (4), 2770–2779. <https://doi.org/10.1021/acscatal.7b00115>.
- (107) Boronat, M.; Corma, A.; Renz, M.; Viruela, P. M. Predicting the Activity of Single Isolated Lewis Acid Sites in Solid Catalysts. *Chemistry A European J* **2006**, *12* (27), 7067–7077. <https://doi.org/10.1002/chem.200600478>.
- (108) Muettterties, E. L.; Wright, C. M. Molecular Polyhedra of High Co-Ordination Number. *Q. Rev., Chem. Soc.* **1967**, *21* (1), 109. <https://doi.org/10.1039/qr9672100109>.
- (109) Mul, G.; Zwijnenburg, A.; van der Linden, B.; Makkee, M.; Moulijn, J. A. Stability and Selectivity of Au/TiO₂ and Au/TiO₂/SiO₂ Catalysts in Propene Epoxidation: An in Situ FT-IR Study. *Journal of Catalysis* **2001**, *201* (1), 128–137. <https://doi.org/10.1006/jcat.2001.3239>.

- (110) Levenspiel, O. *Chemical Reaction Engineering. Hauptbd.*, 3. ed.; Wiley: New York Weinheim, 1999.
- (111) Mostafa, M. R.; Youssef, A. M.; Hassan, S. M. Conversion of Ethanol and Isopropanol on Alumina, Titania and Alumina-Titania Catalysts. *Materials Letters* **1991**, *12* (3), 207–213. [https://doi.org/10.1016/0167-577X\(91\)90176-7](https://doi.org/10.1016/0167-577X(91)90176-7).
- (112) Kang, M.; DeWilde, J. F.; Bhan, A. Kinetics and Mechanism of Alcohol Dehydration on γ -Al₂O₃: Effects of Carbon Chain Length and Substitution. *ACS Catal.* **2015**, *5* (2), 602–612. <https://doi.org/10.1021/cs501471r>.
- (113) Fraile, J.; Garcia, J.; Mayoral, J.; Vispe, E. Catalytic Sites in Silica-Supported Titanium Catalysts: Silsesquioxane Complexes as Models. *Journal of Catalysis* **2005**, *233* (1), 90–99. <https://doi.org/10.1016/j.jcat.2005.04.018>.
- (114) Luts, T.; Katz, A. Chemisorption and Dehydration of Ethanol on Silica: Effect of Temperature on Selectivity. *Top Catal* **2012**, *55* (1–2), 84–92. <https://doi.org/10.1007/s11244-012-9771-9>.
- (115) Lin, F.; Chen, Y.; Zhang, L.; Mei, D.; Kovarik, L.; Sudduth, B.; Wang, H.; Gao, F.; Wang, Y. Single-Facet Dominant Anatase TiO₂ (101) and (001) Model Catalysts to Elucidate the Active Sites for Alkanol Dehydration. *ACS Catal.* **2020**, *10* (7), 4268–4279. <https://doi.org/10.1021/acscatal.9b04654>.
- (116) Laidler, K. J. *Chemical Kinetics*, 3rd ed.; Harper & Row: New York, 1987.
- (117) Knozinger, H. The Dehydration of Alcohols on Alumina XII. Kinetic Isotope Effects in the Olefin Formation from Butanols. *Journal of Catalysis* **1970**, *17* (2), 252–263. [https://doi.org/10.1016/0021-9517\(70\)90098-9](https://doi.org/10.1016/0021-9517(70)90098-9).
- (118) Carey, F. *Advanced Organic Chemistry*, 5th ed.; Advanced Organic Chemistry; Springer US: Boston, MA, 2007. <https://doi.org/10.1007/978-0-387-44899-2>.
- (119) Zwijnenburg, M. A.; Simperler, A.; Wells, S. A.; Bell, R. G. Tetrahedral Distortion and Energetic Packing Penalty in “Zeolite” Frameworks: Linked Phenomena? *J. Phys. Chem. B* **2005**, *109* (31), 14783–14785. <https://doi.org/10.1021/jp0531309>.
- (120) Duffy, J. A.; Macphee, D. E. The Coordination Number of Silicon in Silicon–Oxygen Compounds: The Special Case of 6-Fold Coordination in Thauasite. *J. Phys. Chem. B* **2007**, *111* (30), 8740–8745. <https://doi.org/10.1021/jp071343n>.